

Investigation of Ultrasonic Acoustic Standing Wave Separation of Particles  
in a Multi-wavelength Macro-scale Resonator

by

Alireza Setayeshgar

A thesis submitted in partial fulfillment of the requirements for the degree of

Doctor of Philosophy

Department of Mechanical Engineering  
University of Alberta

© Alireza Setayeshgar, 2014

## **ABSTRACT**

This thesis presents an investigation of macro-scale (>5mm) multi-wavelength acoustophoresis. This is a technique used for the filtration of micro-particles from the containing suspension. It uses the primary acoustic force generated by an ultrasonic acoustic pressure standing wave. Primary acoustic force is isolated in different multi-wavelength acoustic separator experiments and imaging methods are used to capture the motion of particles separating from the containing fluid. Different investigation methods and models for analyzing the macro-scale acoustic resonators are developed and the experimented acoustic resonators are characterized.

A particle tracking velocimetry (PTV) approach for measuring individual particle motion is developed specifically to track particles over the lifetime of their motion as they densify to an acoustic pressure node. The applicability of primary acoustic force theory to the macro-scale acoustic resonators is validated by applying the PTV method to images of densification of mono-disperse size and poly-dispersed size particles. Utilizing the developed validated PTV method, the acoustic energy density, a parameter that can only be derived from experiments is also determined. A probability density function (PDF) modeling the location of particles for determination of acoustic energy density is also developed which is in agreement with the PTV method.

The influence of dampening and scattering of the acoustic wave in macro-scale multi-wavelength is studied. This is performed by variation of piezo-electric transducer (PZT) voltage and changing the viscosity of the suspension by using different solutions of

glycerol in water. The resulting acoustic energy density dependence on PZT voltage in macro-scale multi-wavelength acoustic resonators is observed to be different from that of micro-scale acoustic resonators. This effect, which is visible in all different experimented suspensions, indicates that macro-scale multi-wavelength acoustic resonators inherently show more dampening effects than micro-scale acoustic resonators.

This dissertation is dedicated to my father, my mother and my wife for their continual support.

## **ACKNOWLEDGEMENT**

This thesis is submitted as partial fulfillment for obtaining the degree of Doctor of Philosophy (PhD) at University of Alberta. Funding support for this PhD project was by the Centre for Oil Sands Innovation (COSI), Alberta Ingenuity Fund, the Natural Sciences and Research Council (NSERC) of Canada and the Canadian Foundation of Innovation (CFI). The project was carried out at Mechanical Engineering department. The project was supervised by Dr. David S. Nobes and Dr. Charles R. Koch.

I would like to acknowledge the people whom I was meeting during my PhD program. Primarily I would like to thank Dr. David S. Nobes for always having his office door open for scientific discussions. He made sure I grew as an independent researcher by allowing me to solve various issues. He is a great mentor in designing experimental setups as well. We had many great non-academic times together in Netherland during PIV2013 conference and Poland during ICU2011 conference. I would like also to thank Dr. Charles R. Koch as my co-supervisor for having different scientific discussion meeting and guiding me in technical writing. Thanks to all my friends and family whose support through this project is highly appreciated.

Alireza Setayeshgar

# TABLE OF CONTENT

## Contents

Abstract .....	ii
List of Tables .....	x
List of Figures.....	xii
CHAPTER 1: Introduction.....	1
1.1 Introduction.....	1
1.2 Ultrasonic acoustophoresis filtration .....	2
1.2.1 Micro-scale acoustic filtration .....	3
1.2.2 Macro-scale acoustic filtration .....	5
1.3 Theory of acoustic force on particles .....	9
1.3.1 Primary acoustic force theory .....	10
1.3.2 Other acoustic forces .....	14
1.3.3 Theoretical transverse velocity of particles .....	18
1.4 Experimental investigation of acoustophoresis .....	21
1.4.1 Particle trapping techniques .....	22
1.4.2 Imaging techniques .....	23
1.5 Objectives .....	28

1.6 Thesis outline.....	29
1.7 List of contribution .....	31
CHAPTER 2: Experimental method and apparatus .....	33
2.1 Introduction.....	33
2.2 Preliminary experimental setup .....	33
2.2.1 Static chamber.....	34
2.2.2 Acoustic channel.....	44
2.3 Main experimental setup .....	52
2.3.1 Macro-scale acoustic resonator .....	53
2.3.2 Imaging system.....	56
2.3.3 Experiment procedure.....	57
2.3.4 Initial results .....	59
2.4 Summary.....	61
CHAPTER 3: Development of a PTV algorithm for investigating macro-scale acoustophoresis .....	62
3.1 Introduction.....	62
3.2 PTV-processing .....	69
3.2.1 Image preprocessing .....	69

3.2.2 Particle detection .....	70
3.2.3 Particle motion .....	77
3.2.4 Uncertainty analysis .....	85
3.3 Summary.....	87
CHAPTER 4: Investigation of primary acoustic force using PTV .....	88
4.1 Introduction.....	88
4.2 PTV algorithm validation .....	88
4.2.1 Synthetic images of particles.....	89
4.2.2 Acoustophoresis simulation of particles .....	91
4.2.3 Variation of particle density of fluid system in synthetic images .....	93
4.2.4 Synthetic images analysis using the developed PTV algorithm .....	94
4.2.5 Summary.....	102
4.3 Experimental transverse velocity of particles .....	102
4.3.1 Mono-dispersed particles.....	102
4.3.2 Poly-dispersed particle sizes.....	109
4.3.3 Independency analysis .....	114
4.4 Summary.....	117

CHAPTER 5: Multi-wavelength macro-scale acoustic resonator characterization	
using PTV.....	118
5.1 Introduction.....	118
5.2 Theoretical background.....	120
5.2.1 Acoustic resonator characterization .....	120
5.2.2 Suspension fluid properties effect on characterization .....	122
5.3 Experimental particle motion.....	123
5.4 Acoustic resonator performance parametric study .....	129
5.5 Acoustic energy density.....	131
5.5.1 Particle properties effect.....	132
5.5.2 Effect of PZT voltage and glycerol concentration .....	134
5.6 Conclusion .....	140
CHAPTER 6: Characterization of multi-wavelength macro-scale acoustic resonator	
using a PDF model.....	142
6.1 Introduction.....	142
6.2 Image intensity analysis.....	144
6.2.1 Intensity envelope .....	144
6.2.2 Effect of PZT voltage and glycerol concentration .....	145

6.3 Particles location PDF model.....	148
6.3.1 Theoretical model.....	148
6.3.2 PDF model analysis.....	152
6.3.3 Acoustic energy density determination .....	155
6.4 Acoustic energy density envelope.....	164
6.5 Conclusion .....	167
CHAPTER 7: Conclusions and Future work .....	168
7.1 Conclusions.....	168
7.2 Future work .....	170
References.....	173
Appendix A. Static chamber drawings.....	198
Appendix B. Acoustic channel drawings.....	212
Appendix C. Matlab codes.....	214

## LIST OF TABLES

Table 1-1: Acoustic specifications of different materials .....	13
Table 2-1: Acoustic phantom ingredients.....	38
Table 2-2: Acoustic channel PZT specification.....	48

Table 2-3: Properties of particle sets used in experiments (at 25 °C) .....	55
Table 2-4: List of material properties in experiments/calculations.....	56
Table 5-1: Experimental signal generator voltage (amplified 50 dB for PZT input) .....	124
Table 5-2: Power law coefficients for different glycerol concentrations .....	140

## LIST OF FIGURES

Figure 1-1: The concept of a single half-wavelength microchannel; (a) Micro-scale separation of erythrocytes (gathered in the center) from lipids (gathered in the side walls) in blood (Petersson et al., 2005); (b) Particles are separated using a spatial filter in the form of a triple channel ..... 5

Figure 1-2: The concept of a batch macro-scale multi-wavelength acoustic resonator; the acoustic pressure wave (the sine wave), gathers the particles to the PNs resulting in higher particles sedimentation rate ..... 8

Figure 1-3: Achieved ACF for constant speed of sound values; Indicated ACF for different materials in water is  $c$ , speed of sound in particle ..... 13

Figure 1-4: Consideration of a generalized set of forces acting on a particle in an applied acoustic field ..... 14

Figure 1-5: Pressure node and anti-node locations and transverse (horizontal) forces directions on particles; Longitudinal acoustic wave is shown in the transverse direction. .... 19

Figure 2-1: (a) Schematic of the static chamber experiment; (b) Digital image of static chamber experiment ..... 36

Figure 2-2: Frequency spectrum of the NDT PZT used in acoustic chamber..... 37

Figure 2-3 : Preliminary images of formation of particles to PNs in the static chamber setup; (a) The original image; (b) The grey scale inverted image..... 40

Figure 2-4: Raw data images (inverted color map) highlighting the separation process with the associated time of capture.....	43
Figure 2-5 : (a) Schematic of the acoustic channel experiment; (b) Digital image of acoustic channel experiment.....	47
Figure 2-6: Frequency spectrum of the acoustic channel PZT (Precision acoustics, custom-made) used in preliminary experimental system.....	48
Figure 2-7 : Preliminary images of formation of particles to PNs in the acoustic channel setup; .....	49
Figure 2-8: Raw data images of the separation process in the acoustic channel experiment; The associate time of capture is below each image .....	51
Figure 2-9 : Schematic of the main experimental components .....	53
Figure 2-10 : Digital image of the experimental setup .....	53
Figure 2-11: Frequency spectrum of the acoustic chamber PZT used in main experimental system.....	54
Figure 2-12: Schematic of the timing of the experiments procedure .....	58
Figure 2-13: Experimentally captured images of acoustic separation of particles, (a) a sample image of particles before densification process, (b) Color inverted version of images shown in (a); (c) a sample image of densified particles (d), Color inverted version of image shown in (c).....	60
Figure 3-1: Limitations of particles following the motion of fluid element .....	64

Figure 3-2: Overlapping of particles and bubbles at pressure nodes and pressure anti-nodes respectively ..... 65

Figure 3-3: Particles in images in different situations, (a) even distribution of particles before applying the acoustic wave, (b) densification of particles to bands due to the acoustic radiation force ..... 67

Figure 3-4: Variation of the summed intensity of a sample image at a PN and PAN indicating the change in the homogeneity of the image during densification of particles..... 68

Figure 3-5 A block diagram of the implemented PTV algorithm ..... 69

Figure 3-6: Application of image preprocessing and erosion to detect overlapped particles, (a) a sample image of particles in densification process, (b) magnified image of the rectangle containing an example of overlapping particles in image (a) is shown, (c) detected particles in the processed image (a) are circled, (d) detected particles in the magnified image of the rectangle in image (b) are depicted. .... 72

Figure 3-7 : Definition of the Moore neighbor pixels ..... 74

Figure 3-8 : Description of Moore neighborhood algorithm for detection of particles in an image..... 75

Figure 3-9 Effect of image preprocessing of images on number of detected particles during the densification process..... 77

Figure 3-10: Relaxation algorithm in classical PTV algorithm, (a) definition of frame 1 and frame 2 particles, (b) Definition of search radius for potential frame 2 particles and neighbor particles (c) Finding the potential displacement for the core particle (d) Investigation of the potential displacement  $x_1$  (e) Investigation of the potential displacement  $x_2$  (f) Investigation of the potential displacement  $x_3$ ..... 79

Figure 3-11 : A schematic of different neighbor objects velocity in acoustophoresis separation process..... 82

Figure 3-12 Particle/bubble trajectories in the field-of-view in a sample pressure acoustic force experiment; short time history particles(a sample highlighted by a solid line rectangle) and bubbles (a sample highlighted by a dashed-line rectangle) are filtered out ..... 83

Figure 3-13: A schematic of the time/image shift between consecutive images showing particle motion..... 84

Figure 3-14: A schematic of mapping of location of particles to a single wavelength..... 85

Figure 4-1: Sample of synthetic image of a particle with Gaussian intensity distribution89

Figure 4-2: Sample of synthetic image of acoustophoresis separation of particles in field-of-view, (a) an inverted grey scale sample image of particles in densification process; the rectangle is showing a group of particles travelling toward an acoustic pressure node, (b) magnified image of the rectangle containing an example of overlapping particles in image (a)..... 90

Figure 4-3: Synthetic images of the separation process with the associated time..... 92

Figure 4-4 : Variation of number of particles per unit volume for a single wavelength of 1mm for synthetic images analysis..... 93

Figure 4-5: (a) Summed intensity of (Figure 4-3,  $t = 0.250$  s) in the x direction, locations of pressure nodes are found via these intensity plots, (b) FFT of the image intensity plot in Figure 4-5(a)..... 96

Figure 4-6: Transverse velocity of a single wavelength for application of PTV algorithm to the synthetic images; The particles distribution size CV is set to 0%, 10%, 20% and 30 % in figures a, b, c and d respectively ..... 101

Figure 4-7: Raw data images (inverted color map) highlighting the separation process with the associated time of capture ..... 104

Figure 4-8: (a) Summed intensity of (Figure 4-7,  $t = 0.600$  s) in the x direction, locations of pressure nodes are found via these intensity plots, (b) FFT of the image intensity plot in Figure 4-8 (a)..... 106

Figure 4-9 Transverse velocity of PS-1, experimental vs. single particle theory values; The variation bars of experimental values fall within the theoretical variation lines shown by solid lines ..... 108

Figure 4-10: (a) PS-2 densified image, (b) in x direction, locations of PNs are found via these strong intensity plots for PS-2..... 110

Figure 4-11: (a)PS-3 densified image, (b) in x direction, locations of PNs are found via these strong intensity plots for PS-3.....	111
Figure 4-12: Transverse velocity of PS-2, experimental vs. single particle theory values .....	113
Figure 4-13: Transverse velocity of PS-3, experimental vs. single particle theory values .....	113
Figure 4-14: Normalized average difference independency with respect to image shift in achieving horizontal velocity .....	115
Figure 4-15: Effect of number of considered particles on the normalized error in achieving horizontal velocity for PS-1, PS-2 and PS-3 .....	116
Figure 5-1: Calculated effect of glycerol concentration on acoustic contrast factor and individual particle velocity .....	123
Figure 5-2: Experimental horizontal velocity for a single wavelength for different PZT voltage; (a) For 0% glycerol concentration, (b) 10%, (c) 20%, (d) 30%.....	126
Figure 5-3: Effect of number of considered particles on the normalized average error; (a) Variation of glycerol concentration for PZT voltage $U_{pp}= 4.7$ V; (b) Variation of PZT voltage for glycerol concentration= 10%.....	128
Figure 5-4: Study of influence of PZT excitation voltage on acoustic resonator performance .....	130

Figure 5-5: Study of influence of glycerol concentration on acoustic resonator performance .....	131
Figure 5-6: Acoustic energy density independency with respect to the number of tracked particles for PS-1, PS-2 and PS-3, good agreement for 3 different particle sets .....	133
Figure 5-7: Acoustic energy density for different concentrations for different voltage	135
Figure 5-8: Validity analysis of predicted quadratic proportionality of acoustic energy density on PZT voltage, experimental fitted line comparison with quadratic theoretical one; (a) for glycerol concentration 0 % (b) 10 % (c) 20 % (d) 30 %.....	139
Figure 6-1. A false color light intensity envelope for different times in the measurement; The intensity of PN increase as particles propagate to them.....	145
Figure 6-2: Variation of summed intensity of a PN; (a) Effect of variation of PZT voltage on summed intensity for pure water, (b) Effect of variation of glycerol concentration on summed intensity for $U_{pp} = 3.2$ V.....	146
Figure 6-3: Densification time for different glycerol concentration and PZT voltage.....	147
Figure 6-4: Raw data images (inverted color map) highlighting the separation process; (a) particles distribution just before actuating the PZT, (b) particles distribution after applying primary acoustic force; The rectangle highlights the modeled area .....	149

Figure 6-5: Schematic of the densification of particles in the particles locations PDF model .....	151
Figure 6-6: PDF of final location of particles in the studied acoustic resonator, (a)Effect of acoustic energy density at $t = 0.02s$ (b) effect of changing time at at $E_{ac} = 3 J/m^3$ .....	153
Figure 6-7: A sample fitting of the PDF model to the normalized light intensity envelope, this sample is associated with $U_{pp} = 6.3 V$ and experimental densification time $t = 0.045 s$ .....	155
Figure 6-8: Samples of fitting of the PDF model to the normalized light intensity envelope associated with experimental densification time.....	159
Figure 6-9: Fitting residual and the resulting acoustic energy density change as experimental fitting time varies (a) Variation of RMS of residual as the densification time changes, (b) Variation of $\chi^2$ with respect to densification time.....	162
Figure 6-10: Fitting residual skewness and kurtosis variation as experimental fitting time varies.....	164
Figure 6-11. Acoustic energy density versus voltage, equation 5-5 fitted line comparison with PTV results shown in chapter 5; Coefficient of determination for the fit ( $R^2$ ) is 0.97. ....	165
Figure 6-12. Effect of glycerol concentration on acoustic energy density obtained using the PDF model.....	166

## LIST OF SYMBOLS AND ACRONYMS

Symbol/Acronym	Description	Unit
$a$	Particle radius	m
$c$	Speed of sound	m/s
$D_{avg}$	Average distance between particles	m
$\hat{e}$	Normalized average error	-
$E_{ac}$	Acoustic energy density	J/m <sup>3</sup>
$f$	Acoustic wave frequency	1/s
$f_X$	PDF of location of particles	1/m
$F_{ac}$	Primary acoustic force	N
$I$	Image intensity envelope	-
$\langle KE \rangle$	Time-averaged acoustic kinetic energy	
$n$	Number of particles per unit volume	1/m <sup>3</sup>
$p$	Fluid pressure	Pa
$p_a$	Acoustic wave pressure amplitude	Pa
$\langle PE \rangle$	Time-averaged acoustic potential energy	
$Q$	Q-factor	-
$U$	Acoustic potential energy	J
$U_{pp}$	PZT peak-to-peak excitation voltage	V
$V$	Fluid velocity	m/s
$v_a$	Acoustic wave velocity amplitude	m/s
$V_{max}$	Maximum velocity of particle in a single wavelength	m/s
$V_0$	Particle volume	m <sup>3</sup>
$x$	Particle location	m
$x_0$	Particle initial location	m
$y$	location in Y direction	m
$z$	location in Z direction	m
$\alpha$	Acoustic wave absorption coefficient	1/m
$\beta_2$	Fitting kurtosis	-
$\tilde{\beta}$	Particle-to-fluid compressibility	-
$\beta_f$	Fluid compressibility	1/Pa
$\beta_p$	Particle compressibility	-
$\gamma$	Acoustic energy density coefficient	-
$\gamma_1$	Fitting skewness	-
$\delta$	Acoustic boundary layer thickness	m
$\eta$	Acoustic contrast factor	-
$\kappa$	Acoustic wave number	1/m
$\chi^2$	Chi squared fitting	-
$\lambda$	Acoustic wavelength	-
$\mu$	Viscosity	Pas
$\rho_f$	Fluid density	kg/m <sup>3</sup>
$\tilde{\rho}$	Particle-to-fluid density	-
$\rho_p$	Particle density	-
$\tau$	Characteristic time	s

$\omega$	Acoustic wave angular frequency	1/s
ACF	Acoustic Contrast Factor	-
CV	Coefficient of Variation	-
fps	Frames Per Second	-
FFT	Fast Fourier Transform	-
PAN	Pressure Anti-Node	-
PDF	Probability Density Function	-
PIV	Particle Image Velocimetry	-
PTV	Particle Tracking Velocimetry	-
PN	Pressure Node	-
$\mu$ PIV	Micro-PIV	-
PS	Particle Set	-
PZT	Piezo-electric Transducer	-

# CHAPTER 1: INTRODUCTION

## 1.1 Introduction

Filtration of particles from fluids is used in a broad range of applications such as water treatment (Hafez, Khedr, & Gadallah, 2007), biology (Jackson & Lu, 2013) and medicine (Ohtake et al., 2004). There are different methods for the fractionation of particles depending on the conditions including centrifugation (Ju, Geng, Zhang, Wang, & Li, 2011), dielectrophoresis (Kanagasabapathi & Backhouse, 2004), magnetophoresis (Lim, Yeap, & Low, 2014), electrophoresis (H. Nilsson, Wiklund, Johansson, Hertz, & Nilsson, 2001) and acoustophoresis (Andreas Lenshof, Magnusson, & Laurell, 2012). Each of these separation processes sorts materials based on differences in one or more physical properties such as density, electric charge and compressibility. Compared to other common separation techniques such as centrifugal methods, acoustophoresis fractionates the solid particles from the medium based on particle to medium density and compressibility difference (Castro & Capote,

2007) allowing wider particle selectivity without damage to the particles. Acoustophoresis separation has the potential for scaling up and is the focus of this work.

The word acoustophoresis means migration (phoresis) of particles due to sound waves (acousto) (Andreas Lenshof & Laurell, 2010). The effect of acoustic forces on suspended particles in different fluids has been viewed and reported (Kundt & Lehmann, 1874); (Rayleigh, 1871). It is now being used in different applications (Demiris, 2004; Evander & Nilsson, 2012) with the aid of modern technology. It has attracted progressive interest since the initial application to biotechnology problems in the early 90s (Grosch et al., 1998; Gupta & Feke, 1998; D. A. Johnson & Feke, 1995). It has been well reviewed in different literature such as (Bruus et al., 2011; Evander & Nilsson, 2012; Friend & Yeo, 2011) regarding applications, (Bruus, 2011b) regarding theoretical aspects and (A. Lenshof, Evander, Laurell, & Nilsson, 2012) regarding building applicable devices.

## **1.2 Ultrasonic acoustophoresis filtration**

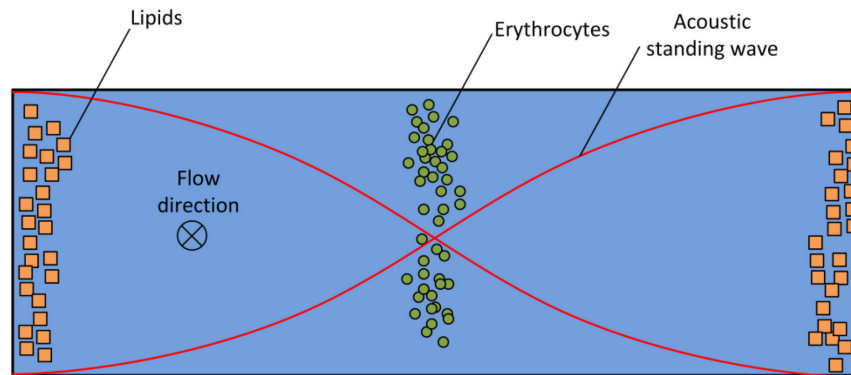
Acoustophoresis driven by ultrasonic acoustic pressure is widely used as a separation technique in various areas such as biological systems (Bazou, Kuznetsova, & Coakley, 2005; Coakley, 1997; Haake et al., 2005; Nightingale, 2003; Sarvazyan, 2010; Wiklund, 2012) and medical sciences (Dayton et al., 2006;

Jönsson et al., 2004; Jönsson, Nilsson, Petersson, Allers, & Laurell, 2005; Lum et al., 2006; Mitri & Fellah, 2006). It is used for pumping (Hu, Yang, Xu, & Du, 2006), trapping (J. Nilsson, Evander, Hammarström, & Laurell, 2009) and sorting (Jeong et al., 2011) particles in both batch (Tolt & Feke, 1993) or continuous flows (Andreas Lenshof & Laurell, 2010). High separation efficiencies in which mammalian cells in a cell culture fermentations are concentrated with efficiencies of up to 99% in removing cells from the stream without cell damage has been reported (Grosch et al., 1998). Applications of acoustophoresis can be classified to micro-scale sub-wavelength (Coakley, 1997; Hu et al., 2006; J. Nilsson et al., 2009) and macro-scale multi-wavelength (Grosch et al., 1998; Hawkes & Coakley, 1996; Trampler, Sonderhoff, Pui, Kilburn, & Piret, 1994).

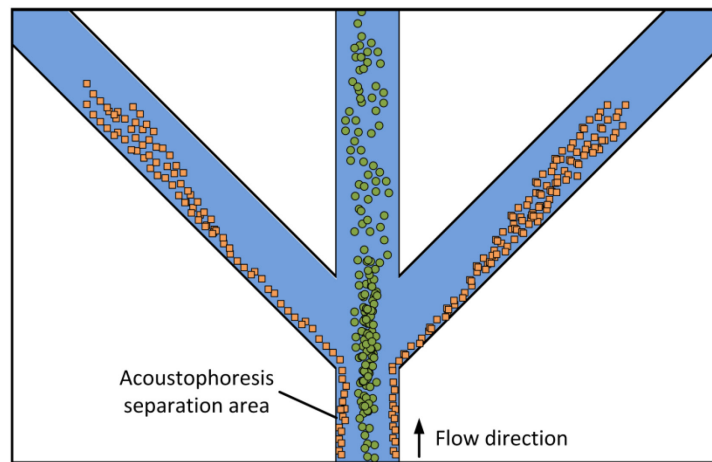
### **1.2.1 Micro-scale acoustic filtration**

An ultrasonic acoustic pressure wave of a wavelength that is at the micro-scale resonates within a micro-chamber/channel with a typical size of sub-millimeter (Bruus, 2011a) at a natural resonance frequency that corresponds to a channel width. Mathematically this means the system is in the eigenmode where the acoustic energy is unbounded but the losses will bound the acoustic energy (Barnkob, 2012). The acoustic energy which is bounded but very large attracts the cells to the single pressure node (PN) of the acoustic pressure wave in the micro-chamber/channel. The cells are spatially filtered from the containing fluid upon densifying at the PN. At this scale, the piezo-electric-transducers (PZT) are

designed to have a single wavelength (A. Nilsson, Petersson, Jönsson, & Laurell, 2004), half-wavelength (Petersson, Nilsson, Holm, Jonsson, & Laurell, 2004) or quarter wavelength (Glynne-Jones, Boltryk, Hill, Harris, & Baclet, 2009) resonance within the width of the micro-channel. The concept of a sample of half-wavelength microchannel resonator for separating erythrocytes from lipid particles in blood is shown in Figure 1-1 following the work of (Petersson, Nilsson, Holm, Jonsson, & Laurell, 2005). In Figure 1-1 (a), the flow direction is into the page and erythrocytes are attracted to the center of the micro-channel where the PN is located (the circles). The lipid particles gather in the pressure anti-nodes (PAN) at the side walls (the squares). These particles are continuously separated via having a triple channel after the resonating section as shown in the plan view of the channel in Figure 1-1 (b). There is a limit to the potential system volume flow rate due to the small dimension of the channel.



(a)



(b)

Figure 1-1: The concept of a single half-wavelength microchannel; (a) Micro-scale separation of erythrocytes (gathered in the center) from lipids (gathered in the side walls) in blood (Pettersson et al., 2005); (b) Particles are separated using a spatial filter in the form of a triple channel

### 1.2.2 Macro-scale acoustic filtration

Macro-scale acoustic filters have larger internal dimensions in the range of 1-100 mm (Hawkes & Radel, 2013) and hence are called macro-scale multi-wavelength filtration systems. An acoustic standing wave is created in these filters as a result of resonating the chamber / channel at the natural frequency

and multi-wavelengths form across the chamber. They can filter particles at a larger volume flow rate than the micro-scale acoustic filters. The dimensions of macro-scale multi-wavelength acoustic separators are also less critical with respect to micro-scale separators which require the careful guiding of separated cells to corresponding outlet channels. Another advantage is the performance of macro-scale multi-wavelength separators which decreases more slowly relative to micro-scale single/half wavelength acoustic separators (Hawkes & Radel, 2013).

There are other types of macro-scale multi-wavelength filters which don't require standing wave acoustic pressure. Sono-chemistry is used for increasing the collisions between the different sizes of particles in (Riera, Gallego-Juárez, & Mason, 2006) and hence agglomeration of them. Powerful ultrasound is used for creation of acoustic cavitation leading to more collision of particles. The main frequency of sono-chemistry systems are typically below 40 KHz (Hawkes & Radel, 2013) and are not the main focus of this work.

Macro-scale multi-wavelength filters using an acoustic standing wave are operated either in batch (Hancock, Insana, & Allen, 2003; Radel, Gherardini, McLoughlin, Doblhoff-Dier, & Benes, 2000; Tolt & Feke, 1993) or continuous mode (Dionne, McCarthy, Ross-Johnsrud, Masi, & Lipkens, 2013; Dutra, Rust, Kennedy, Masi, & Lipkens, 2013; Lipkens et al., 2010). The continuous separation method splits lines of acoustically densified cells and guides them to outlet

channels. These methods are more utilized more often in low cell concentration applications (Hawkes & Radel, 2013). A continuous macro-scale multi-wavelength acoustic resonator is developed for separation of micron-sized particles (Lipkens et al., 2010). Laminar flow is developed in a 2.54 cm x 2.54 cm cross-section channel and a 2 MHz PZT is used for generation of ultrasonic acoustic pressure. Successful separation of 6  $\mu\text{m}$  polystyrene particles at volume flow rate of 150 mL/min is reported. Macro-scale acoustophoresis separation of lipid particles from red blood cell using a continuous mode multi-wavelength acoustic resonator is demonstrated (Dutra et al., 2013). The 10 to 60  $\mu\text{m}$  sized lipid particles are separated at a volume flow rate of 2 L/hr. Acoustophoresis separation for the separation of oil from water (Dionne et al., 2013) with a separation efficiency of 95% up to a volume flow rate of 150 L/hr is reported.

In batch mode, macro-scale multi-wavelength resonators with ultrasonic acoustic pressure have been used for aggregation of cells and the cells are settled under gravity (Grosch et al., 1998). This geometry is schematically shown in Figure 1-2. The sedimentation rate increases by reduction of surface to volume ratio which makes particles larger. This is performed by the creation of a multi-wavelength acoustic resonance (Hawkes & Radel, 2013). Development of such acoustic filters dates back to the early 1990s where it had been used for separation of different bio-cells (Peterson, Perkins, & Baker, 1986; Tolt & Feke, 1993; Whitworth, Grundy, & Coakley, 1991). Blood cells are separated from plasma by concentrating the sediment (Peterson et al., 1986). An ultrasound

acoustic standing wave is used to concentrate and guide 9  $\mu\text{m}$  polystyrene particles in a cylinder (Whitworth et al., 1991). A macro-scale multi-wavelength acoustic filter is developed for separation of hybridoma cells (Trampler et al., 1994) and increases the sedimentation rate of cells without any measurable effect on viability of them. A 70-fold increase in volumetric productivity compared to normal batch culture is reported. Sedimentation rate of plasma from human blood is increased in a circular container using a tubular transducer (Cousins et al., 2000). The cells are aggregated at radial separations of half wavelength with the average efficiency of clarification of blood being 99.76%.

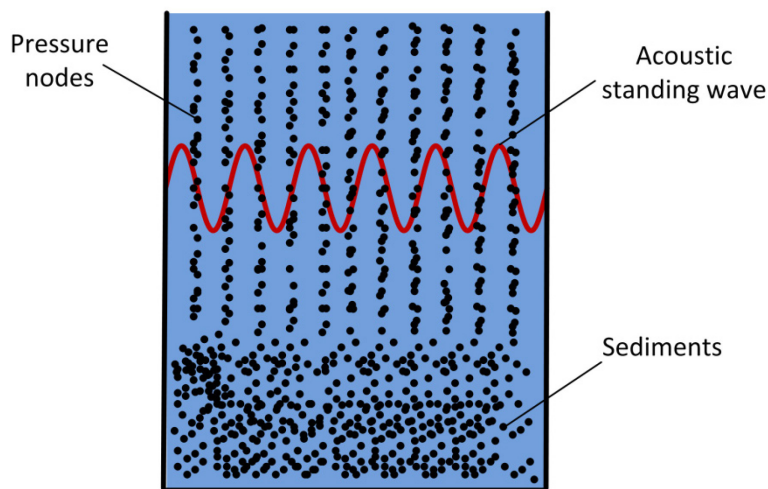


Figure 1-2: The concept of a batch macro-scale multi-wavelength acoustic resonator; the acoustic pressure wave (the sine wave), gathers the particles to the PNs resulting in higher particles sedimentation rate

Modulation of ultrasonic acoustic wave to move the PNs is also reported (Lipkens, Dionne, Costolo, & Rietman, 2008; Manneberg, Vanherberghen, Onfelt, & Wiklund, 2009). In these methods, which are also called drifting acoustic fields

(Sadikova & Pashovkin, 2013), densified particles are displaced by moving the PNs by sweeping frequency (Lipkens et al., 2008) or by using two transducers set at a fixed frequency difference (Whitworth et al., 1991). Macro-scale multi-wavelength acoustic resonance is the focus of this work as it has the potential for separation at high volume flow rates as in treatment of water (Ho et al., 2012) and food processing (Juliano et al., 2011).

### **1.3 Theory of acoustic force on particles**

The acoustic radiation effect was first viewed by (Kundt & Lehmann, 1874) who observed cork dust suspended in water that were trapped in an acoustic tube that was used to measure the speed of sound. While the linear effects of the acoustic pressure wave time averages to zero, the non-linear effects results into non-zero time-averaged forces on the suspended particles. This acoustic force has greater magnitude if there is acoustic standing wave in the chamber and is termed the primary acoustic force (Benes et al., 2001). A theoretical primary acoustic force on an incompressible sphere particle for different conditions can be derived (King, 1934). This can be extended to the primary acoustic force on a compressible spherical particle in an inviscid fluid (Yosioka & Kawasima, 1955). The effects of viscosity of the encompassing fluid has also been theoretically investigated by (Danilov & Mironov, 2000; Doinikov, 1994, 1996; Settnes & Bruus, 2012).

### 1.3.1 Primary acoustic force theory

Assuming that particles are suspended in an inviscid fluid, the particles are compressible, and their diameter are small compared to the wave wavelength of the acoustic field, the time average force on the particle is defined as the gradient of the acoustic potential energy (Gorkov, 1962). The potential function is defined as the summation of the kinetic and potential energy of the acoustic wave at the location of particle. For the case when the acoustic wave is a standing-wave field the radiation force is much larger than a progressive wave case and the acoustic potential energy,  $U$  can be described by:

$$U = V_0 \left[ \frac{\beta_f - \beta_p}{\beta_f} \langle PE \rangle - \frac{3(\rho_p - \rho_f)}{\rho_f + 2\rho_p} \langle KE \rangle \right] \quad (1-1)$$

where  $V_0$  is the volume of the particle,  $\rho$  and  $\beta$  are density and compressibility, and the subscripts  $f$  and  $p$  refer to fluid and particle respectively.  $\langle PE \rangle$  and  $\langle KE \rangle$  are time averaged potential and kinetic energy densities of the field, respectively, and are defined as:

$$\langle PE \rangle = \frac{\beta_f \langle p(x, y, z, t)^2 \rangle}{2} \quad (1-2)$$

$$\langle KE \rangle = \frac{\rho_f \langle v(x, y, z, t)^2 \rangle}{2} \quad (1-3)$$

where  $\langle p(x, y, z, t)^2 \rangle$  and  $\langle v(x, y, z, t)^2 \rangle$  are time-averaged pressure squared and displacement velocity squared of the wave over a single wavelength. For a standing wave these can be expressed as functions of spatial location and time by:

$$p(x, y, z, t) = p_a(y, z) \cos(\kappa x) \sin(\omega t) \quad (1-4)$$

$$v(x, y, z, t) = v_a(y, z) \sin(\kappa x) \cos(\omega t) \vec{k} \quad (1-5)$$

where  $p_a$  and  $v_a = p_a / \rho_f c$  are the fluid pressure and velocity amplitude of the wave as a function of spatial location  $(x, y, z)$  and time  $(t)$ ,  $x$  is the wave propagation direction,  $c$  is the fluid sound speed,  $\rho_f$  is the density of the surrounding fluid,  $\kappa = \frac{2\pi}{\lambda}$  is the wave number of the wave,  $\omega = 2\pi f$  is the angular frequency,  $f$  is the frequency of the acoustic source, and  $\vec{k}$  is the unit vector in the  $x$  direction.

The time-averaged ultrasonic primary acoustic force (Bruus, 2012b) on a single particle in an inviscid fluid due to acoustic pressure is the gradient of the potential energy of the acoustic pressure wave ( $F_{ac} = -\nabla U$ ) and is expressed as:

$$F_{ac} = 3V_0 E_{ac} \kappa \eta \sin(2\kappa x) \vec{k} \quad (1-6)$$

where  $E_{ac}$  is acoustic energy density which is a measure of the efficiency of acoustic resonator through the effect of generated acoustic pressure  $p_a$  in the field and is defined as:

$$E_{ac} = \frac{p_a^2 \beta_f}{4} \quad (1-7)$$

where  $\beta_f$  is the fluid compressibility and is inversely proportional to speed of sound in a material. The acoustic contrast factor (ACF),  $\eta$  is a function of the density ( $\tilde{\rho}$ ) and compressibility ( $\tilde{\beta}$ ) ratio of particle-to-fluid and is defined as:

$$\eta = \frac{1}{3} \left[ \frac{5\tilde{\rho} - 2}{2\tilde{\rho} + 1} - \tilde{\beta} \right] \quad (1-8)$$

where particle-to-fluid density ratio ( $\tilde{\rho}$ ) and particle-to-fluid compressibility ratio ( $\tilde{\beta}$ ) are defined as:

$$\tilde{\rho} = \frac{\rho_p}{\rho_f} \quad (1-9)$$

$$\tilde{\beta} = \frac{\beta_p}{\beta_f} \quad (1-10)$$

The primary acoustic force direction is based on the sign of ACF. Positive values of ACF (i.e. a soda lime glass particle in water) correspond to attraction of the particles to the nearest PNs and negative value (i.e. bubble in water) results in attraction of them to the nearest PANs.

The ACF plays an important role in the primary acoustic radiation force and is a function of two different properties of the system. The influence of this parameter can be investigated by comparing the effect of particles acoustic properties (density and speed of sound) for cases in which particles are suspended in water. The acoustic specifications of different materials discussed here are listed in Table 1-1. These materials are also indicated in Figure 1-3. In this figure, the variation of ACF for a material with a constant speed of sound values but different densities is plotted. According to these curves, the density ratio has more influence on ACF for lower values of particle density where the ACF value is negative. A negative value of ACF indicates that the particle will be attracted to a PAN while as a particle with a positive ACF value such as glass-in-water will be forced toward a PN. As the particle-to-fluid density ratio increases at a constant speed of sound particle-to-fluid ratio, the ACF approaches an asymptote. It is also notable that the constant speed of sound curves for  $c = 3000$  m/s to  $c = 6000$  m/s are approximately coincident. This indicates that the

dependence of speed of sound on the ACF reduces for higher values. The force on the particle-in-water is predominantly from density effects.

Table 1-1: Acoustic specifications of different materials

Material	Density ( $\text{kg/m}^3$ )	Speed of sound (m/s)	ACF
Glass	2500	5600	0.57
Silicone oil	760	1350	-0.26
Polystyrene	1100	2350	0.23

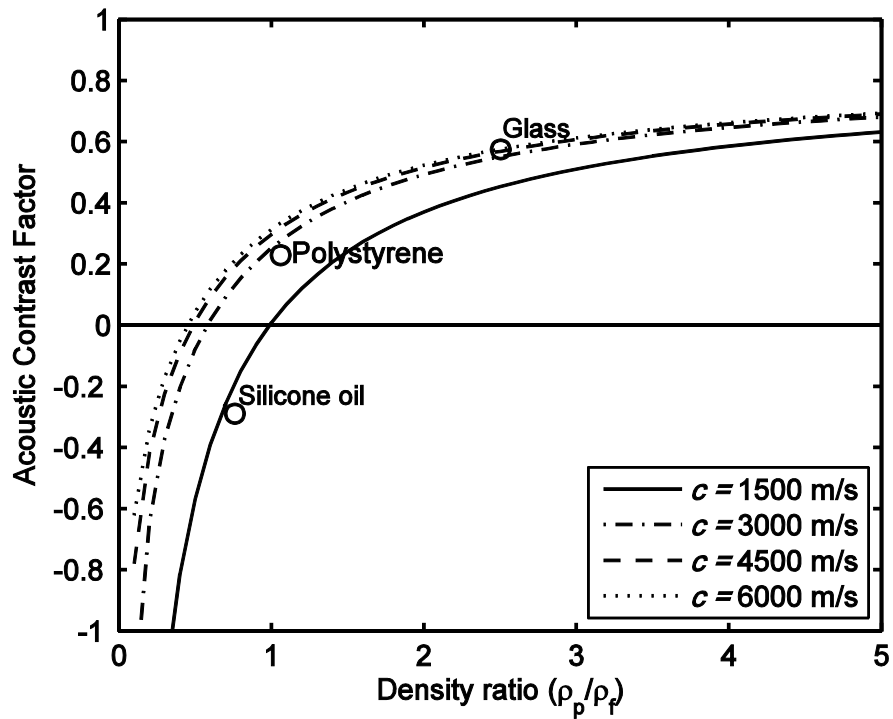


Figure 1-3: Achieved ACF for constant speed of sound values; Indicated ACF for different materials in water is  $c$ , speed of sound in particle

### 1.3.2 Other acoustic forces

A summary of the forces on a particle suspended in a medium affected by acoustic force is shown in Figure 1-4. There can be also effects of electromagnetic forces such as electric force or dielectrophoresis which are neglected assuming there is no electromagnetic field around the particle. Other than the primary acoustic force applying on the particle, there can be the effect of viscosity, acoustic streaming and secondary acoustic force on the particle.

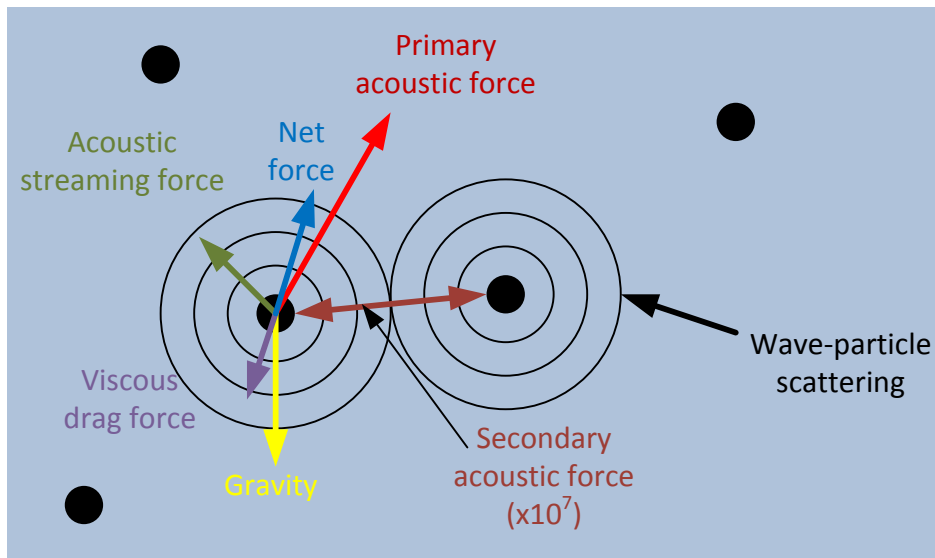


Figure 1-4: Consideration of a generalized set of forces acting on a particle in an applied acoustic field

#### *Viscosity effect*

In the primary acoustic force calculation, the fluid medium is assumed to be inviscid. However, the viscosity of fluid can affect the particles under certain conditions. The viscosity is not negligible in acoustic boundary layer and the primary acoustic force theory is valid for the particles significantly larger than the

thickness  $\delta$  of the acoustic boundary layer. The acoustic boundary layer thickness (or the viscous penetration depth) is the momentum diffusion length (Settnes & Bruus, 2012)

$$\delta = \sqrt{\frac{2\mu}{\rho\omega}} \quad (1-11)$$

For a common ultrasound frequency (1 MHz), the acoustic boundary layer in water is calculated to be  $0.6 \mu m$ . It is expected that the effect of viscosity is observable on particles smaller than  $6 \mu m$  (10 times  $\delta$ ) in diameter (Settnes & Bruus, 2012).

#### *Acoustic streaming*

Acoustic streaming occurs when the bulk fluid moves as a result of absorbing energy of the acoustic wave (Bruus, 2011b). Acoustic streaming is divided into two parts: small scale and large scale acoustic streaming. Small-scale acoustic stream or Schlichting rolls (Barnkob, 2012) which are created in the viscous boundary layer due to attenuation of acoustic wave. This streaming of flow is only considered in the acoustic boundary layer. Due to small size of acoustic boundary layer thickness with typical MHz frequency in water ( $0.6 \mu m$ ), small scale acoustic streaming is not considerable for sub-micron particles.

Large scale acoustic streaming rolls, which are called Rayleigh rolls (Rayleigh, 1884), are generated by the flow due to Schlichting rolls (small-scale acoustic streaming) in acoustic boundary layer. These large-scale rolls which are

in the opposite direction of small-scale acoustic streaming and generate a fluid flow in the suspension which can affect the suspended particles. This force due to the small-scale acoustic streaming can have an effect on particles suspended in water when the size of particles is lower than 2  $\mu\text{m}$  (Barnkob, Augustsson, Laurell, & Bruus, 2012).

### *Particle-particle effects*

The effect of particle-particle interactions are neglected in derivation of primary acoustic force theory. These effects may be divided into hydrodynamic particle-particle effects and the secondary acoustic force. The hydrodynamic particle-particle forces are considered in the influence of concentration particles on settling velocity of particles. This is well experimented that a single solid particle settling velocity in fluid is higher than the settling velocity of a mixture of fluid and particles. This effect which is known as hindered settling velocity (Blazejewski, 2012) is explained by a contraction of the flow between particles. This phenomenon can be important in the acoustophoresis phenomenon by having many particles moving to a pressure node. The velocity of particles can be reduced due to the restriction of back flow replacing their original location. The hydrodynamic particle-particle effects are significant in the suspensions in which inter-particle distances are below 2 particle diameters (Andersen, Nysteen, & Settnes, 2009).

The secondary acoustic force (Doinikov, 2001) is due to the effect of the pressure field scattering off the other particles influencing the particle of interest. These forces are also known as Bernoulli or Koenig forces (Woodside, Piret, Gröschl, Benes, & Bowen, 1998). The magnitude of the secondary acoustic force is

$$F_s = 4\pi a^6 \left[ \frac{(\rho_p - \rho_f)^2 (3 \cos^2 \theta - 1)}{6\rho_f d^4} \langle v \rangle^2 - \frac{\omega^2 \rho_f (\beta_p - \beta_f)^2}{9d^2} \langle p \rangle^2 \right] \quad (1-12)$$

where  $\theta$  is the angle between the centerline of connecting the two particles and the acoustic wave propagation direction,  $d$  is the distance between the two particles. Negative values of this force will cause the particles to move toward each other and positive values result in a repulsive force between the particles.

The order of magnitude of this force is compared with the primary acoustic force in (Hancock, 2001) and it has obtained that secondary acoustic force is  $10^{-10}$  smaller than the primary acoustic force when the distance between two 5  $\mu\text{m}$  particles is 100  $\mu\text{m}$ . When the two particles are 5  $\mu\text{m}$  apart the secondary acoustic force is  $10^{-5}$  times the primary acoustic force.

### *Summary*

Considering dilute suspension of solid particles in water (less than  $10^{15}$  particles/ $\text{m}^3$  to avoid particle-particle interactions (Mikkelsen & Bruus, 2005)), the effect of the secondary acoustic force is negligible with respect to primary acoustic force. The influence of hydrodynamic effects can also be neglected for

these low concentrations of particles. The effect of acoustic streaming and viscosity of suspension fluid can also be neglected in the cases where the size of particles is more than 6  $\mu\text{m}$ . As such, many experiments just considering the primary acoustic force are carried out (Woodside, Bowen, & Piret, 1997). Primary acoustic force is the main focus of this work on systems where particles size and particles concentration is varied.

### **1.3.3 Theoretical transverse velocity of particles**

By considering the forces acting on a single particle in the direction normal to the gravity vector as shown in Figure 1-5, particle velocity due to the primary acoustic pressure force can be determined by accounting only for the drag body force on the particle. For a particle with a positive ACF, its motion in travelling toward the nearest pressure node can be considered to be due only to the primary acoustic force overcoming the drag force. The main assumption is that the inertia of the single particle is negligible due to its relatively low velocity and consequently low Reynolds number of flow which is applicable for micron sized particles (Bruus, 2012b).

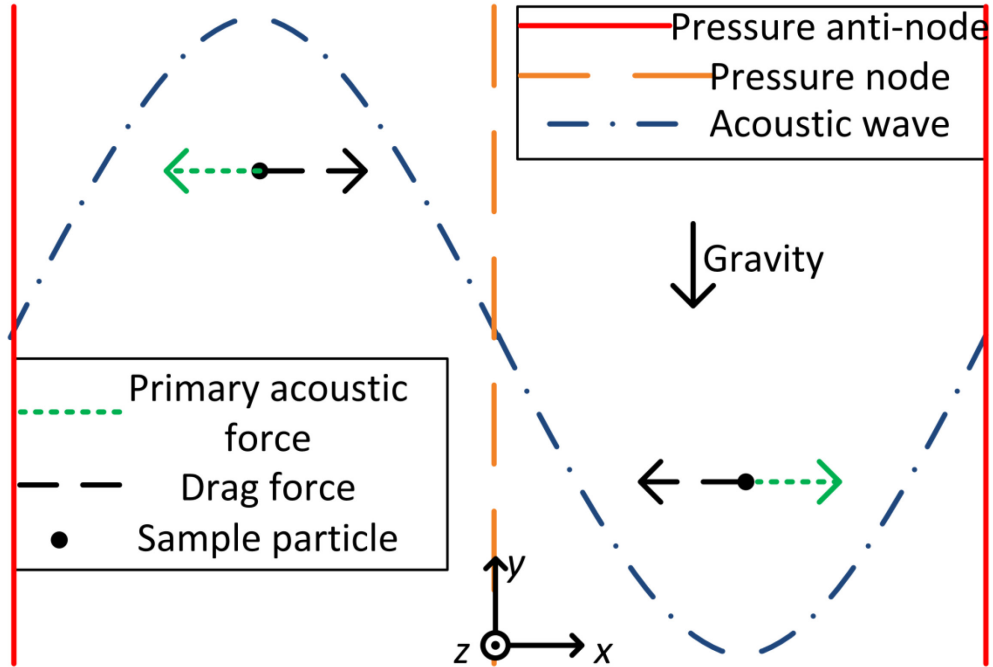


Figure 1-5: Pressure node and anti-node locations and transverse (horizontal) forces directions on particles; Longitudinal acoustic wave is shown in the transverse direction.

Considering a Stokes drag force applied on the particle while influenced by an acoustic pressure force and neglecting the inertial effects, the balance of forces on the single particle can be obtained from

$$3V_0 E_{ac} \kappa \eta \sin(2\kappa x) = 6\pi\mu a V \quad (1-13)$$

where  $\mu$  is the viscosity of the bulk fluid,  $a$  is the particle radius and  $V$  is particle velocity. By manipulating this equation, the velocity of a single particle forced by the acoustic radiation pressure in the wave propagation direction can be found as

$$V = \frac{V_0 E_{ac} \kappa \eta}{2\pi\mu a} \sin(2\kappa x) \quad (1-14)$$

In order to check the assumption of neglecting inertia effects, the relaxation time of a particle can be calculated. Having the summation of the external forces applied on the particle including the acoustic force and the force equal to the inertia of a particle, the equation of motion of particle can be written as:

$$F_{ac} - 6\pi\mu aV_{tr} = m \frac{dV_{tr}}{dt} \quad (1-15)$$

where  $m$  is the mass of particle,  $V_{tr}$  is the transient velocity of particle as it is accelerating to the terminal velocity ( $V$ ) derived in equation (1-14). The transient velocity of the particle can be derived by integrating equation (1-15) as

$$V_{tr} = V(1 - e^{-\frac{t}{\tau}}) \quad (1-16)$$

where  $\tau$  is the relaxation time of a particle. The relaxation time is defined as the time for a particle which responds to an acceleration (ten Cate, Nieuwstad, Derksen, & Van den Akker, 2002) and is derived as

$$\tau = \frac{\rho d^2}{18\mu} \quad (1-17)$$

As an example, consider a 20  $\mu\text{m}$  size particle moving in water, the relaxation time is about 20  $\mu\text{s}$ . This shows that the assumption of neglecting the inertia forces is valid in the range of micro-sized particles studied in this thesis.

The maximum velocity of a particle is found to be proportional to the acoustic energy density,  $E_{ac}$  of the acoustic field. The acoustic energy density is a function of the piezo-electric transducer and its properties, the acoustic chamber properties, their acoustic matching and the manufacturing process which determines how energy is coupled between them. Therefore, it needs to be determined for an acoustofluidics system experimentally. Generally this parameter, which is a constant for a particular acoustic cell is estimated from experiment by studying the motion of different types of particles in various conditions for the acoustic field.

#### **1.4 Experimental investigation of acoustophoresis**

Ultrasonic manipulation of particles / cells has been experimentally investigated using different methods. Some of these investigation methods rely on the study of output separation efficiencies (Hagsäter et al., 2008; Hawkes & Coakley, 2001; Radel, McLoughlin, Groschl, & Benes, 2002) and separation time (Nii, Kikumoto, & Tokuyama, 2009; Önal, Ozer, & Arslan, 2003). A continuous flow micro-scale acoustic filter chamber is introduced and the separation efficiency is defined in terms of the concentration of cells (Hawkes & Coakley, 2001). The concentration of particles is measured using a hemocytometer at the inlet and outlet of the chamber and the efficiency is studied at different PZT excitation voltages. Efficiency of an ultrasonically enhanced settling system is studied in (Radel et al., 2002). The influence of PZT excitation voltage on yeast

suspended in water for separation efficiency of the yeast is investigated. The separation efficiency is based on a comparison of the concentration of yeast suspension at the inlet and the separated yeast by sedimentation at the outlet.

Investigation of separation efficiency and separation time is useful for analyzing an acoustic resonator, however it does not help in understanding the physics of the applied ultrasonic acoustic force in the systems. There is a need for more quantitative approaches for investigation of macro-scale multi-wavelength acoustic resonators.

#### **1.4.1 Particle trapping techniques**

Trapping the particles has been also used as a more quantitative approach for experimental investigation of ultrasonic acoustic force separation of particles. These methods give more understanding of ultrasonic acoustic force inside the chambers and often include other different external forces such as gravity (Hertz, 1995; Y. Liu & Hu, 2009) or electric force (Yasuda, Umemura, & Kazuo, 1996; Yasuda, 1999). The weight of particles such as medical pills up to 256 mg is balanced by ultrasonic acoustic pressure (Y. Liu & Hu, 2009). A similar approach is used (Hancock et al., 2003). The ultrasonic acoustic force is investigated by studying the minimum acoustic pressure required for balancing the particle weight. Polystyrene particles are electrically charged and when the acoustic radiation force on particles balances with electrostatic force the spatial distribution of the acoustic radiation force is obtained (Yasuda, 1999).

Particle trapping methods help in quantifying the maximum value of primary acoustic force needed to balance an external force. This approach is not capable of measuring the primary acoustic force distribution in different locations and hence is not used in this project.

#### **1.4.2 Imaging techniques**

Another approach for investigation of ultrasonic acoustic pressure is the imaging of particle motion which has the capability of investigating the ultrasonic acoustic pressure fundamentally more quantitatively than the previous methods. This is nonintrusive and can be used for investigation of pressure distribution (Möller, Degen, & Dual, 2013) or particle motion due to ultrasonic acoustic pressure effect (Dron, Ratier, Hoyos, & Aider, 2009; Jürg Dual, Hahn, Leibacher, Möller, & Schwarz, 2012; Nabavi, Siddiqui, & Dargahi, 2008). Particle Image Velocimetry (PIV) and Particle Tracking Velocimetry (PTV) are usually used. When being used for quantitative investigation, the entire field-of-view can be studied simultaneously. This enables the study and allows quantitative measurements of the effect of the different parameters involved in primary acoustic force theory (Gorkov, 1962).

##### *Particle Image Velocimetry*

PIV has been used to investigate particle motion in ultrasonic acoustic chambers. It cross-correlates the intensity distributions of imaged particles over

smaller interrogation windows in a field-of-view, spatially averaging the actual velocity field (Raffel, Willert, Wereley, & Kompenhans, 2007) in these sub-regions. The result is a 2D map of the velocity field for single camera, 2D-PIV. It has been used for measurement of primary acoustic force on particles (Spengler et al., 2001) and acoustic streaming (Lee, 2013). Agglomeration of yeast due to application of ultrasonic acoustic force is observed (Spengler et al., 2001). The motion of particles as a result of acoustic streaming is also investigated and compared with Rayleigh micro-streaming theory. A parametric study of ultrasonic acoustic pressure parameters is performed (Dron et al., 2009) in which the particles motion is measured using micro-PIV. The effect of acoustic pressure magnitude, particle diameter and particle concentration are investigated. Thus, PIV has been used widely in investigation of primary acoustic force.

The main assumptions behind PIV is that the particles follow the motion of the fluid and that a group of particles in the same interrogation window move in basically the same direction (R. J. Adrian, 2005). However, in the current investigation the particles move due to the acoustic force and the surrounding fluid imposes only a drag force on them. Also, based on equation (1-6) the force on a particle is a function of the location of the particle within the acoustic field resulting in different velocities for any group of particles. Both these points violate basic PIV assumptions (R. J. Adrian, 2005). At the PN's where the velocity changes direction, there can also be particles traveling in opposite directions.

The accuracy of velocity vectors depends on and is limited by the concentration and homogeneity of particles in the interrogation windows.

Based on these limitations PIV must be used carefully to investigate acoustic fields (Augustsson, Barnkob, Wereley, Bruus, & Laurell, 2011; Barnkob, Augustsson, et al., 2012). The primary acoustic force on single particles is investigated using micro-PIV ( $\mu$ PIV) by (Augustsson et al., 2011) and the results are compared with available primary acoustic force theory (Gorkov, 1962) and experimental results of (Barnkob, Augustsson, Laurell, & Bruus, 2010).  $\mu$ PIV is used for investigation of the primary acoustic force and acoustic streaming in a micro-scale acoustic resonator by (Barnkob, Augustsson, et al., 2012). Primary acoustic force has been studied using a suspension of 10  $\mu$ m particles and 0.6  $\mu$ m particle has been used for investigation of dominant acoustic streaming. Ratio of primary acoustic force and acoustic streaming velocity is compared with primary acoustic force theory (Gorkov, 1962) and boundary driven Rayleigh acoustic streaming (Rayleigh, 1884).

In these cases, the particles are homogeneously mixed at an optimum seeding density for the application of PIV before the acoustic field is applied. Images are captured and processed only during the initial time of application of the acoustic field. No information can be collected on the phenomenon once the particles become too segregated for PIV to be applied consistently. This limits the application only to the initial phases of densification. This approach is only

applicable to mono-dispersed size distribution particles where the velocity magnitude of particles is similar due to the acoustic force being a function of particle size. Mono-dispersed size distribution particles are defined as particles with particles size distribution CV lower than 10 %. The coefficient of variation (CV) of particle size (diameter) distribution is the ratio of standard distribution of probability density function (PDF) of size of particles to the mean value of their size. For poly-dispersed size distribution data sets, particles should be followed individually for a longer time to accurately resolve their velocity and hence their force history. The whole lifetime motion of particles is needed for determination of acoustic energy density which is critical for characterization of acoustic resonators. Therefore, PIV is not used in this work to determine particle motion in an acoustic field.

#### *Particle Tracking Velocimetry*

PTV is typically used for tracking individual particles when particle concentration is low and each particle can be tracked for over the time history of interest (Barnkob et al., 2010; Woodside et al., 1997). Full-time history of tracking of particles is useful to investigate the primary acoustic force on the particle to analyze both spatial and temporal effects.

Acoustophoresis on individual micro-beads in a 377  $\mu\text{m}$  microchannel in the presence of a single wavelength acoustic field was studied (Barnkob et al., 2010). The mono-disperse particles are tracked individually and the resulting

velocity measurements are in good agreement with primary acoustic force theory (Gorkov, 1962). Acoustic energy density is also obtained using the particles motion. The motion of single particles in a macro-scale multi-wavelength acoustic chamber is studied (Woodside et al., 1997) by tracking them individually using a micro-imaging technique. Acoustic energy distribution in a macro-scale multi-wavelength resonator is also obtained by tracking individual particles (Woodside et al., 1998). In (Barnkob et al., 2010; Woodside et al., 1997, 1998) the concentration of particles in the field-of-view is low enough that each individual particle can be detected for the complete acoustic forcing time. The study of PTV for macro-scale multi-wavelength acoustic resonators is limited.

## 1.5 Objectives

Considering the amount of experimental / theoretical investigations in understanding the ultrasonic acoustic pressure at the micro-scale, the physics of macro-scale multi-wavelength acoustic resonators are not well investigated. The complexity of the acoustic separation process in a macro-scale acoustic resonator limits common investigation techniques such as PIV / PTV. The scale of the flow field in these resonators is many times that of the wavelength of the acoustic field. As particles separate to PN or PAN it can be expected that the properties of the acoustic field (i.e. dampening and scattering) may be affected. What direction particles will take due to the existence of multiple pressure nodes in the large scale acoustic chamber with a standing field depends on the particle initial conditions. The applicability of the primary acoustic force theory (Gorkov, 1962) which only describes the forces generated on a single particle suspended in inviscid flow in a homogeneous acoustic field needs to be examined at the macro-scale.

The main motivation for this thesis is therefore to increase the understanding of effect of involving parameters such as acoustic wave dampening and PZT excitation voltage in macro-scale multi-wavelength acoustophoresis. To do this, a set of experiments are performed for understanding and isolating different phenomena. PTV is used as the main imaging processing technique for studying the particles motion in macro-scale

multi-wavelength acoustic resonators. Primary acoustic force theory is examined in macro-scale multi-wavelength acoustic resonators using the PTV technique. A parametric study of the relevant parameters is performed to characterize the macro-scale multi-wavelength acoustic resonator. To understand the physics in these acoustic resonators particle motion is modeled. This is a useful design tool for configuring new macro-scale acoustic resonators or scaling current acoustic resonators.

## **1.6 Thesis outline**

The thesis is divided into 7 chapters and a brief outline of chapters 2 to 7 is given here.

### **Chapter 2 — Experimental setup**

This chapter provides the details of the preliminary and main experimental setups designed and built for studying different aspects of ultrasonic acoustic pressure field.

### **Chapter 3 — Developed PTV method**

A description of the PTV method developed specifically for investigating particle motion and hence the acoustic pressure field is described in this chapter. This PTV approach has been tuned for the study of macro-scale multi-wavelength acoustic resonators.

#### **Chapter 4 — Primary acoustic force theory in macro-scale multi-wavelength resonators**

This chapter analyzes the primary acoustic force theory and discusses the involving parameters. The effect of PZT excitation voltage and viscosity of suspension is investigated using the developed PTV algorithm.

#### **Chapter 5 —Characterization of a macro-scale multi-wavelength resonators using the developed PTV method**

The acoustic energy density, as the main parameter in the primary acoustic force theory is investigated of a macro-scale multi-wavelength resonator in this chapter using the developed PTV approach.

#### **Chapter 6 — Probability density function model of macro-scale multi-wavelength acoustic resonators densification**

This chapter introduces a developed probability density function (PDF) model of the location of particles in an acoustic resonator. It is used for determining the acoustic energy density in a macro-scale multi-wavelength acoustic resonator using a simplified imaging system.

#### **Chapter 7 —Conclusion and Future work**

The thesis concludes with summary of the main outcomes points found in the thesis followed by the outlook of the suggested future work for improving

the understanding of the physics of the macro-scale multi-wavelength acoustic resonators.

## 1.7 List of contribution

The following is a list of contributions from this thesis in the form of conference and journal publications.

### Conference papers:

1. Setayeshgar, A.; Lipsett, M. G.; Koch, C. R. & Nobes, D. S.  
Measurement of particle dynamics in a coherent acoustic field,  
International Symposium on Particle Image Velocimetry – PIV13,  
July 1-3, 2013, The Netherlands.  
*NOTE: awarded best poster at the conference.*
2. Setayeshgar, A.; Lipsett, M. G.; Koch, C. R. & Nobes, D. S. Separation  
of particles in a multi-wavelength macro-channel using an  
ultrasonic acoustic standing wave, USWNET conference, September  
21-22, 2012, Sweden.
3. Setayeshgar, A.; Lipsett, M. G.; Koch, C. R. & Nobes, D. S.  
Investigating the Particles Motion in Ultrasonic Acoustic Wave Field  
Using PIV/PTV, International Congress on Ultrasonics, September 5–  
8, 2011, Poland.

### Journal papers:

1. Setayeshgar, A.; Lipsett, M. G.; Koch, C. R. & Nobes, D. S. Particle motion in a macro-scale multi-wavelength acoustic field, Submitted to ASME Journal of Fluid Engineering, JFE-14-1010 January 2014.
2. Setayeshgar, A.; Lipsett, M. G.; Koch, C. R. & Nobes, D. S. PTV Investigation of Ultrasonic Acoustic Standing Wave Separation of Particles in a Macro-scale Resonator. *In preparation for publication.*
3. Setayeshgar, A.; Lipsett, M. G.; Koch, C. R. & Nobes, D. S. Characterizing a Macro-scale Multi-wavelength Ultrasonic Acoustic Standing Wave Chamber. *In preparation for publication.*
4. Setayeshgar, A.; Lipsett, M. G.; Koch, C. R. & Nobes, D. S. An Image Processing Method for characterizing a Multi-wavelength Macro-scale Acoustic Resonator. *In preparation for publication.*

## **CHAPTER 2: EXPERIMENTAL METHOD AND APPARATUS**

### **2.1 Introduction**

The experimental setup and the procedures for all parts of this thesis are presented in this chapter. To study the application of multi-wavelength ultrasonic acoustic pressure at macro-scale several initial experimental apparatus are developed. These are used to explore and understand the physics of the flow. This understanding is to design a system for the quantitative investigation of macro-scale multi-wavelength acoustic resonators.

### **2.2 Preliminary experimental setup**

Two experimental setups are designed are used for preliminary understanding of the phenomenon. The first setup is a vertically aligned static acoustic chamber for studying the primary acoustic force by trapping the

suspending particles. The second setup is a vertical acoustic channel for continuous separation of particles.

### **2.2.1 Static chamber**

#### *Schematic*

For feasibility analysis and understanding the acoustic phenomenon a vertically aligned chamber is built. It is intended not to have a mean flow which simplifies the configuration. This allows the study of the motion of particles only affected by the acoustic force. The cell is mounted vertically to balance the weight of particles by ultrasonic acoustic pressure.

A schematic diagram and a picture of the setup are shown in Figure 2-1. Engineering drawings of this setup are provided in Appendix A. The cylindrical chamber (30 mm diameter) is filled with a mixture of distilled water and 37  $\mu\text{m}$  diameter soda-lime glass sphere particles with the specific gravity of 2.5. Based on these specifications, the corresponding ACF in equation (1-8) is 0.56 and hence the particles are attracted toward the PNs. A mixing tank and a peristaltic pump (MasterFlex, 07523-80) are used to for assure that the suspension concentration is homogenous. The pump is used to fill the cylindrical chamber with homogenous mixture of water/particles. A 532 nm wavelength laser (New Wave Research, Nd-YAG Solo PIV) is used to illuminate the particles from the

side of the chamber. A high resolution camera (LaVision Inc, Imager Intense) captures the images of the particles.

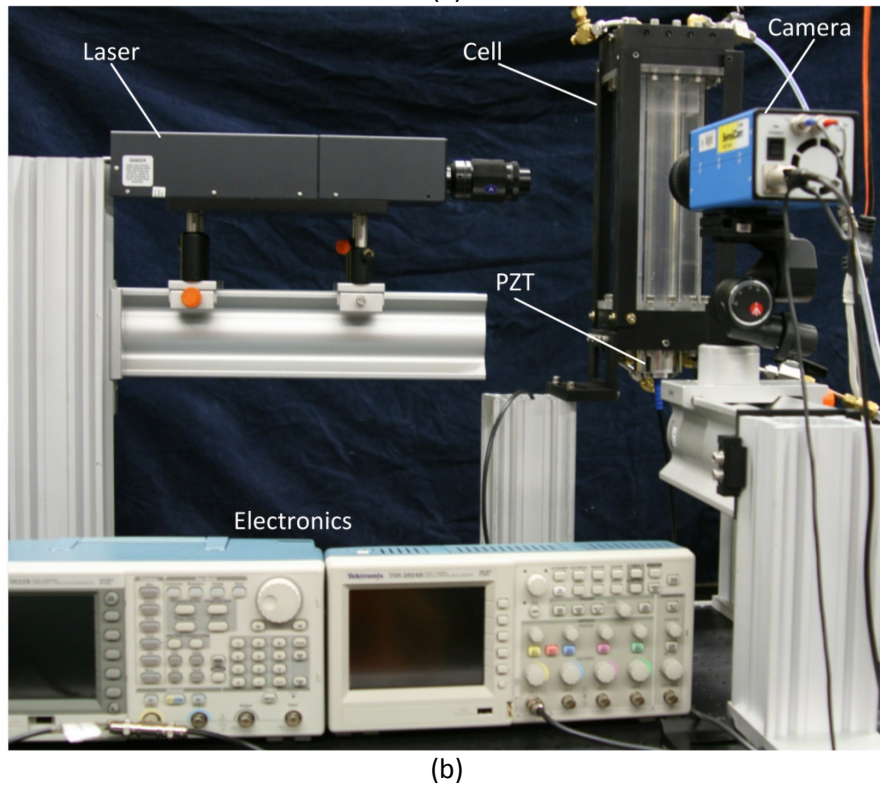
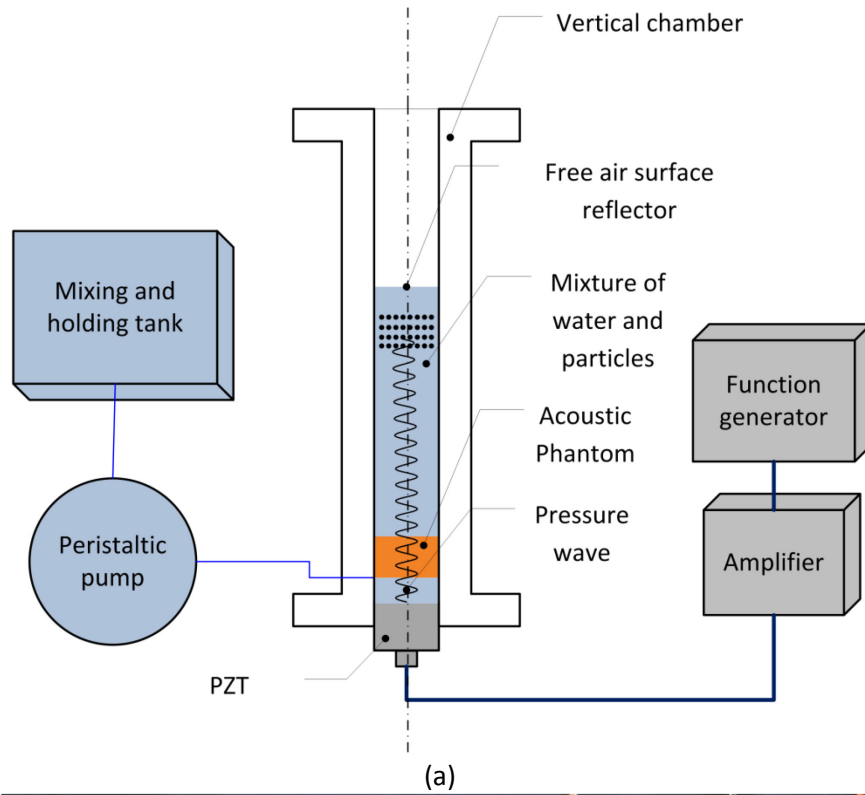


Figure 2-1: (a) Schematic of the static chamber experiment; (b) Digital image of static chamber experiment

### *The Piezo-Electric Transducer (PZT)*

A non destructive testing (NDT) PZT (Olympus-Panametrics A301S, Immersion) with a diameter of 25 mm and resonance frequency of 0.5 MHz is used as the acoustic pressure actuator. The normalized frequency response of the PZT, located at the bottom of the cell, is shown in Figure 2-2. The PZT is excited with a sine wave input and generates an acoustic pressure wave that propagates towards the top of the cylinder. The sine wave input is generated using a function generator (Tektronix, AFG3021B) that is amplified by a high power amplifier (ENI, Model 240L). Voltage measurements are performed using an oscilloscope (Tektronix, TDS 2024B).

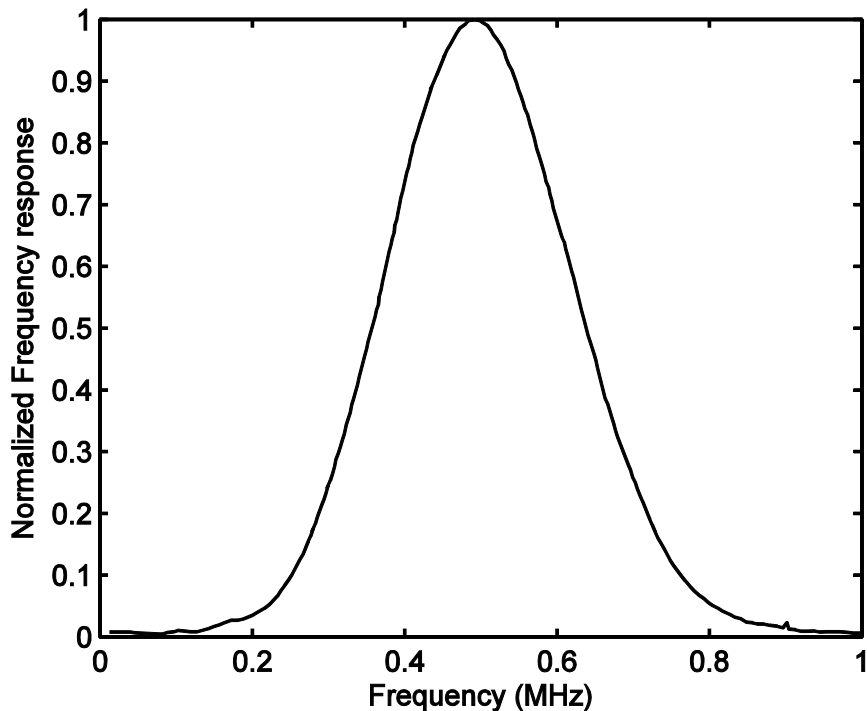


Figure 2-2: Frequency spectrum of the NDT PZT used in acoustic chamber

Above the PZT an acoustic phantom is used to avoid the effects of the acoustic streaming. The acoustic phantom is an acoustically transparent low attenuation layer (Hancock, 2001) which reduces the acoustic streaming effects. The acoustic phantom is made using the procedure by (Hall, Bilgen, Insana, & Krouskop, 1997) with the material in Table 2-1. The acoustic phantom allows the acoustic pressure wave propagation through the particle suspension and reflects back from the free air surface of the fluid. The air acts as a reflector as the acoustic properties of the air is different from that of water (Whitworth, 1992). The superposition of the reflected wave and the PZT acoustic wave results in acoustic standing wave and hence the particles are affected by the primary acoustic force.

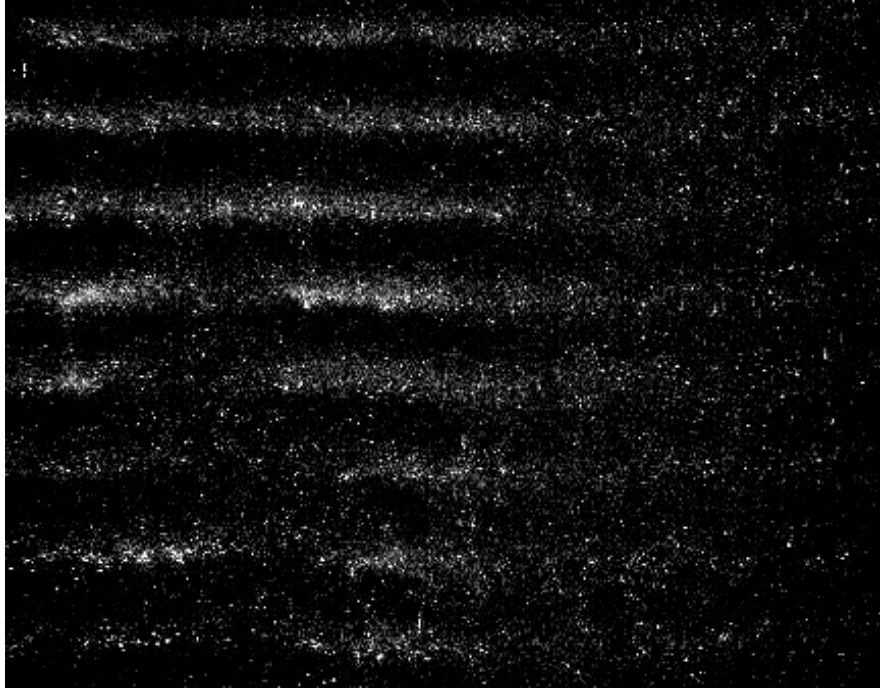
Table 2-1: Acoustic phantom ingredients

Ingredient	Distilled water	Propanol	Formaldehyde (37 %)	Agar
Weight concentration (%)	89	8	0.18	1.97

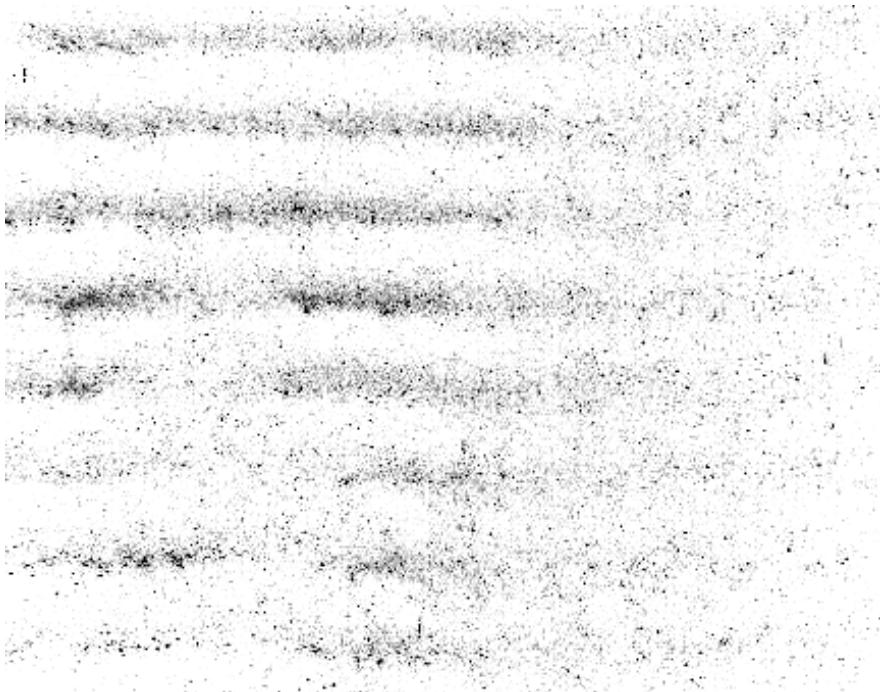
*Preliminary results*

In Figure 2-3, the formation of particles to the PNs is shown. The PZT voltage is set to 21 V in this experiment. The gravity force on particles is balanced by the acoustic radiation force at the PNs causing densification of particles. In Figure 2-3 (a) the originally captured image has been processed to make the particles more visible and Figure 2-3 (b) the black-white color scale is inverted. This inversion allows for better viewing of particle images. Based on these

images, the spacing between PNs is 1.5 mm. The distance between two consecutive PNs is half of the wavelength of the acoustic pressure wave which is calculated to be 3.0 mm based on  $(\lambda = \frac{c}{f})$  assuming speed of sound in water is 1500 m/s.



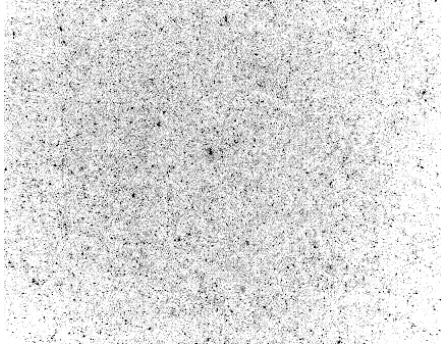
(a)



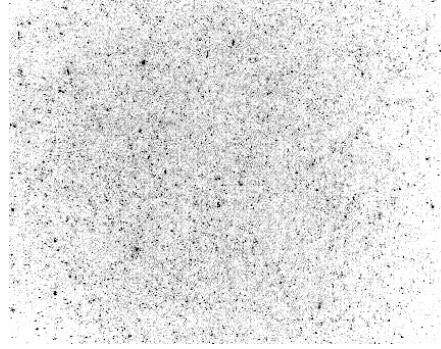
(b)

Figure 2-3 : Preliminary images of formation of particles to PNs in the static chamber setup; (a) The original image; (b) The grey scale inverted image

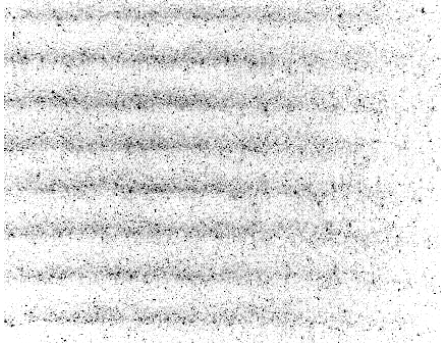
A time sequence of images of showing the time evolution of the separation process with the associated captured time is shown in Figure 2-4. Initially the particles are settling due to their higher density than water and therefore of gravity. After 3.5 s, the PZT transducer is triggered and the primary acoustic force is applied on the particles. During the next 3.5 s, particles are forced by the acoustic force to the nearest PNs and noticeable particle banding is observed. After this initial formation of horizontal particle bands at the PNs at  $t = 7$  s, particles continue to migrate to the PNs but there is no noticeable visual change in the image. The acoustic phenomenon continues to densify more particles to the PNs over the next approximately 30 s. The destruction of some particle bands at the PNs is visible in the image associated with  $t = 35$  s and is highlighted with a rectangle. This phenomenon is attributed to high densification of particles at the PNs and the development of a gravity instability in this region. This leads to a fingering instability (Blanchette & Bush, 2005) of the densified region and breakdown of the formed particle bands at the PNs. It takes  $\sim 6$  seconds for the acoustic field to again dominant partial motion and a reformation of horizontal bands of particles at the PNs ( $t = 42$  s.) to occur. The reformed particle bands become more visible as time approaches the end of the time series a image  $t = 52.5$  s. This destruction of particle bands happens again as the particles densify to the pressure nodes.



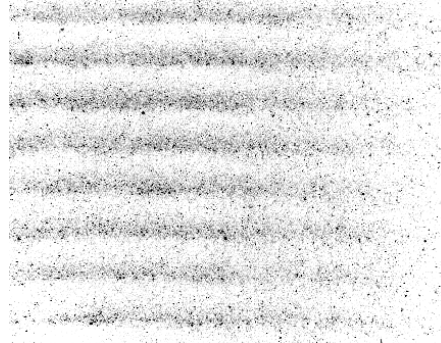
$t = 0 \text{ s}$



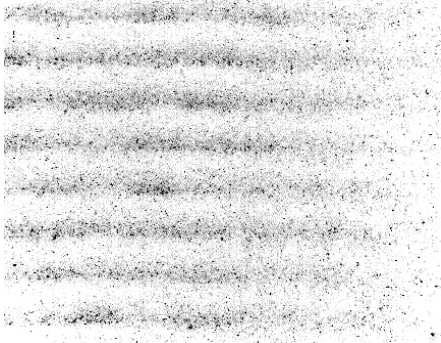
$t = 3.5 \text{ s}$



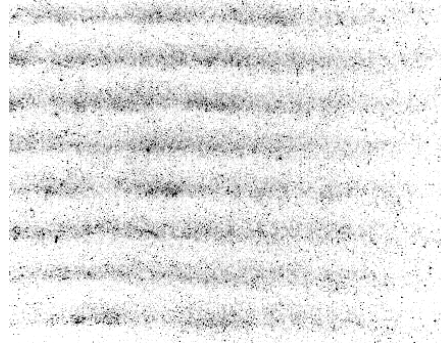
$t = 7 \text{ s}$



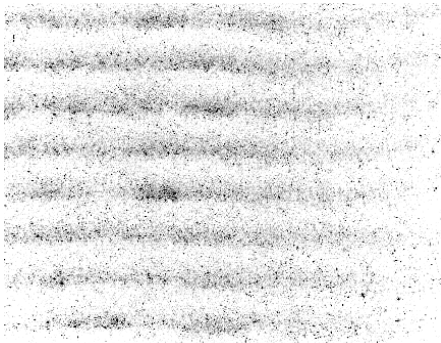
$t = 10.5 \text{ s}$



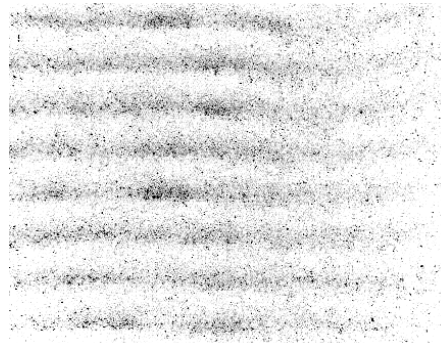
$t = 14 \text{ s}$



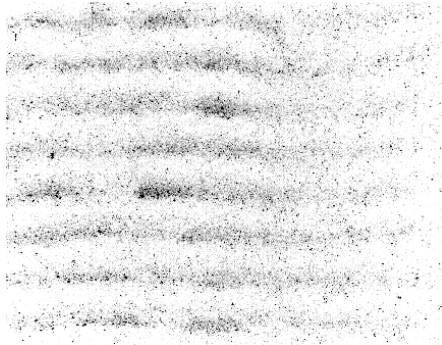
$t = 17.5 \text{ s}$



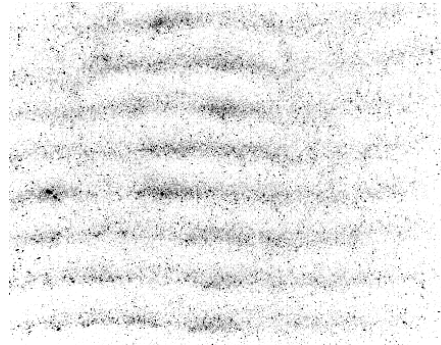
$t = 21 \text{ s}$



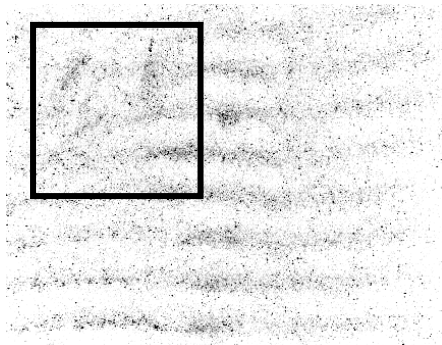
$t = 24.5 \text{ s}$



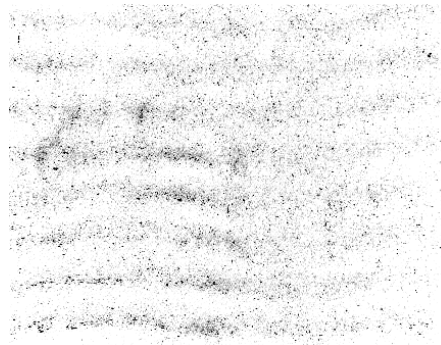
$t = 28 \text{ s}$



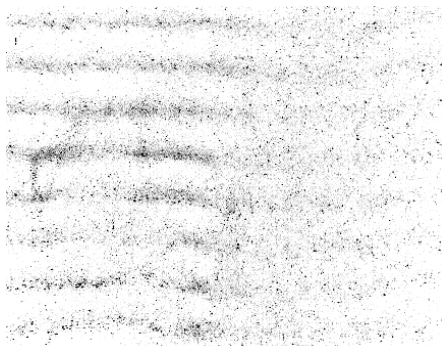
$t = 31.5 \text{ s}$



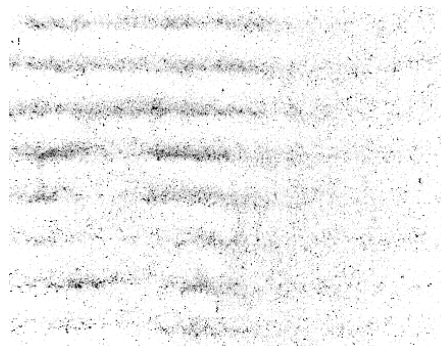
$t = 35 \text{ s}$



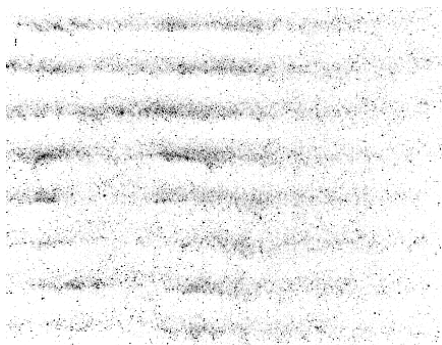
$t = 38.5 \text{ s}$



$t = 42 \text{ s}$



$t = 45.5 \text{ s}$



$t = 49 \text{ s}$



$t = 52.5 \text{ s}$

Figure 2-4: Raw data images (inverted color map) highlighting the separation process with the associated time of capture

## *Conclusions*

The feasibility of the application of macro-scale multi-wavelength acoustophoresis on the 37  $\mu\text{m}$  particles is shown. The particles weight is balanced using the primary acoustic force resulting in densified bands of particles at the PN of the acoustic pressure wave. Once, high densification of particles at the PN occurs, gravity instability is visible in the acoustic static chamber. Since the aim of this work is to study particle motion only under the effect of primary acoustic force without the gravity instability effect present, the next design uses the primary acoustic force horizontally.

### **2.2.2 Acoustic channel**

#### *Setup schematic*

To maintain consistent experiment conditions so the effect of gravity instabilities is minimized, a flowing channel rig as shown in Figure 2-5 is used. The engineering drawings of the acoustic channel are shown in Appendix B. The schematic of the acoustic channel is shown in Figure 2-5 (a). A mixture of particles and water flows through the channel due to gravity. The particles are soda-lime glass sphere particles with the diameter of 37  $\mu\text{m}$  and density of 2500  $\text{kg}/\text{m}^3$ . The acoustic wave generated by PZT reflects back from a glass reflector at the other side of the test section. The glass acts as reflector due to high difference of acoustic properties of water and glass. The superposition of the PZT

travelling acoustic pressure wave and reflected acoustic wave generates an acoustic standing wave which affects the passing particles due to the primary acoustic force. Three dimensional flow structures and instabilities are not present in the test section since flow is laminar.

### *Imaging system*

Particle motion is captured using either shadowgraph or direct illumination of particles. An example of the direct illumination setup is shown in Figure 2-5 (a). In the direct illumination method, a continuous mode laser (Laserglow Technologies, LRS-0532-PF) is used to illuminate field-of-view. This laser is capable of delivering up to 2W of power and operates with wavelength of 532 nm. A high speed camera (DRS's Lightning® RDTPlus) attached to a long working distance lens (Navitar, 12 X) is used to capture the image of particles. The camera resolution is set to (512 x 512) pixels and runs at 1000 frames per second (fps). For the shadowgraphy method, a green 530 nm LED (Thor Labs, Model M530L2,) is mounted facing the camera and the camera captures the shadow images of particle motion.

### *The piezo-electric transducer (PZT)*

A high power immersion PZT (Precision Acoustics, custom-made) is used to generate the acoustic pressure wave. The diameter of PZT is 25 mm and the main resonance frequency of the frequency response is 0.5 MHz. The frequency spectrum of the PZT is shown in Figure 2-6. The pressure generated by the PZT is

tabulated by the supplier and is reported in Table 2-2. The generated pressure reported in this table is measured at a 50 mm distance from the PZT. Based on (Hancock, 2001), these pressure magnitudes are enough for densifying particles in 30  $\mu\text{m}$  range at PNs.

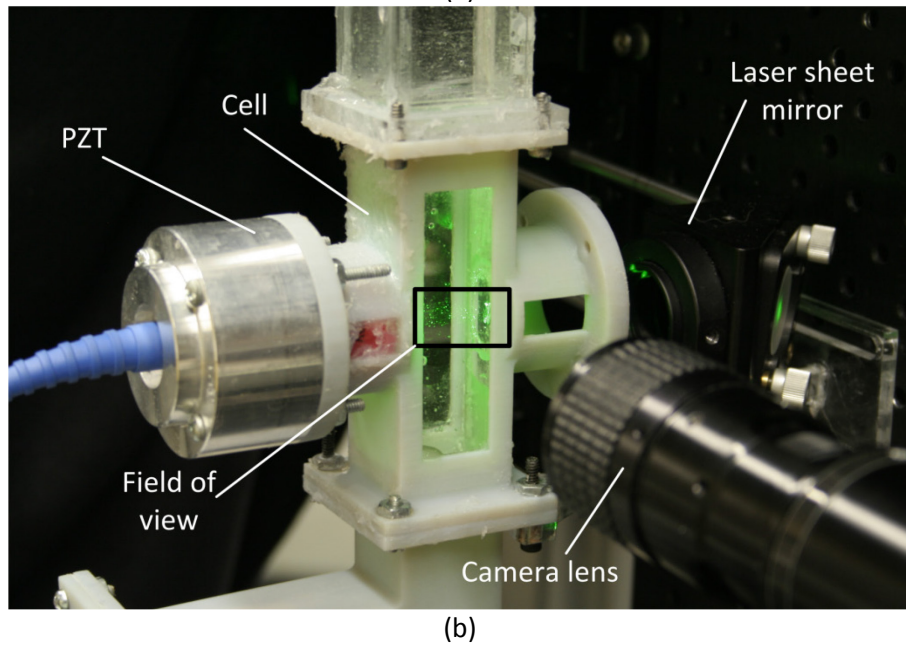
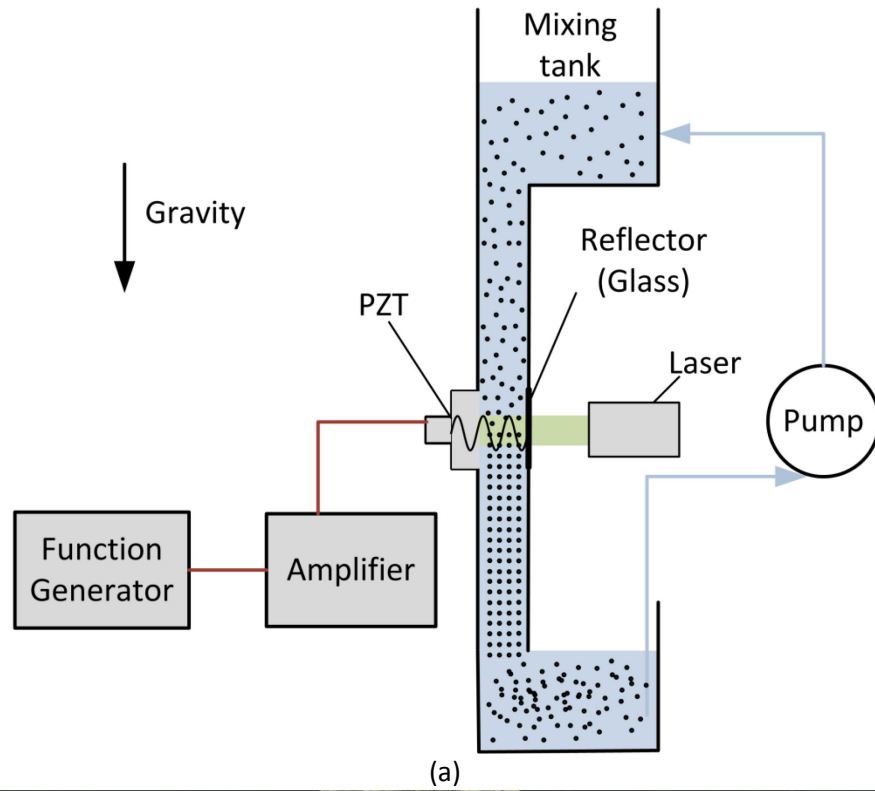


Figure 2-5 : (a) Schematic of the acoustic channel experiment; (b) Digital image of acoustic channel experiment

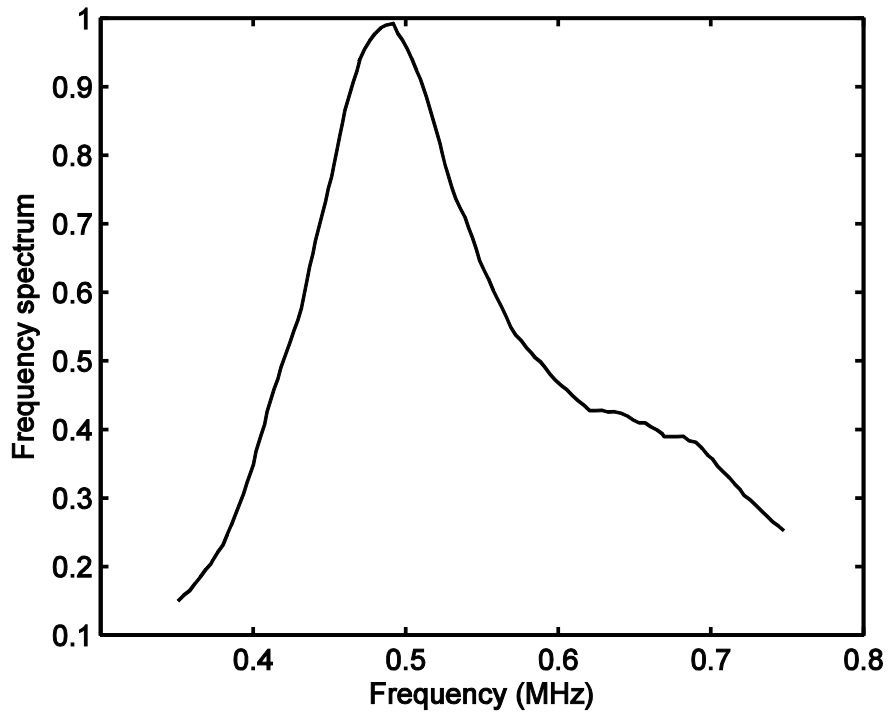


Figure 2-6: Frequency spectrum of the acoustic channel PZT (Precision acoustics, custom-made) used in preliminary experimental system

Table 2-2: Acoustic channel PZT specification

PZT Pk-Pk voltage (V)	Measured acoustic Pressure (kPa)
27	200
60	350
150	490

*Preliminary results*

A sample of the particles formation to the nearest PNs is shown in Figure 2-7. The image is captured using the shadowgraphy technique at  $t = 1.75$  s after turning the PZT on. The darker locations showing the particles shadow are located at the PNs. The bright locations are attributed to the PANs where fewer particles can be found. There are some gas bubbles in the liquid which can be

seen at the PANs. The bubbles are forced to the PAN due to their negative ACF value. Based on these images, the spacing between PNs is measured to be 1.5 mm which is in agreement with the theoretical calculation of the nodal spacing. Theoretically, the distance between two consecutive PNs is half of the wavelength of the acoustic pressure wave. The acoustic wave wavelength is calculated to be 3.0 mm based on  $\left(\lambda = \frac{c}{f}\right)$  assuming speed of sound in water is 1500 m/s with  $f = 0.5$  MHz.

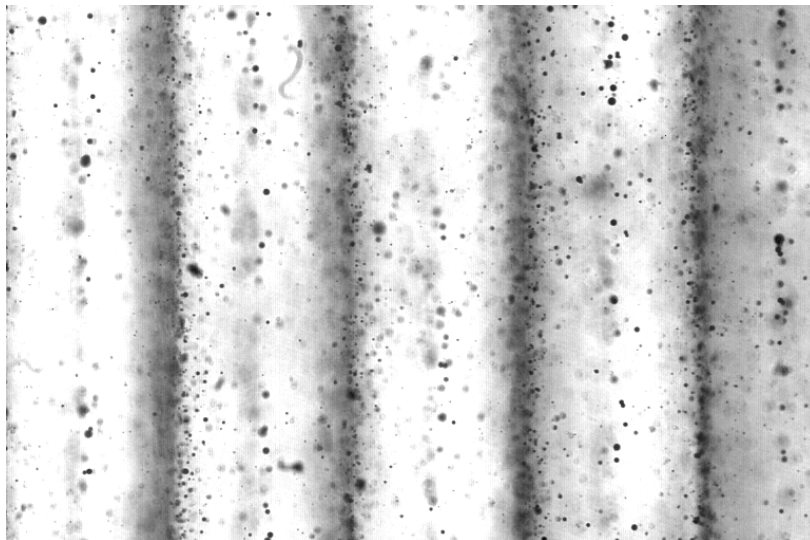


Figure 2-7 : Preliminary images of formation of particles to PNs in the acoustic channel setup;

A time series images of separation process noting the image capture time is shown in Figure 2-8. The PZT is turned on at  $t = 0$  s resulting in a primary acoustic force being applied to the particles. At 0.5 s the particles bands are forming at the PNS and there are remaining particles which are still moving toward the PNs. These particles are moving slower possibly due to their smaller size or non-uniformities in their material resulting in differences in ACF. There

are some bubbles visible at the PANs. After the first formation of vertical particle bands at PNs, more particles move to the PN. The image is devoid of particles at the PANs where the particles are repelled by the primary acoustic force. This densification continues until PZT is turned off at  $t = 1.75$  s

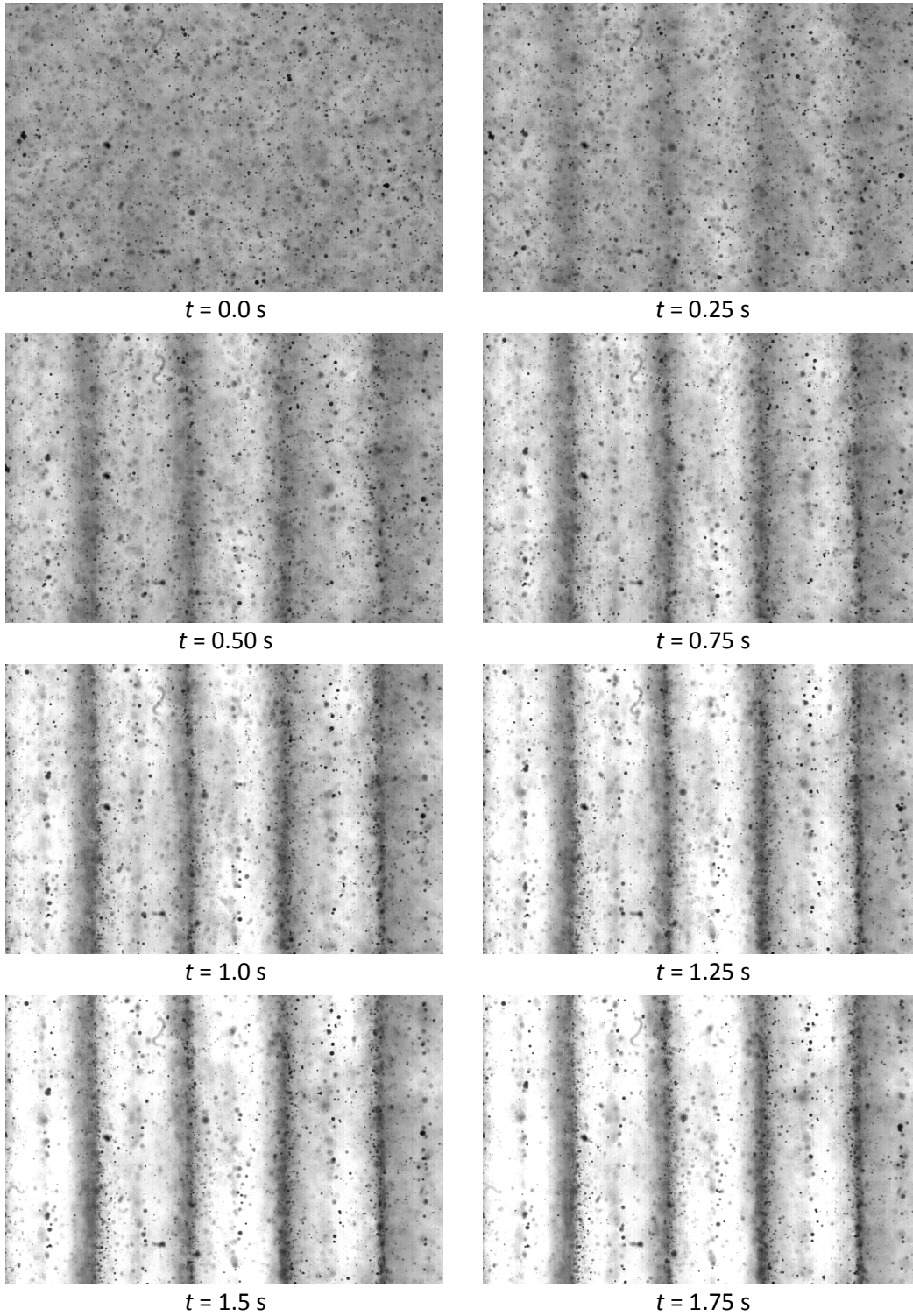


Figure 2-8: Raw data images of the separation process in the acoustic channel experiment; The associate time of capture is below each image

## *Conclusions*

The vertical acoustic channel applies a primary acoustic force horizontally which helps to remove the effect of gravity instability due to the weight of particles. Qualitative observation of primary acoustic force at the acoustic channel is performed providing an understanding of spatial and temporal aspects of primary acoustic force. This insight is used to design the main experimental setup which is described next.

### **2.3 Main experimental setup**

A schematic of the main experimental setup is shown in Figure 2-9 and the actual setup used is shown in Figure 2-10. The acoustic field is generated in a static fluid (degassed distilled water) contained within the acoustic cell. A high frequency resonant high power piezo-electric transducer forms one side of the chamber and is forced using a continuous sine wave voltage. The sine wave is generated via a function generator amplified with a power amplifier. An imaging configuration with a thin light sheet of a laser illuminating the region of interest is shown in Figure 2-9. A high speed camera aligned toward the acoustic cell is used to image the motion of particles affected by ultrasonic acoustic pressure.

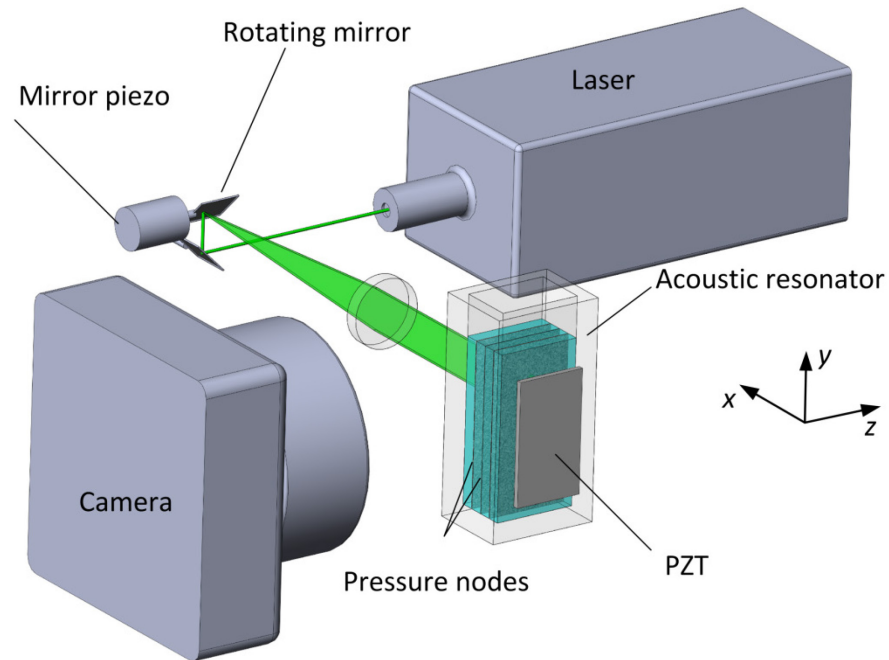


Figure 2-9 : Schematic of the main experimental components

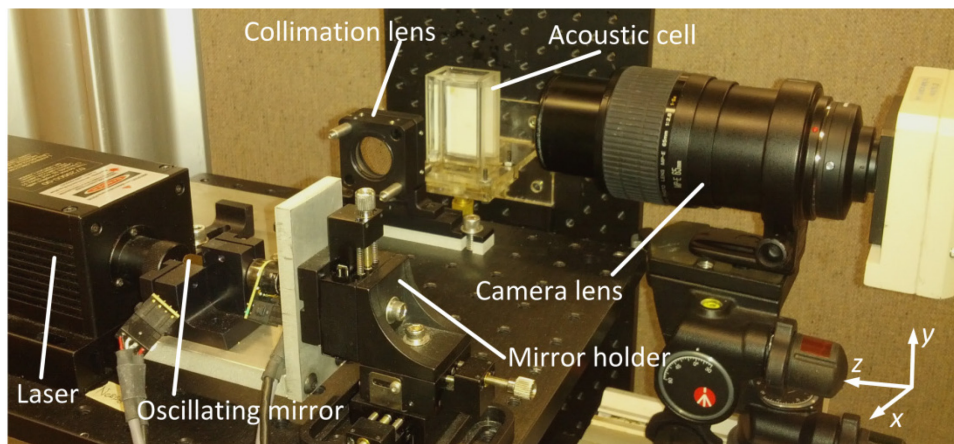


Figure 2-10 : Digital image of the experimental setup

### 2.3.1 Macro-scale acoustic resonator

The acoustic chamber is a  $30 \times 25 \times 65 \text{ mm}^3$  glass cell with a high power PZT (1.5 MHz resonance frequency) forming one side of the chamber (Sonosep Technologies Inc) (Trampler et al., 1994). The cell is aligned vertically and the transverse acoustic pressure wave influences the particles in the transverse

(horizontal) direction. The output frequency spectrum of the PZT is shown in Figure 2-11. The PZT is excited by applying a sinusoidal voltage generated from a function generator, (Tektronix, AFG3021B). That is amplified by a high power amplifier (ENI, Model 240L). Voltage measurements are performed using an oscilloscope (Tektronix, TDS 2024B).

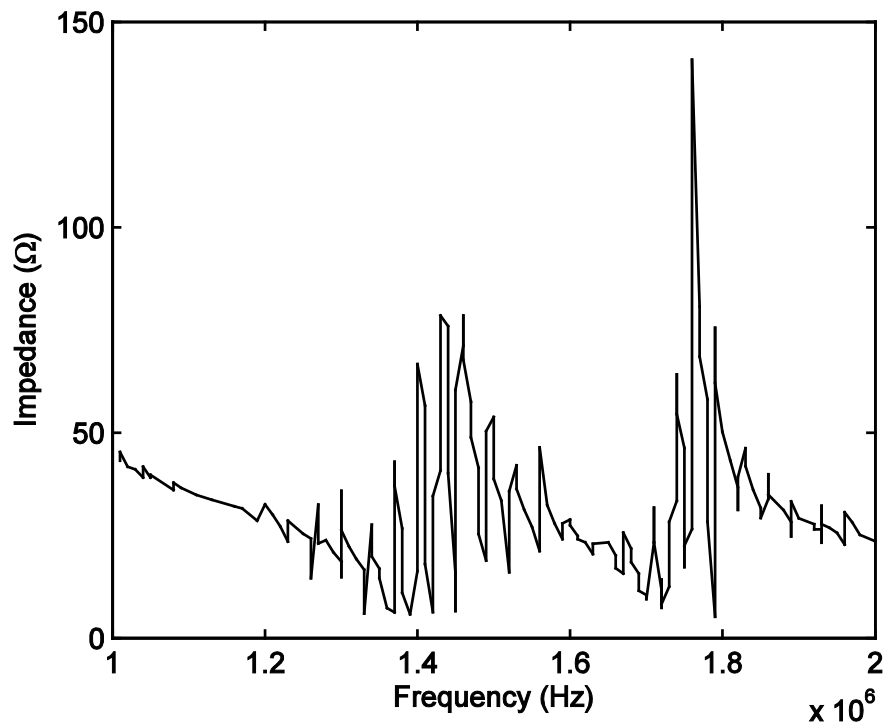


Figure 2-11: Frequency spectrum of the acoustic chamber PZT used in main experimental system

The individual properties of particle that are investigated are detailed in Table 2-3. Based on these properties, the corresponding ACF is always positive so the particles will propagate to PNs in the acoustic field. The particles used in the experiments have a low coefficient of variation (CV) for the particle size distribution which helps in validation of the primary acoustic force theory. A list

of properties of different material used in experiments / calculations (at 25 °C) is reported in Table 2-4.

Table 2-3: Properties of particle sets used in experiments (at 25 °C)

Particle Set	Description	Mean Diameter (μm)	CV	Density (kg/m <sup>3</sup> )	Speed of sound (m/s)	ACF
PS-1	Silica Microspheres (Cospheric)	8	10%	1800	6000	0.49
PS-2	Hollow Microspheres (Potters 60P18)	18	35%	600	6000	0.14
PS-3	Hollow Microspheres (Potters 110P18)	10	45%	1100	6000	0.35
PS-4	Silica Microspheres (Cospheric)	28	10%	2500	6000	0.57

Table 2-4: List of material properties in experiments/calculations

water		
Density ( $\rho$ )	997	kg/m <sup>3</sup>
Speed of sound ( $c$ )	1497	m/s
Viscosity ( $\mu$ )	0.89	mPas
Compressibility ( $\beta$ )	448	1/Tpa
Glycerol		
Density	1261	kg/m <sup>3</sup>
Speed of sound	1920	m/s
Viscosity	1.412	Pas
Compressibility (calculated as $\beta = 1/(\rho c^2)$ )	48	1/Tpa
Silica		
Density	2200	kg/m <sup>3</sup>
Speed of sound	6000	m/s
Compressibility (calculated as $\beta = 1/(\rho c^2)$ )	13	1/Tpa
Glass		
Density	2500	kg/m <sup>3</sup>
Speed of sound	5600	m/s
Compressibility (calculated as $\beta = 1/(\rho c^2)$ )	13	1/Tpa
Ethanol		
Density	800	kg/m <sup>3</sup>
Speed of sound	1144	m/s
Compressibility (calculated as $\beta = 1/(\rho c^2)$ )	955	1/Tpa
Polystyrene		
Density	1100	kg/m <sup>3</sup>
Speed of sound	2350	m/s
Compressibility (calculated as $\beta = 1/(\rho c^2)$ )	165	1/Tpa

### 2.3.2 Imaging system

The imaging system consists of a continuous wave laser and a two-dimensional piezo scanning mirror combined to illuminate the interested area and a high speed camera with a long working distance lens to capture images of the particle fields. The laser beam is swept using one mirror of the 2-dimensional scanner which consists of two rotating mirrors driven using two piezo-electrics. The swept laser beam is passed through a collimation lens located at the focal distance of the mirrors to generate a parallel laser sheet. The beam is reflected

toward the region of interest using the second control mirror which helps in correcting the alignment of the laser plane due to possible misalignment of the illumination components.

On the image capturing side of the setup, there is a high speed camera (DRS's Lightning® RDTPlus) attached to a 65 mm lens (Canon MP-E 65 mm). The camera is capable of collecting images at 500 fps at full frame (1280 × 1024 pixels) and maximum of 16,000 fps at reduced resolution. It has a 10-bit CMOS sensor and equipped with a TTL trigger. The camera lens is an f/2.8 with working distance range of 40-100 mm and capable of magnification factor of up to 5×. Typically the camera is operated at 1000 fps with the resolution of 512 x 512 and the lens magnification is set to 3× leading to a depth of field of 88 μm and working distance of 50 mm.

### **2.3.3 Experiment procedure**

A consistent experimental procedure was followed throughout. First, before each experiment distilled water is degassed by heating and simultaneously creating a vacuum. A vacuum pump (DIVAC 1.2 L) and a hotplate (Jenway, Model 1103) are used. Degassing is used to avoid the generation of cavitation bubbles in regions of low pressure at PANs of the acoustic field in the cell. Particle volume concentration is set to 0.05% by suspending an initially weight measured amount of particles in a known volume of fluid. All

experiments are performed at standard local temperature (between 22°C and 24°C) and local pressure (99 and 103 kPa).

Results are collected from the onset of applying the acoustic field to the suspension. After assuring the mixture has homogeneous particle concentration, the experiment starts by triggering the camera to collect frames at 1000 fps as shown schematically in Figure 2-12. Other components are triggered sequential to the camera acquisition in a specific order. The function generator that drives the PZT is triggered after 0.1 s and hence the exact time of onset of acoustic excitement is known. The particles are subject to the primary acoustic force and start to travel horizontally to the nearest PN following the activation of the PZT. The PZT is actuated for 1 s which typically provides sufficient time to move all particles to a pressure node in the field.

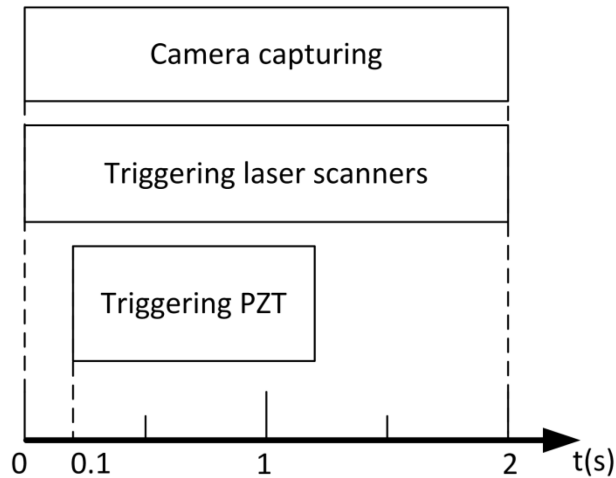


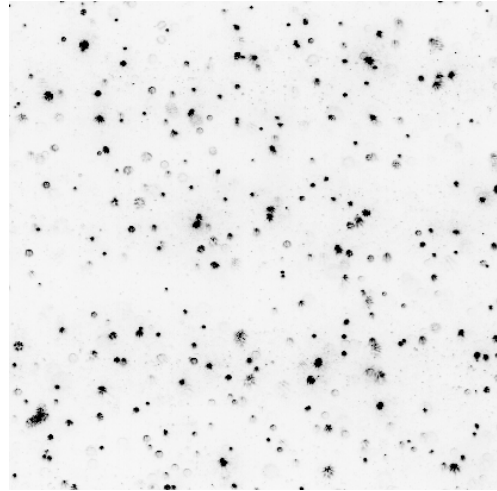
Figure 2-12: Schematic of the timing of the experiments procedure

#### **2.3.4 Initial results**

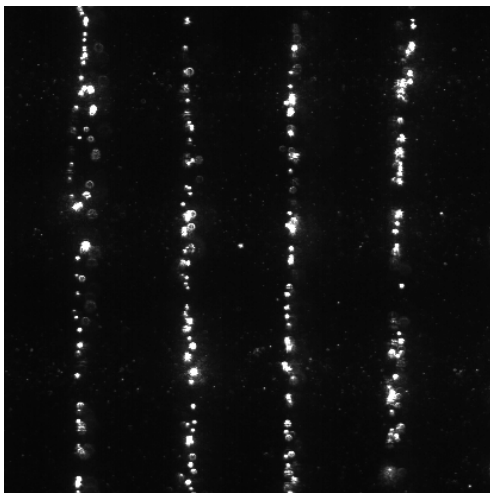
Set of captured images in Figure 2-13 shows typical experimental results. A random, even distribution of particles captured by the imaging system is shown in Figure 2-13 (a). The color inverted version of the image is shown in Figure 2-13 (b) and shows particle locations before the activation of the acoustic field. The effect of turning on the PZT and the densification of particles after applying the acoustic field for 1 s is shown in Figure 2-13 (c) and the color inverted version is shown in Figure 2-13 (d). The color inversion is performed as the first step of image processing and all remaining images in the thesis are shown this way. As shown in Figure 2-13 (d), almost all of the particles have been forced to the nearest PNs and there are few bubbles that are forced to the PANs. The transverse velocity of particles is obtained by further processing the camera images.



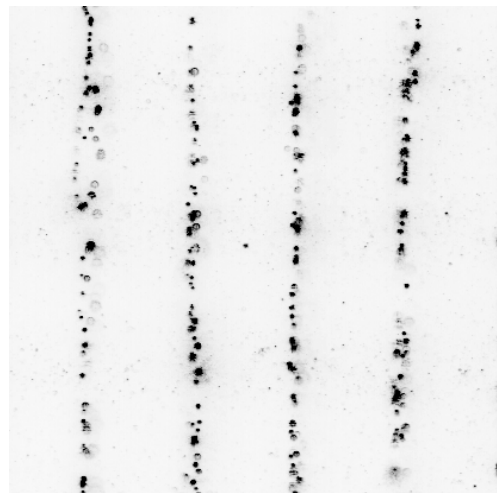
(a)



(b)



(c)



(d)

Figure 2-13: Experimentally captured images of acoustic separation of particles, (a) a sample image of particles before densification process, (b) Color inverted version of images shown in (a); (c) a sample image of densified particles (d), Color inverted version of image shown in (c)

## 2.4 Summary

In this chapter, the experimental setups used for characterizing the primary acoustic force are described. Preliminary experimental setups are designed and built for carrying out a feasibility study of primary acoustic force by trapping particles horizontally (static chamber) and vertically (acoustic channel). Based on the preliminary setups, the main experimental setup is designed in which consistent densification of particles is observed. The sample captured particles in the main experimental setup motion shows few bubbles generated in field-of-view and almost all of the particles travel to the PNs. This experimental system will be used in subsequent chapters for quantitative characterization of a macro-scale multi-wavelength acoustic resonator. To do this, a PTV method is needed for analyzing the captured images of particles as a sample shown in Figure 2-13 is needed and thus is discussed in detail in Chapter 3.

## **CHAPTER 3: DEVELOPMENT OF A PTV ALGORITHM FOR INVESTIGATING MACRO-SCALE ACOUSTOPHORESIS**

### **3.1 Introduction**

Particle tracking velocimetry (PTV) is an imaging technique used to measure fluid flow (Ronald J Adrian, 1991). Determining the velocity field is one of the main steps in determining details of a flow. PTV measures the instantaneous velocity of seeded particles in a flow and hence fully obtains the flow properties through full time history of the particle motion (Doh et al., 2000). This is useful in determining the velocity field in 3D unsteady flows. However the concentration of seeding particles must be limited to allow individual detection of particles (Guezennec, Brodkey, Trigui, & Kent, 1994).

After collecting the images, the general PTV algorithm consists of two main steps (Ronald J Adrian, 1991). The first step is particle identification in which the algorithm detects and locates a particle within an image. This step requires

image preprocessing phases to prepare the image for the particle detection process. In this chapter image preprocessing steps are developed based on the homogeneity, image intensity and noise of the images. In the next step of PTV, particle tracking is performed. Based on the seeding particles concentration and source of flow, particle tracking is used to recognize particles and track them through a series of images resulting in a time history of the tracked particles.

It is assumed that the tracing particles follow the fluid flow and thus the density of tracing particles need to be close to density of containing fluid (Ronald J Adrian, 1991). The size of tracing particles also needs to be much smaller than the scale of the flow structure (C. Liu & Tao, 2007). These requirements set some limitations to the selection of seeding particles. A classic schematic of the displacement of the fluid elements and tracing particles displacements is shown in Figure 3-1. The fluid element and the seeding particle are at the same point initially. The particle does not follow the path of the fluid element due to the difference in density (different inertia) or large size of the particle relative to the curvature of the fluid path. The displacement of the particle also differs from the fluid element displacement by connecting the location of particle in the two frames by straight line. This is in contrast with the fluid element displacement which is in curvature and results in difference in measured particle displacement and fluid element motion.

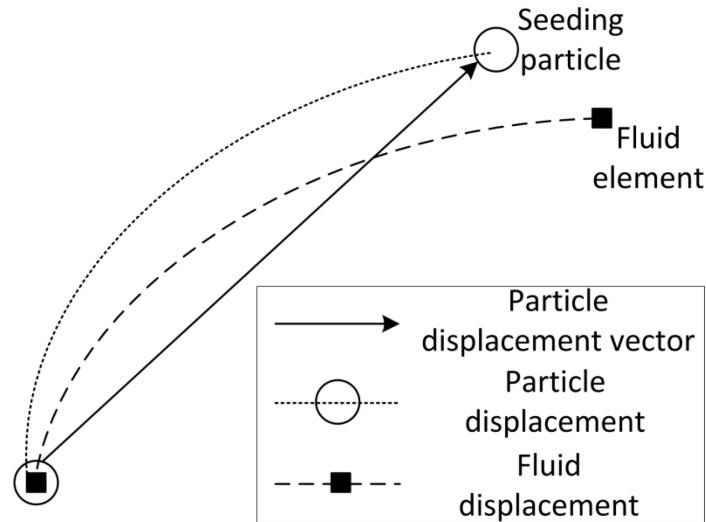


Figure 3-1: Limitations of particles following the motion of fluid element

In developing an appropriate strategy for PTV application to particles under the influence of acoustophoresis, some basic understanding of the flow is needed. There is no general motion of fluid and thus the particles are not following the fluid flow. Particle motion is due to an external force which depends on the location of particle as highlighted in equation (1-14).

A schematic of the motion of particles due to primary acoustic force is shown in Figure 3-2. There are two PANs at either side of the figure and a PN is at the middle of the graph. In this schematic 6 consecutive images of two particles and a bubble are shown to highlight their relative motion. The captured images are shown on top of each other and the location of the particles and the bubble are denoted with the number of the image. The particles move to the closest PN depending on their initial location, which might be in opposite directions. As the particles approach the PN, the magnitude of the primary

acoustic force decreases resulting in a lower velocity and closer spacing. This causes the overlapping of particles as they densify at the pressure nodes and the amount of overlapping maximizes at the pressure nodes. The bubble also shown in the figure travels toward a PAN and is slowing down as it is approaching the PAN. The PTV algorithm needs to detect and track the particles/bubbles within the field-of-view over a long time history to allow investigation of properties of the acoustic field. It is also desirable to distinguish and filter the bubbles from the particles.

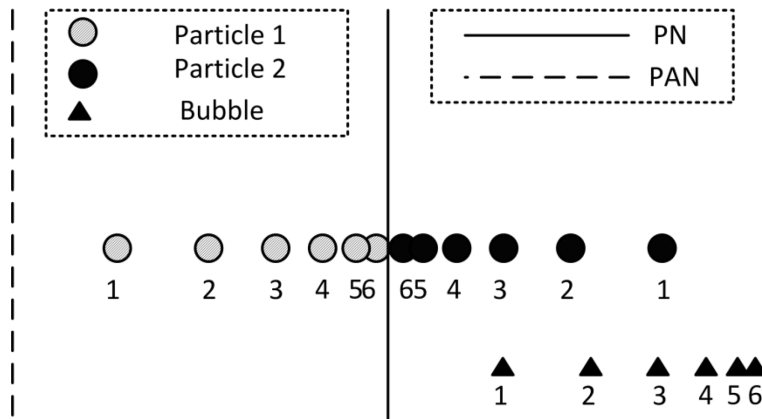


Figure 3-2: Overlapping of particles and bubbles at pressure nodes and pressure anti-nodes respectively

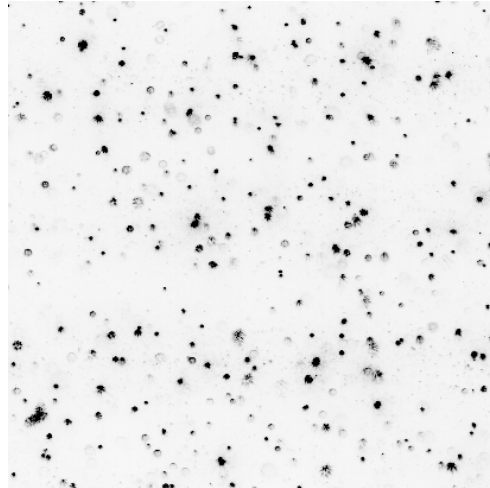
Another characteristic of this flow is the time dependency which changes image parameters such as particle homogeneity and particle distribution. For example a set of raw images are shown in Figure 3-3. The images of particles before and after the acoustic field is applied show how the acoustic field concentrates particles into vertical bands. In Figure 3-3 (a) a homogeneous

particle distribution is shown of in-focus particles. In Figure 3-3 (b) the acoustic field, which has planes of nodal pressure oriented vertically, has been applied and the particles have migrated to PNs in the acoustic field. These figures highlight the challenges of determining the velocity and hence the force acting on the particles. For the homogeneous case before the acoustic field is applied, particle detection is relatively easily with individual particles being clearly defined. As the applied acoustic field concentrates the particles into bands, the inter-particle distance reduces and particle images begin to overlap. Individual particle detection becomes more difficult as particle concentration increases with time.

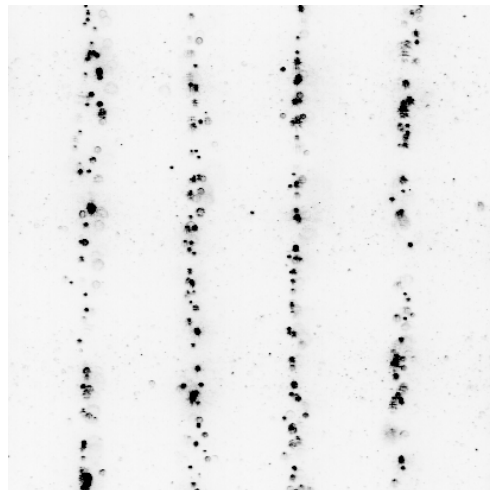
Based on the ACF of a particle, the general direction of a particle is toward a PN. Initially, the direction of motion of a particle is unknown due to the existence of several PN in the field-of-view in a macro-scale multi-wavelength acoustic resonator. There can also be bubbles in the field-of-view which will migrate toward PANs. Detection of a bubble simultaneously to a particle is difficult with common PTV approaches since they move in opposite direction.

Another characteristic of particle motion due to acoustophoresis is the dependence of particles motion on the location (as in equation (1-6)). This violates the assumption of PTV in which the seeding particles are following the flow. However, there is no general motion of the fluid particle system subject to acoustophoresis so the particle motion depends on their absolute location.

There can be two neighbor particles moving with different velocities due to their different size with the application of acoustophoresis so common PTV techniques are inadequate for acoustophoresis and a specialized PTV approach is needed.



(a)



(b)

Figure 3-3: Particles in images in different situations, (a) even distribution of particles before applying the acoustic wave, (b) densification of particles to bands due to the acoustic radiation force

To determine particle motion and particle velocity the time evolution of particle homogeneity and particle distribution must be considered. The aim here is to observe the effect of lack of homogeneity which is changing due to densification and overlapping of particles. To examine how particle homogeneity varies with time, the intensity of inverted images the case in Figure 3-3 is post-processed. Post-processing is composed of summing up the intensity of images in the vertical direction in the region of a sample PN and a PAN and plotting the normalized values versus time. This variation, shown in Figure 3-4 highlights that as the intensity of the pressure node increases; the particle field homogeneity reduces due to densification causing the spacing between particles to decline. This leads to more overlapping of particles obstructing particle detection.

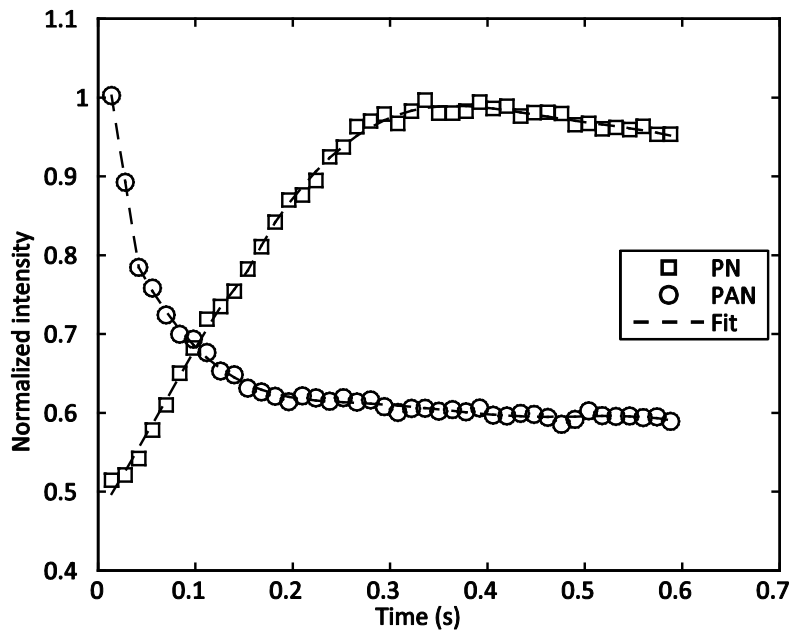


Figure 3-4: Variation of the summed intensity of a sample image at a PN and PAN indicating the change in the homogeneity of the image during densification of particles

## 3.2 PTV-processing

A flow chart of the PTV approach developed is shown in Figure 3-5 outlining the different steps in the algorithm. The captured image series are preprocessed to remove noise and smoothen the images. In the particle detection block, the images are processed to reduce the effect of overlapping of particles and then particle detection is performed. In the particle motion step, the detected particles are tracked and their velocity is calculated. The PTV algorithm is applied to the captured images via a custom-code (see appendix C) and particles are tracked over the whole densification time of 1s.

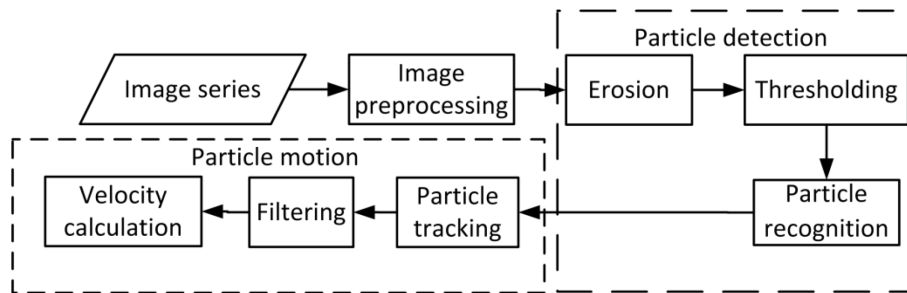


Figure 3-5 A block diagram of the implemented PTV algorithm

### 3.2.1 Image preprocessing

There are different methods in the literature for preprocessing the image. Background subtraction methods (Cowen, Monismith, Cowen, & Monismith, 1997; Nakamura, Zborowski, Lasky, Margel, & Chalmers, 2001) subtract a constant value from the background of an image. This method removes the background but also reduces the value of the particles intensities which leads to reduced contrast of images. This can cause difficulties in detection of particles in

the particle recognition steps. Morphological background subtraction (Guezennec & Kiritsis, 1990; Lecuona, Sosa, Rodríguez, & Zequeira, 2000; Pavlidis, 1982) subtracts a non-linear background from an image. It allows removal of the background noise while maintaining particle intensities. This allows good contrast of the particle to be achieved, which provides good data for the particle detection algorithm. In this work and the background is estimated using a morphological opening approach (Pavlidis, 1982). Image opening is composed of image erosion followed by image dilation (Pavlidis, 1982). This is performed to remove smaller particles and background noise from the camera data images while preserving the shape and size of target particles to prepare the data for particle detection.

### **3.2.2 Particle detection**

The particle detection processing block shown in Figure 3-3 involves three distinct steps. These are erosion, thresholding and particle recognition.

Image erosion is used to reduce the effect of overlapping of particles with the aim to promote individual particle detection. Image erosion shrinks the particles size to separate the probable overlapped particles found at the pressure nodes by setting each image pixel the minimum value of its neighboring pixels (van den Boomgaard & van Balen, 1992). An example of this type of image processing performed on a sample image having overlapped particles is shown in Figure 3-6. In Figure 3-6 (a), a sample field-of-view, in the process of

densification is highlighted. As the particles agglomerate to the pressure nodes they begin to overlap. An example of when such particles are detected in the rectangle is shown in Figure 3-6 (a) and enlarged in Figure 3-6 (b).

The eroded version of the images with the detected particles circled is shown in Figure 3-6 (c). The detected particles in the rectangle shown in Figure 3-6 (a) are circled in Figure 3-6 (d). Using this method, the particles can be tracked longer to positions nearer to the pressure nodes where the particle overlapping is increasing.

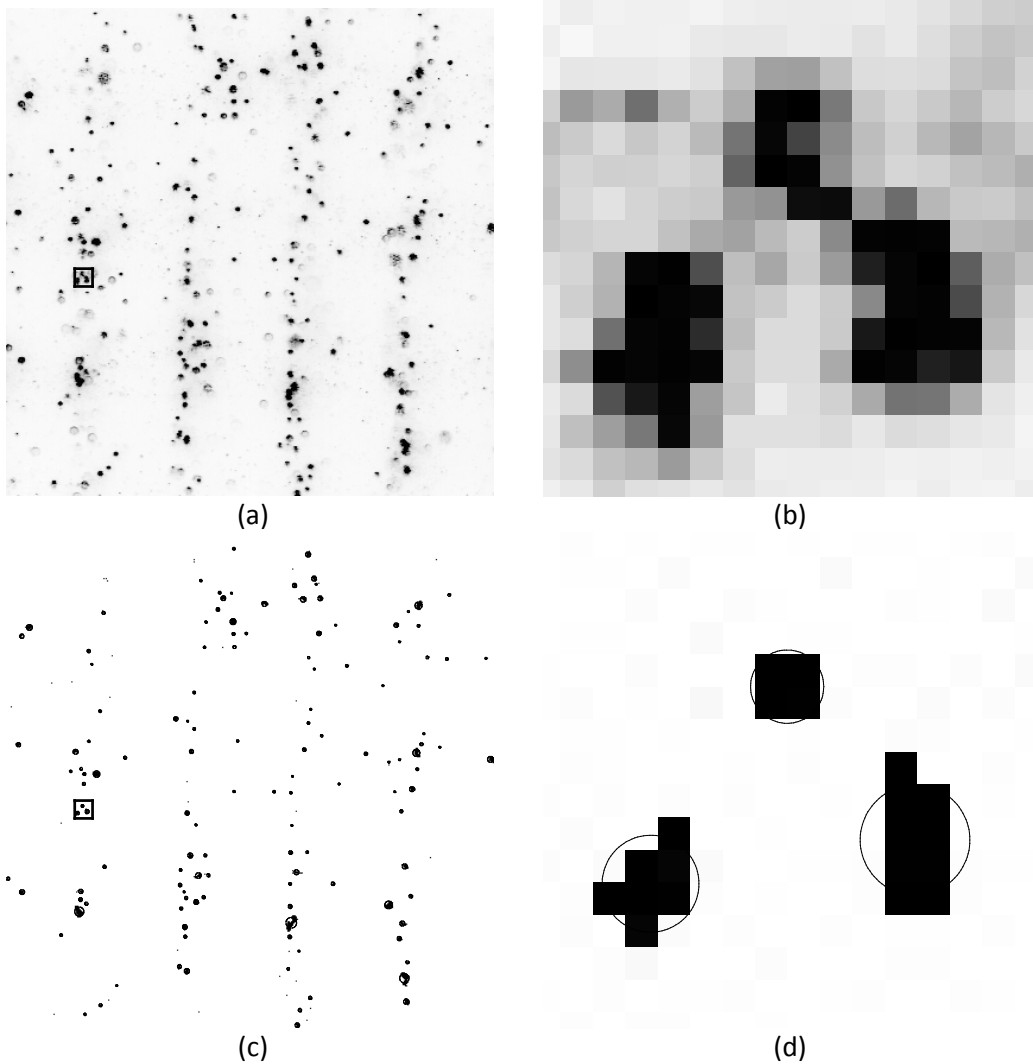


Figure 3-6: Application of image preprocessing and erosion to detect overlapped particles, (a) a sample image of particles in densification process, (b) magnified image of the rectangle containing an example of overlapping particles in image (a) is shown, (c) detected particles in the processed image (a) are circled, (d) detected particles in the magnified image of the rectangle in image (b) are depicted.

The particle detection process is applied by reducing the image to a binary image by defining a threshold. In hard thresholding methods, an input threshold is set by the user for an image or set of images (Kurada, Rankin, & Sridhar, 1997;

Lecuona et al., 2000; Maas, Gruen, & Papantoniou, 1993; Moroni, Cushman, & Cenedese, 2003; Ortiz-Villafuerte & Hassan, 2005; Zitoun, Sastry, & Guezennec, 2001). This method relies on the expertise of the user on setting the threshold and is not used in this work. The threshold value needed for an image can also be determined by soft thresholding methods. Soft thresholding is defined here as an algorithm which determines a proper threshold level autonomously. For example, a threshold can be locally determined as being slightly above the average intensity of 6x6 or 15x15 blocks of pixels in the image (Cowen et al., 1997; Seeger, Affeld, Goubergrits, Kertzsch, & Wellnhofer, 2001).

In this work the threshold is determined using Otsu's method (Otsu, 1979). Each image is assumed to have two classes of pixels which can be defined by a histogram as either black or white. An optimum threshold to minimize their intra-class variance is found. The intra-class variance is defined as the weighted sum of the variances of the two black and white classes. The particles are then recognized by a Moore-neighbour tracing algorithm modified by Jacob's stopping criteria (Pavlidis, 1982). This algorithm traces the exterior boundary of objects in the binary image using a normalized cut-off threshold of the specific image.

#### *Moore neighborhood tracing algorithm*

Having defined the main pixel in an image as Q, there is a set of 8 pixels around the main pixel which are sharing a vertex or edge with pixel Q. These pixels are named Q1 to Q8 as shown in Figure 3-7.

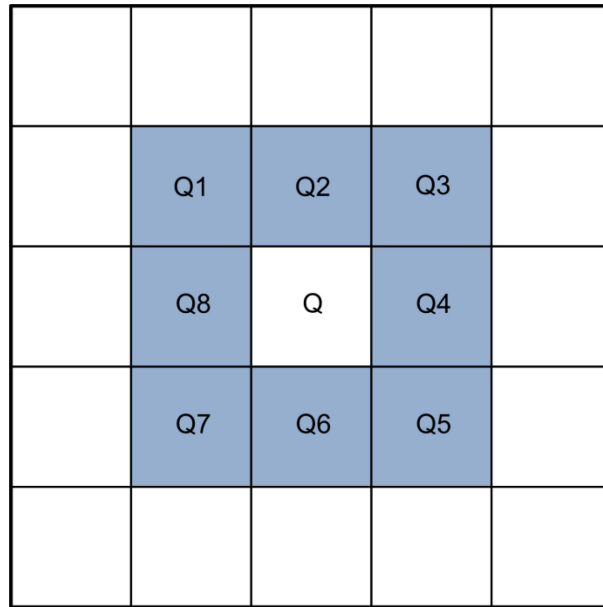


Figure 3-7 : Definition of the Moore neighbor pixels

Having a group of black pixels on white background such as shown in Figure 3-8, the task is to detect the pixels forming a particle. Picking a random Moore neighbor white pixel (shown as with a triangle in Figure 3-8) of a black pixel (shown with a dot in Figure 3-8) as the starting point, the idea is to extract the white pixels in the Moore neighborhood of the main selected particles. This is performed by moving around the Moore neighbor pixels of the main black pixel in a clockwise direction. Every time that a black pixel is selected as the Moore neighbor pixel of pixel Q, we backtrack to the last selected white pixel and start going around the Moore neighbor pixels of new black pixel. The white Moore neighbor pixels are visited again until next black pixel is hit. The algorithm continues until the starting point is revisited for the second time. The black pixels which were hit are detected as the particle in the image.

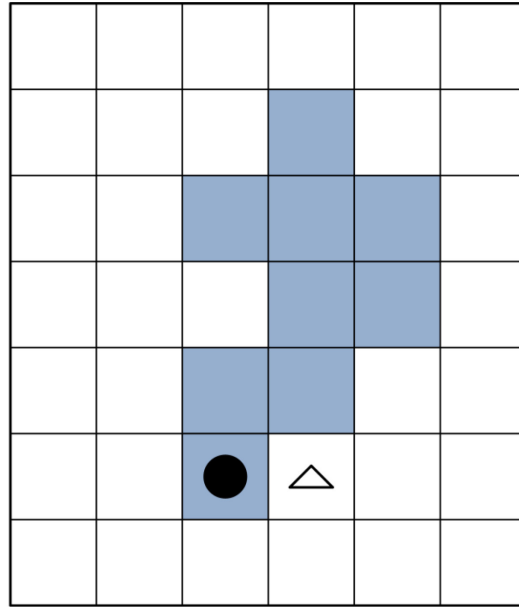


Figure 3-8 : Description of Moore neighborhood algorithm for detection of particles in an image

The particles positions are determined in the next step. One simple method is to use the geometric centre of detected pixels as the center of the particle (Hassan & Canaan, 1991; Moroni et al., 2003; Racca & Dewey, 1988). An alternative method is the polynomial fitting or Gaussian methods (Nobach & Honkanen, 2005; Rogers, Waigh, Zhao, & Lu, 2007; Spinewine, Capart, Larcher, & Zech, 2003). An intensity-weighted centroid method (Feng, Goree, & Liu, 2007; Guezennec et al., 1994; Maas et al., 1993; Stüer, Maas, Virant, & Becker, 1999) are also used to approximate the particle centroid. The intensity-weighted centroid method which is used in this work determines the centroid of a particle as

$$x_c = \frac{\sum_{i=0}^N I(x_i, y_i) \cdot x_i}{\sum_{i=0}^N I(x_i, y_i)} \quad (3-1)$$

where  $x_i$  and  $y_i$  are the location of that each pixel, and  $I$  is the intensity attributed to that each pixel. In (Ivanov & Melzer, 2007; Ouellette, Xu, & Bodenschatz, 2006), the accuracy of locating an individual particle in with different methods are determined.

In (Ivanov & Melzer, 2007), artificial simulated images of particles are generated to determine the errors of intensity-weighted centroid method. A digital image containing 1000 particles considered to have a Gaussian intensity distribution is simulated. The particles are evenly distributed over an image of 820 x 520 pixels. The level of noise on the particle images is varied between 0 to 10 % and root mean square (RMS) of found location of particles using the intensity-weighted centroid method and the simulated ones are calculated. The maximum RMS of the error of locating a particle is found to be 0.2 pixel.

To examine the image processing effects in the particle detection section, the number of detected particles in each image for the whole densification process is investigated and the results is shown in Figure 3-9. The number of detectable particles in the raw images without any preprocessing (labeled as unprocessed) is compared with the number of particles in the preprocessed images (labeled as processed) to examine the effectiveness of the image preprocessing. Comparing the two processed and unprocessed curves indicate the image preprocessing significantly increases the number of detected particles. Increasing the number of particles available for defining particle velocity helps

both with better statistics and increased information of the time history of their motion. A reduction in the detected numbers for the first 0.4 s of particle densification is seen for both cases. This is due to overlapping of particles occurring as the particles densify at the PN. After the initial densification process for 0.4 s, the number of detected particles remains constant for both of the curves indicating that the pressure node particle locations are not changing.

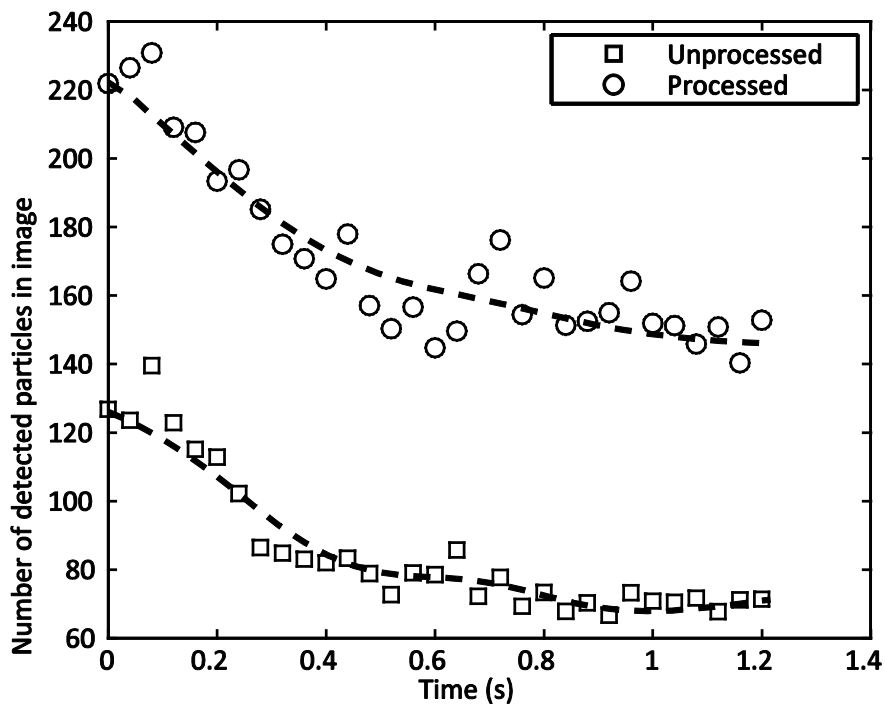


Figure 3-9 Effect of image preprocessing of images on number of detected particles during the densification process

### 3.2.3 Particle motion

There are different methods for tracking particles in fluid motion detected in an image set. The variational approach (Ruhnau, Guetter, Putze, & Schnörr, 2005) uses the concepts of PIV in particle tracking to enforce correct vectors.

Alternatively, two-frame neural networks (Ishikawa et al., 2000; Labonté, 1999) can be used where parameters are changed autonomously. The relaxation technique (Baek & Lee, 1996; Doh et al., 2000) is also a common method which assumes that adjacent particles move in the same direction. A two-frame relaxation algorithm uses two temporally consecutive particle data sets to determine the most probable particle trajectories. A schematic of a two-frame relaxation algorithm is shown in Figure 3-10. The detected particles in two-consecutive frames are defined in Figure 3-10 (a). The relaxation algorithm loops through all of the detected particles in frame 1 looking for corresponding particles in frame 2. The search algorithm is shown for a sample core particle shown in red in Figure 3-10 (a). Potential matches for the core particle in frame 2 are being searched using a search radius defined in the field-of-view for these potential matches for the core particle. This search radius is defined as the maximum displacement expected from a particle between two consecutive frames and is denoted as  $T_s$  in Figure 3-10 (b). For the example shown in Figure 3-10 (b) there are three potential particle matches in the searching circle shown as squares. The next step is to find the neighboring particles for the core particle in frame 1. This is related to the assumption of similar displacement of a group of neighbor particles. A search radius denoted as  $T_n$  in Figure 3-10 (b) is defined for the neighbor particles in frame 1.

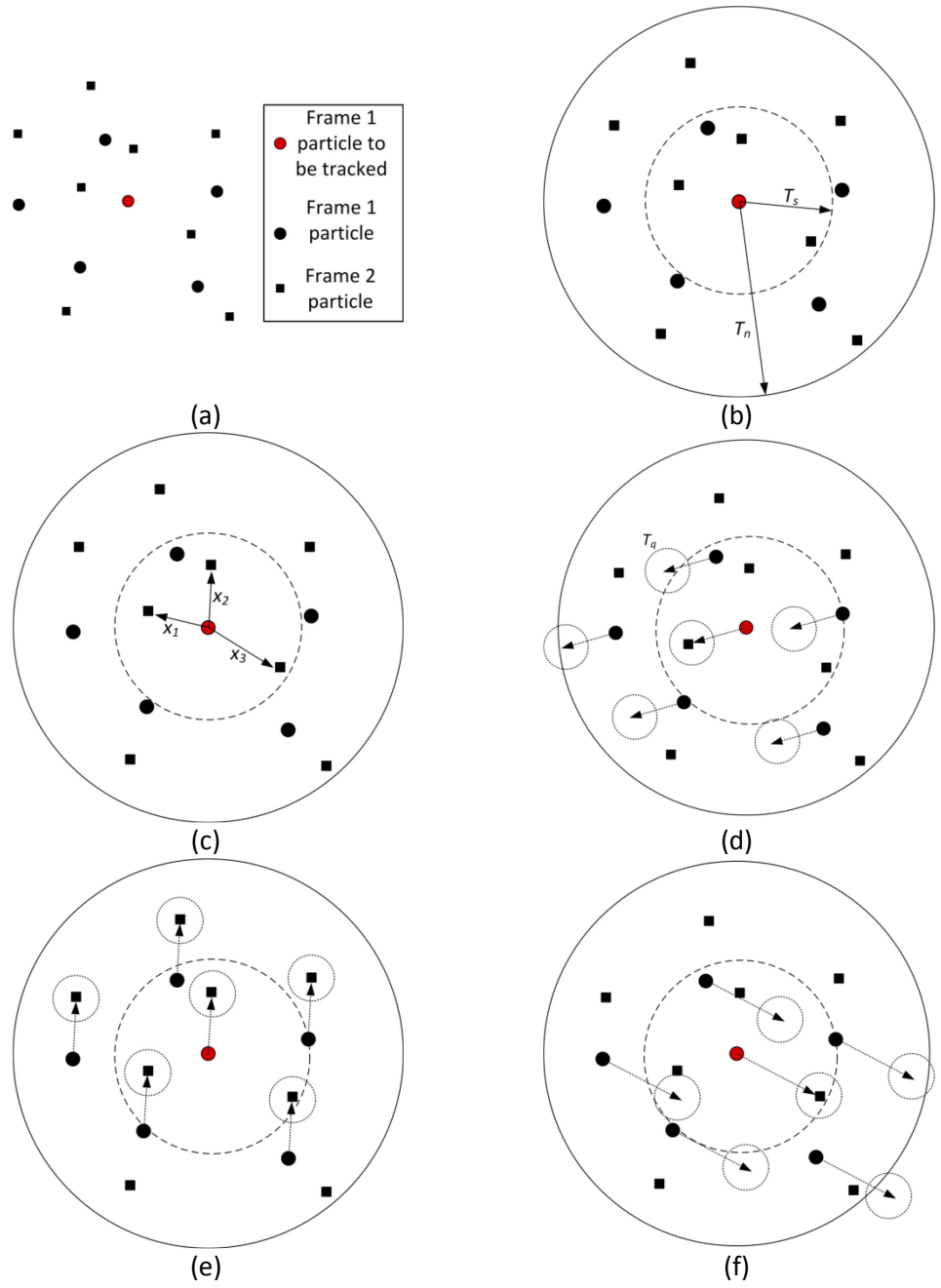


Figure 3-10: Relaxation algorithm in classical PTV algorithm, (a) definition of frame 1 and frame 2 particles, (b) Definition of search radius for potential frame 2 particles and neighbor particles (c) Finding the potential displacement for the core particle (d) Investigation of the potential displacement  $x_1$  (e) Investigation of the potential displacement  $x_2$  (f) Investigation of the potential displacement  $x_3$

The processing is continued by determining the potential displacement for the potential corresponding particles located in frame 2 for the core particle (Figure 3-10 (c)). The potential displacements associated to the three potential particles found in frame 2 are calculated which are  $x_1$ ,  $x_2$  and  $x_3$ . The task is to determine the most probable potential displacement. This is performed by assuming three cases for the potential displacement for the three found particles. The direction and magnitude of the each potential displacement being investigated is extended from every neighbor particle, as seen in Figure 3-10 (d-f). A quasi-rigidity radius, denoted by the variable  $T_q$ , is extended about the end of every potential displacement. This quasi-rigidity region is for some non-rigidity in the particle motion. The most probable trajectory will contain the most frame two particles inside this quasi-rigidity region.

The case for the potential trajectory  $x_1$  is shown in Figure 3-10 (d), while the cases for  $x_2$  and  $x_3$  are shown in Figure 3-10 (e) and Figure 3-10 (f) respectively. The potential displacement  $x_2$  has the most radii filled with a frame 2 particles as shown in Figure 3-10 (e). This means that the  $x_2$  is the most probable displacement for this core particle as higher number of frame 2 particles is found in the quasi-rigidity region.

The algorithm is continued by selecting a new core particle from the list of frame 1 particles and repeats until every frame 1 particle will be a core particle with most probable displacement. In the case of not finding any potential match

or neighbor particle for a core particle, the core particle is discarded and the process is performed for other particles.

As described, the relaxation algorithm assumes that a group of particles move in a similar direction and uses this assumption to correspond particles in two consecutive frames. However, such particle tracking algorithms used for determine fluid motion are not applicable to a particle / bubble under the influence of acoustophoresis because neighboring objects may not move in the same direction. To highlight this, a schematic of the different potential motion of two neighbor objects is shown in Figure 3-11. For particle 1 and particle 2 in the figure, these two neighbor particles are moving in the same direction toward their closet pressure node. However, particle 1 is moving faster than particle 2. This can be due to different initial locations or different size of the two particles being investigated. The other case shown is having a bubble and a particle adjacent to each other. The bubble and particle move in the opposite direction due to their different ACFs and thus the relaxation algorithm is not able to find a dominant motion in this case. Therefore, the relaxation algorithm, a typical particle tracking approach used in fluid mechanics is not applicable to this study.

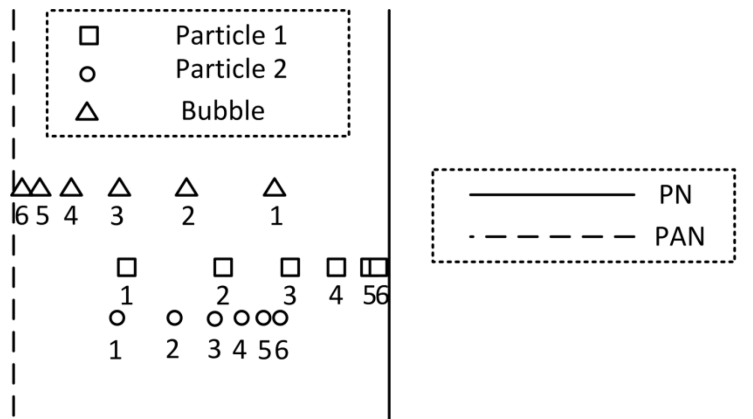


Figure 3-11 : A schematic of different neighbor objects velocity in acoustophoresis separation process

Imaging the densification process at 1,000 fps, the nearest neighbor search method (Hassan & Canaan, 1991) is used to track the particles over as much of the densification time period (1 s) as possible. In this method, a first frame particle is matched with its closest neighbor in the second time frame. An example of typical particle trajectories is shown in Figure 3-12. The location of PNs and PANs are indicated in the figure using the post-experiment, densified image of separated particles to determine their location. The trajectory of particles and bubbles existing in the cell as traveling to the PNs and PANs respectively are also illustrated in the Figure 3-12. In order to be able to compare the experimental captured motion of particles to the theoretical values, the particles with short time history are filtered out in the filtering section of the algorithm. An example of such a filtered particle is highlighted by a solid line rectangle labeled 'A'. Also, by the introduction of high and low acoustic pressure locations in the field-of-view, there are some bubbles generated which are also

removed in the filtration process. The criterion is that the object target is found to be travelling to known PANs rather than the expected PNs. An existing bubble trajectory in the figure is shown by a dashed line rectangle labeled 'B'.

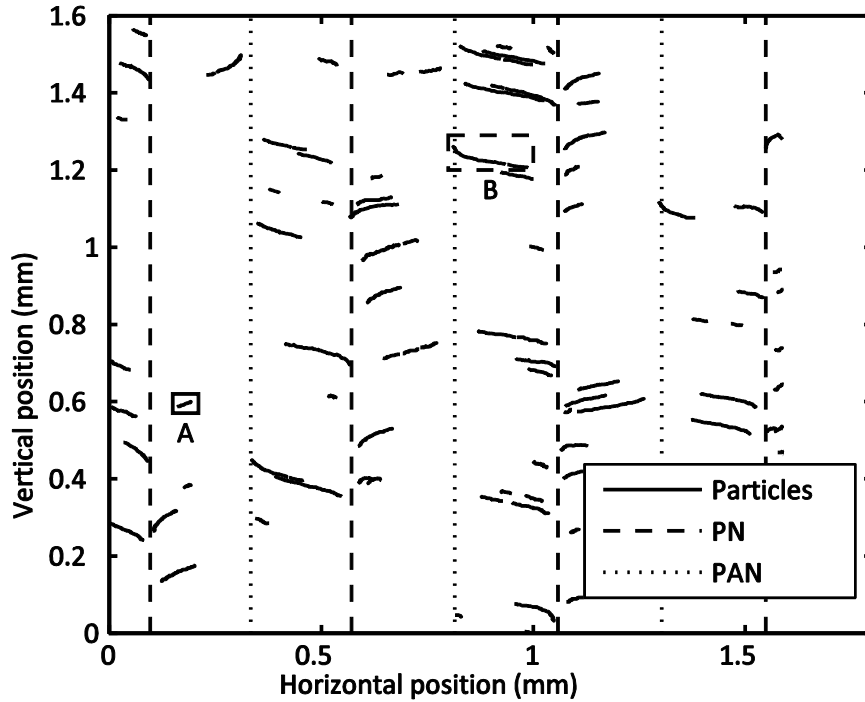


Figure 3-12 Particle/bubble trajectories in the field-of-view in a sample pressure acoustic force experiment; short time history particles (a sample highlighted by a solid line rectangle) and bubbles (a sample highlighted by a dashed-line rectangle) are filtered out

From the time location history of individual particles their horizontal velocity can be determined using:

$$v\left(t + \frac{\Delta t}{2}\right) = \frac{x(t + \Delta t) - x(t)}{\Delta t} \quad (3-2)$$

where  $v$  and  $x$  are velocity and position respectively and  $\Delta t$  is the time shift for the two correlated images used for obtaining velocity. The time shift is defined in Figure 3-13. As the particle is moving from right to left, images are captured and

shown on top of each other in Figure 3-13. The particles overlap due to the high imaging rate (1,000 fps) and correlating two consecutive images has a relatively high uncertainty in finding the small displacement of the particle. This is because the uncertainty in location of a particle in the image is relatively consistent, a longer  $\Delta t$  reduces the uncertainty of the velocity but also reduces the number of velocity data points. This trade-off can be investigated by varying the time/image shift to minimize the uncertainties while minimizing the loss of data due to skipping images. The optimized image time shift can be used for calculating the velocity for each particle.

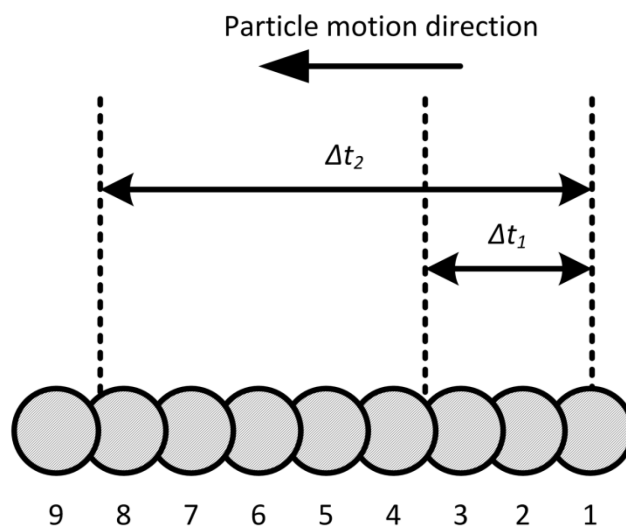


Figure 3-13: A schematic of the time/image shift between consecutive images showing particle motion.

Due to the existence of several PNs in the field-of-view, different particle locations can be mapped to a single acoustic wavelength. A schematic of this process is shown in Figure 3-14 where the particles in three different wavelengths are mapped into a single wavelength. Once the velocity fields for

different particles are determined, the statistically average particle velocity history is determined by averaging over the individually mapped particle's velocity to a single acoustic wavelength. The standard deviation is then calculated obtain the range of values of computed velocity at the single wavelength. This processed result is then compared with theory.

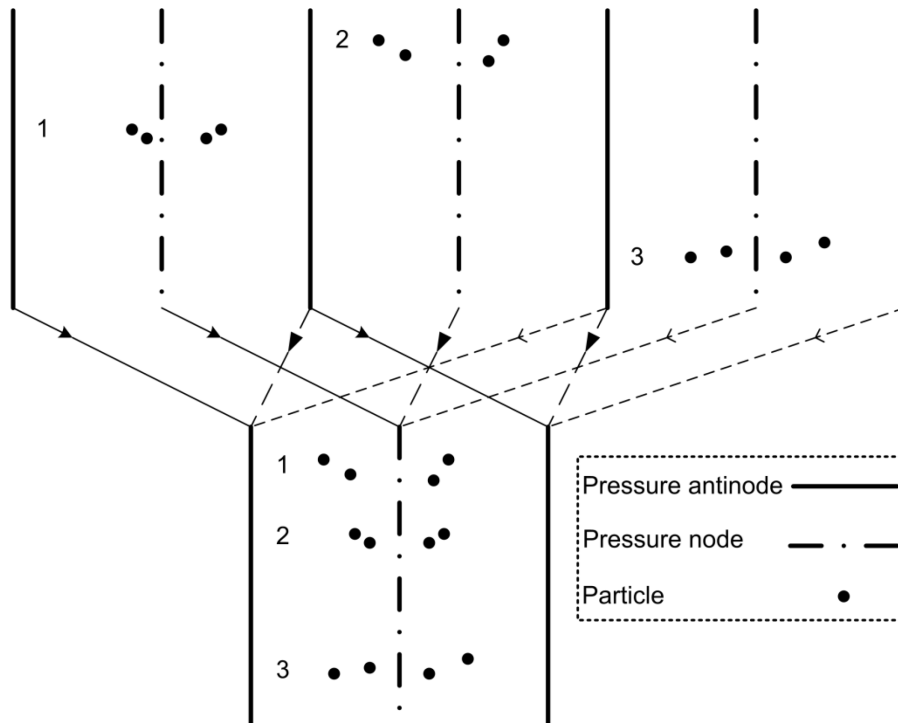


Figure 3-14: A schematic of mapping of location of particles to a single wavelength

### 3.2.4 Uncertainty analysis

The primary acoustic force and PTV uncertainties are the main sources of analysis uncertainties. For the primary acoustic force, the homogeneity of particle properties plays an important role in determining the acoustic contrast factor. As detailed in equation (1-8), the particle density and speed of sound

which determine the acoustic contrast factor are obtained from supplier's datasheets. It is also assumed that the particles are spherical to match with primary acoustic force theory. The size distribution of particles which creates a variation in particle behavior is provided by the manufacturers. It is assumed also that there is no secondary acoustic force effect between particles. The secondary acoustic force (Doinikov, 2001) is due to the effect of pressure field scattering off the other particles influencing the main tracked particle. Since the volume concentration of samples is set to 0.05 % this is neglected.

For the PTV analysis of the experiment, the temporal and spatial measurement uncertainty of particles is examined to estimate the uncertainty of their velocity. The temporal uncertainty of triggering the camera is estimated to be less than 4 ns which is negligible with respect to the 1 ms time difference between captured images. The uncertainty of locating a particle in the images is less than 0.2 of a pixel based on maximum error of particles centroid finding method (Feng et al., 2007). This results in having particle displacement uncertainty of 0.4 of a pixel which is twice as the uncertainty in locating a particle. The horizontal measured velocity uncertainty is also reduced by optimizing the image shift between two correlated images in individual particle velocity calculation.

### **3.3 Summary**

A custom PTV approach has been developed to find solid particle motion in water under the influence of an acoustic standing pressure wave in a macro-scale multi-nodes acoustic chamber. This particle flow field has some unique features, most notable of which is that with time, the homogeneous distribution of particles does not remain constant and significant clustering of particles occurs.

## **CHAPTER 4: INVESTIGATION OF PRIMARY ACOUSTIC FORCE USING PTV**

### **4.1 Introduction**

The PTV technique developed in the previous chapter is used to determine the particle motion and their transverse (horizontal) velocity. Applicability of the primary acoustic force theory is examined in the macro-scale multi-wavelength acoustic resonator using the determined velocity. This examination is performed for particle set 1 (PS-1) which has low particle size distribution and then verified with PS-2 and PS-3. Properties of these particle sets are provided in Table 2-3.

### **4.2 PTV algorithm validation**

To validate the PTV algorithm, synthetic images of particles suspended in water are generated and their separation by acoustophoresis is simulated. The

developed PTV algorithm is applied to the synthetic images and particles motion is compared to the known simulated ones.

#### 4.2.1 Synthetic images of particles

The synthetic images of particle set 4 (PS-4) are generated for 4 different particle distribution size CV (0%, 10%, 20% and 30%). There are also randomly distributed bubbles in field-of-view which travel to PANs. Particles are individually generated using Gaussian intensity distribution defined as

$$I_p(x, y) = I_{\max} \exp\left(-\frac{(x - x_c)^2 + (y - y_c)^2}{a^2}\right) \quad (4-1)$$

where  $I_p(x, y)$  is the intensity of a pixel in the image with coordinates of  $x$  and  $y$ ,  $I_{\max}$  is the maximum intensity of the image,  $x_c$  and  $y_c$  are the particle coordinate and  $a$  is the particle radius. A sample image of particle is shown in Figure 4-1.

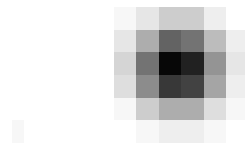


Figure 4-1: Sample of synthetic image of a particle with Gaussian intensity distribution

Individual particles are randomly distributed in an image and noise with uniform distribution is added to each pixel. The noise amplitude is certain fraction of the  $I_{\max}$  so that a bit map image which resembles the experimental

images of particles is generated. Samples of the synthetic images of the motion of particles and bubbles are shown in Figure 4-2. An inverted grey scale synthetic image of PS-4 travelling toward the closest pressure node is shown in Figure 4-2 (a). There are 1500 particles suspended in water in this field-of-view having the concentration of particle equivalent to  $10^{11}$  particles/m<sup>3</sup>. This concentration is less than  $10^{15}$  particles/m<sup>3</sup> to avoid particle-particle interactions (Mikkelsen & Bruus, 2005) and this suspension is considered to be dilute to have the primary acoustic force as the only effective force on particles. A magnified image of the group of particles shown in a rectangle in Figure 4-2 (a) is shown in Figure 4-2 (b).

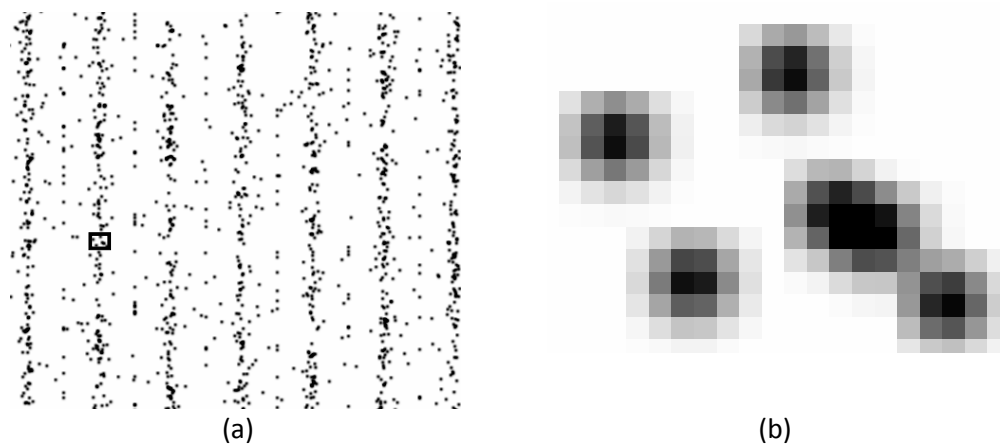


Figure 4-2: Sample of synthetic image of acoustophoresis separation of particles in field-of-view, (a) an inverted grey scale sample image of particles in densification process; the rectangle is showing a group of particles travelling toward an acoustic pressure node, (b) magnified image of the rectangle containing an example of overlapping particles in image (a)

#### 4.2.2 Acoustophoresis simulation of particles

The primary acoustic force as described in equation (1-6) is applied to a random distribution of particles in field-of-view and the synthetic particles are assumed to travel with velocity defined in equation (1-14). A sample of the generated time series of images of gradual motion of particles to the designated PNs is shown in Figure 4-3. The acoustic wave wavelength is set to 1 mm in equation (1-14). The particles are homogeneously distributed in field-of-view in the image associated with  $t = 0$  s. As the primary acoustic force is applied to the particles and bubbles, the particles and bubbles start their journey toward the closest PN and PAN respectively. After approximately 0.100 s from the start of the acoustic field, the PNs are distinguishable and the particle and bubble bands are formed completely at  $t = 0.200$  s. The formed bands are consistent afterwards and there is no other motion of particles or bubbles.

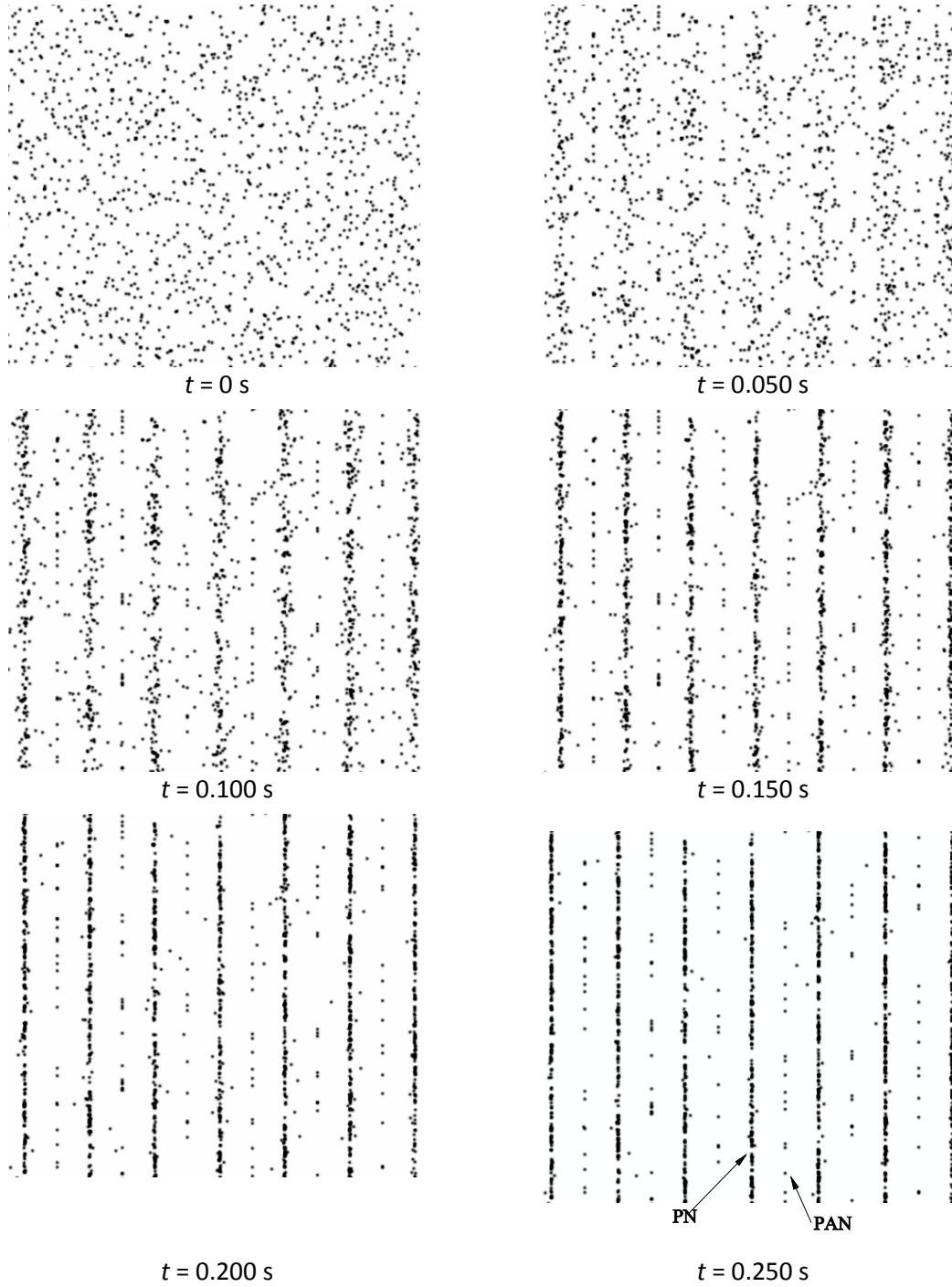


Figure 4-3: Synthetic images of the separation process with the associated time

### 4.2.3 Variation of particle density of fluid system in synthetic images

The particles density of a single wavelength in the synthetic images analysis is calculated by binning the images and summing the number of particles in each bin. The number of particles per unit volume ( $n$ ) is calculated for each bin for different experimenting time. The variation of number of particles per unit volume in a single wavelength divided into 100 bins is shown in Figure 4-4.

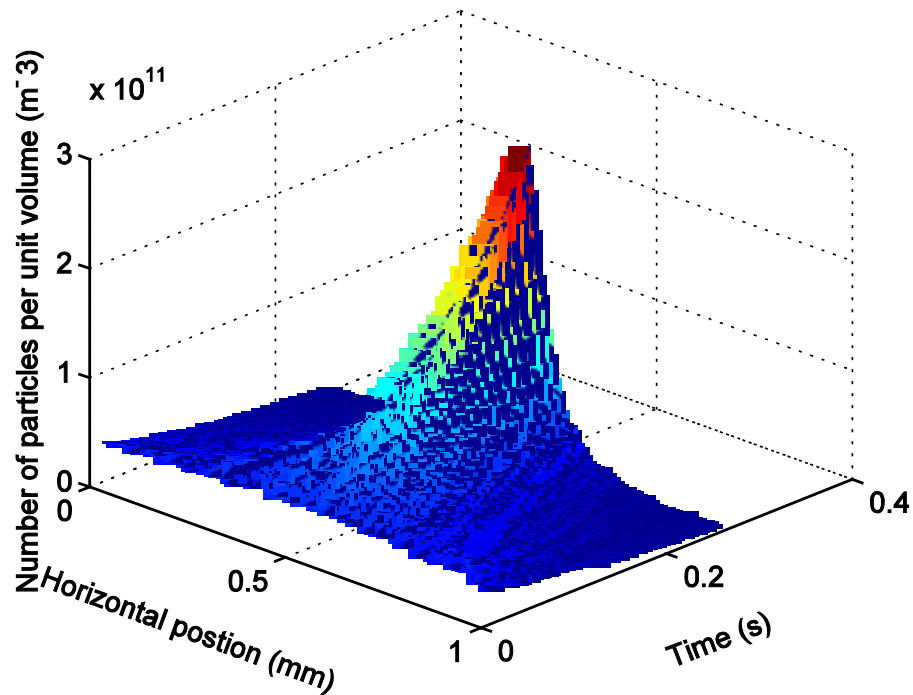


Figure 4-4 : Variation of number of particles per unit volume for a single wavelength of 1mm for synthetic images analysis

At  $t = 0$  s, the volume concentration of particles which are evenly distributed in a synthetic image is 0.05 %. The number of particles per unit volume corresponding to this concentration is approximately  $4 \times 10^{10} \text{ m}^{-3}$ . As the primary acoustic force is attracting the particles to the pressure node, the number of particles per unit volume for the pressure node bin is increasing. At  $t$

= 0.250 s the number of particles per unit volume at the pressure node is  $2.6 \times 10^{11} \text{ m}^{-3}$ . The average distance between the particles ( $D_{avg}$ ) having the number of particles per unit volume can be calculated as (Chandrasekhar, 1943)

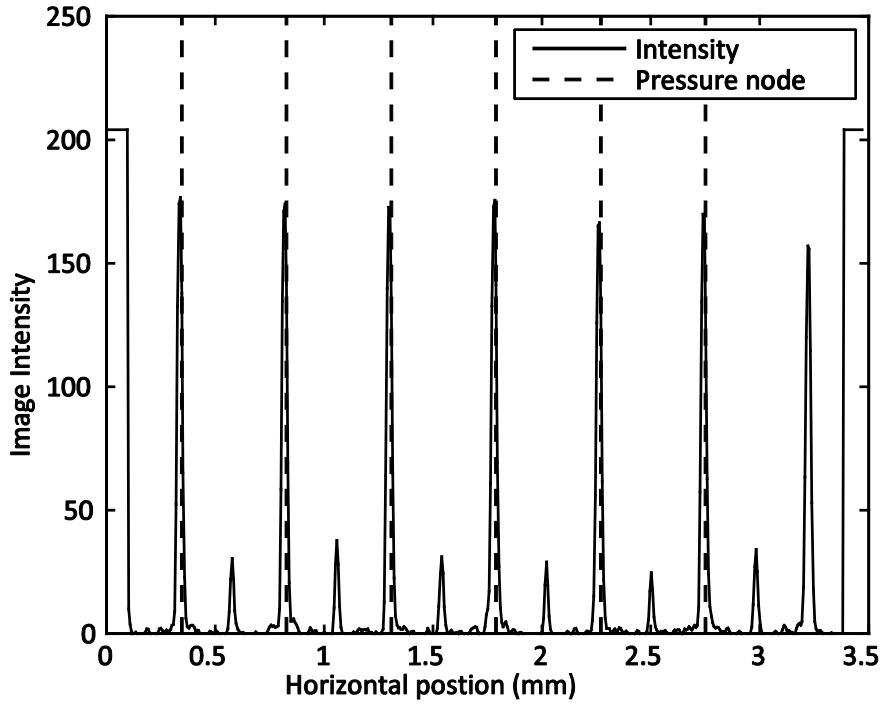
$$D_{avg} = 0.55396n^{-\frac{1}{3}} \quad (4-2)$$

Based on this relation, the minimum distance between the particles at a pressure node is 75  $\mu\text{m}$ . This value is larger than the 2 particle diameters and consequently the hydrodynamic particle-particle effects are negligible (Andersen et al., 2009). Also the order of magnitude of the secondary acoustic force when the two particles are 75  $\mu\text{m}$  apart is  $10^{-10}$  smaller than the primary acoustic force (Hancock, 2001). Therefore the assumption of having only the primary acoustic force is valid for the analysis.

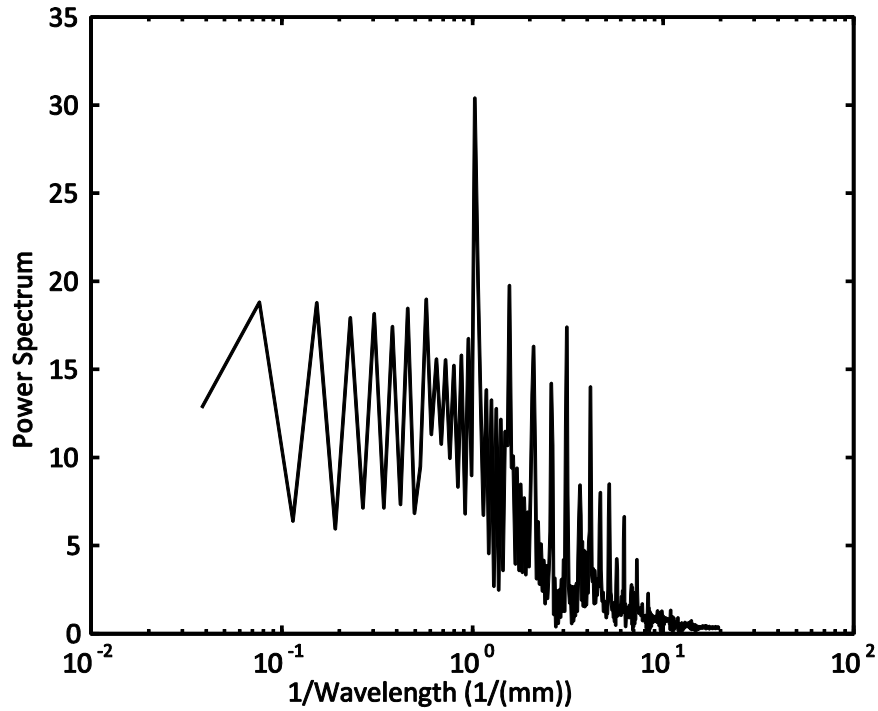
#### **4.2.4 Synthetic images analysis using the developed PTV algorithm**

Particles locations can be normalized to a single wavelength to average their velocity located in the field-of-view. In order to map the particle velocity to the normalized locations, the position of the pressure nodes where the particles density to is needed. Image processing can be used to assess the amount of particle concentration that occurs in different regions of the field-of-view. The graph of original image intensity summed in the vertical direction of the densified image (Figure 4-3,  $t = 0.250 \text{ s}$ ) is shown in Figure 4-5 (a). The determined positions of pressure nodes based on particle locations are shown in

the figure by dashed lines. A fast Fourier transform (FFT) can be applied to figure to determine the wavelength of the field and the resultant spectral plot is shown in Figure 4-5 (b). The wavelength of the wave is achieved to be 1 mm which is in good agreement with imposed wavelength in equation (1-14).



(a)



(b)

Figure 4-5: (a) Summed intensity of (Figure 4-3,  $t = 0.250$  s) in the  $x$  direction, locations of pressure nodes are found via these intensity plots, (b) FFT of the image intensity plot in Figure 4-5(a)

The normalized average transverse velocity for the studied particles in the synthetic images mapped onto a single wavelength is plotted in Figure 4-6. The particle distribution size CV is set to 0% in Figure 4-6 (a). The PANs, where the particles are repelled from, are located at each end of the wavelength. The location of the PN, where the particles are densified, is located at the center. The normalized velocity obtained by application of the PTV algorithm to synthetic images (denoted by PTV-Synthetic) includes bars to show the range of measured velocity. Bars show the range of measured velocity and indicate two standard deviations of the attributed averaged normalized velocity. The normalized theoretical particle velocity applied to the synthetic images as in equation (1-14) is shown in the same figure. There is a good agreement observed between the pattern of the PTV-Synthetic velocity profile and the theoretical velocity profile. The variation bars of the PTV-Synthetic velocity are low as expected due to the mono-disperse size distribution of particles. The discrepancy between the PTV-Synthetic velocity and theoretical velocity profiles is quantified by calculating the normalized average error ( $\hat{e}$ ) of the two profiles as in equation (4-3)

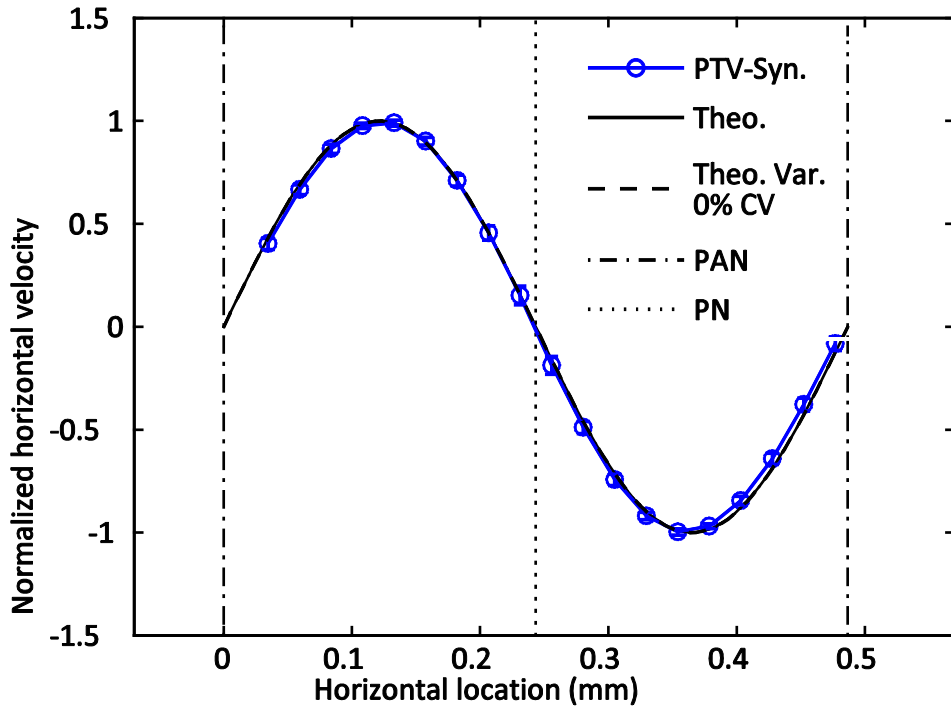
$$\hat{e} = \frac{1}{N} \sum_{x_l=0}^{x_l=\lambda} \frac{|v_{syn}^l - v_{theo}^l|}{v_{theo}^l} \quad (4-3)$$

where  $x_l$  is the  $l$ th transverse position in a single acoustic wavelength,  $\lambda$  is the acoustic wavelength and  $v_{syn}^l$  and  $v_{theo}^l$  are the PTV-Synthetic and theoretical velocity corresponding to location  $x_l$  respectively and  $N$  is the number of

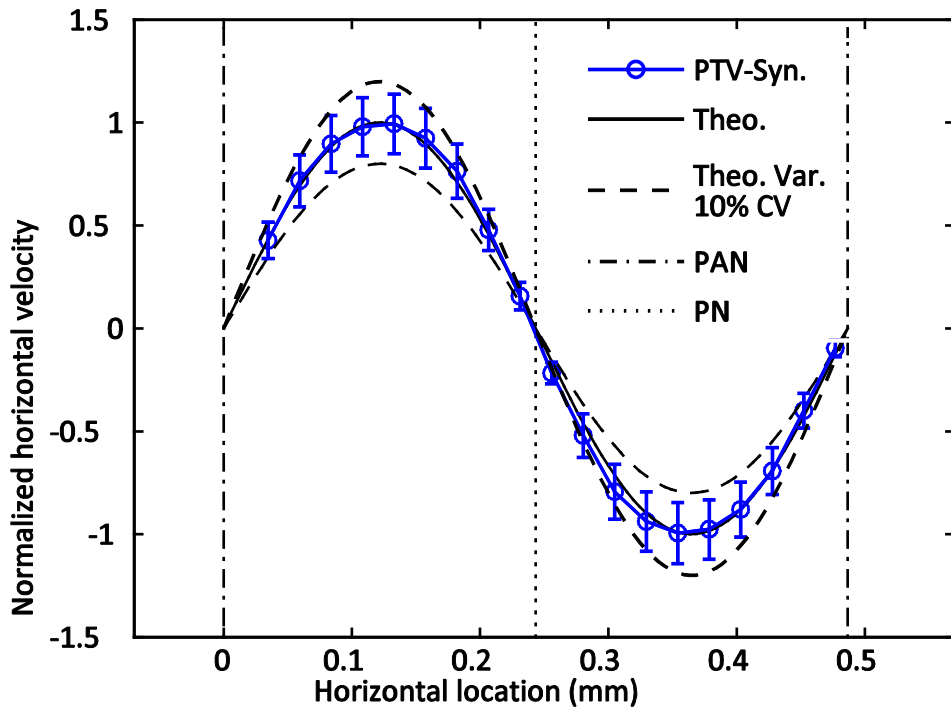
considered horizontal locations in the single wavelength. The normalized average error for this case where particle distribution size CV is 0 % is 0.03 %. This determines the uncertainty of the developed PTV method for calculation of velocity of profile.

The particle distribution size CV is set to 10% in Figure 4-6 (b). The normalized velocity the PTV-Synthetic algorithm includes bars to show the range of measured velocity. This spread in velocity is due to the distribution of particle size present in the synthetic images. There are also two other graphs plotted indicating the expected range of theoretical values given the uncertainties of parameters used in the calculation. These two graphs are the limits of theoretical variation due to an imposed particle size distribution to show the deviation of the transverse theoretical velocity. Based on the provided particles size distribution CV (10%), the particles horizontal velocity standard deviation can be determined based on the propagation of uncertainties analysis (Taylor, 1982) as 20%. The pattern of the PTV-Synthetic normalized transverse velocity field in Figure 4-6 (b) is in good agreement with the applied velocity profile due to primary acoustic force theory for single particles as in equation (1-14). The measured velocity range of the PTV-Synthetic velocity profiles generally falls within the theoretical velocity range obtained based on the size distribution of particles.

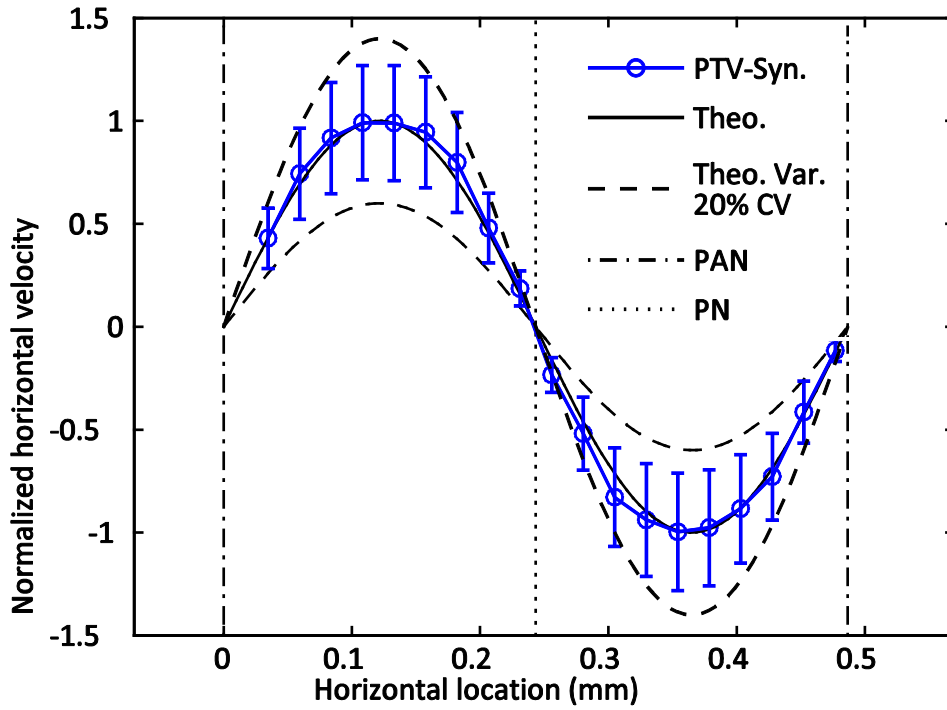
The normalized transverse velocity associated with synthetic images of particles suspensions with particle distribution size CV of 20% and 30 % are shown in Figure 4-6 (c) and (d) respectively. The variation bars of the PTV-Synthetic analysis are larger than the graph associated with particle distribution size CV of 10 % shown in Figure 4-6 (b). The limiting solid lines showing the expected theoretical variation range of normalized transverse velocity are plotted in both Figure 4-6 (c) and Figure 4-6 (d). Based on the provided particles size distribution CV of 20% and 30%, the particles horizontal velocity standard deviation is calculated to be 40% and 60 % shown in Figure 4-6 (c) and Figure 4-6 (d) respectively. The pattern of the PTV-Synthetic normalized transverse velocity field in both Figure 4-6 (c) and Figure 4-6 (d) are matching the imposed velocity profile as in equation (1-14). The analyzed PTV-Synthetic velocity range is generally within the expected theoretical velocity range calculated based on the generated size distribution of particles (CV) in synthetic images.



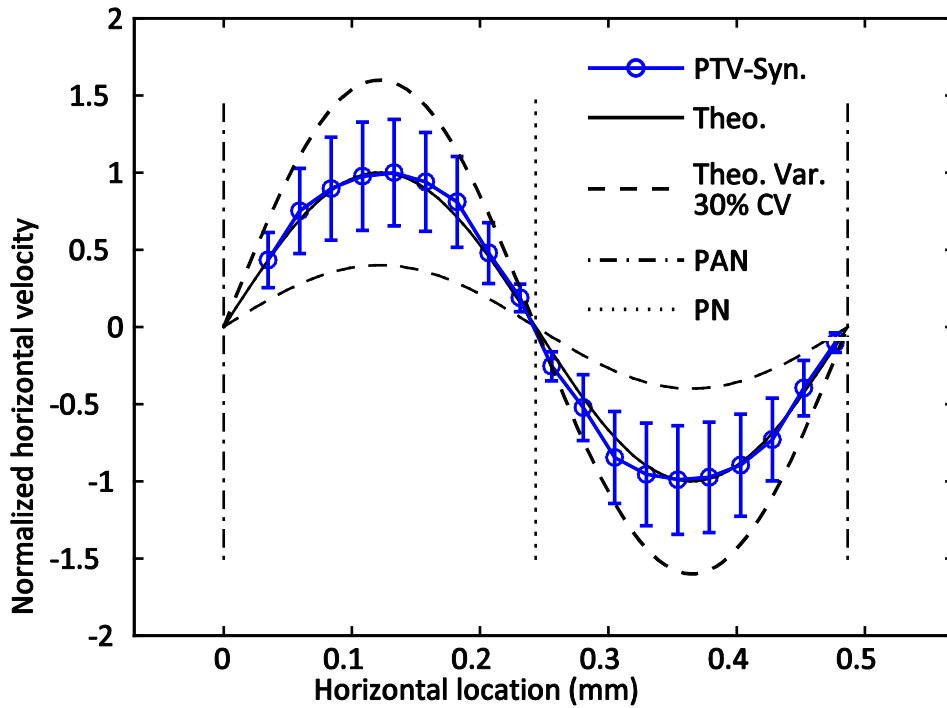
(a)



(b)



(c)



(d)

Figure 4-6: Transverse velocity of a single wavelength for application of PTV algorithm to the synthetic images; The particles distribution size CV is set to 0%, 10%, 20% and 30 % in figures a, b, c and d respectively

#### **4.2.5 Summary**

Synthetic images of suspended particles with particle size distribution (CV) of 0%, 10%, 20% and 30% are generated and their acoustophoresis separation in water is simulated. The developed PTV algorithm is applied to the synthetic images and particles motion is compared to the known simulated ones. The pattern of normalized velocity of particles in a single wavelength is matching the known simulated values. The analyzed PTV-Synthetic velocity range is generally within the expected theoretical velocity range calculated based on the generated size distribution of particles (CV) in synthetic images. This shows the capability of the developed PTV algorithm for investigation of the macro-scale multi-wavelength acoustophoresis separation of mono-disperse sized and poly-disperse sized particles in water.

### **4.3 Experimental transverse velocity of particles**

#### **4.3.1 Mono-dispersed particles**

To validate the single particle theory (Gorkov, 1962) low CV particles (PS-1) are first used where the particle motion is expected to have low variance. The PZT voltage is set to 21 V and concentration of particles is 0.05 %.

In Figure 4-7, a time series of images highlighting the motion of particles to the designated PNs are shown. The initially randomly distribution of particles are forced by the pressure acoustic force and are attracted to the closest pressure

nodes. After  $\sim 0.160$  s from PZT trigger, the pressure nodes are distinguishable. The separation continues until approximately 0.320 s where most of the particles are at the pressure nodes. The vertical particle bands are unchanging after 0.320 s and there is no general motion thereafter.

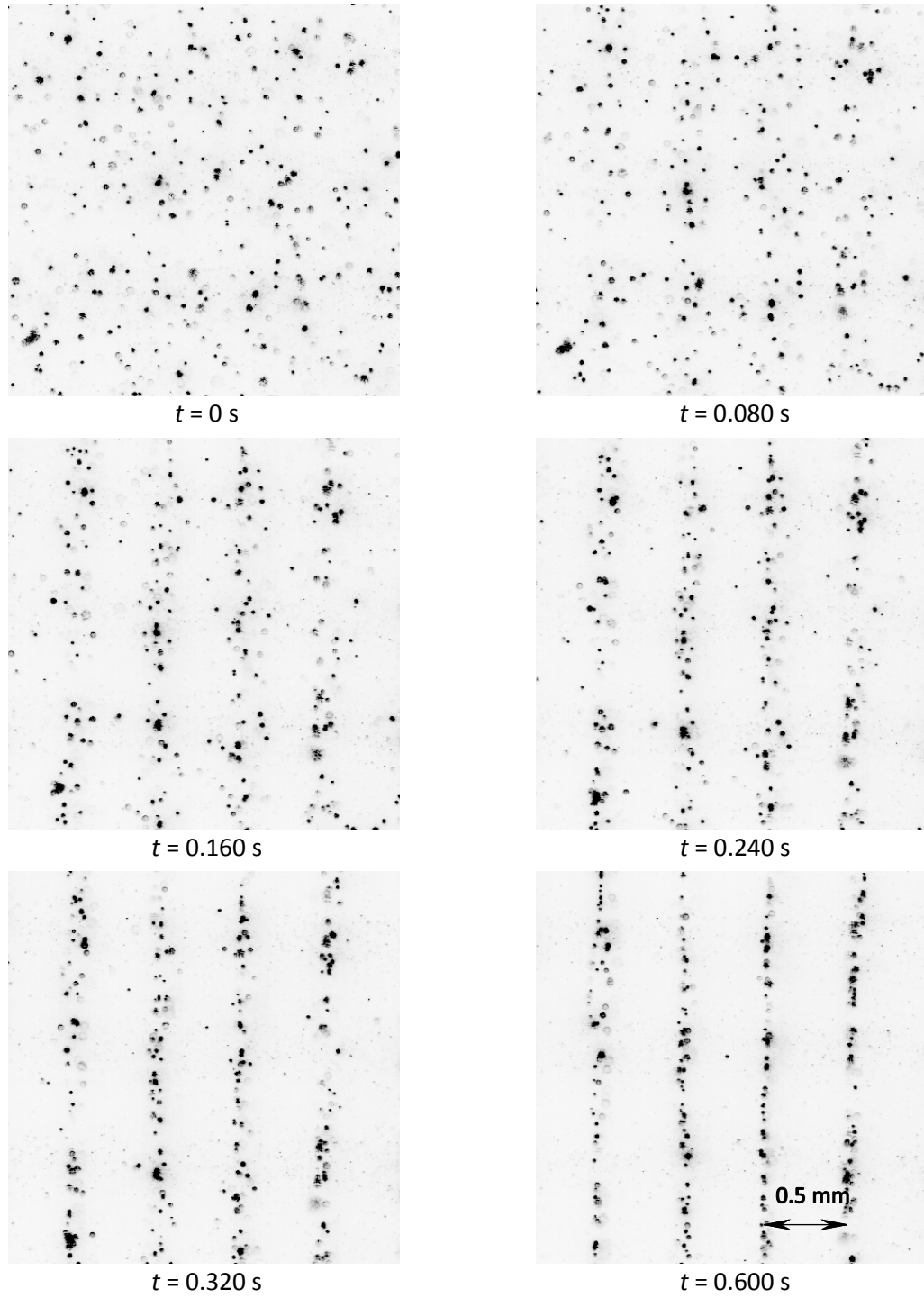
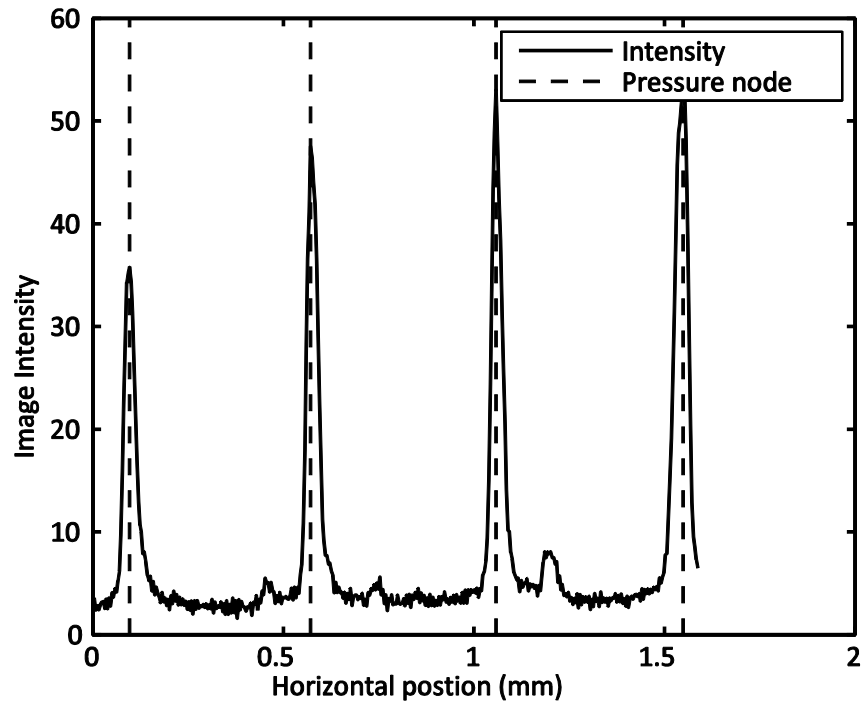
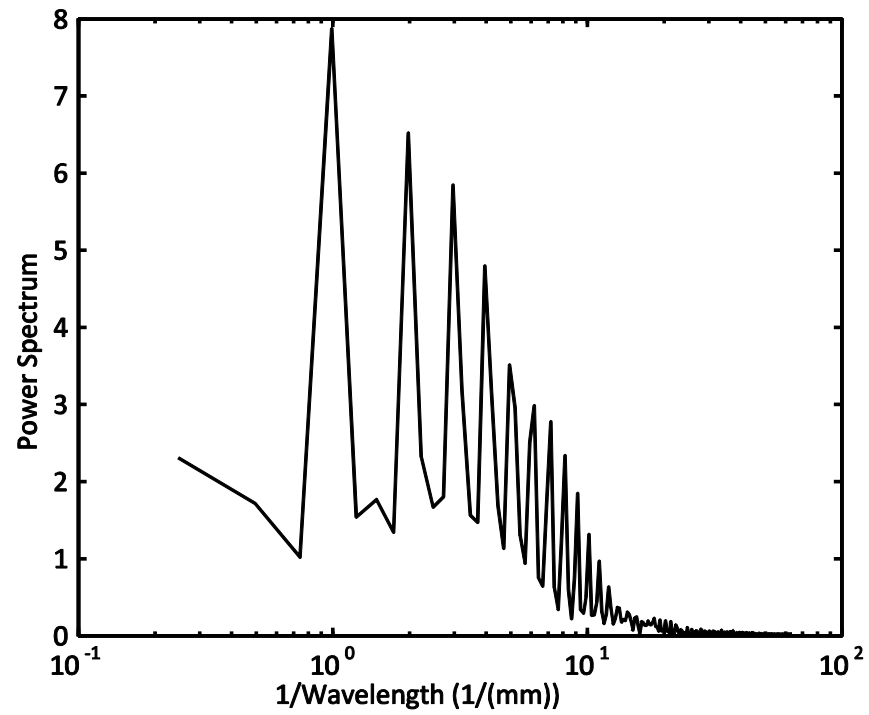


Figure 4-7: Raw data images (inverted color map) highlighting the separation process with the associated time of capture

Particles locations in the field-of-view can be normalized to a single wavelength interval to average their velocity. The position of the pressure nodes is determined to map the particle velocity to the normalized locations. In Figure 4-8 (a), the graph of original image intensity summed in the vertical direction of the densified image (Figure 4-7,  $t = 0.600$  s) is shown. The determined positions of pressure nodes based on particle locations are shown in the figure by dashed lines. The wavelength of the acoustic field is determined by application of a fast Fourier transform (FFT) to Figure 4-8 (a) and the resultant spectral plot is shown in Figure 4-8 (b). The wavelength of the wave is achieved based on this graph which is 0.98 mm which agrees with the analytical value of 0.975 mm obtained by assuming the speed of sound in water and wave frequency.



(a)



(b)

Figure 4-8: (a) Summed intensity of (Figure 4-7,  $t = 0.600$  s) in the  $x$  direction, locations of pressure nodes are found via these intensity plots, (b) FFT of the image intensity plot in Figure 4-8 (a)

In Figure 4-9, the normalized experimental measured average transverse velocity for the studied particles in a wavelength is plotted. Particles are repelled from the two pressure anti-nodes at the start and end of the curve. The particles densify at the pressure node. Bars show the range of measured velocity and indicate two standard deviations of the attributed averaged normalized velocity. This range is mostly attributed to the distribution of particle size present in the sample. The expected particle normalized velocity determined from the single particle theory (equation (1-14)) is also plotted. The range of the theoretical variation calculated based on assumed particle size distribution is also shown. A value of 20% is based on the provided CV value of particle size distribution standard deviation of 10%. The pattern of the measured transverse velocity field closely matches the primary acoustic force theory curve for a single particle (Gorkov, 1962). The range of the measured velocity profiles (experimental standard deviation) falls within the range obtained based on the theoretical standard deviation of the size of particles in Figure 4-9.

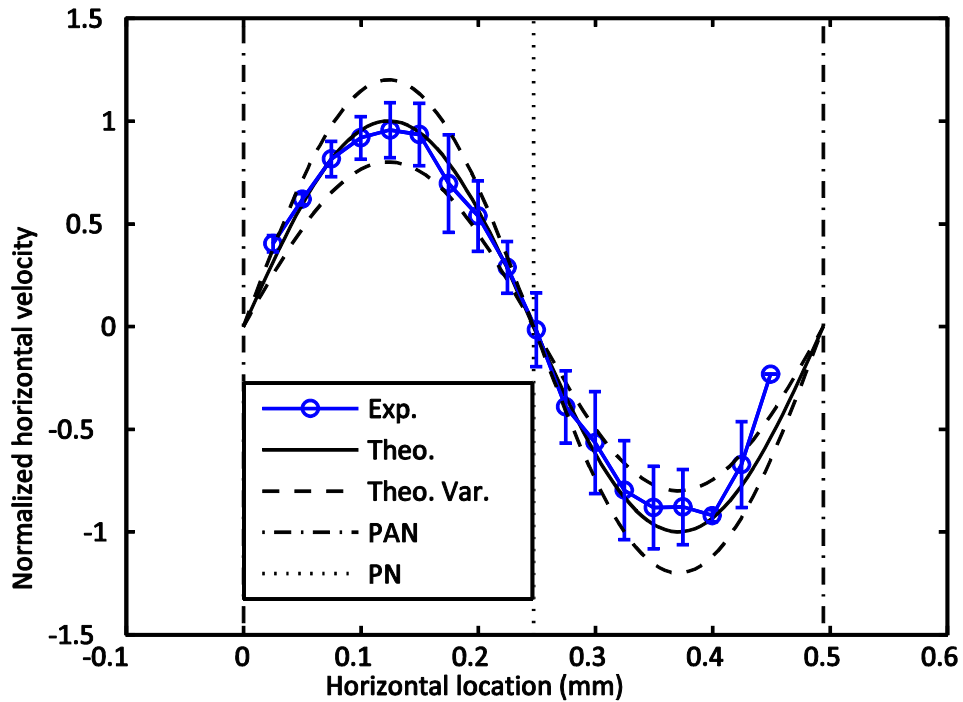


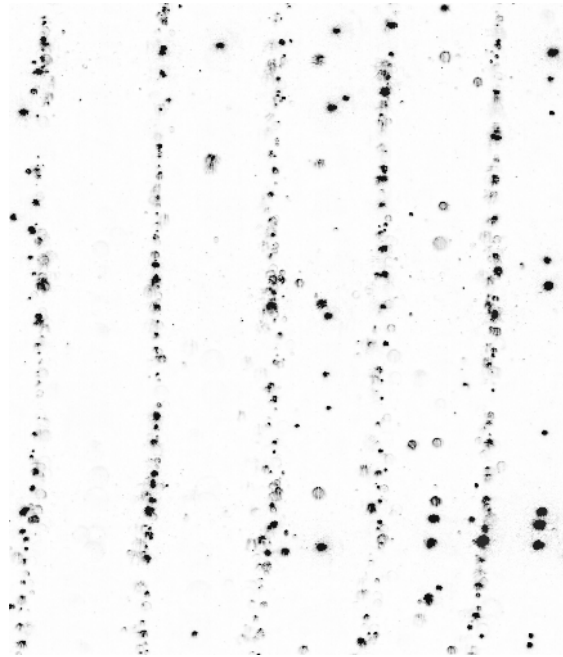
Figure 4-9 Transverse velocity of PS-1, experimental vs. single particle theory values; The variation bars of experimental values fall within the theoretical variation lines shown by solid lines

The observed discrepancies between the experimentally measured transverse velocity and the theoretical values are larger at the pressure nodes. At pressure node locations the tracking of particles is more complex due to the overlapping of the particles. Another issue is direction change of velocity of particles near the pressure node which increases the variation bars of experimental transverse velocity. Observations indicate that once particles arrive at the PN they can oscillate about the line of the pressure node.

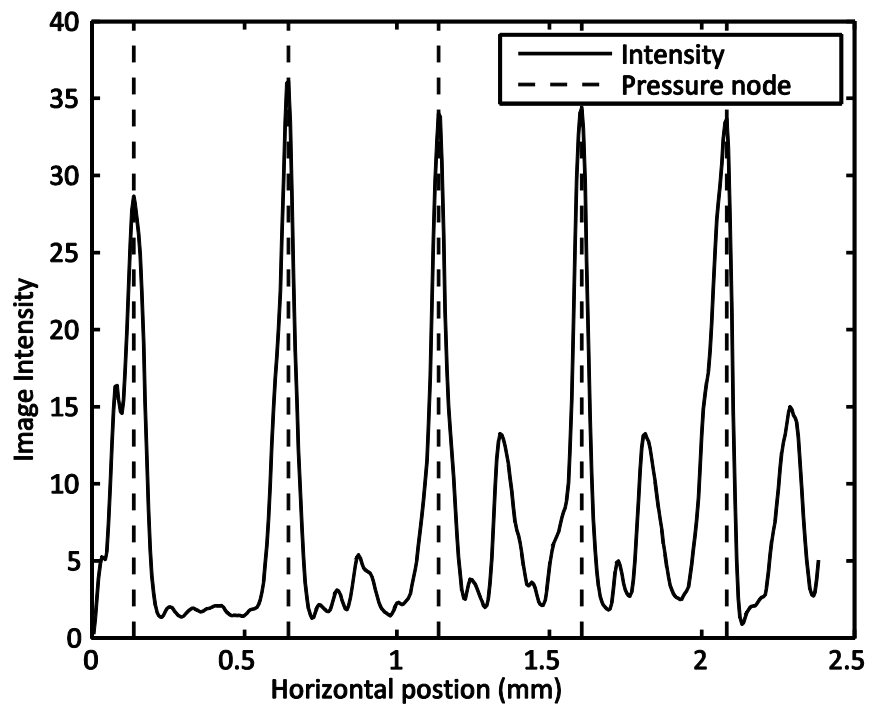
### 4.3.2 Poly-dispersed particle sizes

Having determined the limits and verified the experimental method with the primary acoustic force theory for the mono-dispersed sized particles, poly-dispersed particles sizes (hollow glass sphere particles, PS-2 and PS-3) are investigated. In this study, the aim is to determine the validity and applicability of theoretical primary acoustic force calculation. The properties of particles listed in Table 2-3 and PS-2 and PS-3 are attracted to the pressure nodes and their ACF is 0.14 and 0.35 respectively. The mono-dispersed particles case has an ACF of 0.49

The same experimental procedure and post processing algorithm is used to study the motion of the two new particles. Sample images of densified particles are shown in Figure 4-10 (a) and Figure 4-11 (a) for each particle groups. Again, particle densification lines are formed clearly at PN while there is some cavitation bubbles located at the pressure antinodes. The intensity plots resulting from the analyze are shown in Figure 4-10 (b) and Figure 4-11 (b). Using these plots, the locations of pressure nodes are obtained and the wavelength of the wave is found to be 0.98 mm for both data sets.

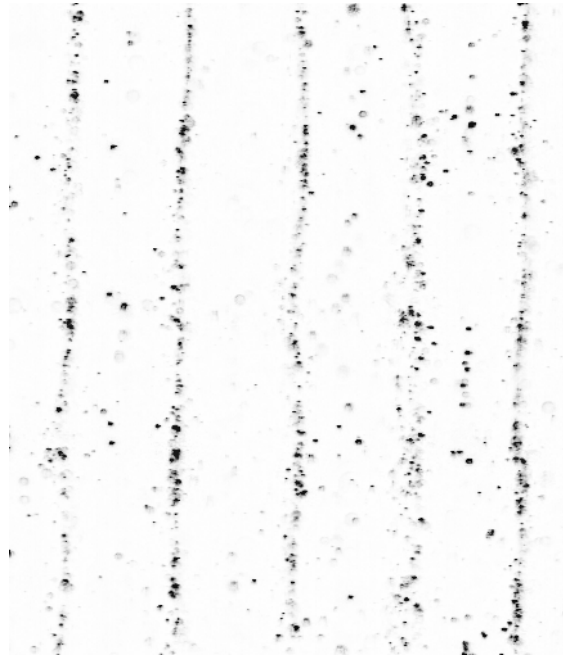


(a)

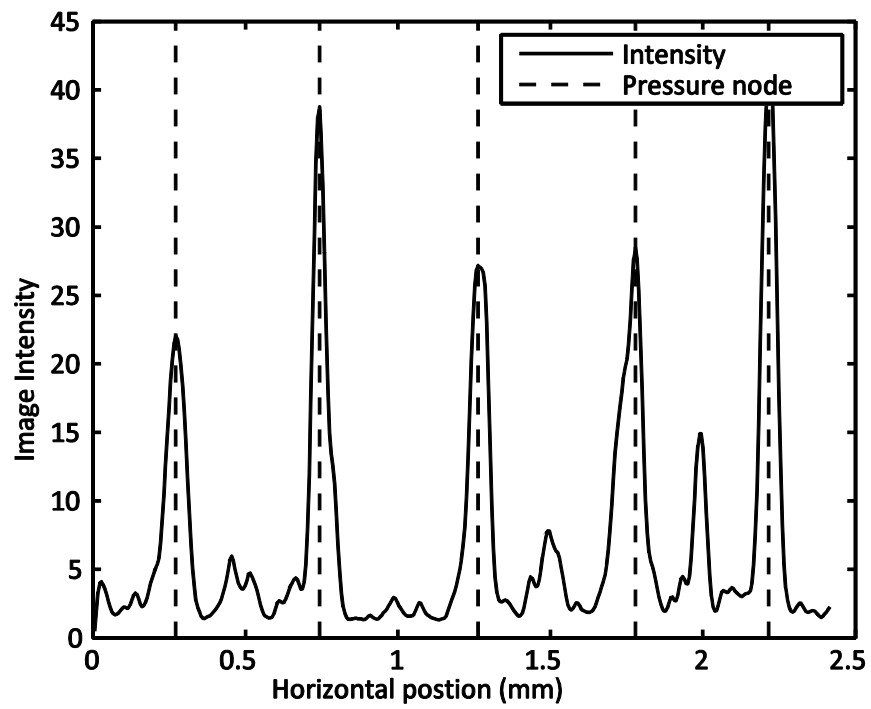


(b)

Figure 4-10: (a) PS-2 densified image, (b) in x direction, locations of PNs are found via these strong intensity plots for PS-2



(a)



(b)

Figure 4-11: (a)PS-3 densified image, (b) in x direction, locations of PNs are found via these strong intensity plots for PS-3

The normalized experimental measured average horizontal velocities for PS-2 and PS-3 for a single wavelength are plotted in Figure 4-12 and Figure 4-13. The bars located at the experimental points again show the range of obtained values due to the distribution of particle size present in the sample. The theoretical horizontal velocity expected by primary acoustic force theory for a single particle is also shown in both of the figures along with the limitations of theoretical variation. These are the deviation of the horizontal theoretical velocity due to an imposed particle CV of 35 % (PS-2) and 45 % (PS-3) and are determined to be 64 % and 88 % respectively. The experimental variation bars fall within the theoretical variation limits except for at the middle of the wavelength at the pressure node. This is attributed to the overlapping of particles and velocity changing direction at the pressure node making particle tracking difficult. The agreement between the experimental and theoretical results confirm that the primary acoustic force theory is applicable to poly-disperse particles in the macro-scale acoustic chambers for this particle loading. The discrepancies are mostly located near pressure nodes and antinodes. This is mostly due to overlapping of particles at the pressure nodes making them difficult to detect and also change of velocity direction at these points.

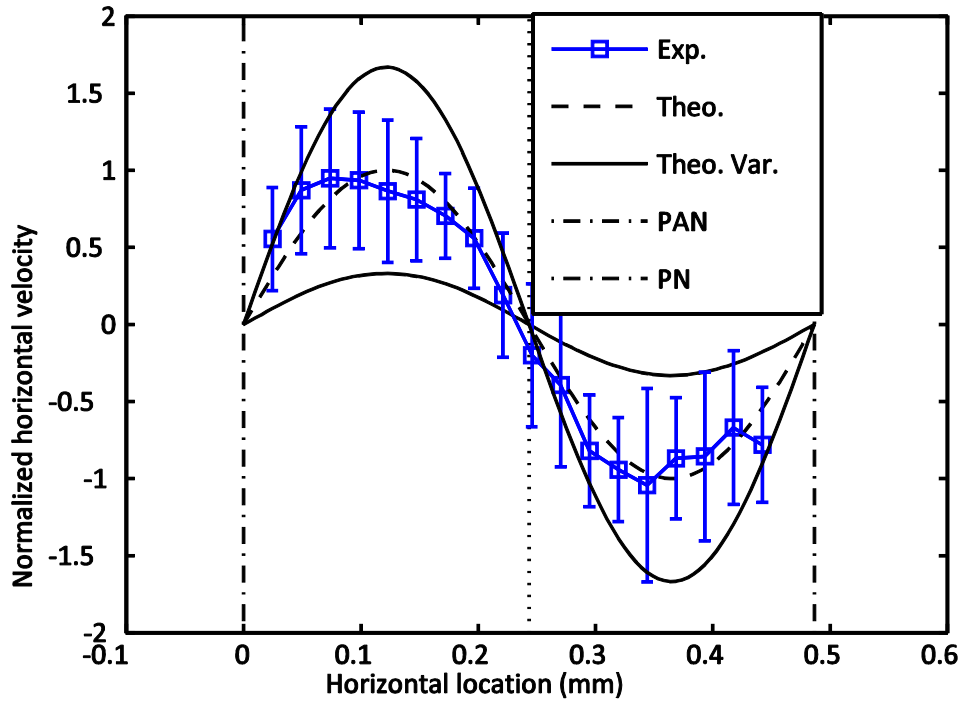


Figure 4-12: Transverse velocity of PS-2, experimental vs. single particle theory values

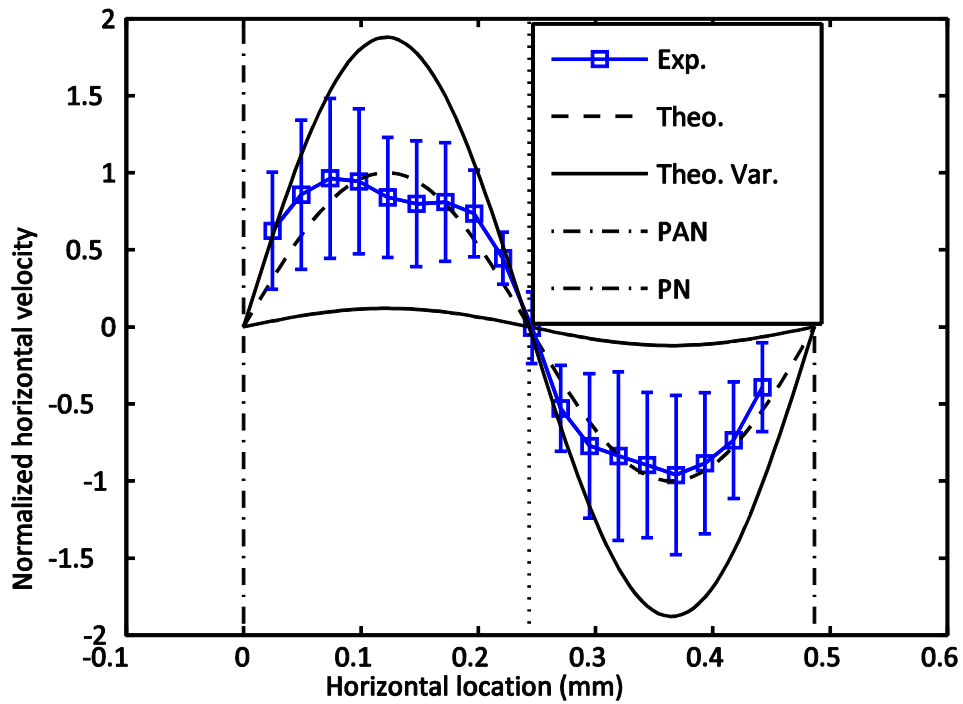


Figure 4-13: Transverse velocity of PS-3, experimental vs. single particle theory values

### 4.3.3 Independency analysis

In order to investigate the effect of the number of particles used in statistical averaging on the particles velocity profile over a single wavelength, normalized average error is introduced. The normalized average error ( $\hat{e}$ ) is defined to quantify the difference between the experimental and theoretical transverse velocity and is defined as:

$$\hat{e} = \sum_{x_l=0}^{x_l=\lambda} \frac{|v_{exp}^l - v_{theo}^l|}{v_{theo}^l} / N \quad (4-4)$$

where  $x_l$  is the  $l$ th transverse position in a single acoustic wavelength,  $\lambda$  is the acoustic wavelength and  $v_{exp}^l$  and  $v_{theo}^l$  are the measured experimental and theoretical velocity corresponding to location  $x_l$  respectively and  $N$  is the number of considered horizontal locations in the single wavelength. This error is determined by averaging the normalized difference between the theoretical and experimental values of transverse velocity in different locations in a single acoustic wavelength ( $\lambda$ ). When averaging over the wavelength, the initial point and final point where the pressure anti-nodes lie are not counted. This is due to the fact the theoretical value of velocity is zero which results in making the normalized relative error infinity.

The normalized average error is investigated by varying the time difference between images as shown in Figure 4-14. The particles individual transverse

velocity is determined separately and the corresponding difference is obtained for that specific image shift interval. The normalized average difference reduces as the image shift interval is increased until image shift number reaches ~10. According to the fitted line to the experiment data, there is an asymptotic trend seen in the normalized average difference and it is independent of the image shift number after value of 12 which correspond to time shift of 12 ms between images. Thus, the optimized image shift number is determined to be 12 based on this figure and the normalized transverse velocity is determined using this number.

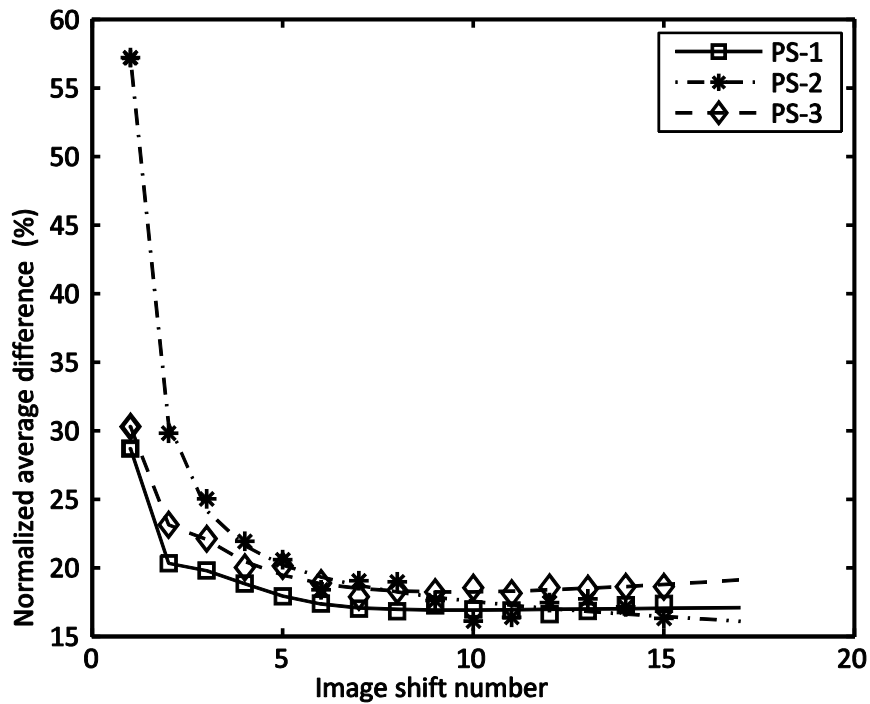


Figure 4-14: Normalized average difference independency with respect to image shift in achieving horizontal velocity

The normalized error is accomplished for different particle sets and varied for different number of particles accounted in statistical averaging (Figure 4-15).

The fitted line to the experiment data shows that there is an asymptotic trend seen in the error and the error is independent of the number of particles assessed after value of 800. As the number of accounted tracked particles increases, the effect of the number of them reduces. This graph validates the independency of results with respect to number of tracked particles in the analysis.

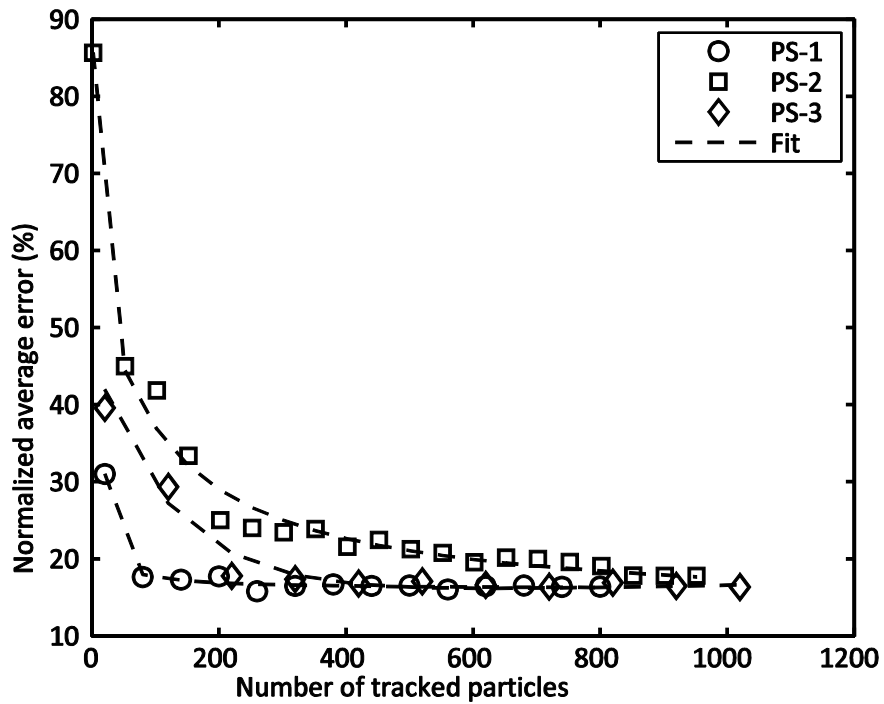


Figure 4-15: Effect of number of considered particles on the normalized error in achieving horizontal velocity for PS-1, PS-2 and PS-3

#### **4.4 Summary**

Applicability of current primary acoustic force theory (Gorkov, 1962) for predicting single particle motion in an acoustic is validated for macro-scale multi-wavelength acoustic chambers for poly-dispersed sized particles. This particle flow field has some unique features; most notable is that, the initial homogeneous distribution of particles has significant clustering of particles over time. A PTV algorithm is developed for the mono-dispersed size particles separation and the validated for two different poly-dispersed size particle distributions. The dependency of image time shift and number of tracked particles is presented for the three different cases. The results show that the primary acoustic force theory for a single particle is capable of predicting the motion of particles for both mono and poly-dispersed size particle distribution in macro-scale multi-wavelength acoustic chambers.

## **CHAPTER 5: MULTI-WAVELENGTH MACRO-SCALE ACOUSTIC RESONATOR CHARACTERIZATION USING PTV**

### **5.1 Introduction**

The primary acoustic force is described as a function of acoustic energy density which represents the coupling of the PZT and the acoustic chamber (Bruus, 2012b). An acoustic resonator is generally characterized using this fundamental parameter. Based on (Bruus, 2012b), the effect of PZT excitation voltage on acoustic energy density (Jurg Dual & Möller, 2012) and loss of acoustic energy (Settnes & Bruus, 2012) due to viscosity of bulk fluid can be calculated. However, there are other sources of loss of energy such as viscous friction and scattering of acoustic wave from the walls and resonator holder (Bruus, 2012a). Losses due to particles densification on coherence and penetration of acoustic field within macro-scale multi-wavelength acoustic resonators (Hawkes & Radel, 2013) should also be considered. This effect is

accounted for in the characterization of acoustic resonators through their acoustic energy density. However, acoustic energy density is hard to estimate (Bruus, 2012b) but can be determined from experiments.

Techniques on measuring acoustic energy density inside an acoustic resonator include trapping particles using external forces such as electrostatic force (Yasuda et al., 1996) and gravity (Hancock et al., 2003) and imaging techniques (Augustsson et al., 2011; Barnkob et al., 2010; Barnkob, Augustsson, et al., 2012; Spengler et al., 2001; Woodside et al., 1997). Imaging techniques have been widely used to study and characterize the primary acoustic force by different investigators. Individual particle motion is obtained by tracking single particles affected by the primary acoustic force inside a micro-channel by (Barnkob et al., 2010). Acoustic energy density is determined using the velocity derived for the individual particles. A microchannel is also characterized by (Augustsson et al., 2011) via measuring the velocity field using micro-PIV. In this work the acoustic energy density is determined as the PZT voltage is changed and the performance of the micro-scale acoustic resonator is derived. Acoustic energy density is also determined in (Barnkob, Augustsson, et al., 2012) using the particle motion in a micro-scale acoustic resonator using PIV. Only the initial phases of densification are used in determining the acoustic energy density in these cases to avoid the overlapping of the particles occurring while the particles densify at PNs.

In this work the developed PTV approach is used to characterize the multi-wavelength acoustic chamber through determining the acoustic force exerted on particles by tracking their motion. The effect of PZT excitation voltage and suspension fluid properties on the acoustic chamber properties is the main focus of this study. The suspension fluid properties are varied by changing the concentration of dissolved glycerol in water. The experimental setup is described and the velocity field results for different conditions are reported. The predicted influence of suspension fluid properties and PZT excitation voltage from theoretical models are also examined and compared to experimental results.

## **5.2 Theoretical background**

### **5.2.1 Acoustic resonator characterization**

Acoustic energy density affects the primary acoustic force as in (1-6), and is a measure of the coupling effect between the PZT and the acoustic chamber (Bruus, 2012a). This coupling is mainly a function of the PZT excitation voltage and resonance properties of the acoustic chamber. A linear relationship between the generated acoustic pressure amplitude ( $p_a$ ) and the PZT peak-to-peak voltage ( $U_{pp}$ ) is shown for ultrasonic resonances in silicon/glass microchannels using PZT in (Jurg Dual & Möller, 2012). Considering this proportionality and equation (1-7), the acoustic energy density is related to the PZT excitation voltage as

$$E_{ac} = \gamma U_{pp}^2 \quad (5-1)$$

where  $\gamma$  is the acoustic energy density coefficient. Based on this equation, the maximum velocity of a particle is linearly proportional to the energy density of the acoustic field. The acoustic energy density is a function of the PZT used to generate the acoustic field and the acoustic chamber properties, specifically the acoustic coupling between them. The acoustic coupling is typically constant for a particular acoustic cell and system setting, so it can be estimated by studying the particles motion in the acoustic field.

Total losses in acoustic energy density are usually expressed by the absorption coefficient  $\alpha$  (Hawkes & Radel, 2013) which is related to defined resonance quality factor (Q-factor)  $Q$  as

$$\alpha = \frac{\kappa}{2Q} \quad (5-2)$$

The Q-factor represents the efficiency of an acoustic chamber and is obtained by measuring the rate of stored acoustic energy relative to the dissipated acoustic energy in the system. An expression for  $Q$  is derived for a simplified acoustic chamber in which the loss of acoustic energy is only a function of viscous dissipation in the bulk fluid in (Bruus, 2011b). However, the losses are much higher in the macro-scale acoustic chambers with multiple-wavelengths. The losses in these systems are mostly due to scattering of acoustic wave from the walls and particles which reduces the primary acoustic force efficiency more significantly in macro-scale acoustic chambers.

### 5.2.2 Suspension fluid properties effect on characterization

To characterize the acoustic chamber, the effect of fluid properties on acoustic energy density is investigated. The fluid properties are changed by varying the concentration of glycerol in water. Changing the weight concentration of dissolved glycerol in water will affect the viscosity, density, acoustic contrast factor and the damping of the fluid to change. The viscosity for different water-glycerol solutions is calculated using the empirical equation presented by (Cheng, 2008).

The predicted variation of normalized particle velocity as a function of glycerol weight concentration is shown in Figure 5-1. The velocity of a single particle in different cases calculated using equation (1-14) is normalized by its velocity in pure water ( $v_{water}$ ). Based on Figure 5-1, the normalized particle velocity with its velocity in water is inversely proportional to the viscosity of fluid suspension.

The variation of the acoustic contrast factor as the glycerol-water solution concentration changes is also shown in Figure 5-1. The experimental data points (Glycerol weight concentration: 0 %, 10 %, 20 % and 30 %) are denoted in the figure by square symbols. The value of the acoustic contrast factor does not change significantly for the experimental cases with only a change of 4% for the maximum glycerol concentration used of 30 %. However, the theory predicts that the change in the particle velocity is considerable as the maximum velocity

variation is approximately 40 % for the 30 % glycerol concentration based on equation (1-14) compared to pure water. This velocity change is only attributed to the viscosity term in equation (1-14) while the change due to losses and damping (in  $E_{ac}$  of equation (1-14)) are neglected in the calculation.

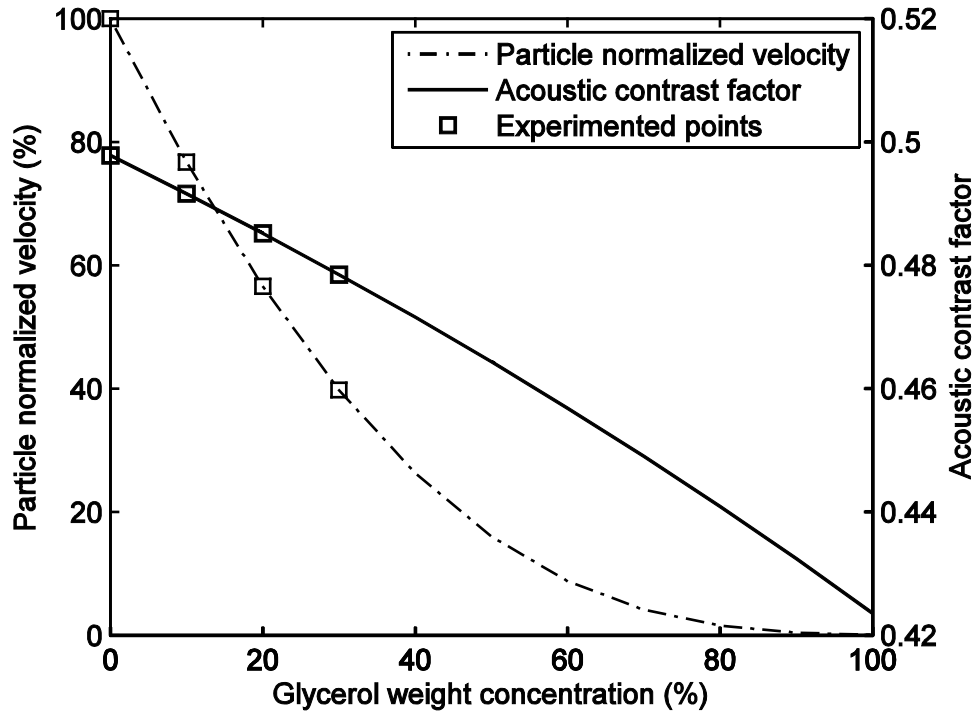


Figure 5-1: Calculated effect of glycerol concentration on acoustic contrast factor and individual particle velocity

### 5.3 Experimental particle motion

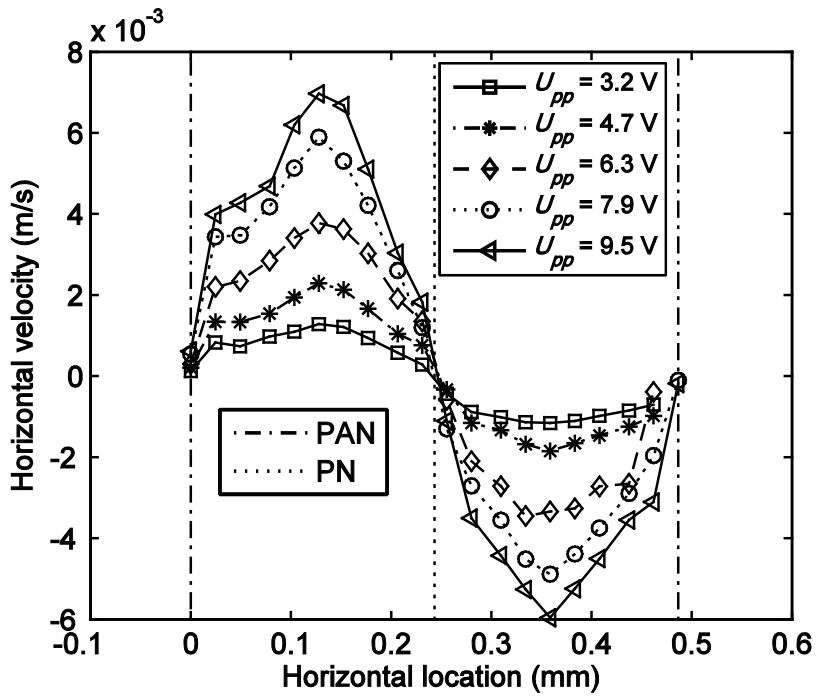
Having the normalized transverse velocity validated with the primary acoustic force theory, the acoustic resonator performance is investigated. It is fulfilled by obtaining the particle motion for particle set PS-4 and varying PZT excitation voltage to 5 different settings. The glycerol concentration of suspension fluid is also varied. PZT voltage was set to 5 different voltages that

are amplified by 50 dB and input to the PZT as shown in Table 5-1. These experimented points have been selected to enable the post processing algorithm to capture the nonlinear dependability of acoustic energy density on excitation voltage.

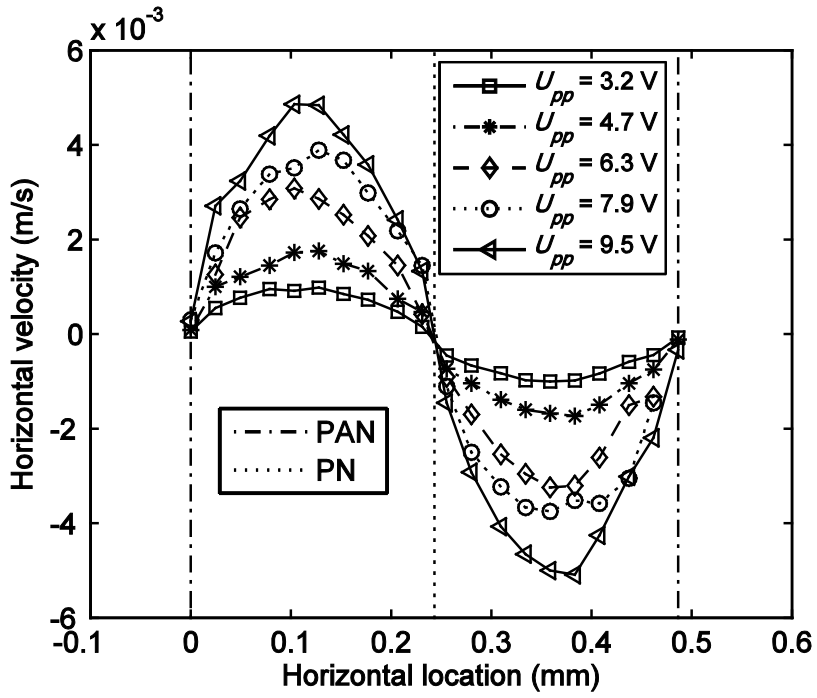
Table 5-1: Experimental signal generator voltage (amplified 50 dB for PZT input)

Experimented excitation	Exp. 1	Exp. 2	Exp. 3	Exp. 4	Exp. 5
PZT voltage, $U_{pp}$ (V)	3.2	4.7	6.3	7.9	9.5

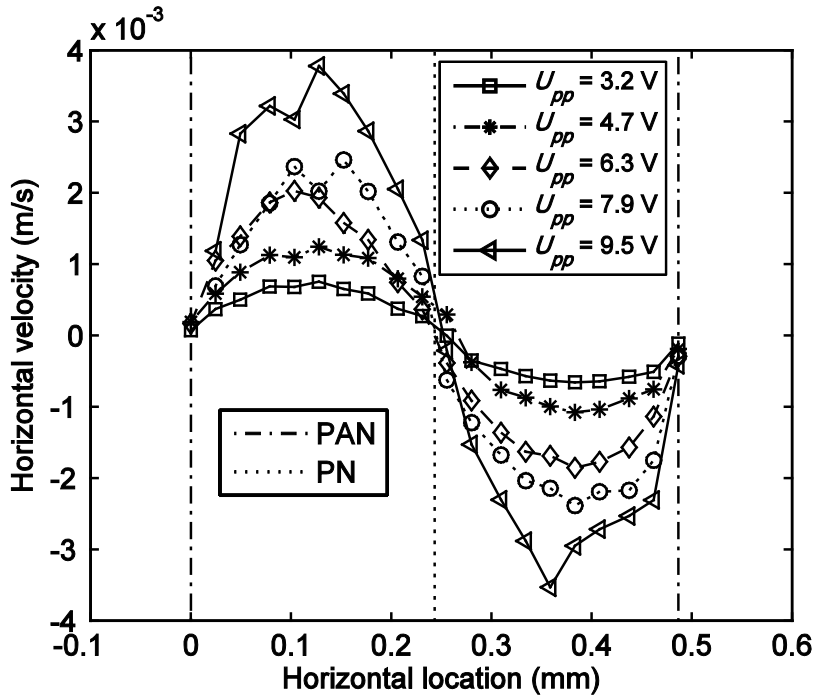
The effect of PZT excitation voltage for different glycerol weight concentrations is studied and shown in Figure 5-2. The horizontal velocity profile for a single wavelength of the acoustic wave is plotted for different experimented excitation voltages for 0 % glycerol weight concentration in Figure 5-2 (a). As the PZT excitation voltage increases, the maximum value of transverse velocity increases as expected by primary acoustic force theory. In Figure 5-2 (b), (c) and (d), the horizontal velocity profile attributed to 10 %, 20 % and 30 % glycerol weight concentrations are plotted. Note the re-scaling of the data. The same effect of PZT excitation voltage is seen in different glycerol weight concentrations. As the glycerol weight concentration is increased, the maximum velocity of horizontal velocity profile is decreasing. This is due to Stokes drag effect on the particles.



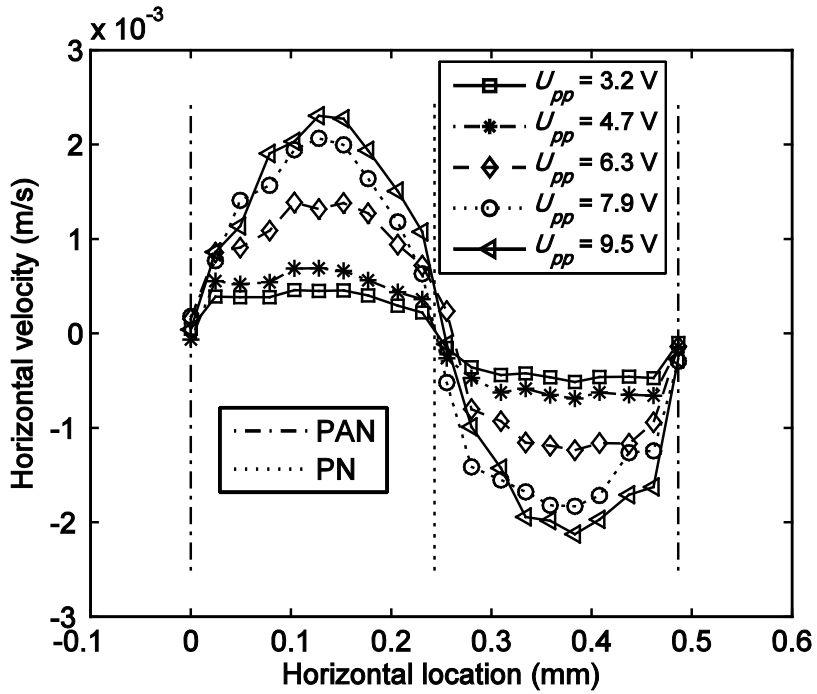
(a)



(b)



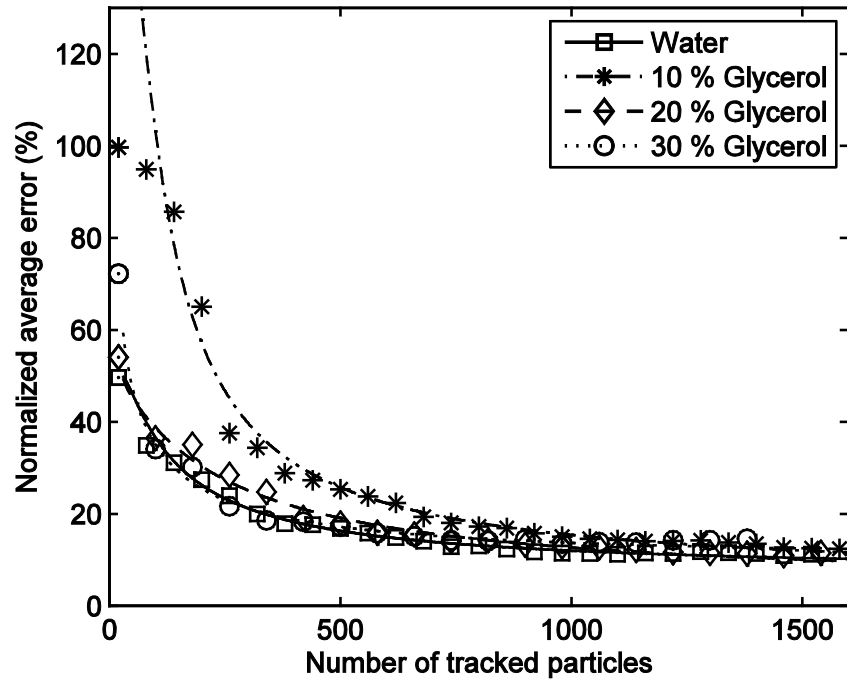
(c)



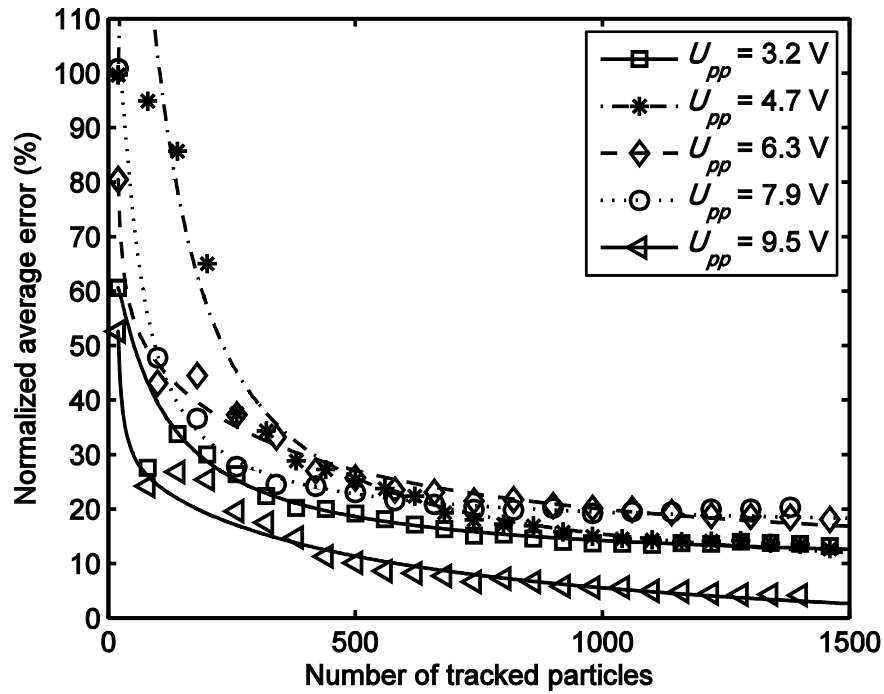
(d)

Figure 5-2: Experimental horizontal velocity for a single wavelength for different PZT voltage; (a) For 0% glycerol concentration, (b) 10%, (c) 20%, (d) 30%

The effect of number of tracked particles is also investigated by observing the defined normalized difference ( $\hat{\epsilon}$ ) in equation (4-4). This is performed for each dataset (different PZT excitation voltage and different glycerol-water concentration). For example, PZT voltage ( $U_{pp} = 4.7$  V) and different glycerol-water concentrations are shown in Figure 5-3 (a). Glycerol weight concentration (10 %) and different PZT voltage are shown in Figure 5-3 (b). The normalized difference error asymptotically approaches a constant value showing that the results are independent of number of particles and glycerol concentration if the number of particles is large enough.



(a)



(b)

Figure 5-3: Effect of number of considered particles on the normalized average error; (a) Variation of glycerol concentration for PZT voltage  $U_{pp} = 4.7$  V; (b) Variation of PZT voltage for glycerol concentration= 10%

## 5.4 Acoustic resonator performance parametric study

Based on the velocity profile in a single wavelength, the effect of viscosity of the containing fluid on the acoustic resonator performance is investigated. The maximum velocity ( $V_{max}$ ) of a single velocity profile for a single wavelength is found. This is carried out for each dataset (different PZT excitation voltage and glycerol-water concentration) and the results are shown in Figure 5-4. For each specific glycerol-water concentration, the maximum average velocity of the velocity profile increases as the PZT excitation voltage increases. This is predicted by primary acoustic force theory as in equations (1-14) and (5-1) in a quadratic relation.

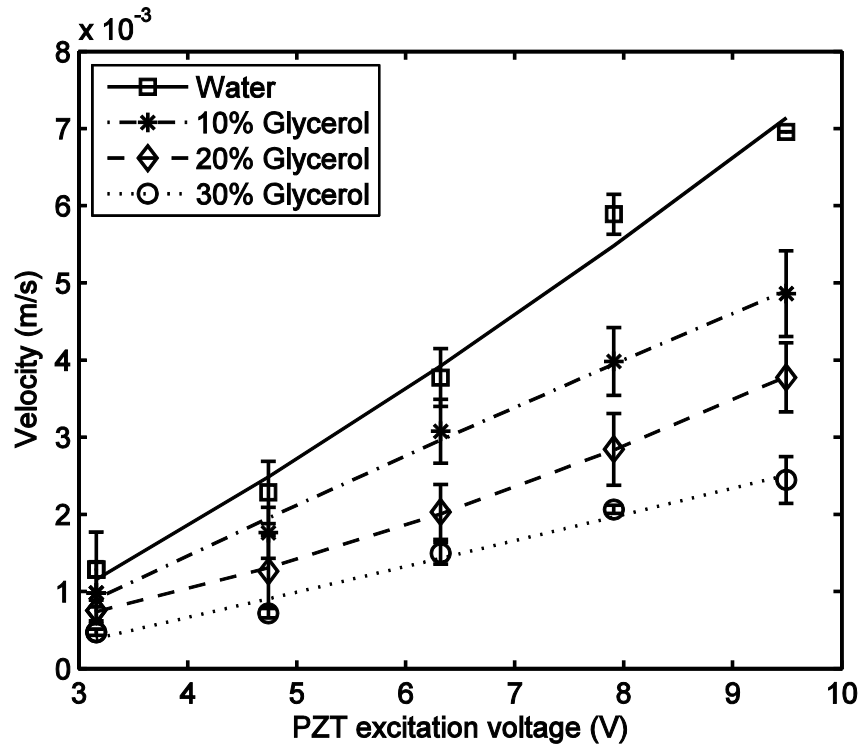


Figure 5-4: Study of influence of PZT excitation voltage on acoustic resonator performance

The effect of viscosity on each PZT voltage is studied and shown in Figure 5-5. For each specific PZT voltage, as the concentration of the glycerol increases the viscosity of the fluid increases leading to lower particle maximum velocity. This is observed for all of the PZT excitation voltages. These effects are caused by Stokes drag as predicted in equation (1-14).

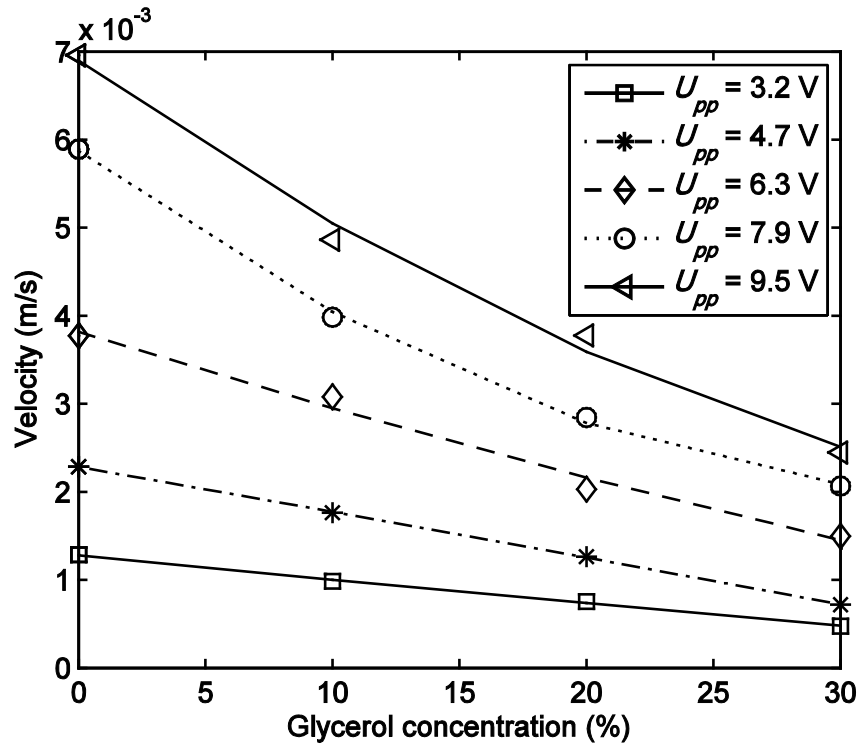


Figure 5-5: Study of influence of glycerol concentration on acoustic resonator performance

### 5.5 Acoustic energy density

To examine the acoustic resonator performance, the acoustic energy density attributed to the acoustic resonance is investigated as the PZT excitation voltage and the fluid glycerol concentration varies. The performance of an acoustic resonator is often expressed via the acoustic energy density parameter (Hawkes & Radel, 2013). While it is a term in the primary acoustic force theory derivation in equation (1-14) (Bruus, 2012b), it is generally an unknown for a specific resonator. A quadratic proportionality to the pressure amplitude of generated acoustic wave is predicted in the primary acoustic force in equation

(1-7). However, the coupling efficiency of acoustic energy into the chamber containing fluid is hard to estimate but its dependency on PZT excitation voltage is predicted in (Jurg Dual & Möller, 2012). The effect of suspension fluid properties such as viscosity on acoustic wave damping and therefore acoustic coupling is difficult to predict (Hawkes & Radel, 2013). Using the experimental particle motion analysis (Augustsson et al., 2011; Bruus, 2012b), acoustic energy density in micro-channels/chambers has been estimated. Based on this analysis, the acoustic energy density for the typical acoustic chambers is estimated to be in the range of 10-100 J/m<sup>3</sup> (Bruus, 2012b). Using (1-14), the acoustic energy density for the chamber in this study is estimated as

$$E_{ac} = \frac{2\pi\mu a V_{max}}{V_0 \kappa \eta} \quad (5-3)$$

### 5.5.1 Particle properties effect

To study the independency of acoustic energy density to particle properties, the acoustic energy density for different particles experimented in validation of primary acoustic force theory in chapter 4 is evaluated. The suspension fluid is pure water and the PZT voltage is set to 21 V. The acoustic energy density is determined as the number of tracked particles is varied and is presented in Figure 5-6. As shown in the figure, the final value of the acoustic energy density is not varying for different numbers of tracked particles and it reaches approximately the same value for the three different experimented particles. Normally, the value of the acoustic energy density solely depends on

acoustic chamber parameters and is expected to be the same value for different particle sets. However, due to assumptions of different particles parameters such as particle density and particle compressibility based on the particle supplier's information, there are some variations of computed acoustic energy density for different particle sets. Considering the variation due to this fact, there is a good agreement observed between the achieved acoustic energy density for different particle sets which is estimated approximately  $25 \pm 2 \text{ J/m}^3$ . This value is in the normal range of acoustic chambers acoustic energy density.

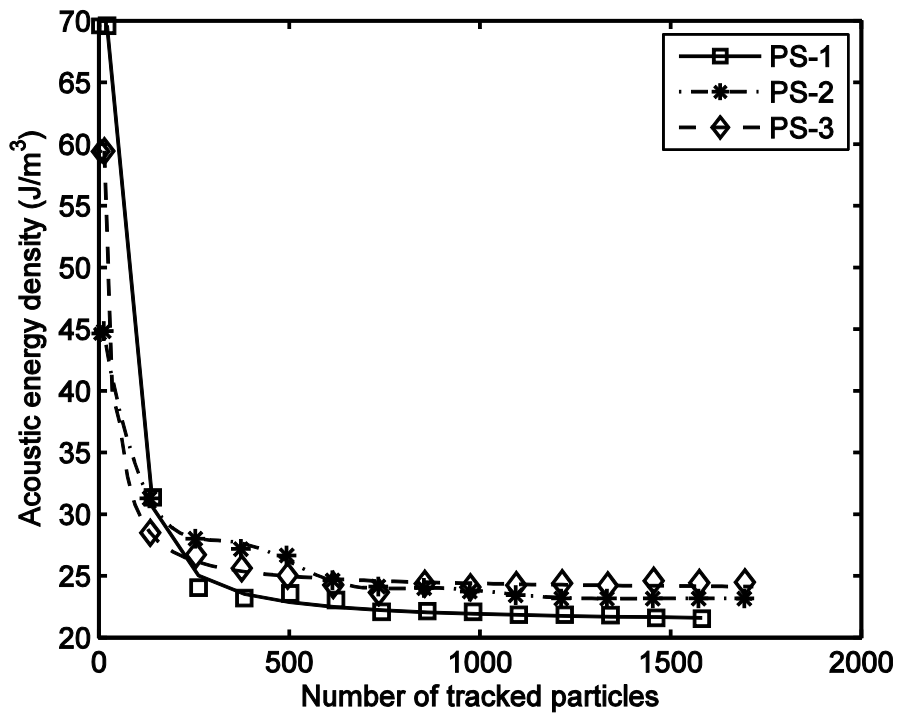


Figure 5-6: Acoustic energy density independency with respect to the number of tracked particles for PS-1, PS-2 and PS-3, good agreement for 3 different particle sets

### 5.5.2 Effect of PZT voltage and glycerol concentration

The known viscosity of each glycerol-water solution and the maximum velocity of averaged horizontal velocity are used in equation (5-3) and the achieved acoustic energy density as a function of PZT excitation voltage and fluid glycerol concentration is presented in Figure 5-7. The values fall in the range suggested by (Bruus, 2012b). This value is found to be independent of number of tracked particles for all of the experiments performed. The acoustic energy density increases with increasing the PZT excitation voltage for all of different glycerol-water concentrations as predicted by primary acoustic force theory. Good agreement between the experimental acoustic energy density values for different glycerol concentrations is also obtained. Maximum difference of 12 % in acoustic energy density measurement is observed at PZT voltage  $U_{pp} = 6.3$  V for 30 % glycerol concentration.

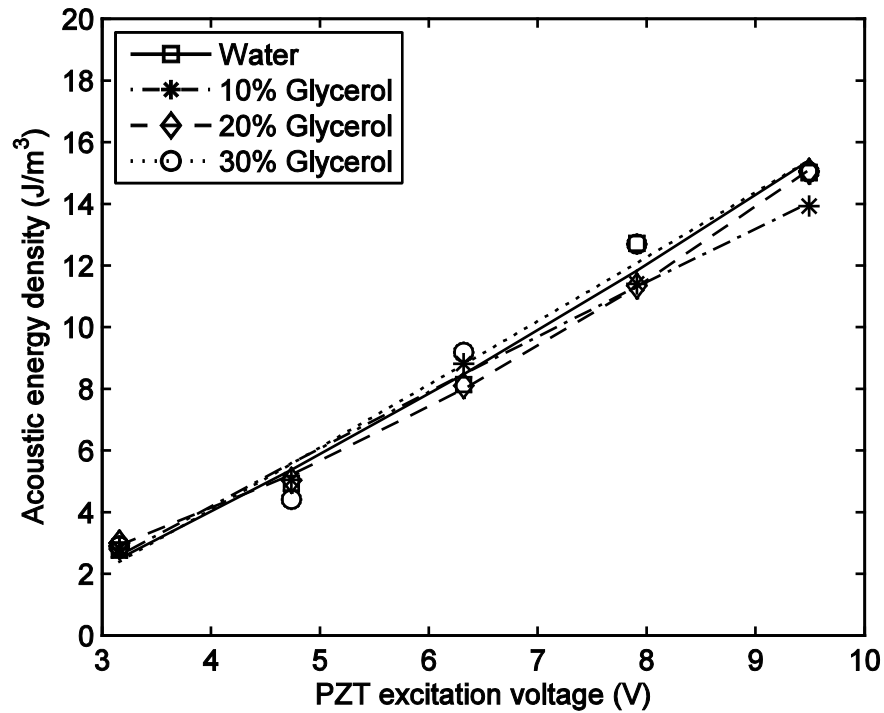


Figure 5-7: Acoustic energy density for different concentrations for different voltage

The effect of variation of fluid viscosity is investigated in more detail. The acoustic energy density is related to the square of the PZT voltage as seen in equation (5-1). The variation of experimentally measured acoustic energy density versus the PZT voltage for glycerol concentrations, 0 %, 10 %, 20 % and 30 % is plotted in Figure 5-8 (a), (b), (c) and (d) respectively. For each measured acoustic energy density point, measured range is also indicated. The range is twice the standard deviation of the achieved acoustic energy density. The experimental data points for each glycerol solution is fitted to

$$E_{ac} = aU_{pp}^b \quad (5-4)$$

where  $a$  and  $b$  are the power law coefficients. The measured values of power law coefficient  $b$  for different glycerol solutions are given are in Table 5-2. Using

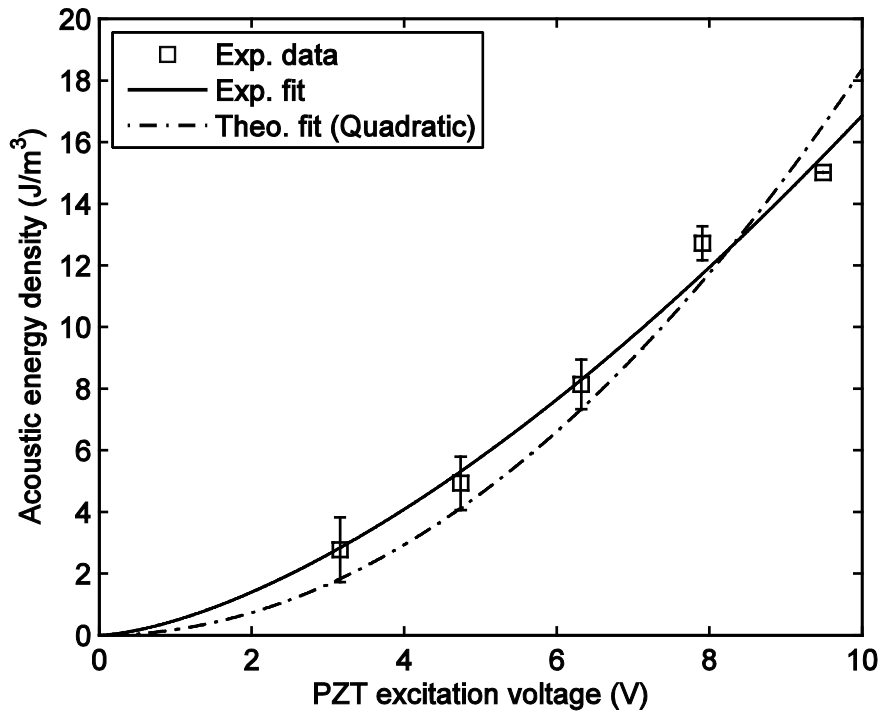
the quadratic relation expected by primary acoustic force theory, the data is fit to

$$E_{ac} = \gamma_{exp} U_{pp}^2 \quad (5-5)$$

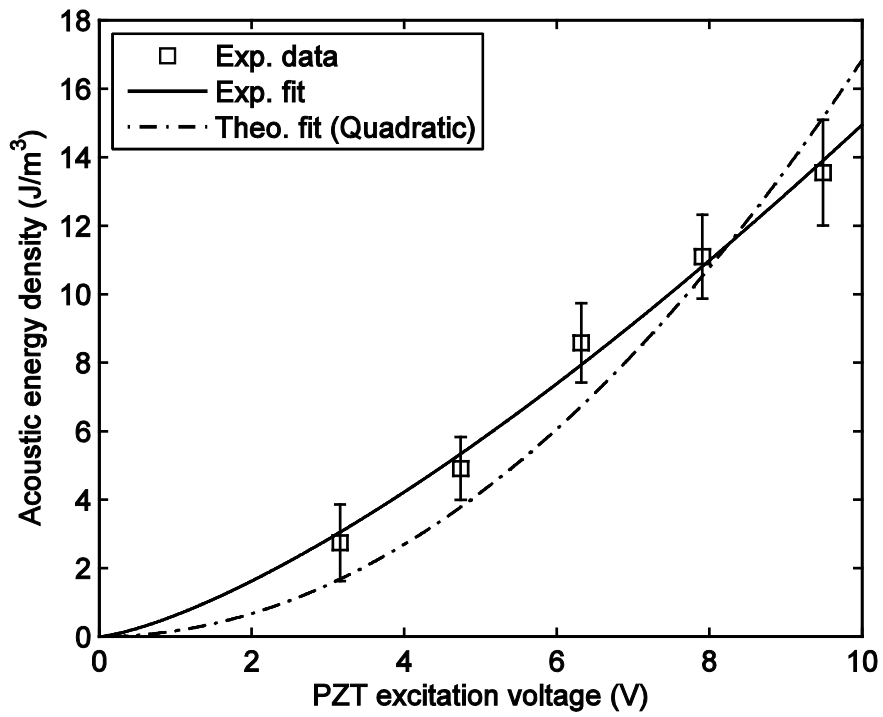
where  $\gamma_{exp}$  is the fitting parameter for experimentally measured acoustic energy density coefficient as defined in equation (5-1). Both curves in Figure 5-8 (a-d) show good agreement with the data. The coefficients of the two equations are listed in Table 5-2. There is a discrepancy observed between the experimentally measure power law coefficient which is  $b \sim 1.5$  and the one predicted by primary acoustic force theory  $b = 2$ . This parameter is reported in (Barnkob et al., 2010) to be 2.07. Acoustic energy density is measured by tracking individual particles affected by primary acoustic force in a micro-scale acoustic resonator. The power law coefficient ( $b$ ) is also reported in (Augustsson et al., 2011) to be between 1.87 to 2 where the acoustic energy density is investigated for a micro-channel acoustic resonator using PIV. A lower power law coefficient in the current work compared to a micro-channel single wavelength resonator is attributed to a higher damping factor that exists in multi-wavelength acoustic resonators (Hawkes & Radel, 2013).

The experimentally determined acoustic energy density coefficient ( $\gamma$ ) for all the glycerol-water solutions are also reported in Table 5-2. The value of this parameter does not vary with the viscosity of the fluid and characterizes the acoustic resonator. Changing viscosity does not affect the fitting parameters significantly considering the two different fitting curves to the experimentally

measured acoustic energy density values. However, the discrepancy in the measured power law coefficient ( $b$ ) indicated the difference between the macro-scale and micro-scale acoustic chambers damping factors.



(a)



(b)

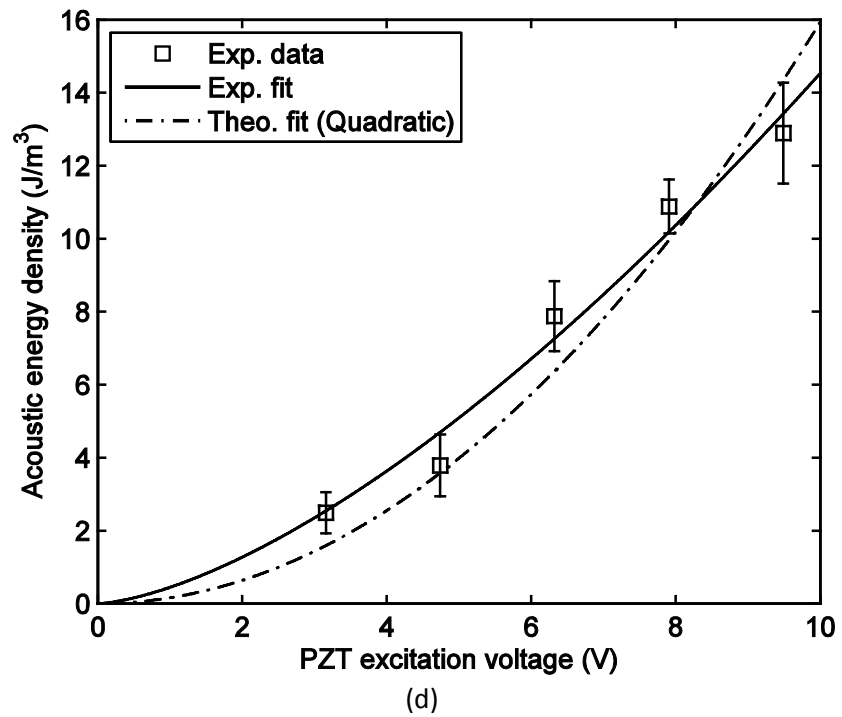
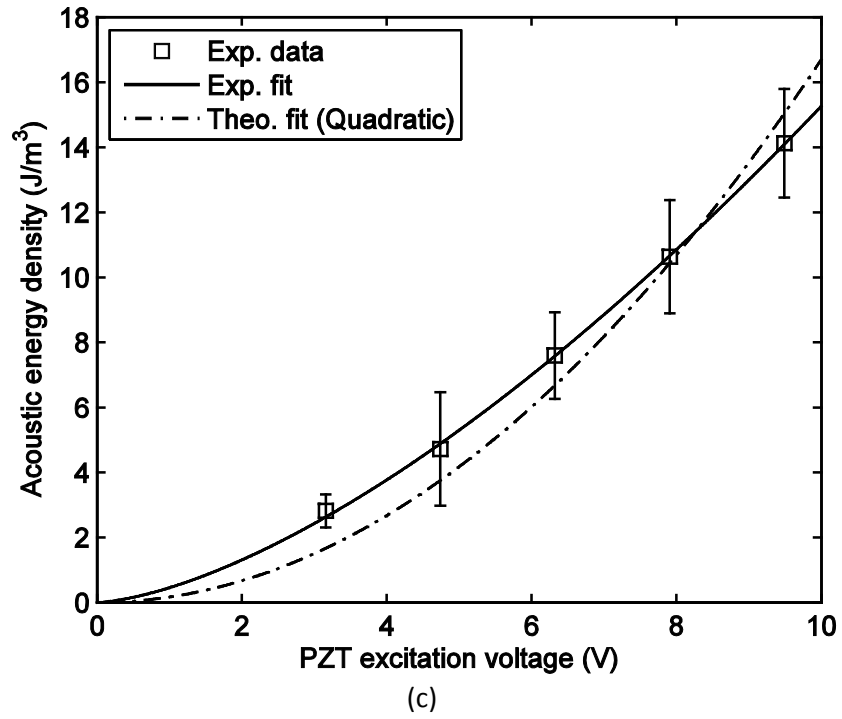


Figure 5-8: Validity analysis of predicted quadratic proportionality of acoustic energy density on PZT voltage, experimental fitted line comparison with quadratic theoretical one; (a) for glycerol concentration 0 % (b) 10 % (c) 20 % (d) 30 %

Table 5-2: Power law coefficients for different glycerol concentrations

	Glycerol weight concentration			
	0 % (water)	10 %	20 %	30 %
Power law coefficient ( $a$ )	0.48	0.62	0.45	0.45
Power law coefficient ( $b$ )	1.54	1.51	1.40	1.45
equation (5-4) fit error RMS	0.53	0.42	0.11	0.62
Exp. acoustic energy density coefficient ( $\gamma_{max}$ )	0.18	0.17	0.17	0.16

## 5.6 Conclusion

Particle motion in a macro-scale multi-wavelength acoustic chamber is experimentally investigated using the developed PTV approach. Using the measured particle motion the multi-wavelength acoustic chamber is studied. The characterization is performed by determining the chamber acoustic energy density for different conditions. The PZT excitation voltage and fluid properties are varied and dependency of acoustic energy density is studied. The acoustic energy density independency of suspension fluid viscosity is shown. The relation of acoustic energy density and PZT excitation voltage is also achieved and compared with micro-scale single pressure node acoustic micro-channels/chambers.

The observations show an important difference between macro-scale multi-wavelength and micro-scale acoustic resonators. A quadratic relation between the acoustic energy density and PZT voltage is theoretically predicted in (Jurg Dual & Möller, 2012). This dependency is validated for micro-scale acoustic resonators in (Augustsson et al., 2011; Barnkob et al., 2010). However the power law coefficient for experimented macro-scale acoustic resonator is calculated to be  $b = 1.5$  which is lower than the predicted value  $b = 2$ . The higher damping factor in multi-wavelength acoustic resonators is believed to be the main source of variance (Hawkes & Radel, 2013).

## **CHAPTER 6: CHARACTERIZATION OF MULTI-WAVELENGTH MACRO-SCALE ACOUSTIC RESONATOR USING A PDF MODEL**

### **6.1 Introduction**

Imaging techniques have been widely used to characterize an acoustic resonator (Augustsson et al., 2011; Barnkob et al., 2010; Barnkob, Augustsson, et al., 2012; Spengler et al., 2001; Woodside et al., 1997). Particle tracking velocimetry (PTV) is used in cases where particles are individually detectable and the acoustic energy density is estimated by tracking their motion (Barnkob et al., 2010; Woodside et al., 1997). Particle imaging velocimetry (PIV) is also used in the cases where particle loading is higher than PTV. In (Augustsson et al., 2011; Barnkob, Augustsson, et al., 2012) in which the primary acoustic force on single particles is investigated using PIV, acoustic energy density is determined using the PIV velocity vectors. Acoustic energy density is also determined in (Barnkob, Iranmanesh, Wiklund, & Bruus, 2012) by analyzing the change in intensity of

images during densification of particles in a microchannel. It is obtained by fitting a model of image light intensity to the measured variation of intensity of images during the densification time. The model includes the acoustic energy density as a fitting parameter.

In this chapter, a method for determining acoustic energy density in multi-wavelength acoustic resonators is presented. Initially the intensity envelope of captured images of acoustophoresis separation of particles is introduced. Preliminary analysis and the effect of PZT excitation voltage and viscosity of the liquid in particle-fluid mixture on densification time are investigated. Next, a probability of density function (PDF) of the location of particles is modeled, using a different approach to (Barnkob, Iranmanesh, et al., 2012). The model is fitted to the light intensity distribution of captured particle images from which the acoustic energy density is determined. An advantage of this method compared to other imaging techniques is that there is less limitation on the overall particle concentration and no requirement of the imaging system to image individual particles. The theory behind the modeling is described and is compared with experimental results. The determined acoustic energy density is compared with the available experimental results for different PZT excitation voltages.

## 6.2 Image intensity analysis

### 6.2.1 Intensity envelope

Considering a set of raw images of densification process such as those shown in Figure 2-13 (a), the intensity of each pixel ranging from 0 (black) to 255 (white) can be used as an indication of the presence of a particle. The intensity of each image can be summed in the vertical direction. The intensity which is normalized with the maximum intensity in the transverse direction is plotted in Figure 6-1 for a typical time series of images as particles are densified by the acoustic field. In this example the particles are particle set PS-4 and the PZT voltage is  $U_{pp}= 3.2$  V. At the initial time step, the particles are homogeneously distributed resulting in a uniform intensity plot. As the PZT is triggered the primary acoustic force starts to densify the particles to the nearest PNs. The light intensity increases at a PN until it reaches a limit where particle separation is near completion. The peaks in this plot which indicate the maximum densification locations and are at the PNs of the acoustic wave. The minima of the plot where the particles are repelled from are the PANs.

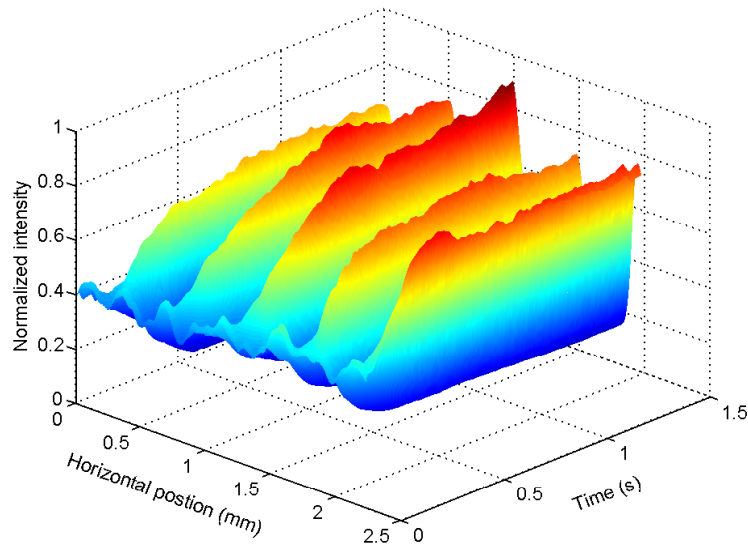
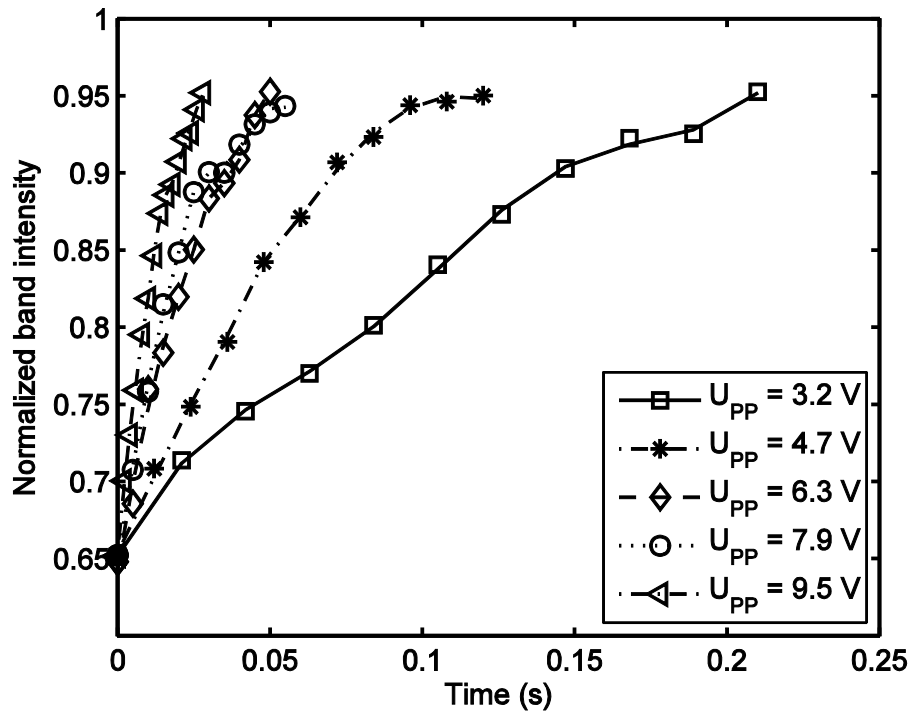


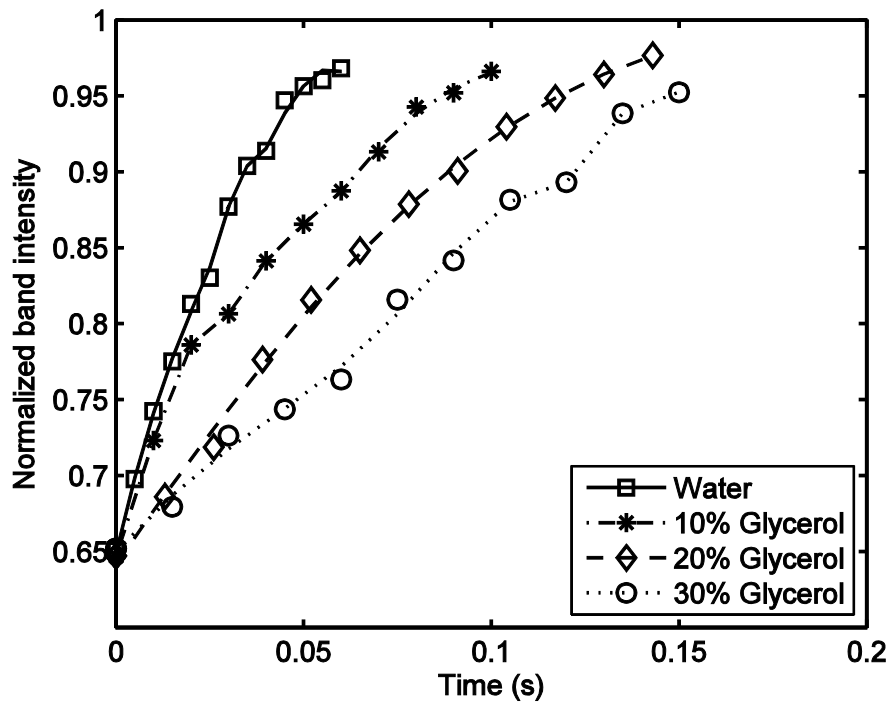
Figure 6-1. A false color light intensity envelope for different times in the measurement; The intensity of PN increase as particles propagate to them

### 6.2.2 Effect of PZT voltage and glycerol concentration

The PZT voltage and the glycerol concentration can be varied and their effect are determined from normalized intensities, considered once they have reached 95 % of the final value. The effect of PZT voltage on intensity of the PN is shown in Figure 6-2 (a). As the PZT voltage is increased, the intensity of the analyzed PN increases sharply in the initial stages. However, as the PZT voltage is increased, the variation in densification time of experiments reduces. Effect of glycerol concentration is also shown in Figure 6-2 (b). The PZT voltage is set to  $U_{pp} = 3.2$  V in this figure. As the glycerol concentration is increased, the densification time also increases as the increased viscosity of the fluid retards particle motion.



(a)



(b)

Figure 6-2: Variation of summed intensity of a PN; (a) Effect of variation of PZT voltage on summed intensity for pure water, (b) Effect of variation of glycerol concentration on summed intensity for  $U_{pp} = 3.2$  V

The densification time using the normalized band intensities shown in Figure 6-2 can be found. The time at which the intensity of the particle bands reaches 95% is considered as the final point of densification. The densification time for each glycerol weight concentration and PZT excitation voltage is calculated and plotted in Figure 6-3. Considering the densification time for a constant glycerol solution or water, the densification time reduces as the PZT excitation voltage is increased. This is visible for all of the glycerol weight solutions. The effect of glycerol weight concentration is also shown in Figure 6-3. As the glycerol weight concentration is increased for a constant PZT excitation voltage, the densification time increases. Increase viscosity leads to a stronger influence of the Stokes drag force which will slow densification.

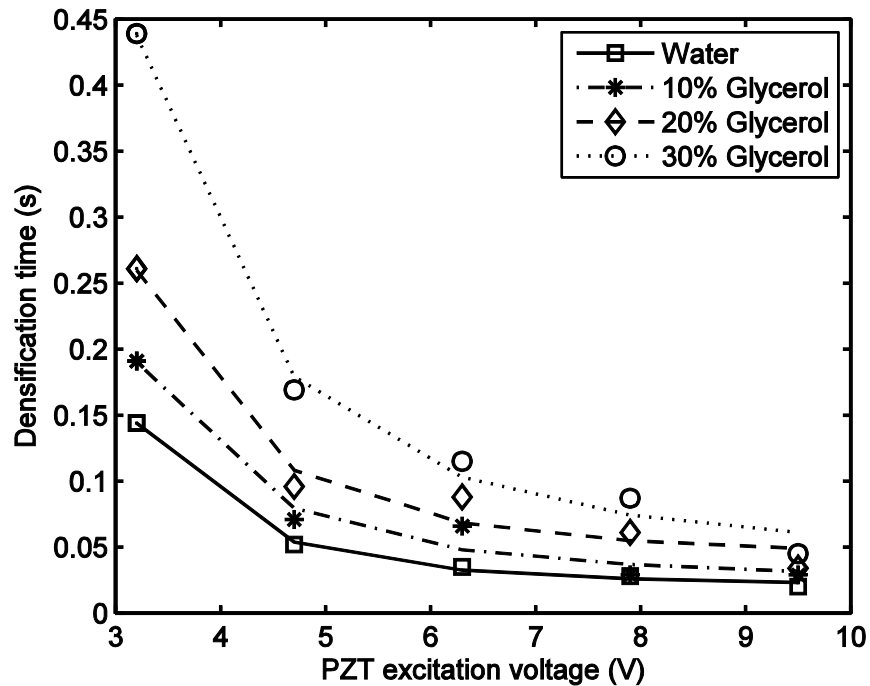
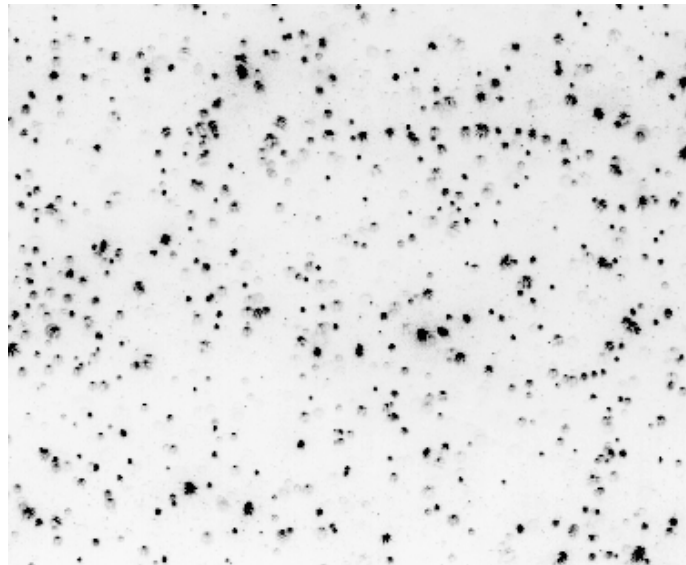


Figure 6-3: Densification time for different glycerol concentration and PZT voltage

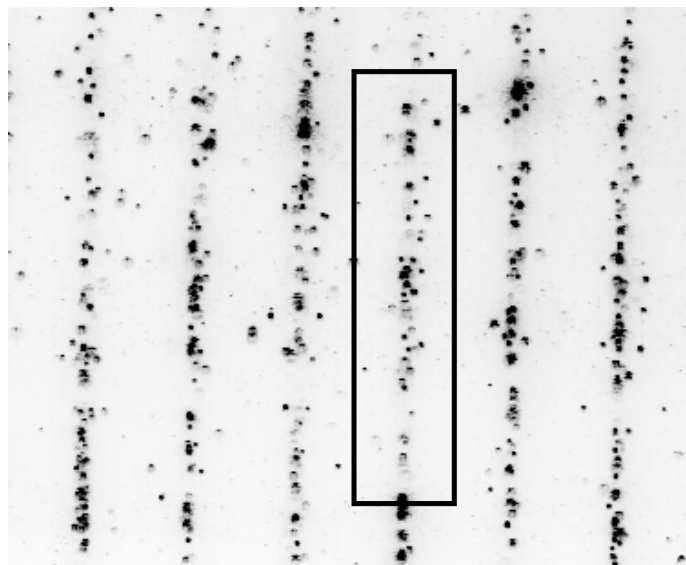
## **6.3 Particles location PDF model**

### **6.3.1 Theoretical model**

A sample of densification of particles to the nearest pressure nodes is shown in Figure 6-4. The acoustic pressure force drives the randomly distributed particles shown in Figure 6-4 (a) to the closest PN as in Figure 6-4 (b). A sample of a PN is indicated in a rectangle in Figure 6-4 (b). The particles in this region are attracted to the PN located in the middle of the rectangle.



(a)



(b)

Figure 6-4: Raw data images (inverted color map) highlighting the separation process; (a) particles distribution just before actuating the PZT, (b) particles distribution after applying primary acoustic force; The rectangle highlights the modeled area

Considering the particles located within the rectangle in Figure 6-4 (b), their path is investigated theoretically. Note that the sides of the rectangle are located at the PANs from which particles are forced away from. This is shown schematically in Figure 6-5. A particle velocity profile affected by the primary acoustic force and Stokes drag force can be presented in the form

$$\frac{dx}{dt} = \frac{V_0 E_{ac} \kappa \eta}{2\pi \mu a} \sin(2\kappa x) \quad (6-1)$$

Assuming the particle starting location is  $(x_0)$ , the particle horizontal path  $(x)$  can be found by integrating equation (6-1) as

$$x(x_0, t) = \frac{w}{\pi} \arctan[\exp(t/\tau) \tan(\pi x_0/w)] \quad (6-2)$$

where  $w = \frac{\pi}{\kappa}$  is the width of this rectangle (half of the pressure acoustic wave wavelength) and  $\tau$  is the characteristic time (Barnkob, Iranmanesh, et al., 2012) as

$$\tau = \frac{3\mu}{4E_{ac}\eta(\pi a/w)^2} \quad (6-3)$$

The characteristic time, which is inversely proportional to the acoustic energy density determines how quickly the particle is moving toward the PN.

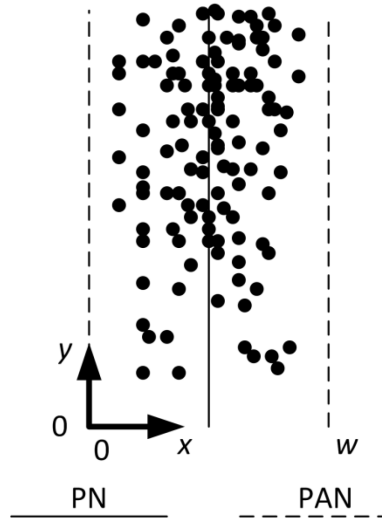


Figure 6-5: Schematic of the densification of particles in the particles locations PDF model

Considering a uniform distribution of particles before applying the acoustic pressure as illustrated in Figure 6-4 (a), the PDF of initial location of particles ( $f_{x_0}$ ) can be described as

$$f_{x_0}(x_0) = \frac{1}{w} \quad 0 \leq x_0 \leq w \quad (6-4)$$

in which the initial location of particles ( $x_0$ ) ranging between 0 and  $w$  and does not have any effect on this function.

Given a monotonic and continuous transformation function as  $y = g(x)$  applied on a variable ( $x$ ) with known PDF function  $f_x(x)$ , the PDF function  $f_Y(y)$  of the transformed variable ( $y$ ) can be found in (Billingsley, 1995) as

$$f_Y(y) = f_x(g^{-1}(y)) \left| \frac{d}{dy} g^{-1}(y) \right| \quad (6-5)$$

where  $g^{-1}(y)$  is the inverse function of the function  $g(y)$ . Considering equation (6-2) at a constant time ( $t$ ), it can be interpreted as a transform function of the

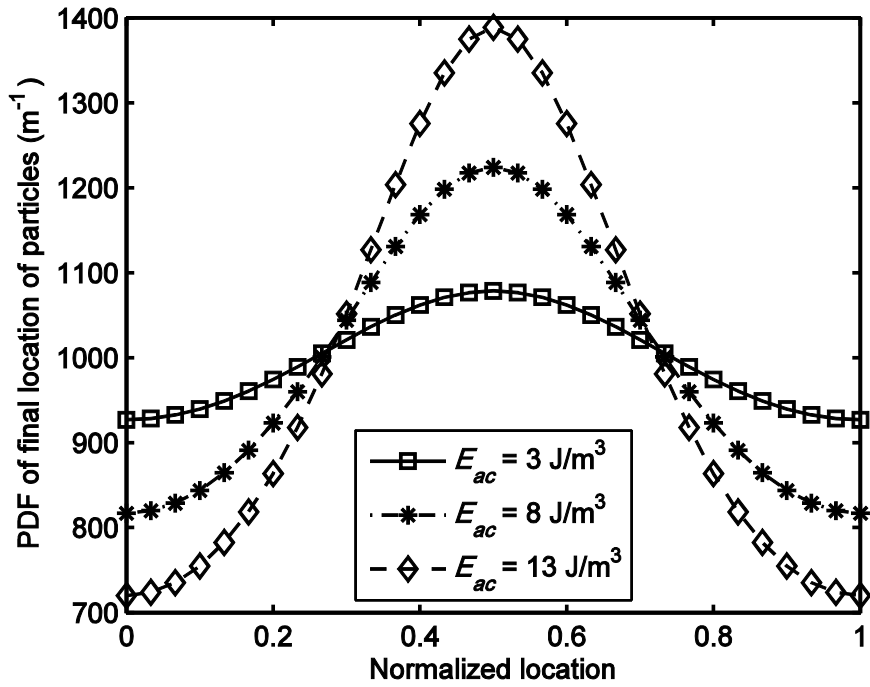
form  $x = g(x_0)$ . Also, as the function is monotonic and continuous, the PDF of final location of particles ( $f_x$ ) can be derived to be

$$f_x(x, t) = \frac{1}{w} \left[ \frac{\exp\left(-\frac{t}{\tau}\right)}{\exp\left(-\frac{2t}{\tau}\right) \sin^2\left(\frac{\pi x}{w}\right) + \cos^2\left(\frac{\pi x}{w}\right)} \right] \quad (6-6)$$

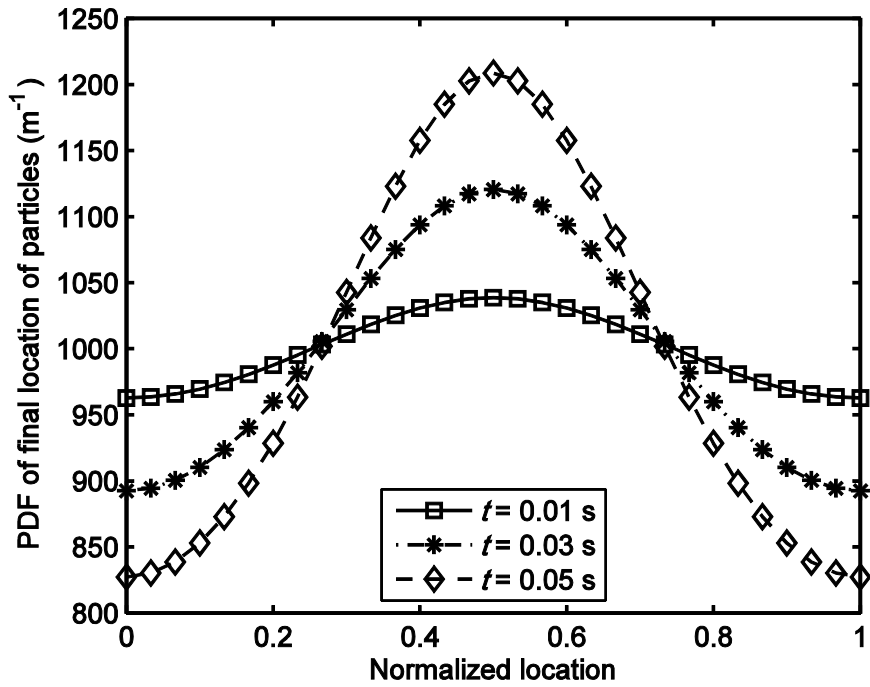
This equation represents the PDF of final location of particles as a function of time. This approach, which models the intensity distribution as a function of time differs from in (Barnkob, Iranmanesh, et al., 2012) who summed all intensities over an area in field-of-view to have a single intensity map. Their approach removes all influence of location. The developed PDF model can now be investigated by studying the effect of time and acoustic energy density in the next section prior to applying to the intensity plot of the images.

### 6.3.2 PDF model analysis

The PDF of final location of particles is investigated. In Figure 6-6 (a), the PDF of final location of particles is plotted at time  $t= 0.02$  s for example systems with a different acoustic energy densities. As the acoustic energy density is increased, more particles are densified at the PN located at the middle of the acoustic resonator. The intensity of PANs at the sides is also reducing consequently. In Figure 6-6 (b), the acoustic energy density is held at  $E_{ac} = 3$  J/m<sup>3</sup> and the PDF is plotted for different times. As time increases, more particles move as expected to the PN resulting in a higher PDF value.



(a)



(b)

Figure 6-6: PDF of final location of particles in the studied acoustic resonator, (a) Effect of acoustic energy density at  $t = 0.02 \text{ s}$  (b) effect of changing time at  $E_{ac} = 3 \text{ J/m}^3$

As the increase in the intensity of a pixel is an indication of the presence of one or more particles, a plot of intensity can be used to compare with theoretically derived PDF of location of particles to determine acoustic energy density. Particle distribution before applying the acoustic wave is homogenous and consequently the intensity plot and the PDF of location of particles are uniform as in equation (6-4). Depending on the value of the specific acoustic energy density and densification time, the PDF of location of particles and intensity plot of image changes as in Figure 6-6 (a) and Figure 6-6 (b) respectively. These two plots are compared at fixed densification time and the intensity plot is fitted to the analytical PDF of location of particles as

$$\frac{I}{I_{max}}(x) = \frac{f_X(x)}{f_X(w/2)} \quad (6-7)$$

Note that the PDF of particle location is normalized with its maximum which is located at the PN. The only unknown is the acoustic energy density for the system which is can now be determined by this fitting. In order to minimize the effects of secondary acoustic force (Doinikov, 2001), any hydrodynamic forces and any overlapping of particles at the PN, a dilute suspension is analyzed. Overlapping of particles causes the increase in intensity in the image at a PN to be less than expected by the PDF of location of particles. The effect of overlapping is also minimized by performed the fitting for the initial densification stages where the particles distribution is not highly concentrated at the PN.

### 6.3.3 Acoustic energy density determination

A sample of fitting the PDF model to the intensity envelope for a pressure node is shown in Figure 6-7. This intensity plot is attributed to the excitation voltage  $U_{pp} = 6.3$  V and experimental densification time  $t = 0.045$  s. The PDF model fits with minimum residual at this time. As the PDF model fits the intensity plot with low residual at all of the horizontal locations, the acoustic energy density is found to be  $7.8 \text{ J/m}^3$ .

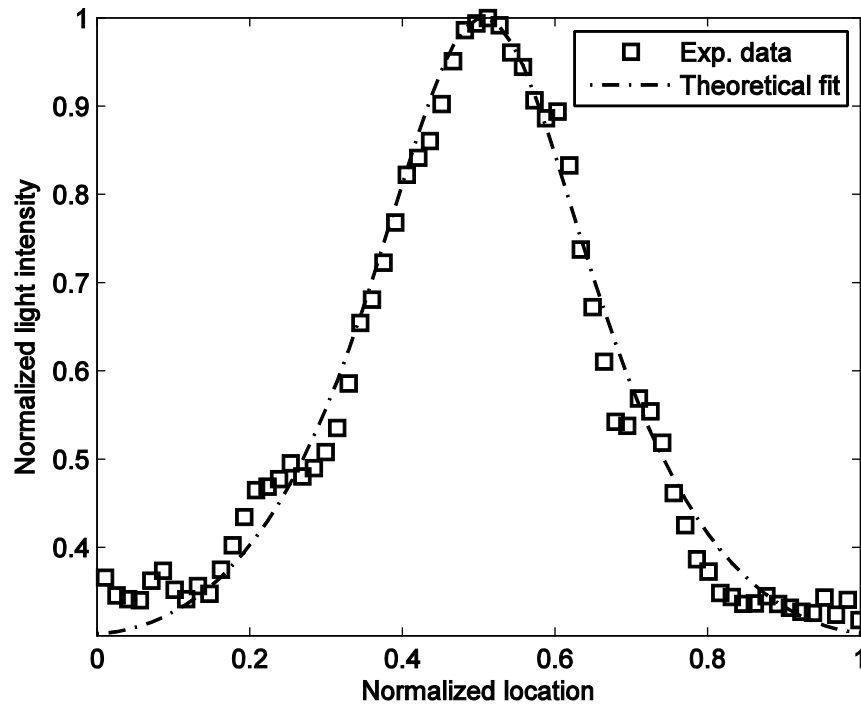
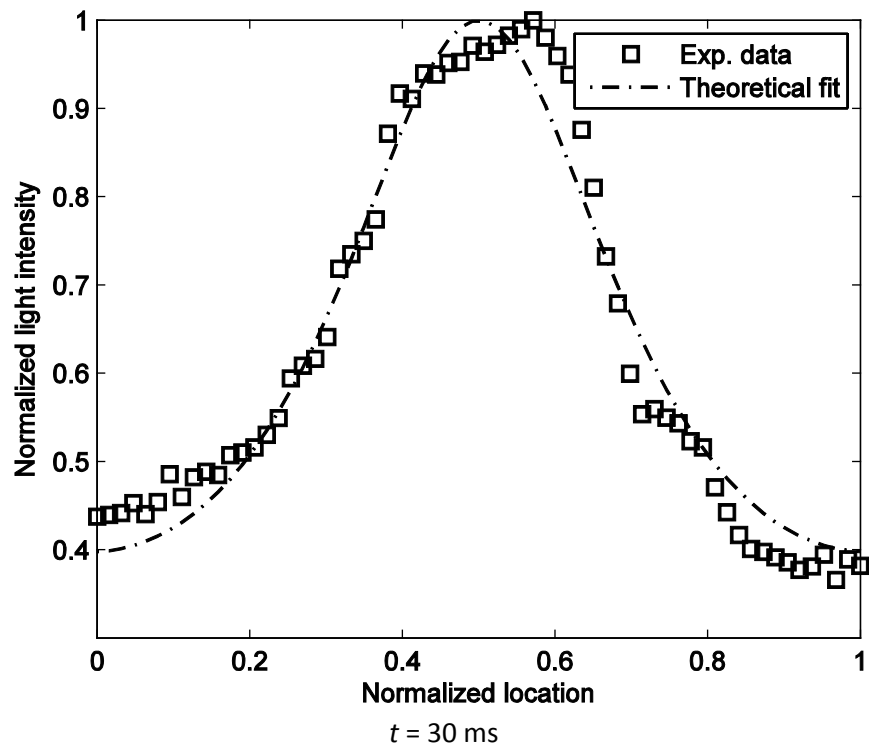
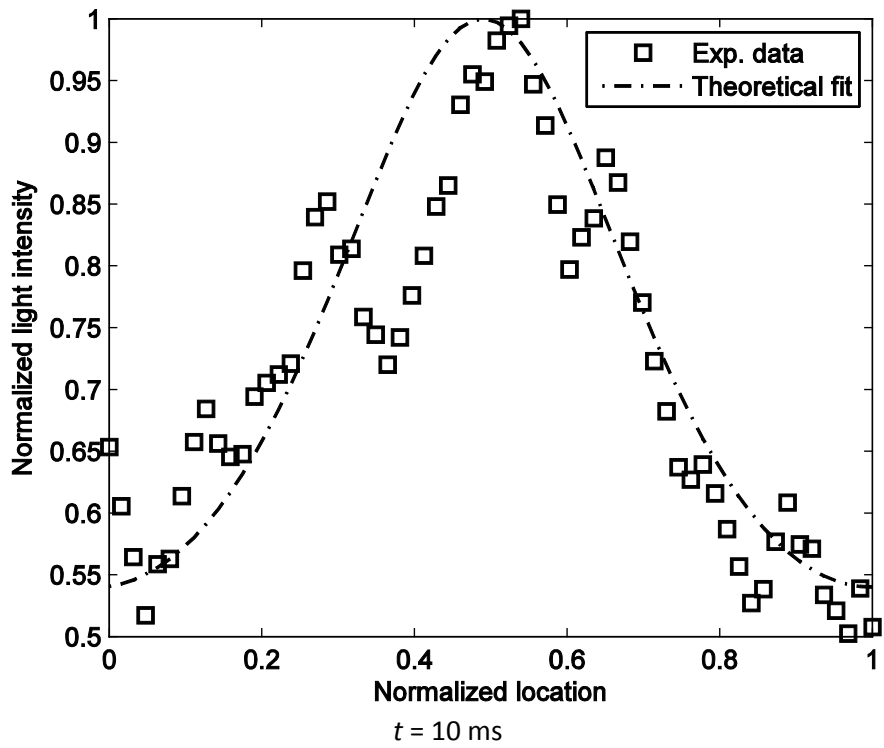
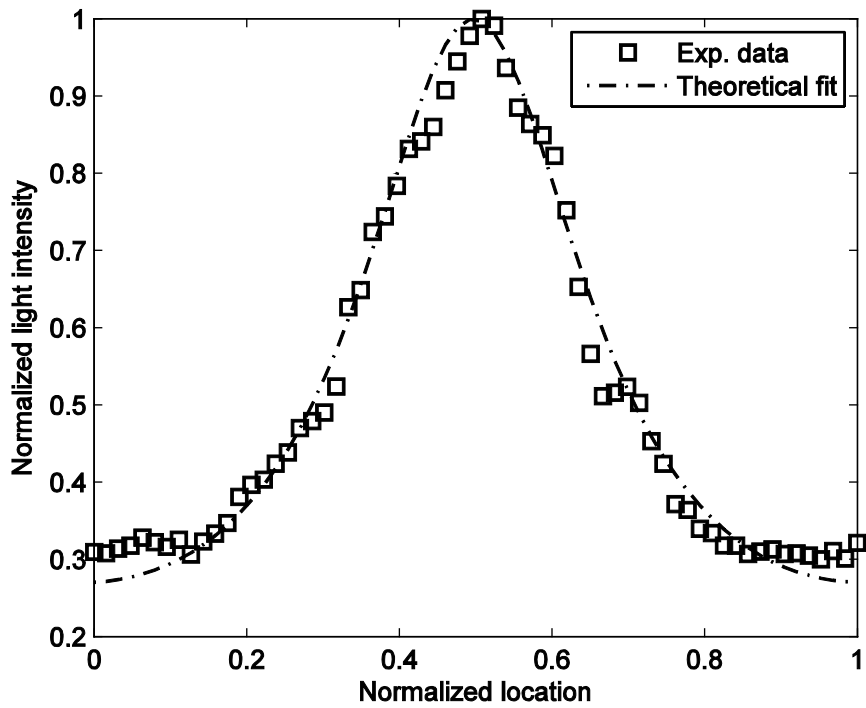


Figure 6-7: A sample fitting of the PDF model to the normalized light intensity envelope, this sample is associated with  $U_{pp} = 6.3$  V and experimental densification time  $t = 0.045$  s

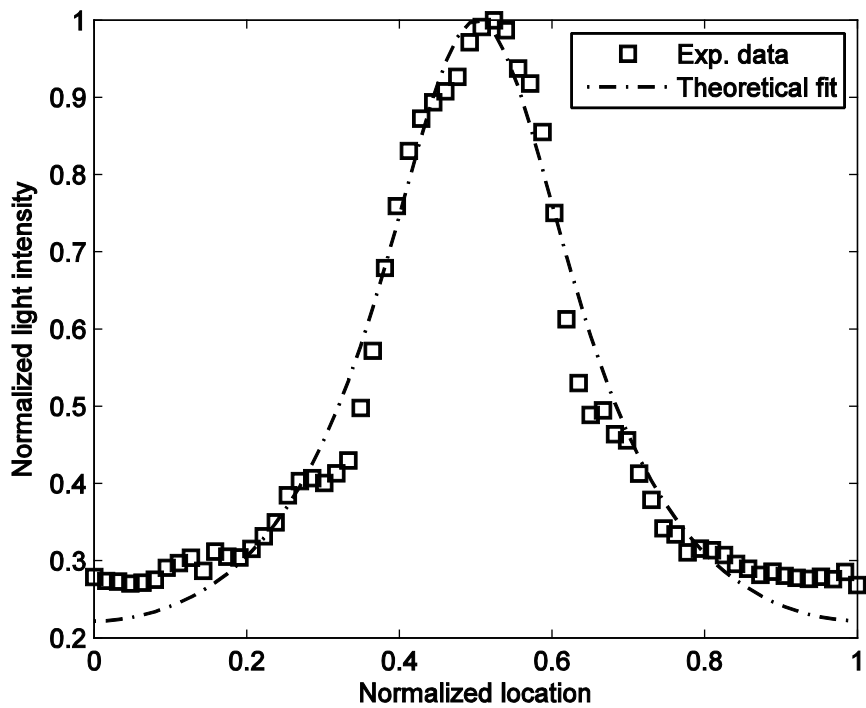
This experimental fitting time is limited by 1) the initial high residual zone as the lower limit and 2) the effect of overlapping particles increasing over time as the higher limit. Samples of fitting the PDF model to different experimental

densification times are shown in Figure 6-8. At the initial time of densification (samples are associated with experimental time  $t = 10$  ms and  $t = 30$  ms in Figure 6-8), the intensity envelope is close to the homogenous intensity plot and consequently the uncertainty of fitting the PDF model to the intensity plot is high. At the experimental densification time of  $t = 50$  ms, the residual of the fit is low and the PDF model well matches the experimental data. At higher experimental fitting time (samples are associated with experimental time  $t = 70$  ms,  $t = 100$  ms and  $t = 150$  ms in Figure 6-8), the overlapping of particles is limiting the fitting of the model. As more particles overlap at the pressure node, the expected PDF value difference with the intensity envelope increases which consequently results in an increase in the uncertainty in the fitted acoustic energy density.





$t = 50 \text{ ms}$



$t = 70 \text{ ms}$

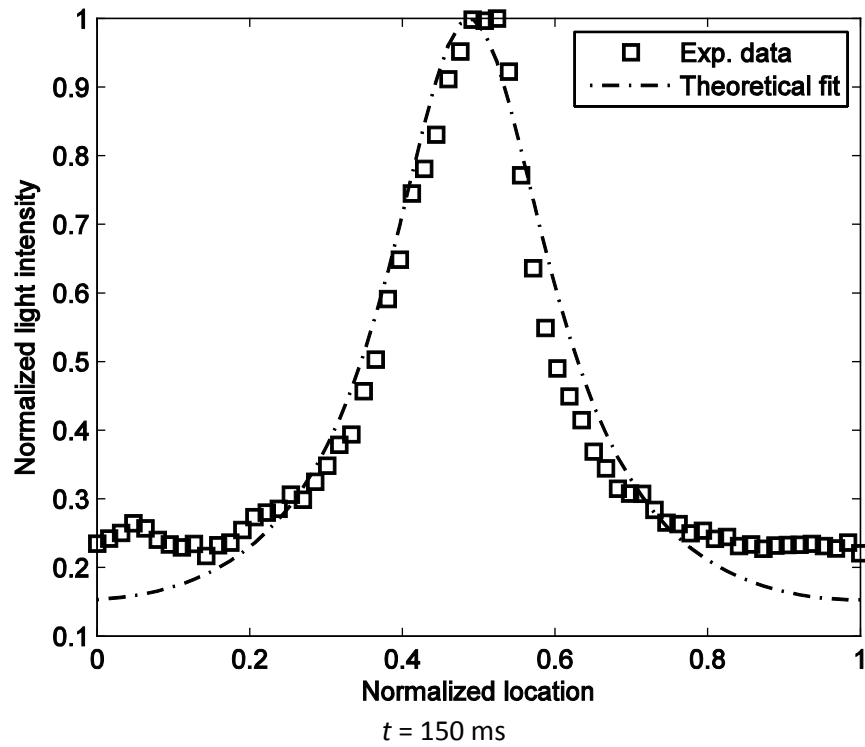
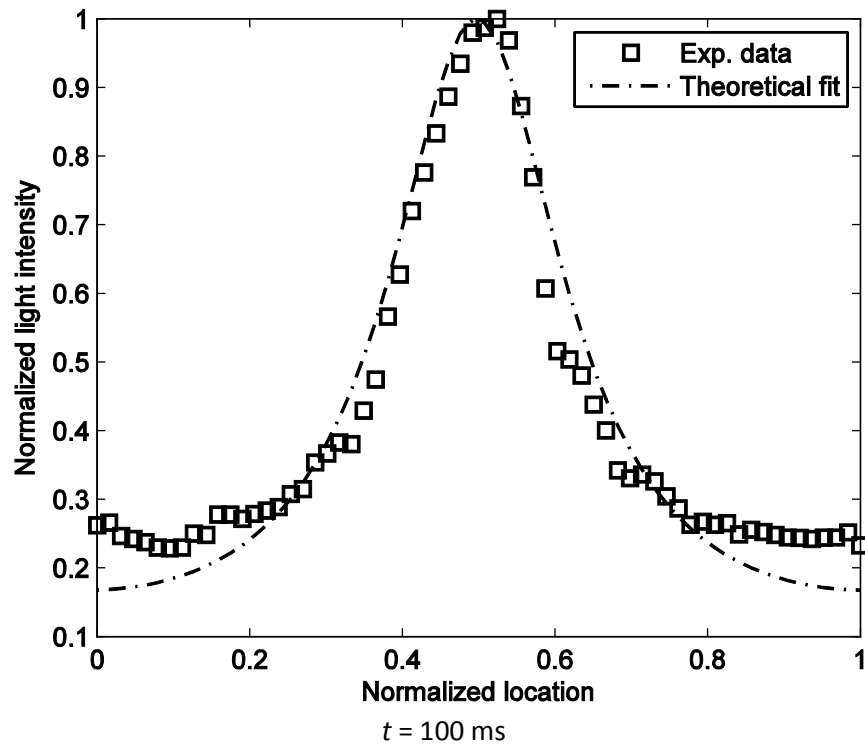


Figure 6-8: Samples of fitting of the PDF model to the normalized light intensity envelope associated with experimental densification time

The effect of experimental fitting time on the determined acoustic energy density is studied and shown in Figure 6-9. RMS of normalized residual of the fitted PDF model to the intensity plots is shown in Figure 6-9 (a). On the left vertical axis, the RMS of normalized fitting residual for different experimental fitting times is shown. This is the RMS of residual observed between the fitted PDF model and the experimentally measured intensity plot. It is a measure of how well the PDF model is fitted to the experimental data and acts as a filter on selection of the experimental fitting time. The calculated acoustic energy density from the PDF model is fitted to the intensity plot is shown on the right vertical axis in Figure 6-9 (a).

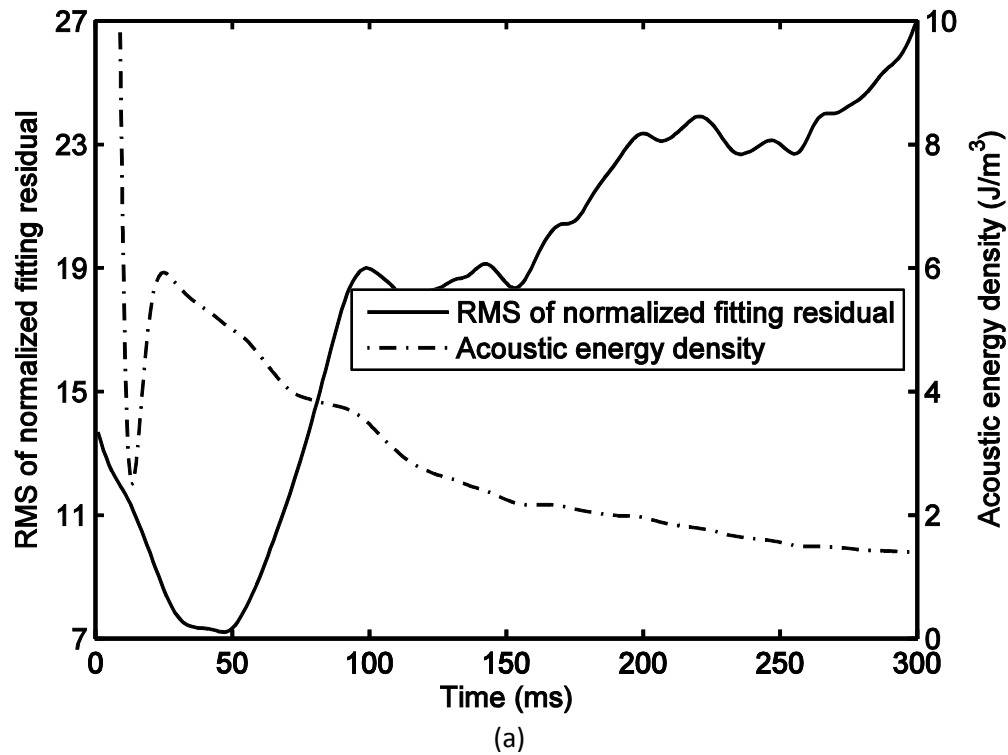
A  $\chi^2$  test is also performed on the fitting and the variation of  $\chi^2$  with time is shown in Figure 6-9 (b). The  $\chi^2$  is calculated using

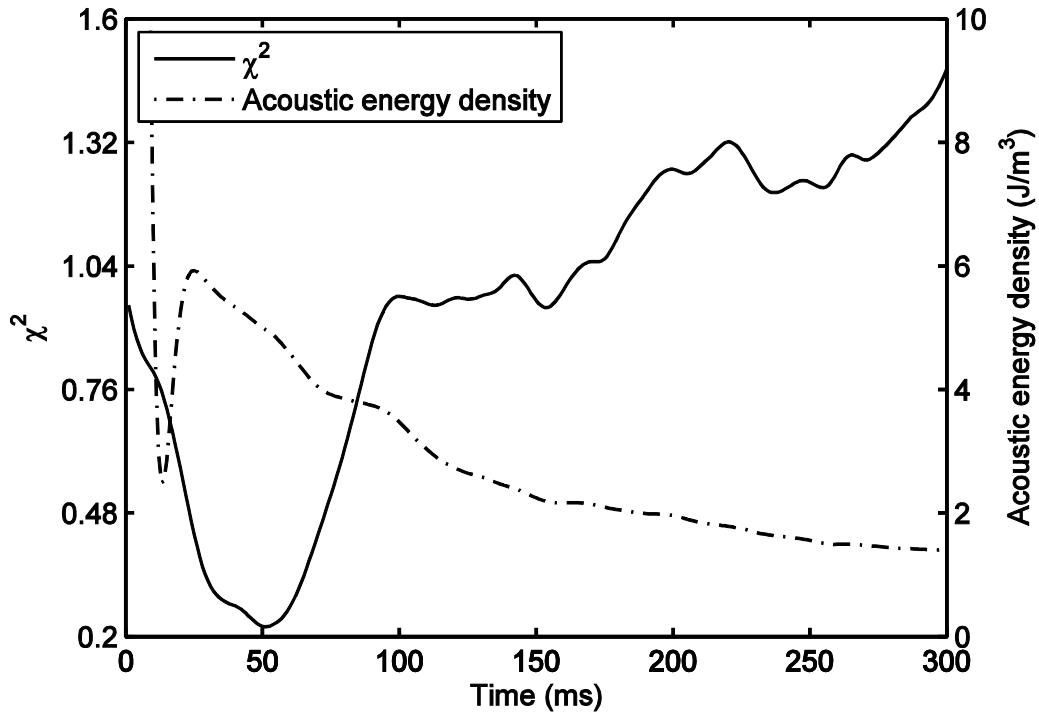
$$\chi^2 = \sum_{i=1}^n \frac{\left( \frac{I(x_i)}{I_{max}} - \frac{f_X(x_i)}{f_X\left(\frac{W}{2}\right)} \right)^2}{\frac{I(x_i)}{I_{max}}} \quad (6-8)$$

where  $n$  is the number of points in horizontal location.

For the initial time of densification ( $t < 20\text{ms}$ ), the RMS of residual (Figure 6-9 (a)) and the  $\chi^2$  (Figure 6-9 (b)) are high. This indicates that the PDF model is not well fitted to the intensity plot and the resulting acoustic energy density is not valid. The RMS of residual and the  $\chi^2$  reduce as the experimental fitting time increases and the corresponding acoustic energy density stabilizes. There is a

minima at experimental fitting time equal to 50 ms in both Figure 6-9 (a) and Figure 6-9 (b). This indicates that both normalized fitting residual and the  $\chi^2$  value are at a minimum and show a best fit of the PDF model to the experimental data. The RMS of residual remains below 6 % until the experimental fitting time reaches approximately 70 ms. In this region, the value of acoustic energy density ranges from 7 to 9 J/m<sup>3</sup>. As the experimental fitting time increases beyond 70 ms, the overlapping of particles effect on the fitting process increases and the corresponding RMS residual is increased. Based on this example of variation of RMS fitting residual and  $\chi^2$  the criterion for densification time is defined.





(b)

Figure 6-9: Fitting residual and the resulting acoustic energy density change as experimental fitting time varies (a) Variation of RMS of residual as the densification time changes, (b) Variation of  $\chi^2$  with respect to densification time

Beside the RMS of fitting residual and  $\chi^2$  fitting test which are used for determination of the densification time for fitting, skewness and kurtosis of the residual are used for investigation of selected densification time (Figure 6-10). Skewness is calculated based on equation (6-9) and measures the asymmetry of the probability distribution of a random variable about its mean value (N. L. Johnson, Kotz, & Balakrishnan, 1994)

$$\gamma_1 = \frac{\frac{1}{n} \sum_{i=1}^n (x_i - \bar{x})^3}{\left(\frac{1}{n} \sum_{i=1}^n (x_i - \bar{x})^2\right)^{\frac{3}{2}}} \quad (6-9)$$

in which  $x_i$  are the data-points,  $\bar{x}$  is the mean of the data-points and  $n$  is the number of data-points. Negative values of the skewness show that data are skewed left while positive values of the skewness show that data are skewed right.

Kurtosis of the residual of fitting which is calculated based on equation (6-10) is also shown in Figure 6-10. Kurtosis is a measure of peakedness of a probability distribution of a variable (N. L. Johnson et al., 1994)

$$\beta_2 = \frac{\frac{1}{n} \sum_{i=1}^n (x_i - \bar{x})^4}{\left(\frac{1}{n} \sum_{i=1}^n (x_i - \bar{x})^2\right)^2} \quad (6-10)$$

Skewness and kurtosis of the fitting performed on the dataset shown in Figure 6-8 is performed and shown in Figure 6-10. Both of skewness and the kurtosis of the fitting varies at the initial stages of the densification but are leveling as the densification time increases. The skewness of the fitting is close to zero showing the fittings are close to symmetric. The value of the skewness at densification time equal to 50 ms where the best fit is determined is -0.11. The time at which the skewness is zero is determined to be 49 ms. This indicates the fitting residual is not asymmetric and validates the selected 50 ms as the densification fitting time.

The shape of a probability distribution of residual of the fit is compared with the shape of a normal distribution by investigating the value of kurtosis. Based on Pearson's excess kurtosis (Joanes & Gill, 1998), the kurtosis of the normal probability distribution is 3. The value of the kurtosis at the densification time equal to 50 ms is 2.6. This indicates that the residual of the fit is close to

normal distribution. The densification time at which the kurtosis is equal to 3 is 35 ms. This is attributed to the fact that the number of data-points in this investigation (~70 points) is not enough for performing a fourth moment analysis of the residual of the fit.

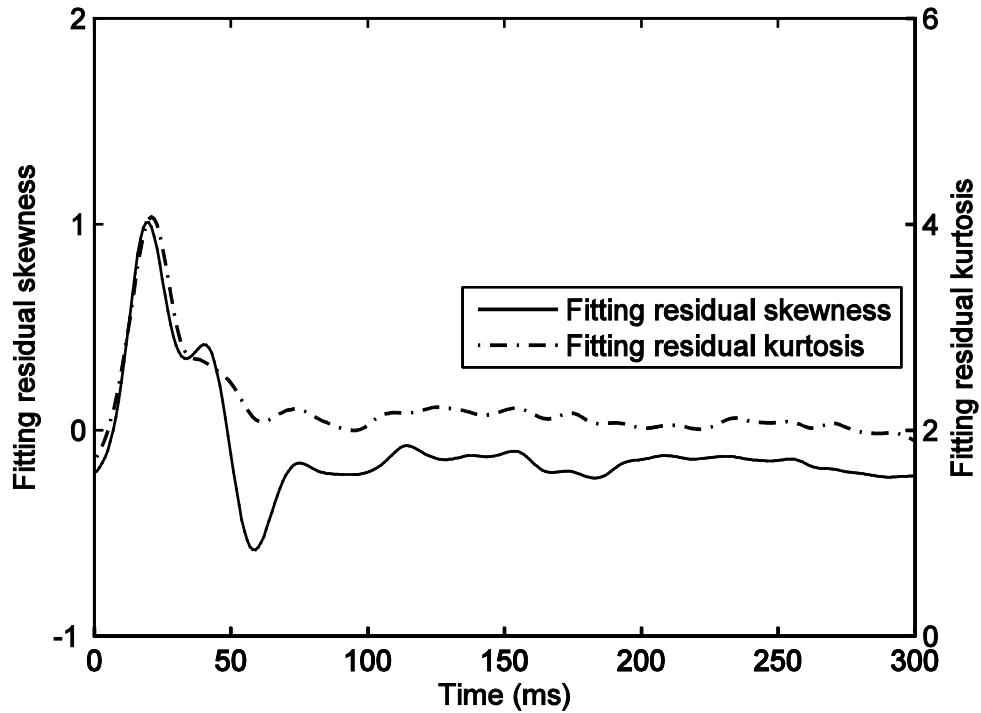


Figure 6-10: Fitting residual skewness and kurtosis variation as experimental fitting time varies

#### 6.4 Acoustic energy density envelope

The acoustic energy density is a function of the PZT excitation voltage used to generate the acoustic field. The PDF model is fitted to each wavelength within a data image for image in the time series. The best fit to the intensity envelopes which has the minimum residual for different densification time is selected and the corresponding fitted acoustic energy density is determined. This is then

averaged for all wavelengths in a data image. The variation of the calculated acoustic energy density with respect to the excitation voltage is shown in Figure 6-11. The experimented particles for this example set are PS-4. The range bars show the standard deviation of the calculated energy densities. This is the same data set used previously to determine the acoustic energy density using the PTV method in chapter 5. The achieved acoustic energy density values using the PTV method are also plotted in Figure 5-7. Based on fitting the data to equation 5-5,  $\gamma_{exp}$  is 0.17. Coefficient of determination for the fit ( $R^2$ ) is 0.97. This is in good agreement with the obtained value using PTV method which is 0.18 in Table 5-2.

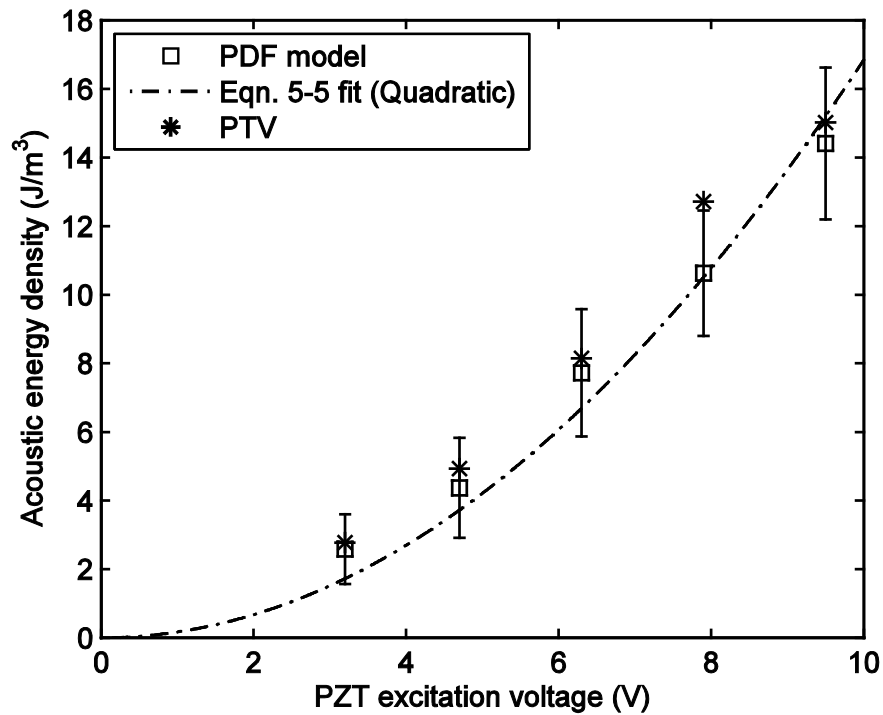


Figure 6-11. Acoustic energy density versus voltage, equation 5-5 fitted line comparison with PTV results shown in chapter 5; Coefficient of determination for the fit ( $R^2$ ) is 0.97.

The effect of glycerol weight concentration on obtained acoustic energy density using the PDF model is shown in Figure 6-12. The acoustic energy density envelope associated with different glycerol concentrations shows a similar trend invariant with the viscosity of the solution. This is in good agreement with the PTV method for determining the acoustic energy density as shown in Figure 5-7. The maximum difference between the values in Figure 6-12 is 16% at a PZT voltage of  $U_{pp}=4.7$  V.

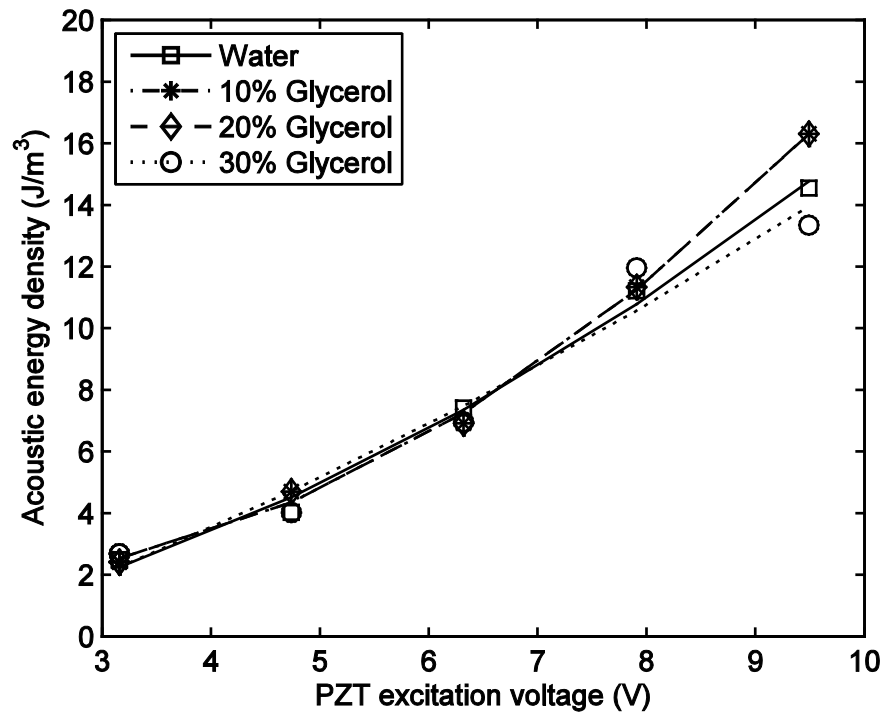


Figure 6-12. Effect of glycerol concentration on acoustic energy density obtained using the PDF model

## 6.5 Conclusion

This chapter introduces a method for characterizing an acoustic resonator to determine its acoustic energy density. This parameter is result of a complex interaction of the acoustic chamber and the PZT which converts electrical energy to acoustic energy. The PDF model determines the acoustic energy density of pressure acoustic force applied on a mixture of fluid and particles by modeling the light intensity envelope of particles as they densify. The resulting acoustic energy density is compared with the result obtained with the PTV method of chapter 5 in which individual particles are tracked. There is good agreement on ht e acoustic energy density between the PDF model and the PTV results. The PDF model approach has the advantage of characterization of an acoustic resonator at higher particles concentrations. Also, relative to the PTV method in which each particle is studied individually, the requirements of the imaging and optical systems can be significantly lowered as only the integrated light intensity needs to be measured.

## **CHAPTER 7: CONCLUSIONS AND FUTURE WORK**

### **7.1 Conclusions**

Acoustophoresis in macro-scale multi-wavelength acoustic resonators has been investigated. Experimental and analytical methods have been developed for understanding the physics of macro-scale multi-wavelength acoustic resonators. This physical understanding and analysis tools provide a useful aid in characterizing acoustic resonators. The characterization of a macro-scale multi-wavelength acoustic resonator which to date has not been reported in the literature will be useful in designing new high volume flow rate acoustic resonators and scaling up current acoustic resonators.

First, a custom PTV method was developed. It is utilized to investigate the primary acoustic force theory originally developed for a single sphere particle in an inviscid fluid to predict the force on a poly-dispersed sized distribution particle set. An image pre-processing approach is developed specifically for the

detection of particles clustering to PNs in the acoustic field. This clustering results in a complex time-dependent inhomogeneous motion. The independence of particles motion with respect to number of tracked particles and time shift between images is also investigated.

Second, the physics of acoustophoresis in macro-scale multi-wavelength acoustic resonators is investigated. Utilizing the developed PTV method and experimental setup, the influence of dampening and scattering of the acoustic wave in macro-scale multi-wavelength is studied. This is performed by varying glycerol concentration in water and changing the viscosity of suspension fluid. The PZT excitation voltage is also varied and the particles motion is captured using high speed camera. The acoustic energy density associated with the experimented acoustic resonator is also calculated. This crucial parameter is first theoretically estimated, neglecting the dampening and scattering of the acoustic wave, and then experimentally measured in acoustic micro-channels. Next the acoustic energy density determination in a macro-scale acoustic resonator, which is not reported in literature, is determined in this work. This helps to improve the understanding of physics of acoustophoresis in macro-scale acoustic resonators significantly.

Third, a separate approach for determination of acoustic energy density as the key parameter in primary acoustic force theory is developed. This is performed by modeling the probability density function (PDF) of location of

particles. In the macro-scale acoustic resonator this PDF model is compared with the intensity of captured images during particle densification and acoustic energy density is determined. This is performed for different glycerol-water solutions and PZT excitation voltages and the resulting acoustic energy density values are in good agreement with corresponding values of the previous PTV based method. The PDF method is a simple and computationally efficient alternative method compared to the PTV method for understanding acoustophoresis in macro-scale acoustic resonators via determination of acoustic energy density.

## **7.2 Future work**

This thesis has contributed to the developing of image processing tool and PDF model for improving the understanding of acoustophoresis in macro-scale multi-wavelength acoustic resonators. However, it has triggered new analytical and experimental ideas for better understanding of the phenomenon.

To reduce the effect of secondary acoustic force and hydrodynamic particle-particle interaction forces, the concentration of samples in the experiments were consistent at 0.05 %. However, one step in scaling up the acoustic system is to consider these effects by studying the acoustic force on particles at higher concentrations. It is proposed that in the acoustic resonators they can be characterized at higher concentrations using the PDF model. The

resulting acoustic energy densities can be compared with the values obtained in this work and hence the effect of concentration can be calibrated. Based on this calibration, the primary acoustic force can be corrected via defining an empirical relation to account for higher concentrations.

Another phenomenon which is not accounted in this work is acoustic streaming. This force which is an effect of absorption of acoustic energy by fluid is important for particles smaller than  $2\ \mu\text{m}$ . However, in a scaled up version of macro-scale multi-wavelength acoustic resonator particles smaller than  $2\ \mu\text{m}$  could be present and hence influenced by acoustic streaming. Using the same techniques developed in this thesis (PTV tool and PDF model) small particle could be experimentally examined using the current acoustic resonator. The resulting acoustic energy densities could be compared to experiments with larger particles and a correction term that takes into account the acoustic streaming force could be augmented to the existing model.

The imaging system used to capture the particles motion and hence characterizing the acoustic resonator can be further improved. One step is to measuring the flow field around the particles during their motion due to acoustic force. This can be performed by incorporating smaller particles which are much smaller than the main ones and follow the flow during the experiment. The second step is three-dimensional measurement of motion of particles which is needed to fully characterize an acoustic resonator. This could be significantly

enhance designing macro-scale multi-wavelength acoustic resonators by analyzing and understanding the full path of particles which are affected by acoustic force. When analyzing higher concentrated samples this could improve the PDF model by taking into account the three-dimensional motion and subsequent intensity envelope of particles on images.

## REFERENCES

- Adrian, R. J. (1991). Particle imaging techniques for experimental fluid mechanics. *Annual Review of Fluid Mechanics*, 23, 261–304.
- Adrian, R. J. (2005). Twenty years of particle image velocimetry. *Experiments in Fluids*, 39(2), 159–169. doi:10.1007/s00348-005-0991-7
- Andersen, L. M., Nysteen, A., & Settnes, M. (2009). *Forces acting on microparticles in acoustofluidic systems*. Bachelor Thesis, Technical University of Denmark.
- Augustsson, P., Barnkob, R., Wereley, S. T., Bruus, H., & Laurell, T. (2011). Automated and temperature-controlled micro-PIV measurements enabling long-term-stable microchannel acoustophoresis characterization. *Lab on a Chip*, 11(24), 4152–64. doi:10.1039/c1lc20637k
- Baek, S. J., & Lee, S. J. (1996). A new two-frame particle tracking algorithm using match probability. *Experiments in Fluids*, 22(1), 23–32. doi:10.1007/BF01893303
- Barnkob, R. (2012). *Physics of microparticle acoustophoresis Bridging theory and experiment Rune Barnkob*. PhD Thesis, Technical University of Denmark.

- Barnkob, R., Augustsson, P., Laurell, T., & Bruus, H. (2010). Measuring the local pressure amplitude in microchannel acoustophoresis. *Lab on a Chip*, *10*(5), 563–70. doi:10.1039/b920376a
- Barnkob, R., Augustsson, P., Laurell, T., & Bruus, H. (2012). Acoustic radiation- and streaming-induced microparticle velocities determined by microparticle image velocimetry in an ultrasound symmetry plane. *Physical Review E*, *86*(5), 056307 1–11. doi:10.1103/PhysRevE.86.056307
- Barnkob, R., Iranmanesh, I., Wiklund, M., & Bruus, H. (2012). Measuring acoustic energy density in microchannel acoustophoresis using a simple and rapid light-intensity method. *Lab on a Chip*, 2337–2344. doi:10.1039/c2lc40120g
- Bazou, D., Kuznetsova, L. A., & Coakley, W. T. (2005). Physical environment of 2-D animal cell aggregates formed in a short pathlength ultrasound standing wave trap. *Ultrasound in Medicine & Biology*, *31*(3), 423–30. doi:10.1016/j.ultrasmedbio.2004.12.007
- Benes, E., Groschl, M., Nowotny, H., Trampler, F., Keijzer, T., Bohm, H., ... Delouvroy, C. (2001). Ultrasonic separation of suspended particles. *2001 IEEE Ultrasonics Symposium Proceedings*, 649–659. doi:10.1109/ULTSYM.2001.991812
- Billingsley, P. (1995). *Probability and Measure* (3rd ed.). New York: Wiley.

- Blanchette, F., & Bush, J. W. M. (2005). Particle concentration evolution and sedimentation-induced instabilities in a stably stratified environment. *Physics of Fluids*, 17(7), 073302. doi:10.1063/1.1947987
- Blazejewski, R. (2012). Apparent viscosity and settling velocity of suspensions of rigid monosized spheres in Stokes flow. *International Journal of Multiphase Flow*, 39, 179–185. doi:10.1016/j.ijmultiphaseflow.2011.10.006
- Bruus, H. (2011a). Acoustofluidics 1: Governing equations in microfluidics. *Lab on a Chip*, 11(22), 3742–3751. doi:10.1039/c1lc20658c
- Bruus, H. (2011b). Acoustofluidics 2: Perturbation theory and ultrasound resonance modes. *Lab on a Chip*, 12(1), 20–28. doi:10.1039/c1lc20770a
- Bruus, H. (2012a). Acoustofluidics 10: Scaling laws in acoustophoresis. *Lab on a Chip*, 12(9), 1578–1586. doi:10.1039/c2lc21261g
- Bruus, H. (2012b). Acoustofluidics 7: The acoustic radiation force on small particles. *Lab on a Chip*, 12(6), 1014–21. doi:10.1039/c2lc21068a
- Bruus, H., Dual, J., Hawkes, J., Hill, M., Laurell, T., Nilsson, J., ... Wiklund, M. (2011). Forthcoming Lab on a Chip tutorial series on acoustofluidics: acoustofluidics-exploiting ultrasonic standing wave forces and acoustic streaming in microfluidic systems for cell and particle manipulation. *Lab on a Chip*, 11(21), 3579–80. doi:10.1039/c1lc90058g

- Castro, M. D. L. De, & Capote, F. P. (2007). *Analytical Applications of Ultrasound. Techniques and Instrumentation in Analytical Chemistry*. Elsevier Science.
- Chandrasekhar, S. (1943). Stochastic Problems in Physics and Astronomy. *Rev. Mod. Phys.*, 15(1), 1–89. doi:10.1103/RevModPhys.15.1
- Cheng, N. S. (2008). Formula for the Viscosity of a Glycerol–Water Mixture. *Industrial & Engineering Chemistry Research*, 47(9), 3285–3288.  
doi:10.1021/ie071349z
- Coakley, W. T. (1997). Ultrasonic separations in analytical biotechnology. *Trends in Biotechnology*, 15(12), 506–11. Retrieved from  
<http://www.ncbi.nlm.nih.gov/pubmed/9418305>
- Cousins, C. M., Holownia, P., Hawkes, J. J., Limaye, M. S., Price, C. P., Keay, P. J., & Coakley, W. T. (2000). Plasma preparation from whole blood using ultrasound. *Ultrasound in Medicine & Biology*, 26(5), 881–888.  
doi:[http://dx.doi.org/10.1016/S0301-5629\(00\)00212-X](http://dx.doi.org/10.1016/S0301-5629(00)00212-X)
- Cowen, E. A., Monismith, S. G., Cowen, E. A., & Monismith, S. G. (1997). A hybrid digital particle tracking velocimetry technique. *Experiments in Fluids*, 22(3), 199–211. doi:10.1007/s003480050038

- Danilov, S., & Mironov, M. (2000). Mean force on a small sphere in a sound field in a viscous fluid. *The Journal of the Acoustical Society of America*, *107*, 143. Retrieved from <http://link.aip.org/link/?jas/107/143>
- Dayton, P. A., Zhao, S., Bloch, S. H., Schumann, P., Penrose, K., Matsunaga, O., ... Ferrara, K. W. (2006). Application of ultrasound to selectively localize nanodroplets for targeted imaging and therapy. *Molecular Imaging*, *5*(3), 160–174.
- Demiris, G. (2004). Physical Principles of Medical Ultrasonics, 2nd edition [Book Review]. In *Physical Principles of Medical Ultrasonics, 2nd edition [Book Review]* (Vol. 23, pp. 81–82). doi:10.1109/MEMB.2004.1337957
- Dionne, J., McCarthy, B., Ross-Johnsrud, B., Masi, L., & Lipkens, B. (2013). Large volume flow rate acoustophoretic phase separator for oil water emulsion splitting. In *Proceedings of Meetings on Acoustics, ICA 2013* (Vol. 19). doi:10.1121/1.4799373
- Doh, D.-H., Kim, D.-H., Choi, S.-H., Hong, S.-D., Saga, T., & Kobayashi, T. (2000). Single-frame (two-field image) 3-D PTV for high speed flows. *Experiments in Fluids*, *29*(1), S085–S098. doi:10.1007/s003480070011

- Doinikov, A. A. (1994). Acoustic Radiation Pressure on a Rigid Sphere in a Viscous Fluid. *Proceedings of the Royal Society A: Mathematical, Physical and Engineering Sciences*, 447(1931), 447–466. doi:10.1098/rspa.1994.0150
- Doinikov, A. A. (1996). Acoustic radiation pressure exerted by a spherical wave on a bubble in a viscous liquid. *Wave Motion*, 24(3), 275–279.  
doi:10.1016/S0165-2125(96)00019-4
- Doinikov, A. A. (2001). Acoustic radiation interparticle forces in a compressible fluid. *Journal of Fluid Mechanics*, 444(1), 1–21.  
doi:10.1017/S0022112001005055
- Dron, O., Ratier, C., Hoyos, M., & Aider, J.-L. (2009). Parametric study of acoustic focusing of particles in a micro-channel in the perspective to improve micro-PIV measurements. *Microfluidics and Nanofluidics*, 7(6), 857–867.  
doi:10.1007/s10404-009-0477-7
- Dual, J., Hahn, P., Leibacher, I., Möller, D., & Schwarz, T. (2012). Acoustofluidics 6: Experimental characterization of ultrasonic particle manipulation devices. *Lab on a Chip*, 12(5), 852–62. doi:10.1039/c2lc21067c
- Dual, J., & Möller, D. (2012). Acoustofluidics 4: Piezoelectricity and application in the excitation of acoustic fields for ultrasonic particle manipulation. *Lab on a Chip*, 12(3), 506–14. doi:10.1039/c1lc20913b

- Dutra, B., Rust, M., Kennedy, D., Masi, L., & Lipkens, B. (2013). Macro-scale acoustophoretic separation of lipid particles from red blood cells. *ICA2013*, 19. doi:10.1121/1.4799371
- Evander, M., & Nilsson, J. (2012). Acoustofluidics 20: applications in acoustic trapping. *Lab on a Chip*, 12(22), 4667–76. doi:10.1039/c2lc40999b
- Feng, Y., Goree, J., & Liu, B. (2007). Accurate particle position measurement from images. *Review of Scientific Instruments*, 78(5), 053704. doi:10.1063/1.2735920
- Friend, J., & Yeo, L. (2011). Microscale acoustofluidics: Microfluidics driven via acoustics and ultrasonics. *Reviews of Modern Physics*, 83(2), 647–704. doi:10.1103/RevModPhys.83.647
- Glynne-Jones, P., Boltryk, R. J., Hill, M., Harris, N. R., & Baclet, P. (2009). Robust acoustic particle manipulation: A thin-reflector design for moving particles to a surface. *The Journal of the Acoustical Society of America*, 126(3), EL75–9. doi:10.1121/1.3186800
- Gorkov, L. P. (1962). On the forces acting on a small particle in an acoustic field in an ideal fluid. *Soviet Physics Doklady*, 6, 773–775.
- Grosch, M., Burger, W., Handl, B., Doblhoff-Dier, O., Gaida, T., & Schmatz, C. (1998). Ultrasonic separation of suspended particles - part III: application in

biotechnology. *Acustica*, 84(5), 815–822. Retrieved from  
<http://www.ingentaconnect.com/content/dav/aaua/1998/00000084/00000005/art00007>

Guezennec, Y. G., Brodkey, R. S., Trigui, N., & Kent, J. C. (1994). Algorithms for fully automated three-dimensional particle tracking velocimetry. *Experiments in Fluids*, 17(4), 209–219. doi:10.1007/BF00203039

Guezennec, Y. G., & Kiritsis, N. (1990). Statistical investigation of errors in particle image velocimetry. *Experiments in Fluids*, 10(2-3), 138–146.  
doi:10.1007/BF00215022

Gupta, S., & Feke, D. L. (1998). Filtration of particulate suspensions in acoustically driven porous media. *AIChE Journal*, 44(5), 1005–1014.  
doi:10.1002/aic.690440502

Haake, A., Neild, A., Kim, D.-H., Ihm, J.-E., Sun, Y., Dual, J., & Ju, B.-K. (2005). Manipulation of cells using an ultrasonic pressure field. *Ultrasound in Medicine & Biology*, 31(6), 857–64. doi:10.1016/j.ultrasmedbio.2005.03.004

Hafez, A., Khedr, M., & Gadallah, H. (2007). Wastewater treatment and water reuse of food processing industries. Part II: Techno-economic study of a membrane separation technique. *Desalination*, 214(1-3), 261–272.  
doi:10.1016/j.desal.2006.11.010

- Hagsäter, S. M., Lenshof, A., Skaftø-Pedersen, P., Kutter, J. P., Laurell, T., & Bruus, H. (2008). Acoustic resonances in straight micro channels: beyond the 1D-approximation. *Lab on a Chip*, 8(7), 1178–84. doi:10.1039/b801028e
- Hall, T. J., Bilgen, M., Insana, M. F., & Krouskop, T. A. (1997). Phantom materials for elastography. *IEEE Transactions on Ultrasonics, Ferroelectrics and Frequency Control*, 44(6), 1355–1365. doi:10.1109/58.656639
- Hancock, A. (2001). *Observation of Forces on Microparticles in Acoustic Standing Waves*. MSc Thesis, University of California Davis.
- Hancock, A., Insana, M. F., & Allen, J. S. (2003). Microparticle column geometry in acoustic stationary fields. *The Journal of the Acoustical Society of America*, 113(1), 652. doi:10.1121/1.1528171
- Hassan, Y. A., & Canaan, R. E. (1991). Full-field bubbly flow velocity measurements using a multiframe particle tracking technique. *Experiments in Fluids*, 12(1-2), 49–60. doi:10.1007/BF00226565
- Hawkes, J. J., & Coakley, W. T. (1996). A continuous flow ultrasonic cell-filtering method. *Enzyme and Microbial Technology*, 19(1), 57–62. doi:10.1016/0141-0229(95)00172-7

- Hawkes, J. J., & Coakley, W. T. (2001). Force field particle filter, combining ultrasound standing waves and laminar flow. *Sensors and Actuators B: Chemical*, 75(3), 213–222. doi:10.1016/S0925-4005(01)00553-6
- Hawkes, J. J., & Radel, S. (2013). Acoustofluidics 22: Multi-wavelength resonators, applications and considerations. *Lab on a Chip*, 13(4), 610–27. doi:10.1039/c2lc41206c
- Hertz, H. M. (1995). Standing-wave acoustic trap for nonintrusive positioning of microparticles. *Journal of Applied Physics*, 78(8), 4845. doi:10.1063/1.359770
- Ho, L., Braun, K., Fabris, R., Hoefel, D., Morran, J., Monis, P., & Drikas, M. (2012). Comparison of drinking water treatment process streams for optimal bacteriological water quality. *Water Research*, 46(12), 3934–3942. doi:10.1016/j.watres.2012.04.041
- Hu, J., Yang, J., Xu, J., & Du, J. (2006). Extraction of biologic particles by pumping effect in a pi-shaped ultrasonic actuator. *Ultrasonics*, 45(1-4), 15–21. doi:10.1016/j.ultras.2006.05.216
- Ishikawa, M., Murai, Y., Wada, A., Iguchi, M., Okamoto, K., & Yamamoto, F. (2000). A novel algorithm for particle tracking velocimetry using the velocity

gradient tensor. *Experiments in Fluids*, 29(6), 519–531.

doi:10.1007/s003480000120

Ivanov, Y., & Melzer, A. (2007). Particle positioning techniques for dusty plasma experiments. *The Review of Scientific Instruments*, 78(3), 033506 1–7.

doi:10.1063/1.2714050

Jackson, E. L., & Lu, H. (2013). Advances in microfluidic cell separation and manipulation. *Current Opinion in Chemical Engineering*, 2(4), 398–404.

doi:10.1016/j.coche.2013.10.001

Jeong, J. S., Lee, J. W., Lee, C. Y., Teh, S. Y., Lee, A., & Shung, K. K. (2011). Particle manipulation in a microfluidic channel using acoustic trap. *Biomedical*

*Microdevices*, 13(4), 779–88. doi:10.1007/s10544-011-9548-0

Joanes, D. N., & Gill, C. A. (1998). Comparing measures of sample skewness and kurtosis. *Journal of the Royal Statistical Society (Series D): The Statistician*, 47(1), 183–189.

Johnson, D. A., & Feke, D. L. (1995). Methodology for fractionating suspended particles using ultrasonic standing wave and divided flow fields. *Separations Technology*, 5(4), 251–258. Retrieved from

<http://www.sciencedirect.com/science/article/pii/0956961895001301>

- Johnson, N. L., Kotz, S., & Balakrishnan, N. (1994). *Continuous univariate distributions* (2nd ed.).
- Jönsson, H., Holm, C., Nilsson, A., Petersson, F., Johnsson, P., & Laurell, T. (2004). Particle separation using ultrasound can radically reduce embolic load to brain after cardiac surgery. *The Annals of Thoracic Surgery*, *78*(5), 1572–7. doi:10.1016/j.athoracsur.2004.04.071
- Jönsson, H., Nilsson, A., Petersson, F., Allers, M., & Laurell, T. (2005). Particle separation using ultrasound can be used with human shed mediastinal blood. *Perfusion*, *20*(1), 39–43. doi:10.1191/0267659105pf782oa
- Ju, Y. R., Geng, Z. X., Zhang, L. Q., Wang, W., & Li, Z. H. (2011). High-efficiency blood separation utilizing spiral filtration microchannel with gradually varied width. In *Solid-State Sensors, Actuators and Microsystems Conference (TRANSDUCERS)* (pp. 298–301). doi:10.1109/TRANSDUCERS.2011.5969447
- Juliano, P., Kutter, A., Cheng, L. J., Swiergon, P., Mawson, R., & Augustin, M. A. (2011). Enhanced creaming of milk fat globules in milk emulsions by the application of ultrasound and detection by means of optical methods. *Ultrasonics Sonochemistry*, *18*(5), 963–73. doi:10.1016/j.ultsonch.2011.03.003

- Kanagasabapathi, T. T., & Backhouse, C. J. (2004). Dielectrophoresis (DEP) of Cells and Microparticle in PDMS Microfluidic Channels. In *Technical proceedings of the 2004 nsti nanotechnology conference and trade show* (Vol. 1, pp. 81–84).
- King, L. V. (1934). On the acoustic radiation pressure on spheres. *Proceedings of the Royal Society of London. Series A, Mathematical and Physical Sciences (1934-1990)*, 147(861), 212–240. doi:10.1098/rspa.1934.0215
- Kundt, A., & Lehmann, O. (1874). Longitudinal vibrations and acoustic figures in cylindrical columns of liquids. *Annual Physics Chemistry*, 153, 1–11.
- Kurada, S., Rankin, G. W., & Sridhar, K. (1997). A new particle image velocimetry technique for three-dimensional flows. *Optics and Lasers in Engineering*, 28(5), 343–376. doi:http://dx.doi.org/10.1016/S0143-8166(97)00025-0
- Labonté, G. (1999). A new neural network for particle-tracking velocimetry. *Experiments in Fluids*, 26(4), 340–346. doi:10.1007/s003480050297
- Lecuona, A., Sosa, P. A., Rodríguez, P. A., & Zequeira, R. I. (2000). Volumetric characterization of dispersed two-phase flows by digital image analysis. *Measurement Science and Technology*, 11(8), 1152. Retrieved from <http://stacks.iop.org/0957-0233/11/i=8/a=309>

- Lee, D.-R. (2013). Flow analysis of acoustic streaming pattern produced by ultrasonic transducer using stereoscopic PIV. *The European Physical Journal Applied Physics*, 61(1), 11101. doi:10.1051/epjap/2012110265
- Lenshof, A., Evander, M., Laurell, T., & Nilsson, J. (2012). Acoustofluidics 5: Building microfluidic acoustic resonators. *Lab on a Chip*, 12(4), 684–95. doi:10.1039/c1lc20996e
- Lenshof, A., & Laurell, T. (2010). Continuous separation of cells and particles in microfluidic systems. *Chemical Society Reviews*, 39(3), 1203–17. doi:10.1039/b915999c
- Lenshof, A., Magnusson, C., & Laurell, T. (2012). Acoustofluidics 8: Applications of acoustophoresis in continuous flow microsystems. *Lab on a Chip*, 12(10), 1210–1223. doi:10.1039/c2lc21256k
- Lim, J., Yeap, S. P., & Low, S. C. (2014). Challenges associated to magnetic separation of nanomaterials at low field gradient. *Separation and Purification Technology*, 123, 171–174. doi:10.1016/j.seppur.2013.12.038
- Lipkens, B., Dionne, J., Costolo, M., & Rietman, E. (2008). Frequency sweeping and fluid flow effects on particle trajectories in ultrasonic standing waves. *The Journal of the Acoustical Society of America*, 123(5), 3406. doi:10.1121/1.2934116

- Lipkens, B., Dionne, J., Trask, A., Szczur, B., Stevens, A., & Rietman, E. (2010). Separation of micron-sized particles in macro-scale cavities by ultrasonic standing waves. *Physics Procedia*, 3(1), 263–268.  
doi:10.1016/j.phpro.2010.01.035
- Liu, C., & Tao, L. (2007). Two-dimensional digital particle tracking velocimetry algorithm based on the image of particle trace. *Journal of Coastal Research*, (50), 415–419.
- Liu, Y., & Hu, J. (2009). Trapping of particles by the leakage of a standing wave ultrasonic field. *Journal of Applied Physics*, 106(3), 034903.  
doi:10.1063/1.3169517
- Lum, A. F. H., Borden, M. A., Dayton, P. A., Kruse, D. E., Simon, S. I., & Ferrara, K. W. (2006). Ultrasound radiation force enables targeted deposition of model drug carriers loaded on microbubbles. *Journal of Controlled Release*, 111(1-2), 128–134. doi:10.1016/j.jconrel.2005.11.006
- Maas, H. G., Gruen, A., & Papantoniou, D. (1993). Particle tracking velocimetry in three-dimensional flows. *Experiments in Fluids*, 15(2), 133–146.  
doi:10.1007/BF00190953

- Manneberg, O., Vanherberghen, B., Onfelt, B., & Wiklund, M. (2009). Flow-free transport of cells in microchannels by frequency-modulated ultrasound. *Lab on a Chip*, *9*(6), 833–7. doi:10.1039/b816675g
- Mikkelsen, C., & Bruus, H. (2005). Microfluidic capturing-dynamics of paramagnetic bead suspensions. *Lab on a Chip*, *5*(11), 1293–1297. doi:10.1039/B507104F
- Mitri, F. G., & Fella, Z. E. A. (2006). Amplitude-modulated acoustic radiation force experienced by elastic and viscoelastic spherical shells in progressive waves. *Ultrasonics*, *44*(3), 287–96. doi:10.1016/j.ultras.2006.03.001
- Möller, D., Degen, N., & Dual, J. (2013). Schlieren visualization of ultrasonic standing waves in mm-sized chambers for ultrasonic particle manipulation. *Journal of Nanobiotechnology*, *11*, 21. doi:10.1186/1477-3155-11-21
- Moroni, M., Cushman, J. H., & Cenedese, A. (2003). A 3D-PTV two-projection study of pre-asymptotic dispersion in porous media which are heterogeneous on the bench scale. *International Journal of Engineering Science*, *41*(3–5), 337–370. doi:http://dx.doi.org/10.1016/S0020-7225(02)00237-9
- Nabavi, M., Siddiqui, K., & Dargahi, J. (2008). Measurement of the acoustic velocity field of nonlinear standing waves using the synchronized PIV

technique. *Experimental Thermal and Fluid Science*, 33(1), 123–131.

doi:10.1016/j.expthermflusci.2008.07.013

Nakamura, M., Zborowski, M., Lasky, L. C., Margel, S., & Chalmers, J. J. (2001).

Theoretical and experimental analysis of the accuracy and reproducibility of cell tracking velocimetry. *Experiments in Fluids*, 30(4), 371–380.

doi:10.1007/s003480000211

Nightingale, K. (2003). Shear-wave generation using acoustic radiation force: in

vivo and ex vivo results. *Ultrasound in Medicine & Biology*, 29(12), 1715–

1723. doi:10.1016/j.ultrasmedbio.2003.08.008

Nii, S., Kikumoto, S., & Tokuyama, H. (2009). Quantitative approach to ultrasonic

emulsion separation. *Ultrasonics Sonochemistry*, 16(1), 145–9.

doi:10.1016/j.ultsonch.2008.07.005

Nilsson, A., Petersson, F., Jönsson, H., & Laurell, T. (2004). Acoustic control of

suspended particles in micro fluidic chips. *Lab on a Chip*, 4(2), 131–135.

doi:10.1039/b313493h

Nilsson, H., Wiklund, M., Johansson, T., Hertz, H. M., & Nilsson, S. (2001).

Microparticles for selective protein determination in capillary

electrophoresis. *Electrophoresis*, 22(12), 2384–90. doi:10.1002/1522-

2683(200107)22:12<2384::AID-ELPS2384>3.0.CO;2-W

- Nilsson, J., Evander, M., Hammarström, B., & Laurell, T. (2009). Review of cell and particle trapping in microfluidic systems. *Analytica Chimica Acta*, *649*(2), 141–57. doi:10.1016/j.aca.2009.07.017
- Nobach, H., & Honkanen, M. (2005). Two-dimensional Gaussian regression for sub-pixel displacement estimation in particle image velocimetry or particle position estimation in particle tracking velocimetry. *Experiments in Fluids*, *38*(4), 511–515. doi:10.1007/s00348-005-0942-3
- Ohtake, N., Nakai, Y., Yamamoto, M., Sakakibara, I., Takeda, S., Amagaya, S., & Aburada, M. (2004). Separation and isolation methods for analysis of the active principles of Sho-saiko-to (SST) oriental medicine. *Journal of Chromatography. B, Analytical Technologies in the Biomedical and Life Sciences*, *812*(1-2), 135–48. doi:10.1016/j.jchromb.2004.06.051
- Önal, G., Ozer, M., & Arslan, F. (2003). Sedimentation of clay in ultrasonic medium. *Minerals Engineering*, *16*(2), 129–134. doi:10.1016/S0892-6875(02)00309-6
- Ortiz-Villafuerte, J., & Hassan, Y. A. (2005). Investigation of Microbubble Boundary Layer Using Particle Tracking Velocimetry. *Journal of Fluids Engineering*, *128*(3), 507–519. doi:10.1115/1.2174062

Otsu, N. (1979). A Threshold Selection Method from Gray-Level Histograms. *IEEE Transactions on Systems, Man, and Cybernetics*, 9(1), 62–66.

doi:10.1109/TSMC.1979.4310076

Ouellette, N. T., Xu, H., & Bodenschatz, E. (2006). A quantitative study of three-dimensional Lagrangian particle tracking algorithms. *Experiments in Fluids*, 40(2), 301–313. doi:10.1007/s00348-005-0068-7

Pavlidis, T. (1982). *Algorithms for Graphics and Image Processing*. Computer Science Press.

Peterson, S., Perkins, G., & Baker, C. (1986). Development of an Ultrasonic Blood Cell Separator. In *IEEE Proceedings of the Eighth Annual Conference of Engineering in Medicine & Biology Society* (pp. 154–156).

Petersson, F., Nilsson, A., Holm, C., Jonsson, H., & Laurell, T. (2004). Separation of lipids from blood utilizing ultrasonic standing waves in microfluidic channels. *The Analyst*, 129(10), 938–43. doi:10.1039/b409139f

Petersson, F., Nilsson, A., Holm, C., Jonsson, H., & Laurell, T. (2005). Continuous separation of lipid particles from erythrocytes by means of laminar flow and acoustic standing wave forces. *Lab on a Chip*, 5(1), 20–2.

doi:10.1039/b405748c

Racca, R. G., & Dewey, J. M. (1988). A method for automatic particle tracking in a three-dimensional flow field. *Experiments in Fluids*, 6(1), 25–32.

doi:10.1007/BF00226131

Radel, S., Gherardini, L., McLoughlin, A. J., Doblhoff-Dier, O., & Benes, E. (2000).

Breakdown of immobilisation/separation and morphology changes of yeast suspended in water-rich ethanol mixtures exposed to ultrasonic plane standing waves. *Bioseparation*, 9(6), 369–77. Retrieved from

<http://www.ncbi.nlm.nih.gov/pubmed/11518240>

Radel, S., McLoughlin, A. J., Groschl, M., & Benes, E. (2002). Ultrasonically

Enhanced Settling: Influence of process parameters on separation efficiency of yeast cells at 2.2 MHz. In *Forum Acusticum* (pp. 1–6).

Raffel, M., Willert, C. ., Wereley, S. ., & Kompenhans, J. (2007). *Particle Image*

*Velocimetry: A Practical Guide*.

Rayleigh, J. W. S. (1871). On the theory of resonance. *Philosophical Transactions of the Royal Society*, 161, 77–181.

Rayleigh, J. W. S. (1884). On the circulation of air observed in Kundt's tubes, and on some allied acoustical problems. *Philosophical Transactions of the Royal Society of London*, 175, 1–21.

- Riera, E., Gallego-Juárez, J. A., & Mason, T. J. (2006). Airborne ultrasound for the precipitation of smokes and powders and the destruction of foams. *Ultrasonics Sonochemistry*, *13*(2), 107–116.  
doi:<http://dx.doi.org/10.1016/j.ultsonch.2005.04.001>
- Rogers, S. S., Waigh, T. A., Zhao, X., & Lu, J. R. (2007). Precise particle tracking against a complicated background: polynomial fitting with Gaussian weight. *Physical Biology*, *4*(3), 220. doi:[10.1088/1478-3975/4/3/008](https://doi.org/10.1088/1478-3975/4/3/008)
- Ruhnau, P., Guetter, C., Putze, T., & Schnörr, C. (2005). A variational approach for particle tracking velocimetry. *Measurement Science and Technology*, *16*(7), 1449. doi:[10.1088/0957-0233/16/7/007](https://doi.org/10.1088/0957-0233/16/7/007)
- Sadikova, D. G., & Pashovkin, T. N. (2013). Cell Concentration and Separation in the Field of a Standing Ultrasonic Wave for Medicine and Biotechnology. *Journal of Biophysics*, *3*(February), 70–75.
- Sarvazyan, A. (2010). Diversity of biomedical applications of acoustic radiation force. *Ultrasonics*, *50*(2), 230–4. doi:[10.1016/j.ultras.2009.10.001](https://doi.org/10.1016/j.ultras.2009.10.001)
- Seeger, A., Affeld, K., Goubergrits, L., Kertzsch, U., & Wellenhofer, E. (2001). X-ray-based assessment of the three-dimensional velocity of the liquid phase in a bubble column. *Experiments in Fluids*, *31*(2), 193–201.  
doi:[10.1007/s003480100273](https://doi.org/10.1007/s003480100273)

- Settnes, M., & Bruus, H. (2012). Forces acting on a small particle in an acoustical field in a viscous fluid. *Physical Review E*, *85*(1), 016327 1–12.  
doi:10.1103/PhysRevE.85.016327
- Spengler, J. F., Jekel, M., Christensen, K. T., Adrian, R. J., Hawkes, J. J., & Coakley, W. T. (2001). Observation of yeast cell movement and aggregation in a small-scale MHz-ultrasonic standing wave field. *Bioseparation*, *9*(6), 329–341.
- Spinewine, B., Capart, H., Larcher, M., & Zech, Y. (2003). Three-dimensional Voronoï imaging methods for the measurement of near-wall particulate flows. *Experiments in Fluids*, *34*(2), 227–241. doi:10.1007/s00348-002-0550-4
- Stüer, H., Maas, H.-G., Virant, M., & Becker, J. (1999). A volumetric 3D measurement tool for velocity field diagnostics in microgravity experiments. *Measurement Science and Technology*, *10*(10), 904–913. doi:10.1088/0957-0233/10/10/311
- Taylor, J. R. (1982). *An Introduction to Error Analysis: The Study of Uncertainties in Physical Measurements*. University Science Books.
- Ten Cate, a., Nieuwstad, C. H., Derksen, J. J., & Van den Akker, H. E. a. (2002). Particle imaging velocimetry experiments and lattice-Boltzmann simulations

on a single sphere settling under gravity. *Physics of Fluids*, 14(11), 4012.

doi:10.1063/1.1512918

Tolt, T. L., & Feke, D. L. (1993). Separation of dispersed phases from liquids in acoustically driven chambers. *Chemical Engineering Science*, 48(3), 527–540.

doi:10.1016/0009-2509(93)80307-C

Trampler, F., Sonderhoff, S. A., Pui, P. W. S., Kilburn, D. G., & Piret, J. M. (1994).

Acoustic Cell Filter for High Density Perfusion Culture of Hybridoma Cells.

*Nat Biotech*, 12(3), 281–284. Retrieved from

<http://dx.doi.org/10.1038/nbt0394-281>

Van den Boomgaard, R., & van Balen, R. (1992). Methods for fast morphological image transforms using bitmapped binary images. *CVGIP: Graphical Models and Image Processing*, 54(3), 252–258. doi:[http://dx.doi.org/10.1016/1049-](http://dx.doi.org/10.1016/1049-9652(92)90055-3)

[9652\(92\)90055-3](http://dx.doi.org/10.1016/1049-9652(92)90055-3)

Whitworth, G. (1992). Particle column formation in a stationary ultrasonic field.

*The Journal of the Acoustical Society of America*, 91(1), 79.

doi:10.1121/1.402622

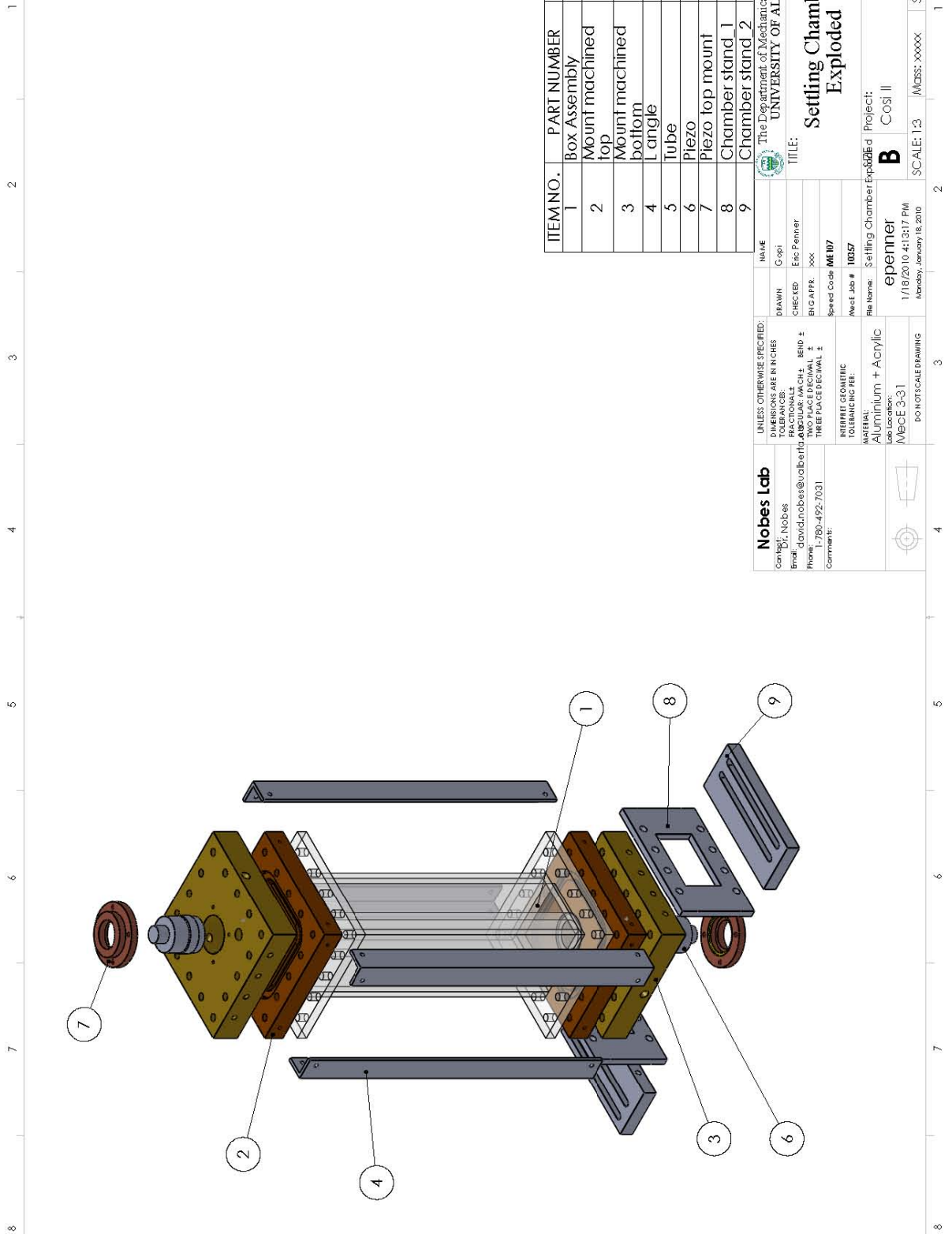
Whitworth, G., Grundy, M. A., & Coakley, W. T. (1991). Transport and harvesting of suspended particles using modulated ultrasound. *Ultrasonics*, 29, 439–

444.

- Wiklund, M. (2012). Acoustofluidics 12: Biocompatibility and cell viability in microfluidic acoustic resonators. *Lab on a Chip*, *12*(11), 2018–2028.  
doi:10.1039/c2lc40201g
- Woodside, S. M., Bowen, B. D., & Piret, J. M. (1997). Measurement of ultrasonic forces for particle–liquid separations. *AIChE Journal*, *43*(7), 1727–1736.  
doi:10.1002/aic.690430710
- Woodside, S. M., Piret, J. M., Gröschl, M., Benes, E., & Bowen, B. D. (1998). Acoustic force distribution in resonators for ultrasonic particle separation. *AIChE Journal*, *44*(9), 1976–1984. doi:10.1002/aic.690440905
- Yasuda, K. (1999). Measurement of Microscopic Spatial Distribution of Acoustic Radiation Force Using Microspheres and Electrostatic Force. *Japanese Journal of Applied Physics*, *38*(5), 3316–3319.
- Yasuda, K., Umemura, S., & Kazuo, T. (1996). Particle separation using acoustic radiation force and electrostatic force. *Journal of Acoustic Society of America*, *99*(4), 1965–1970.
- Yosioka, K., & Kawasima, Y. (1955). Acoustic radiation pressure on a compressible sphere. *Acustica*, *5*(3), 167–173. Retrieved from <http://www.mendeley.com/research/acoustic-radiation-pressure-compressible-sphere-1/>

Zitoun, K. B., Sastry, S. K., & Guezennec, Y. (2001). Investigation of three dimensional interstitial velocity, solids motion, and orientation in solid–liquid flow using particle tracking velocimetry. *International Journal of Multiphase Flow*, 27(8), 1397–1414. doi:[http://dx.doi.org/10.1016/S0301-9322\(01\)00011-8](http://dx.doi.org/10.1016/S0301-9322(01)00011-8)

## **APPENDIX A. STATIC CHAMBER DRAWINGS**



ITEM NO.	PART NUMBER	QTY.
1	Box Assembly	1
2	Mount machined top	2
3	Mount machined bottom	2
4	L angle	4
5	Tube	1
6	Piezo	2
7	Piezo top mount	2
8	Chamber stand 1	2
9	Chamber stand 2	2

**Nobes Lab**  
 Contact: Nobes  
 Email: david.nobes@ualberta.ca  
 Phone: 1-780-492-7031  
 Comments:

UNLESS OTHERWISE SPECIFIED:  
 DIMENSIONS ARE IN INCHES  
 TOLERANCES:  
 FRACTIONS: ± 1/16"  
 DECIMALS: ± 0.005"  
 HOLE DIA: ± 0.002"  
 TWO PLACE DECIMAL: ± 0.01"  
 THREE PLACE DECIMAL: ± 0.001"  
 HOLE DIA: ± 0.002"  
 MATERIAL: ALUMINUM + ACRYLIC  
 Lab Location: MECE 3-31  
 DO NOT SCALE DRAWING

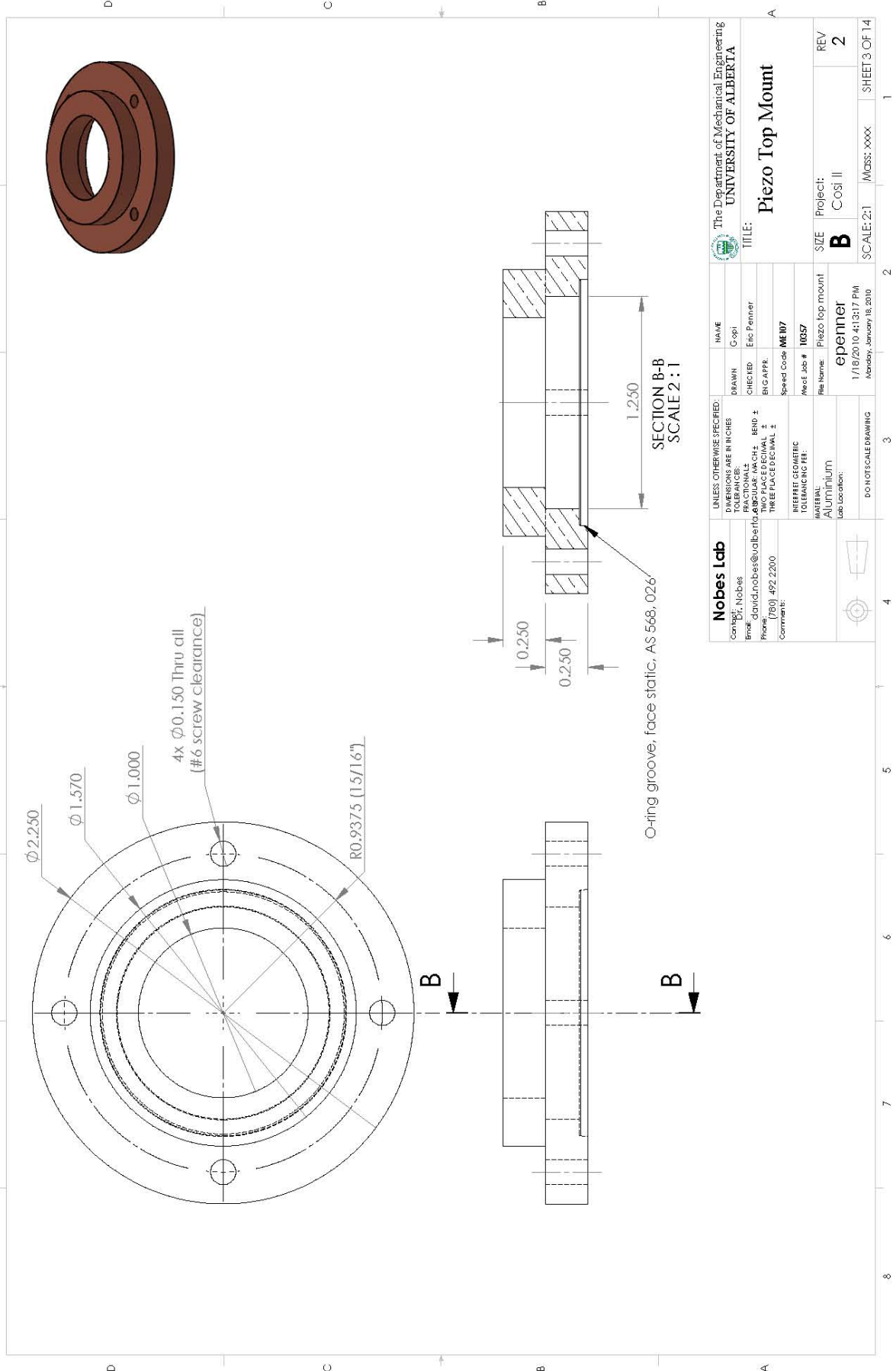
DRAWN: Gopi  
 CHECKED: Eric Penner  
 ENCL APPR: xxx  
 Speed Code: ME B07  
 West Job #: 110357

TITLE:  
**Settling Chamber Exploded**

Project: Settling Chamber Exploded  
 Cost: I  
 epenner  
 1/18/2010 4:13:17 PM  
 Monday, January 18, 2010

SCALE: 1:3 (MISC: XXXX)  
 SHEET 2 OF 14

REV	REV
2	2



<b>Nobes Lab</b>		UNLESS OTHERWISE SPECIFIED:		NAME	
Contact: Dr. Nobes		DIMENSIONS ARE IN INCHES		C:opi	
Email: david.nobes@ualberta.ca		FRACTIONS:		DRAWN	
Phone: (780) 492-2200		TWO PLACE DECIMAL 1/8, 3/16, 1/4, 3/8, 1/2, 5/8, 3/4, 7/8		CHECKED: Eric Penner	
Comment:		THREE PLACE DECIMAL 1/16, 1/8, 3/16, 1/4, 3/8, 1/2, 5/8, 3/4, 7/8		BIG APPR:	
		INTERFIT GEOMETRIC TOLERANCING PER:		Speed Code: ME07	
		MATERIAL: Aluminium		Mach. Job #: 110357	
		Lab Location:		File Name: Piezo top mount	
		DO NOT SCALE DRAWING		epenner	
				1/18/2010 4:13:17 PM	
				Monday, January 18, 2010	
				SIZE: B	
				Project: Cost II	
				REV: 2	
				SCALE: 2:1	
				MIDSS: XXXX	
				SHEET 3 OF 14	

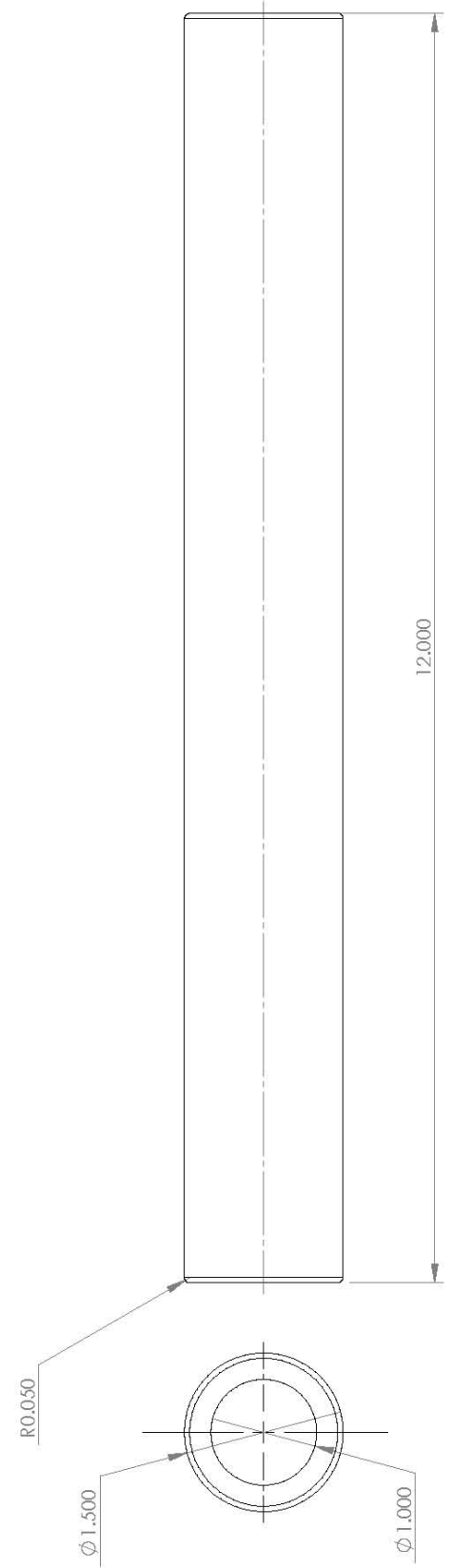
The Department of Mechanical Engineering  
UNIVERSITY OF ALBERTA

**Piezo Top Mount**

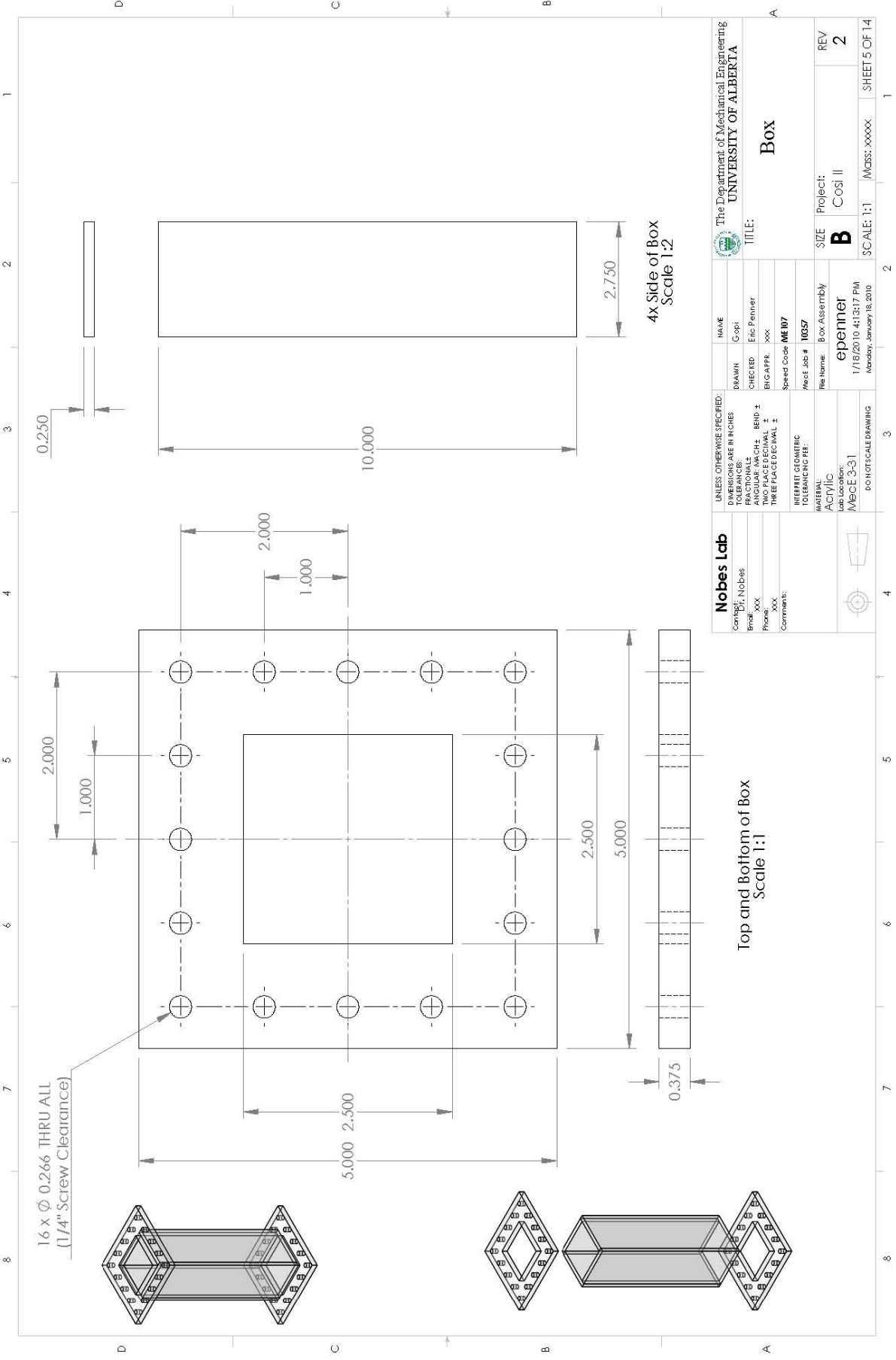
TITLE:

1 2 3 4 5 6 7 8

D C B A



<b>Nobes Lab</b>		UNLESS OTHERWISE SPECIFIED:		NAME		The Department of Mechanical Engineering UNIVERSITY OF ALBERTA	
Contact: Dr. Nobes		DIMENSIONS ARE IN INCHES		DRAWN: C-epi		TITLE: Tube	
Email: david.nobes@ualberta.ca		FRACTIONS:		CHECKED:		SIZE: Project: REV	
Phone: (780) 492-7031		TWO PLACE DECIMAL ±		BING APPR:		B Cost II 2	
Comment:		THREE PLACE DECIMAL ±		SPEED CODE: ME107		SCALE: 1:1 M/DSS: XXXX SHEET 4 OF 14	
		TOLERANCING PER:		MATERIAL: Acrylic			
		INTERFERING GEOMETRIC		Lab Location: 1/18/2010 4:13:17 PM			
		TOLERANCING PER:		MATERIAL: Tube			
		TOLERANCING PER:		MATERIAL: epenner			
		TOLERANCING PER:		MATERIAL: 1/18/2010 4:13:17 PM			
		TOLERANCING PER:		MATERIAL: Monday, January 18, 2010			
		TOLERANCING PER:		MATERIAL: DO NOT SCALE DRAWING			

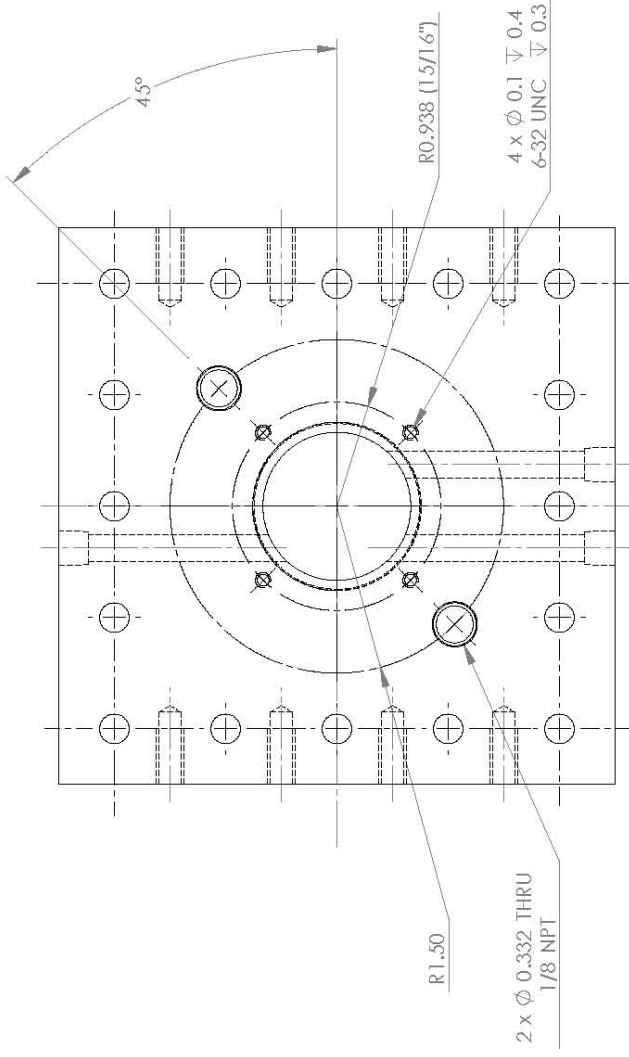
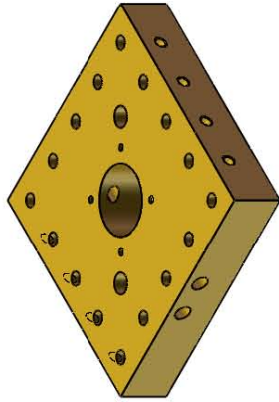


<b>Nobes Lab</b> Contact: Dr. Nobes Email: xxx Phone: xxx Comments:		UNLESS OTHERWISE SPECIFIED: DIMENSIONS ARE IN INCHES DECIMALS: 1/16 FRACTIONS: 1/8 ANGULAR: MACH. TWO PLACE DECIMAL THREE PLACE DECIMAL		NAME: C-epi DRAWN: Eric Penner CHECKED: xxx BIG APPR: xxx Speed Code: ME07 Mecc Job #: 10057		The Department of Mechanical Engineering <b>UNIVERSITY OF ALBERTA</b> TITLE: <b>Box</b>	
MATERIAL: Acrylic Lab Location: MECE 3-31		PROJECT: Box Assembly Designer: <b>epenner</b> Date: 1/18/2010 4:13:17 PM Author: January 18, 2010		SIZE: <b>B</b> Project: <b>Cost II</b> REV: <b>2</b>		SCALE: 1:1 / MIDSS: XXXXX / SHEET 5 OF 14	

DO NOT SCALE DRAWING			
Scale 1:1 <b>Top and Bottom of Box</b>		Scale 1:2 <b>4x Side of Box</b>	



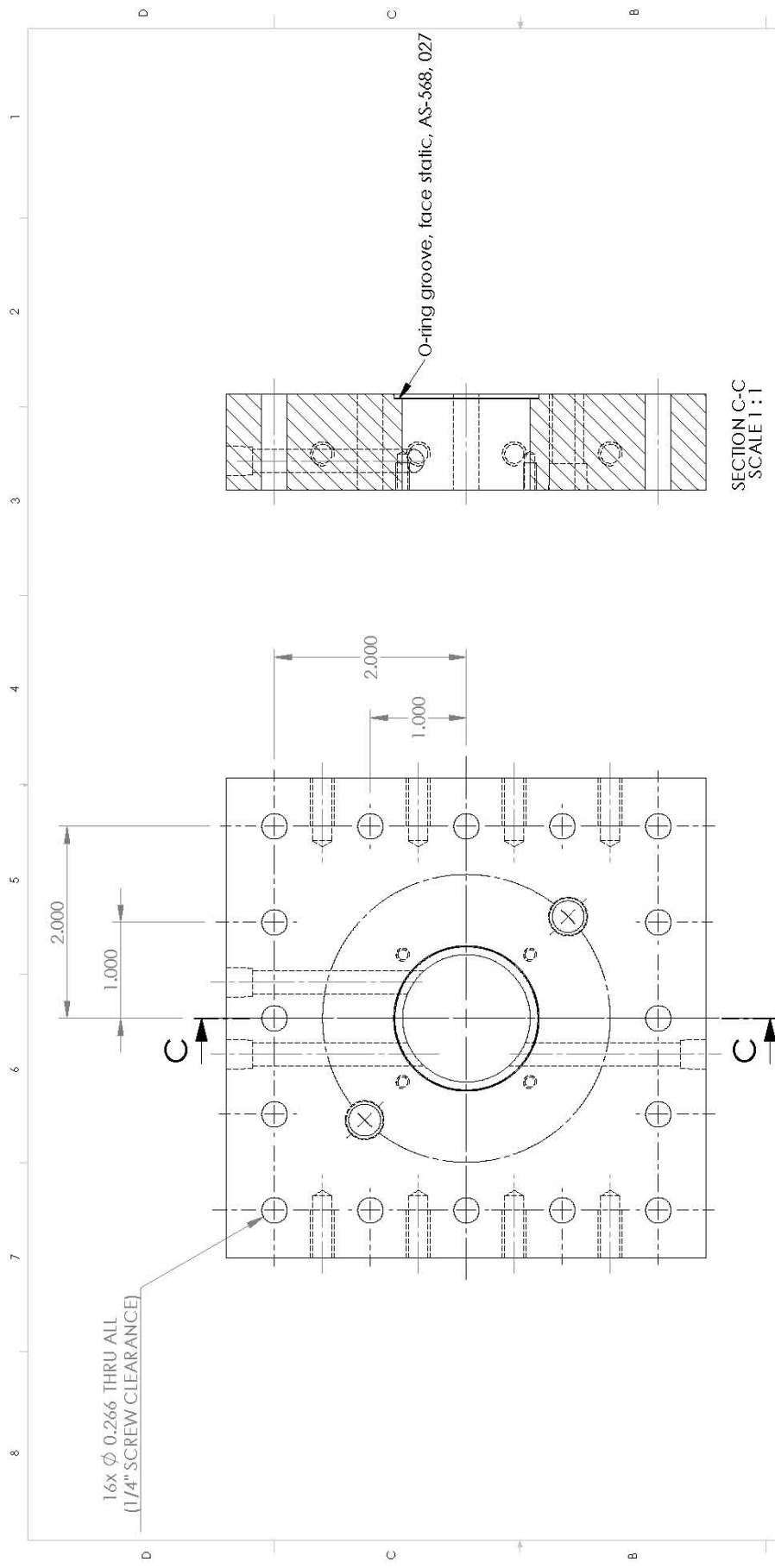
1 2 3 4 5 6 7 8



No Hidden Line

Top View

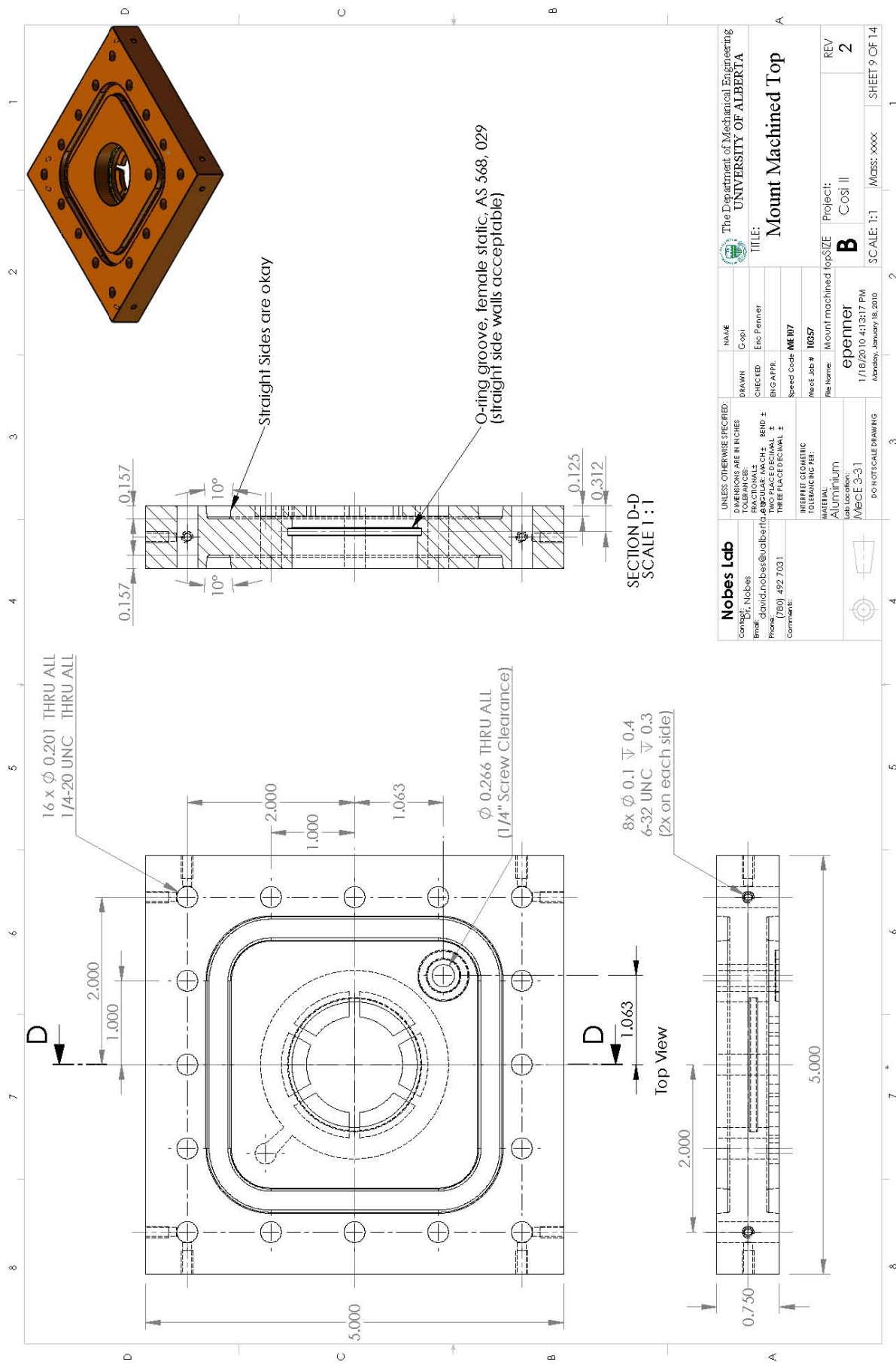
<b>Nobes Lab</b>		NAME		The Department of Mechanical Engineering UNIVERSITY OF ALBERTA	
Cont: Dr. Nobes	Drawn: C-epi	CHECKED: Eric Penner		TITLE: Mount Machined Bottom	
Email: david.nobes@ualberta.ca	MATERIAL: Aluminium		Project: epenner		REV 2
Phone: 780-492-7031	Lab Location: MECE 3-31		1/18/2010 4:13:17 PM		Cost II
Comment:	MATERIAL: Aluminium		1/18/2010 4:13:17 PM		Scale: 1:1
	MATERIAL: MECE 3-31		1/18/2010 4:13:17 PM		Midss: XXXX
	MATERIAL: MECE 3-31		1/18/2010 4:13:17 PM		SHEET 7 OF 14



SECTION C-C  
SCALE 1:1

<b>Nobes Lab</b> Contact: Dr. Nobes Email: david.nobes@ualberta.ca Phone: 780-492-7031 Comment:		UNLESS OTHERWISE SPECIFIED: DIMENSIONS ARE IN INCHES DECIMALS FRACTIONS TWO PLACE DECIMAL ± THREE PLACE DECIMAL ±		NAME: C-epi DRAWN: Eric Penner CHECKED: Eric Penner BIG APPR: Speed Code: ME07 Mech. Job #: 10057		The Department of Mechanical Engineering <b>UNIVERSITY OF ALBERTA</b> TITLE: <b>Mount Machined Bottom</b>	
MATERIAL: Aluminum Lab Location: MECE 3-31		PROJECT: Mount machined bottom Designer: epenner Date: 1/18/2010 4:13:17 PM Modified: January 18, 2010		Project: Cost II Project: Cost II SCALE: 1:1 / MIDSS: XXXX		REV: 2 SHEET 8 OF 14	

No Hidden Lines In this Sheet



16 x  $\phi$  0.201 THRU ALL  
1/4-20 UNC. THRU ALL

$\phi$  0.266 THRU ALL  
(1/4" Screw Clearance)

8 x  $\phi$  0.1  $\nabla$  0.4  
6-32 UNC.  $\nabla$  0.3  
(2x on each side)

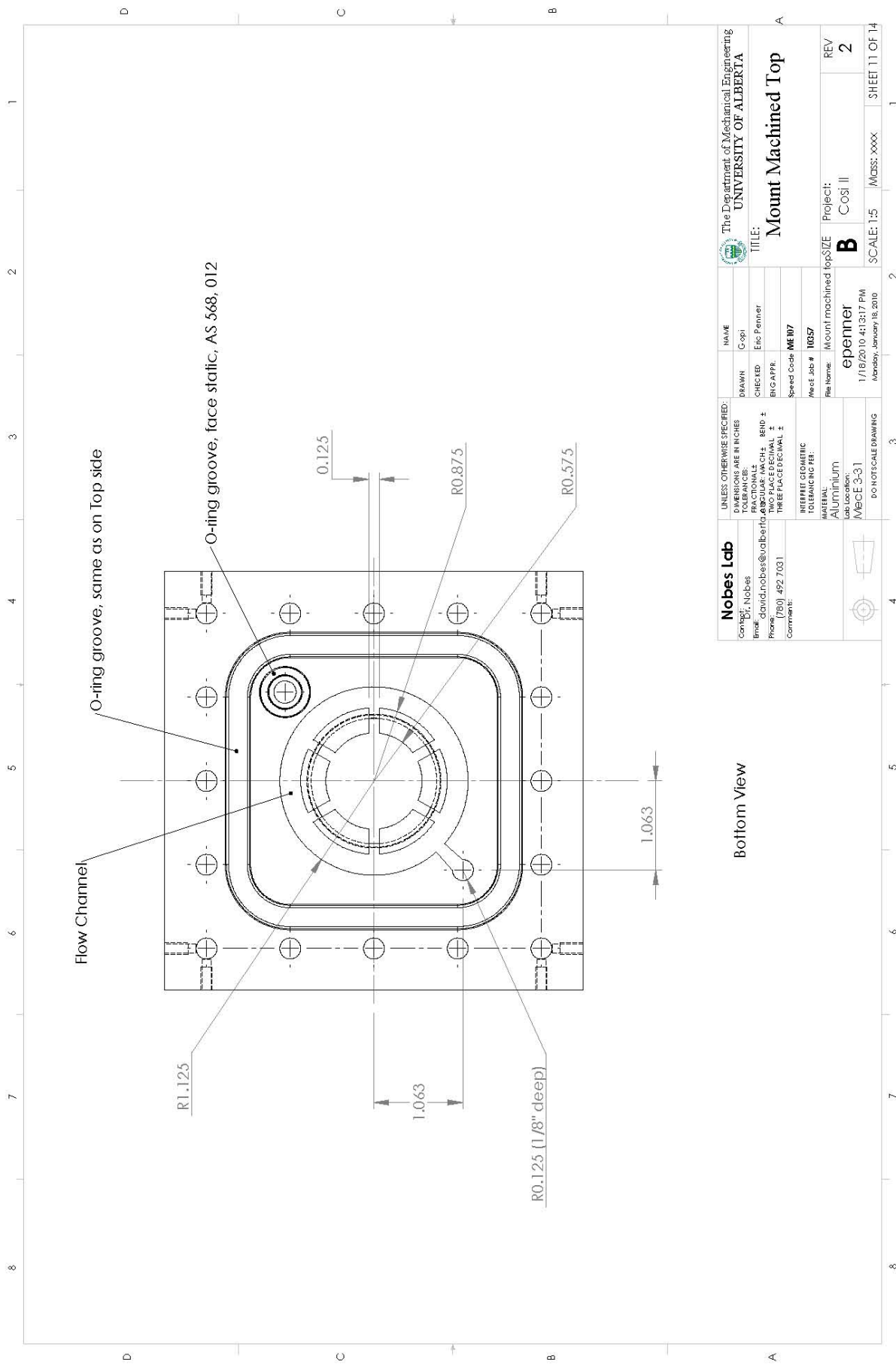
Straight Sides are okay

O-ring groove, female static, AS 568, 029  
(straight side walls acceptable)

SECTION D-D  
SCALE 1 : 1

<b>Nobes Lab</b>		UNLESS OTHERWISE SPECIFIED: DIMENSIONS ARE IN INCHES FRACTIONS DECIMALS		NAME C-epi	PROJECT Mount machined top	REV 2
CONTACT Dr. Nobes	EMAIL david.nobes@ualberta.ca	DATE 1/18/2010 4:13:17 PM	LAB LOCATION MECE 3-31	CHECKED Eric Penner	COST II B	SHEET 9 OF 14
PHONE (780) 492 7031	COMMENT			DESIGNED MEB07	SCALE 1:1	
				SPEED CODE MEB07		
				MATERIAL Aluminium		
				TOLENCING PER MEEC 3-31		
				INTERFER GEOMETRIC		
				FILE NAME epenner		
				DATE 1/18/2010 4:13:17 PM		
				DATE Monday, January 18, 2010		

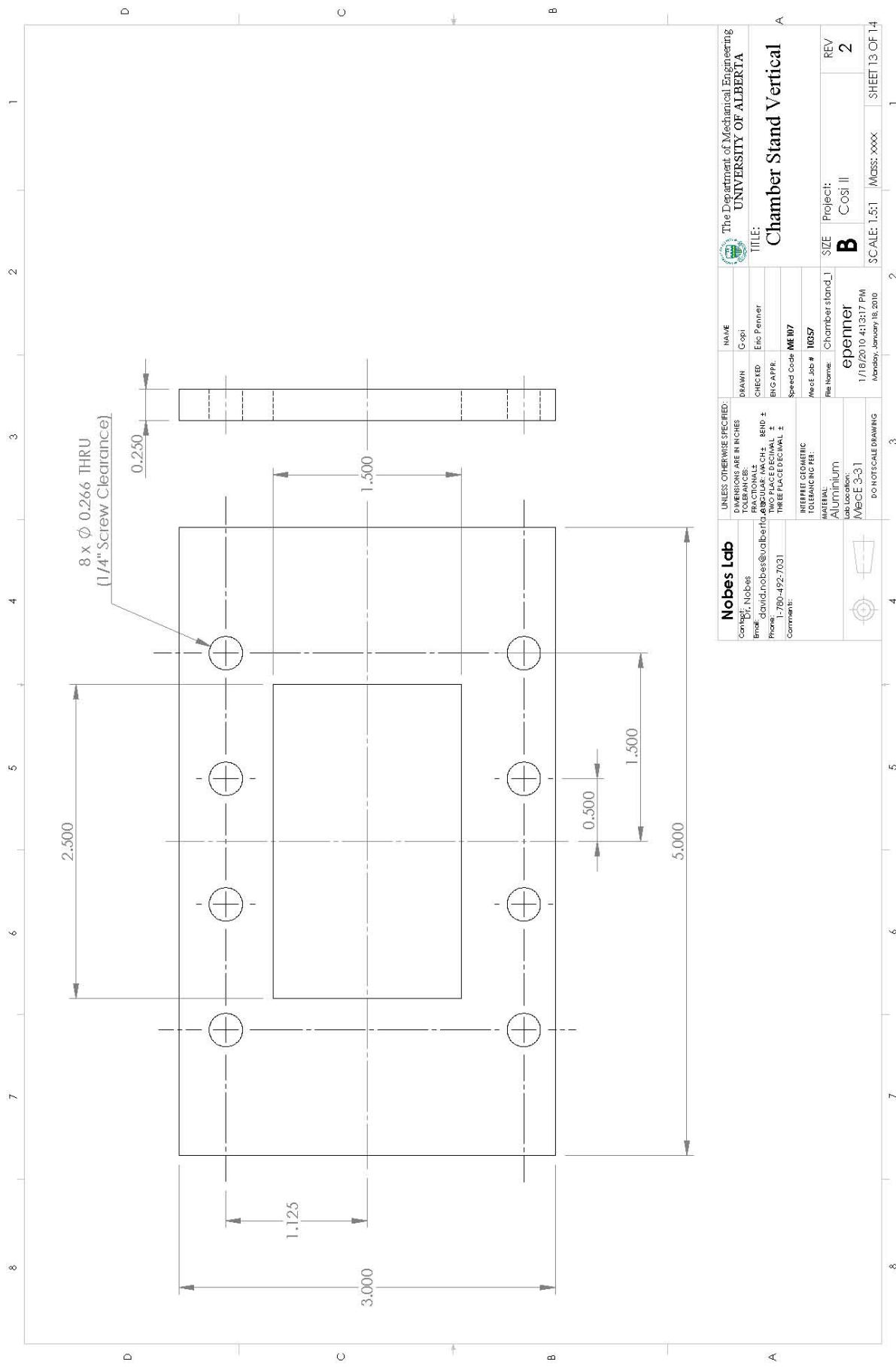




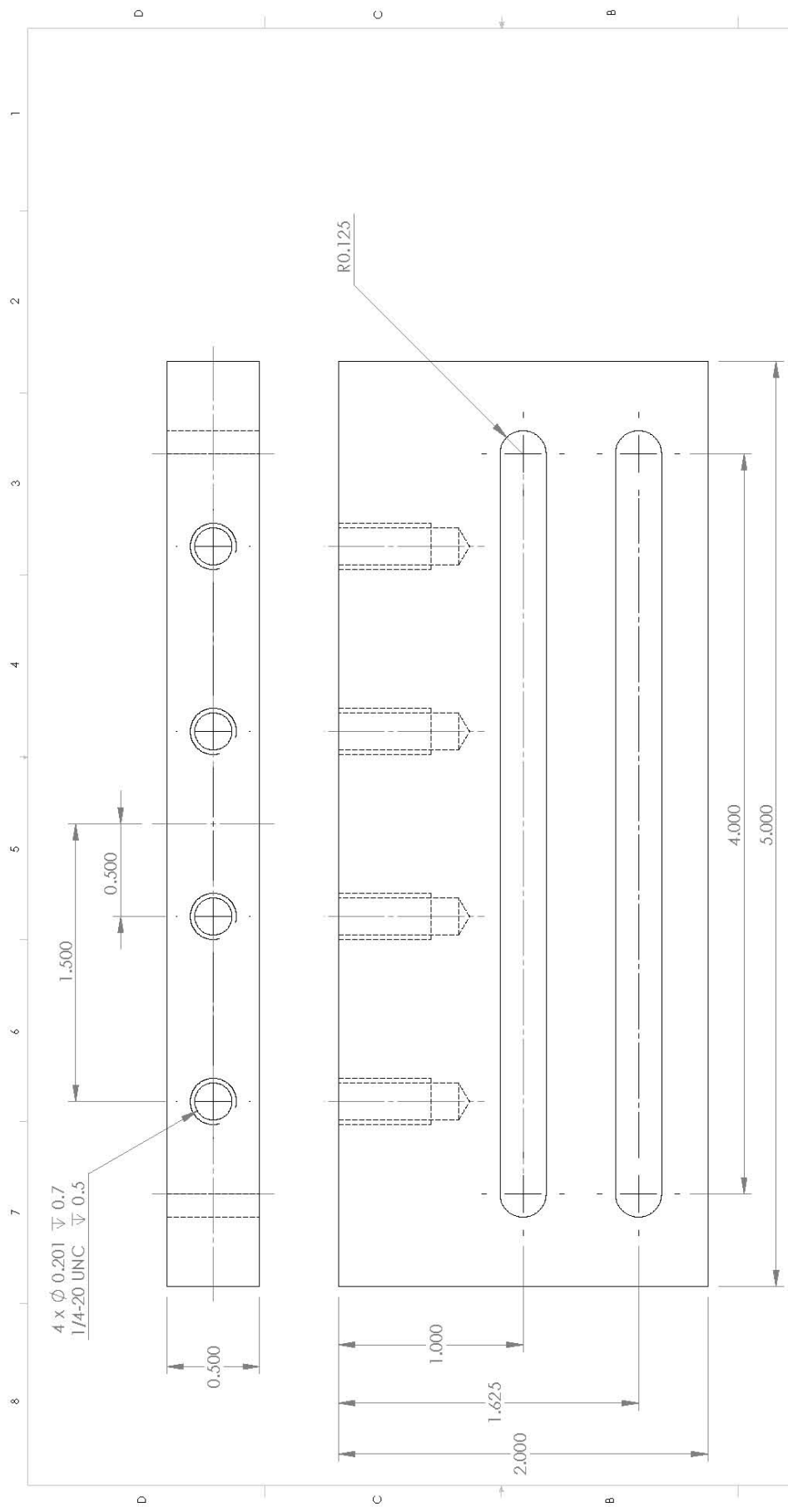
<b>Nobes Lab</b>		UNLESS OTHERWISE SPECIFIED: DIMENSIONS ARE IN INCHES DECIMALS FRACTIONS		NAME C-epi	The Department of Mechanical Engineering UNIVERSITY OF ALBERTA	
Contact: Dr. Nobes	Email: david.nobes@ualberta.ca	Phone: (780) 492-7031	Comment:	DRAWN Eric Penner	CHECKED Eric Penner	TITLE: <b>Mount Machined Top</b>
				BIG APPR:	SPEED CODE: <b>MEB07</b>	
					Mech Job # <b>10057</b>	
					Material: <b>Aluminum</b>	Project: <b>Cost II</b>
					Lab Location: <b>MECE 3-31</b>	Project Size: <b>B</b>
						REV <b>2</b>
						SCALE: 1:5
						MIDSS: XXXX
						SHEET 11 OF 14

Bottom View



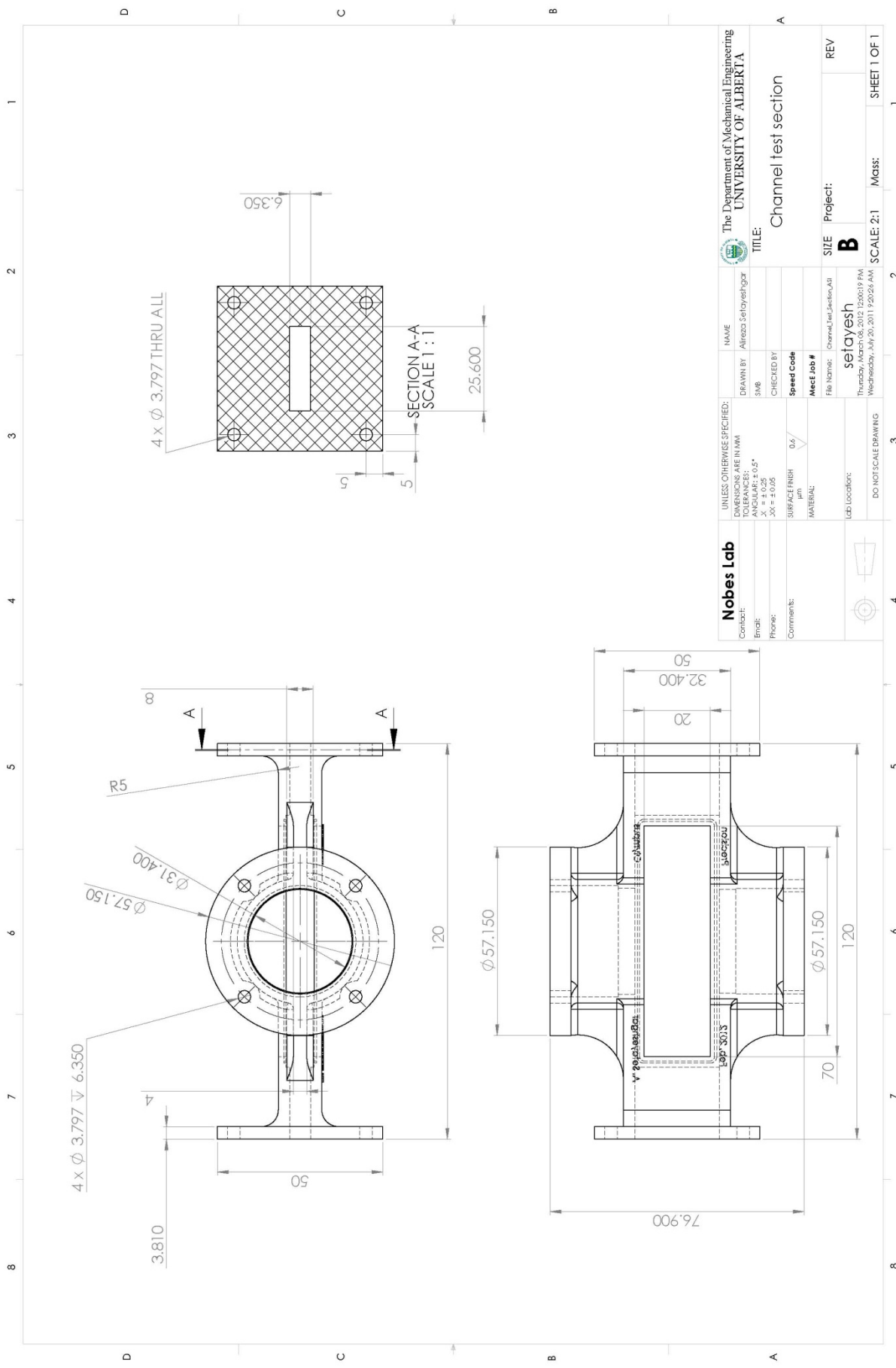


<b>Nobes Lab</b> Contact: Dr. Nobes Email: david.nobes@ualberta.ca Phone: 780-492-7031 Comment:		UNLESS OTHERWISE SPECIFIED: DIMENSIONS ARE IN INCHES DECIMALS FRACTIONS TWO PLACE DECIMAL THREE PLACE DECIMAL TOLERANCING PER:		NAME: C-epi DRAWN: Eric Penner CHECKED: MEB07 FILE NAME: Chamber stand.J FILE DATE: 1/18/2010 4:13:17 PM FILE LOCATION: M:\Mech\January 18, 2010	
The Department of Mechanical Engineering <b>UNIVERSITY OF ALBERTA</b>		TITLE: <b>Chamber Stand Vertical</b>		SIZE: <b>B</b> Project: <b>Cost II</b> REV: <b>2</b>	
SCALE: 1:5:1		MIDSS: XXXX		SHEET 13 OF 14	



<b>Nobes Lab</b> Contact: Dr. Nobes Email: david.nobes@ualberta.ca Phone: 780-492-7031 Comments:		UNLESS OTHERWISE SPECIFIED: DIMENSIONS ARE IN INCHES DECIMALS FRACTIONS ANGLES TWO PLACE DECIMAL ± THREE PLACE DECIMAL ±		NAME: C-ppi DRAWN: Eric Fenner CHECKED: BIGAPPR Speed Code: ME107 Weld Job #: 10357		The Department of Mechanical Engineering <b>UNIVERSITY OF ALBERTA</b> TITLE: <b>Chamber Stand Horizontal</b>	
MATERIAL: Aluminium Lab Location: MECE 3-31 DO NOT SCALE DRAWING		INTERFERE GEOMETRIC TOLERANCING FEE:		Project: Chamberstand_2 Cost II: epenner 1/18/2010 4:13:17 PM Monday, January 18, 2010		SIZE: B Project: Cost II REV: 2 SCALE: 2:1 MCSI: XXXX SHEET 14 OF 14	

## **APPENDIX B. ACOUSTIC CHANNEL DRAWINGS**



<b>Nobes Lab</b>		UNLESS OTHERWISE SPECIFIED: DIMENSIONS ARE IN MM TOLERANCES: FRACTIONS ± 0.25 X ± 0.25 XX ± 0.05		NAME: Alikas Setayeshgar	
Contract:	Drawn By:	Checked By:	Speed Code	The Department of Mechanical Engineering UNIVERSITY OF ALBERTA	
Email:	SMB	Mech Job #	File Name:	Channel test section	
Phone:	Surface Finish: 0.6 $\mu$ m	Lab Location:	Project:	Channel test section	
Comments:	DO NOT SCALE DRAWING	Scale:	Size:	REV	
			setayesh	B	
			Thursday, March 08, 2012 12:00:19 PM	SCALE: 2:1	
			Wednesday, July 20, 2011 9:29:26 AM	Mass:	
				SHEET 1 OF 1	

## APPENDIX C. MATLAB CODES

The codes written in MATLAB are associated with the PTV method and PDF model. The codes names with their brief descriptions are listed in the table below.

Code name	description
main.m	Main function in PTV code, for preprocessing, particle detection and tracking particles. It calls main_parameters_speculation.m, band_plotting and particle_detection.m,
main_parameters_speculation.m	Sets main parameters of PTV
band_plotting.m	Detecting particle bands for PTV
particle_detection	This sub-function detects the particle in PTV code, it include also the preprocessing processes.
find_particles_connections.m	Tracks the detected particles in PTV code
primary_force.m	Finds the normalized velocity of particles and compares that with primary acoustic force theory. It's input is the saved file of the find_particles_connections which is composed of tracked history of particles. This function calls filtering.m, velocity_calculation.m and gathering_velocities.m
filtering.m	Filters possible bubbles and short time history particles in the field-of-view, in PTV code
velocity_calculation.m	Calculates the velocity of tracked particles in PTV code
gathering_velocities	Maps particles velocity profile to a single wavelength in PTV code
Eacfit.m	Determination of acoustic energy density using the PDF model in PDF code

```
% main.m
```

```
% This program is written by Alireza Setayeshgar and is for detecting and  
% tracking particles separated by ultrasonic acoustic force. It calls some  
% other m files, including main_parameters_speculation.m,  
% banding_plotting.m, particle_detection.m, find_particles_connections.m.  
% Date: July 2012, Mechanical Engineering, University of Alberta
```

```
% clearing all variables  
clear;  
% closing all figures  
close all;  
% clearing the command area  
clc;
```

```
code_address = fileparts(mfilename('fullpath'));  
results_address = strcat(code_address, '\results');  
sources_address = strcat(code_address, '\sources');  
other_codes_address = strcat(code_address, '\other codes address');
```

```
addpath(code_address);  
addpath(results_address);  
addpath(sources_address);  
addpath(other_codes_address);
```

```
movie_pathname = uigetfile();
```

```
interval = 1; % Interval between the images for
```

```
% information of specific movie, it contains the time particles have  
% started to move toward PNS
```

```
list_info =  
[1,2,3,4,5,6,7,8,9,10,11,12,13,14,15;615,527,533,460,610,478,550,583,513,545,465,5  
24,536,353,515;866,700,675,547,660,866,700,660,610,620,790,720,625,420,573];
```

```
% list of movies to analyze and their info
```

```
avi_list = list_info(1,:);  
init_list = list_info(2,:);  
last_list = list_info(3,:);  
band_list = last_list;
```

```
avi_number_counts = 1:size(list_info,2);  
avi_list = avi_list(avi_number_counts);  
init_list = init_list(avi_number_counts);  
last_list = last_list(avi_number_counts);  
band_list = band_list(avi_number_counts);  
counter_n = length(avi_list);
```

```
for count_spec = 1 : counter_n  
    count_spec  
    avi_count = avi_list(count_spec);
```

```
avi_name = strcat(num2str(avi_count),'.avi');
save_file_name = strcat('p4_',movie_pathname((length(movie_pathname)- 1) :
end),'pdp = ',num2str(particle_detection_param),' ',avi_name(1:length(avi_name)-
3),'mat');
% start
cd(other_codes_address);
main_parameters_speculation;
banding_plotting;
particle_detection;
find_particles_connections
cd(sources_address);
save(save_file_name);
end
```

```
% band_plotting
```

```
This program is written by Alireza Setayeshgar and is  
% for detecting particle bands due to acoustic field.  
% Date: July 2012, Mechanical Engineering, University of Alberta
```

```
display('banding_plotting');
```

```
tic;  
cd(movie_pathname);
```

```
video = VideoReader(avi_name);  
num_frames = video.NumberOfFrames;  
image_size = [video.Width video.Height video.Width video.Height];  
rect = image_size.*image_crop;  
image_N_bands = floor(num_frames*image_N_bands_percent);
```

```
% Filtering the lines definition  
[b,a] = butter(2,[0.5],'low');
```

```
% number of image to analysis to find the bands from, in the band_address  
% folder, should be close to ending where the bands are stronger  
% image_N_bands = floor(num_frames*90/100);  
image_first_number = initial_image;
```

```
% loading the first image  
Frm = read(video,image_first_number);  
image_first = rgb2gray(Frm);  
image_first = imcrop(image_first,rect);
```

```
% finding the intensity of images and their time  
% Filtering the particles, if needed  
Intensity_first = mean(image_first);
```

```
% loading the first image  
Frm = read(video,image_N_bands);  
image_bands = rgb2gray(Frm);  
image_bands = imcrop(image_bands,rect);
```

```
% finding the intensity of images and their time  
% Filtering the particles, if needed  
Intensity = mean(image_bands);
```

```
% Filtering the intensity to remove the noises  
Filtered_Intensity = filter(b,a,Intensity);
```

```
% Second method for find the location of bands  
% In this method, using FFT Analysis, the distance between the bands is found.  
% Then by finding the most obvious band, which simply should have the  
% minimum intensity, the other bands are also found. By guessing the  
% location of other bands using the expected distance between the bands,
```

```

% the location of others are found.
% FFT Analysis

% putting the x axis values in a separate variable
Imagex = 1:size(image_bands,2);

T = Imagex(2)-Imagex(1); % Sample time(Here position(mm))
Fs = 1/T; % Sampling frequency (1/displacement)
L = length(Imagex); % Length of signal
t = (0:L-1)*T; % Generating the time(position)

% Finding the mean subtracted Intensity
Intensity_Fluctuation = Filtered_Intensity-mean(Filtered_Intensity);

NFFT = 2^nextpow2(L); % Next power of 2 from length of y
FFT_In_Fl = fft(Intensity_Fluctuation,NFFT)/L;
f = Fs/2*linspace(0,1,NFFT/2+1);

% finding the location of maximum of the spectrum which should be related
% to the wavelength of the system
spectrum = abs(FFT_In_Fl(1:NFFT/2+1));
difference = sign(diff(spectrum));
ddifference = (diff(difference));
incex1 = [false (ddifference == -2) false];
index = find(((incex1) == 1));
[maxfft, indexfft] = max(spectrum(index(2:end)));

% finding the wavelength which is simply twice the distance between the
% nodes
if shadow_or_laser == 1;wavelength = 2/f(index(indexfft+1));else wavelength =
2/f(index(indexfft+1));end
Filtered_Intensity = filter(b,a,Intensity);

% firstly, finding the location of the most obvious band
% [min_filtered_intensity index_filtered_intensity] = min(Intensity);
if shadow_or_laser == 1;
[min_filtered_intensity index_filtered_intensity] = min(Intensity);
else
[min_filtered_intensity index_filtered_intensity] = max(Intensity);
end

% the interval size in which the bandsk are to be found, this is chosen to
% be 15 percent of the wavelength. The index interval of that is saved.
span_changable_index = floor(0.15*wavelength/(Imagex(2)-Imagex(1)));

% The exoected distance between the bands are found.
bands_expected_distance_index = floor(wavelength/2/(Imagex(2)-Imagex(1)));

% starting to find the location of bands after the main band (right hand side of
that).
count = 1;

```

```

% leftspan is the most left side of interval in which the band is going to
% be found. Rightspan is the most right side of interval in which the band is
% going to
% be found.
leftspan = max(index_filtered_intensity+(bands_expected_distance_index*(count-1)-
span_changable_index),1);
rightspan = min(index_filtered_intensity+(bands_expected_distance_index*(count-
1)+span_changable_index),length(Imagex));
bandindexright = [];

% while we have not reached the right end of the data:
while ((rightspan<=length(Imagex)) && (leftspan>=0) && (rightspan>=1) &&
(leftspan<=length(Imagex)))

    % find the minimum of the intensity in thsi interval and relating that
    % to the band
    % [min_filtered_intensity_span index_filtered_intensity_span] =
min(Intensity(leftspan:rightspan));
    if shadow_or_laser == 1;
        [min_filtered_intensity_span index_filtered_intensity_span] =
min(Intensity(leftspan:rightspan));
    else
        [min_filtered_intensity_span index_filtered_intensity_span] =
max(Intensity(leftspan:rightspan));
    end

    % saving the index of that
    bandindexright(count) = index_filtered_intensity_span+leftspan-1;
    count = count+1;

    % finding the left side and right side of the interval
    leftspan = max(index_filtered_intensity+(bands_expected_distance_index*(count-
1)-span_changable_index),1);
    rightspan =
min(index_filtered_intensity+(bands_expected_distance_index*(count-
1)+span_changable_index),length(Imagex));
end

bands = Imagex(bandindexright);
bandsindex = bandindexright;

% starting to find the location of bands after the main band (right hand side of
that).
count = 1;

% leftspan is the most left side of interval in which the band is going to
% be found.
% rightspan is the most right side of interval in which the band is going to
% be found.
leftspan = max(index_filtered_intensity+(bands_expected_distance_index*(0-count)-
span_changable_index),1);
rightspan = min(index_filtered_intensity+(bands_expected_distance_index*(0-

```

```

count)+span_changable_index),length(Imagex));
bandindexleft = [];

% while we have not reached the right end of the data:
while ((rightspan<=length(Imagex)) && (leftspan>=0) && (rightspan>=1) &&
(leftspan<=length(Imagex)))
    % find the minimum of the intensity in thsi interval and relating that
    % to the band
    % [min_filtered_intensity_span index_filtered_intensity_span] =
min(Intensity(leftspan:rightspan));
    if shadow_or_laser == 1;
        [min_filtered_intensity_span index_filtered_intensity_span] =
min(Intensity(leftspan:rightspan));
    else
        [min_filtered_intensity_span index_filtered_intensity_span] =
max(Intensity(leftspan:rightspan));
    end
    % saving the index of that
    bandindexleft(count) = index_filtered_intensity_span+leftspan-1;
    count = count+1;
    % finding the left side and right side of the interval
    leftspan = max(index_filtered_intensity+(bands_expected_distance_index*(0-
count))-span_changable_index),1);
    rightspan = min(index_filtered_intensity+(bands_expected_distance_index*(0-
count))+span_changable_index),length(Imagex));
end

% putting them all together, (left and right hand side of the main band)
bands = [bands Imagex(bandindexleft)];
bands = sort(bands,'ascend');
bandsindex = [bandsindex bandindexleft];

% preparing the matrix for plotting
% filtering bands
if (abs(bands(2)-bands(1))>1.15*(abs(bands(3)-bands(2)))) | (abs(bands(2)-
bands(1))<0.85*(abs(bands(3)-bands(2))))
    bands=bands(2:end);
end
last_band=length(bands);
if (abs(bands(last_band)-bands(last_band-1))>1.15*(abs(bands(last_band-2)-
bands(last_band-1)))) | (abs(bands(last_band)-bands(last_band-
1))<0.85*(abs(bands(last_band-2)-bands(last_band-1))))
    bands=bands(1:(last_band-1));
end
bands_x_location = [bands' bands'];

if figure_spectrum_on
    figure;
    % Plot single-sided amplitude spectrum.
    plot(f,2*abs(FFT_In_F1(1:NFFT/2+1)), 'black');
    semilogx(f,2*abs(FFT_In_F1(1:NFFT/2+1)), 'black', 'Linewidth', 2);
    loglog(f,2*abs(FFT_In_F1(1:NFFT/2+1)), 'black', 'Linewidth', 2);
end

```

```

box on;
set(gca,'Linewidth',2,'FontSize',14);
xlabel('1/wavelength (1/(mm))','FontSize',14);
ylabel('Power Spectrum','FontSize',14)
end

if figure_intensity_on
figure;
hold on;
Intenplot = plot(Imagex,Intensity,'r','linewidth',2);
IntenplotFirst = plot(Imagex,Intensity_first,'b','linewidth',2);
box on;
set(gca,'Linewidth',2,'FontSize',14);
xlabel('Horizontal position(mm)','FontSize',18);
ylabel('Intensity','FontSize',18)
axislim = get(gca,'YLim');
bands_y_location = [ones(1,length(bands_x_location))*axislim(1)
ones(1,length(bands_x_location))*axislim(2)];
for i = 1:length(bands)
bandplot =
plot(bands_x_location(i,:),bands_y_location(i,:), 'black','linewidth',2);
end
LegendTitles = {'Intensity of banded image','Intensity of first
image','Bands'};
LegendPlots = [Intenplot;IntenplotFirst;bandplot];
legend(LegendPlots,legendTitles);
set(gcf,'PaperPositionMode','auto')
print -djpeg -r300 Spectrum1.jpg
end
toc;

```

```
% filtering.m
```

```

% This program is written by Alireza Setayeshgar and is for
% filtering possible bubbles in the field-of-view
% Date: July 2012, Mechanical Engineering, University of Alberta

```

```

filtered_particle_number=zeros(size(track_particle,1),1);
f_filtered_particle_number=zeros(size(track_particle,1),1);
filter_count = 1;
x_dataset = zeros(1,1);
y_dataset = zeros(1,1);
d_dataset = zeros(1,1);

```

```
% finding the direction of found particles
```

```

for i = 1:particle_count
one_direction = ...
abs(mean(sign(final_matrix(track_particle(i,2:track_particle(i,1)),4)-

```

```

final_matrix(track_particle(i,1:track_particle(i,1)-1),4));
    % filtering short history ones
    if ((track_particle(i,1) >= number_of_tracked_particles_criteria) &
one_direction>one_direction_criteria);
        x_dataset(filter_count,2:track_particle(i,1)) =
final_matrix(track_particle(i,2:track_particle(i,1)),4);
        y_dataset(filter_count,2:track_particle(i,1)) =
final_matrix(track_particle(i,2:track_particle(i,1)),5);
        d_dataset(filter_count,2:track_particle(i,1)) =
final_matrix(track_particle(i,2:track_particle(i,1)),6);
        x_dataset(filter_count,1) = track_particle(i,1);
        y_dataset(filter_count,1) = track_particle(i,1);
        d_dataset(filter_count,1) = track_particle(i,1);
        tracked_particle_number(filter_count)=i;
        filtered_particle_number(i)=filter_count;
        filter_count = filter_count+1;
    end
end

number_of_tracked_series = filter_count-1

% sorting anti-nodes
antinodes = zeros(size(bands_x_location,1)-1,1);
for i = 1:size(bands_x_location,1)-1
    antinodes(i) = (bands_x_location(i,1)+bands_x_location(i+1,1))/2;
end
antinodes = flipud(antinodes);
antinodes = sort(antinodes,'ascend');
antinodes = [antinodes(1)-wavelength/2;antinodes;antinodes(end)+wavelength/2];

% filtering bubbles from field-of-view
filter_count = 1;
x_dataset_filtered = x_dataset;
y_dataset_filtered = y_dataset;
d_dataset_filtered = d_dataset;
for i = 1:number_of_tracked_series
    [value index] = min(abs(x_dataset(i,2)-antinodes(:)));
    distance(1) = abs(x_dataset(i,2)-antinodes(index));
    distance(2) = abs(x_dataset(i,x_dataset(i,1))-antinodes(index));
    [value_band index_band] = min(abs(x_dataset(i,2)-bands(:)));
    distance_band(1) = abs(x_dataset(i,2)-bands(index_band));
    distance_band(2) = abs(x_dataset(i,x_dataset(i,1))-bands(index_band));
    if (distance(2)>distance(1)) && ((distance_band(2)<distance_band(1)))
        x_dataset_filtered(filter_count,1:x_dataset(i,1)) =
x_dataset(i,1:x_dataset(i,1));
        y_dataset_filtered(filter_count,1:y_dataset(i,1)) =
y_dataset(i,1:y_dataset(i,1));
        d_dataset_filtered(filter_count,1:d_dataset(i,1)) =
d_dataset(i,1:d_dataset(i,1));
        tracked_particle_number_filtered(filter_count)=tracked_particle_number(i);
    end
end
f_filtered_particle_number(tracked_particle_number_filtered(filter_count))=filter_

```

```

count;
    filter_count = filter_count+1;
end
end

number_of_tracked_series_filtered = filter_count-1;
[b,a] = butter(2,[0.5],'low');
x_dataset_filtered_f = x_dataset_filtered;
y_dataset_filtered_f = y_dataset_filtered;
for i = 1:number_of_tracked_series_filtered
    x_dataset_filtered_f(i,2:x_dataset_filtered(i,1)) =
filter(b,a,x_dataset_filtered(i,2:x_dataset_filtered(i,1)));
    y_dataset_filtered_f(i,2:y_dataset_filtered(i,1)) =
filter(b,a,y_dataset_filtered(i,2:y_dataset_filtered(i,1)));
end

% plotting x vs y
if figure_tracked_particles_image_on
    fig_tracked_particles_image_on = figure;
    set(0,'CurrentFigure',fig_tracked_particles_image_on);
    hold on;
    for i = 1:number_of_tracked_series
        plot(x_dataset(i,2:x_dataset(i,1)),y_dataset(i,2:y_dataset(i,1)),'-sr');
    end
    box on;
    set(gca,'Linewidth',2,'FontSize',14);
    xlabel('X position(mm)','FontSize',14);
    ylabel('Y position (mm)','FontSize',14)
    title('Different particles/bubbles in different images, recognized as the same
particle')
    axislim = get(gca,'YLim');
    bands_y_location = [ones(1,length(bands_x_location))*axislim(1)
ones(1,length(bands_x_location))*axislim(2)];
    for i = 1:length(bands)
        plot(bands_x_location(i,:),bands_y_location(i,:),'black');
    end
end

% plotting trajectories
if figure_particle_trajectory_on
    fig_particle_trajectory = figure;
    hold on;
    box on;
    set(gca,'Linewidth',2,'FontSize',14);
    xlabel('X position(mm)','FontSize',18);
    ylabel('Y position (mm)','FontSize',18)
    title('Particles trajectory, Bubbles filtered','FontSize',18);
    set(0,'CurrentFigure',fig_particle_trajectory);
    for i = 1:number_of_tracked_series_filtered

plot(x_dataset_filtered(i,2:Interval_for_plotting:x_dataset_filtered(i,1)),y_datas
et_filtered(i,2:Interval_for_plotting:y_dataset_filtered(i,1)),'-

```

```
dr', 'MarkerSize', 12, 'linewidth', 1.5);
    plot(x_dataset_filtered(i,2), y_dataset_filtered(i,2), '-dk');
end
axislim = get(gca, 'YLim');
bands_y_location = [ones(1, length(bands_x_location))*axislim(1)
ones(1, length(bands_x_location))*axislim(2)];
for i = 1:length(bands)
    h1 =
plot(bands_x_location(i,:), bands_y_location(i,:), 'black', 'linewidth', 1.5);
end
legend(h1, 'Particle bands', 'FontSize', 18);
print -djpeg -r150 trajectory.jpg
end
```

```

% find_particles_connections.m

% This program is written by Alireza Setayeshgar and is
% tracking particles separated by ultrasonic acoustic force.
% Date: July 2012, Mechanical Engineering, University of Alberta

display('Starting find_particles_connections');

tic;

% finding the image number of the last row which contains the first frame of
% images, from this number on, there will be second frame of the images
% starting. fifth column show the frame number, and 4th shows the image
% number.
ii = find((final_matrix(:,1)) == 1);
final_image_number = final_matrix(ii(end),3);
final_image_number_index = final_matrix(ii(end),2);

% Next task is finding the particle indices associated with each image. so
% ii is the matrix containing the indices of each image and then the result
% is stored in image_indices matrix.
image_indices = zeros(final_image_number,2);
% finding the corresponding image count number indices
for i = 1:final_image_number
    ii = find((final_matrix(1:final_image_number_index,3)-i) == 0);
    image_indices(i,:) = [ii(1) ii(end)];
end

% starting to track the particles, for each frame and for each frame, for
% each partice in that frame, it is started to look for the particle with
% same velocity and diamters in next frames. If this was successfull, they
% will be stored in track_particles matrix and also their first column in
% final_matrix matrix will be the number of recognized particle;
final_matrix=[final_matrix zeros(size(final_matrix,1),3)];

if (final_image_number_tracking == 0)
    final_image_number_tracking = final_image_number;
end
% indices of starting images
image_indices_start=image_indices(:,1);
% indices of ending images
image_indices_end=image_indices(:,2);
final_matrix_x_location=final_matrix(:,4);
final_matrix_y_location=final_matrix(:,5);
final_matrix_diam=final_matrix(:,6);
next_particle_indice=[];
previous_particle_indice=[];

for pari = 1:final_image_number_tracking-1
    for j = image_indices_start(pari):image_indices_end(pari)

```

```

    particle_expected_position_x = final_matrix_x_location(j);
    particle_expected_position_y = final_matrix_y_location(j);
    % finding the distance between neighbors
    Residual = ...

x_position_weight*abs(final_matrix_x_location(image_indices_start(pari+1):image_in
dices_end(pari+1))-particle_expected_position_x)+...

y_position_weight*abs(final_matrix_y_location(image_indices_start(pari+1):image_in
dices_end(pari+1))-particle_expected_position_y)+...

diameter_weight*abs(final_matrix_diam(image_indices_start(pari+1):image_indices_en
d(pari+1))-final_matrix_diam(j));
    [value next_particle_index] = min(Residual);
    % finding the corresponding index in the other image
    particle_index=next_particle_index+image_indices_end(pari);
    if (abs(final_matrix_x_location(particle_index)-
particle_expected_position_x)<maximum_error_x &
abs(final_matrix_y_location(particle_index)-
particle_expected_position_y)<maximum_error_y)
        next_particle_indice=[next_particle_indice;particle_index];
        previous_particle_indice=[previous_particle_indice;j];
    end
end
end

final_matrix(next_particle_indice,7) = previous_particle_indice;
particle_count = 0;
for i = 1 : total_number_of_particles
    if (final_matrix(i,7) == 0)
        particle_count = particle_count + 1;
        final_matrix(i,8) = particle_count;
    else
        final_matrix(i,8) = final_matrix(final_matrix(i,7),8);
    end
end
end
% Tracking the particles
particle_count1 = 1;
for j = 1 : particle_count
    indices = find(final_matrix(:,8) == j);
    if length(indices) > 10
        track_particle(particle_count1,2:length(indices) + 1 ) = indices;
        track_particle(particle_count1, 1 ) = length(indices);
        particle_count1 = particle_count1 + 1;
    end
end
end
particle_count = particle_count1 - 1;
toc;

```

```

% gathering_velocities.m

% This program is written by Alireza Setayeshgar and is
% for mapping all of the velocities to one single wavelength
% Date: July 2012, Mechanical Engineering, University of Alberta

display('gathering velocity');
tic;
normalized_location_velocity = linspace(0,(wavelength/2),100);
normalized_velocity = [];
simulation_normalized_velocity = [];
if figure_normalized_velocity_on
    fig_normalized_velocity = figure;
end
if figure_simulation_normalized_velocity_on
    fig_simulation_normalized_velocity = figure;
end

% main loop
for i = 1:number_of_tracked_series_filtered
    distance =
abs((location_velocity(i,2)+(location_velocity(i,location_velocity(i,1))))/2-
antinodes);
    [value index] = min(distance);
    if
((location_velocity(i,2)+(location_velocity(i,location_velocity(i,1))))/2<antinode
s(index))
        index = index-1;
    end
    if index == 0
        reference = antinodes(1)-wavelength/2;
    else
        reference = antinodes(index);
    end

    location_velocity(i,2:location_velocity(i,1)) =
location_velocity(i,2:location_velocity(i,1))-reference;
    [B INX] = sort(location_velocity(i,2:location_velocity(i,1)));
    for test=1:100
        B(diff(B) == 0) = B(diff(B) == 0)+10^9*eps;
    end
    atemp(INX) = B;
    % finding the location of particle in series
    xn_location_velocity(i,2:location_velocity(i,1)) = atemp(1:length(INX));
    xn_location_velocity(i,1) = location_velocity(i,1);
    % sort particles locations
    matrix_to_sort=[xn_location_velocity(i,2:xn_location_velocity(i,1))'
velocity_calculated(i,2:velocity_calculated(i,1))'];
    matrix_to_sort=sortrows(matrix_to_sort,1);
    xn_location_velocity(i,2:xn_location_velocity(i,1))=matrix_to_sort(:,1);
    % calculating velocity

```

```

velocity_calculated(i,2:velocity_calculated(i,1))=matrix_to_sort(:,2);
normalized_velocity(i,:) =
interp1(xn_location_velocity(i,2:xn_location_velocity(i,1)),velocity_calculated(i,
2:velocity_calculated(i,1)),normalized_location_velocity);
% plotting normalized velocity
if figure_normalized_velocity_on
    set(0,'CurrentFigure',fig_normalized_velocity);
    hold on;

plot(normalized_location_velocity,normalized_velocity(i,:),properties2{mod(i,5)+1}
);

text(normalized_location_velocity(find(isfinite(normalized_velocity(i,:)),1)),norm
alized_velocity(i,find(isfinite(normalized_velocity(i,:)),1)),num2str(i),'FontSize
',16);
end
if figure_simulation_normalized_velocity_on
    set(0,'CurrentFigure',fig_simulation_normalized_velocity);
    hold on;

plot(normalized_location_velocity,simulation_normalized_velocity(i,:),properties2{
mod(i,5)+1});

text(normalized_location_velocity(find(isfinite(normalized_velocity(i,:)),1)),simu
lation_normalized_velocity(i,find(isfinite(normalized_velocity(i,:)),1)),num2str(i
),'FontSize',16);
end
end

% averaging
avg_normalized_velocity = nanmean(normalized_velocity,1);
std_normalized_velocity = nanstd(normalized_velocity,0,1);

% setting the normalized velocity plot
if figure_normalized_velocity_on;
    set(0,'CurrentFigure',fig_normalized_velocity);
    hold on;
    box on;
    set(gca,'Linewidth',2,'FontSize',14);
    xlabel('X postion(mm)','FontSize',14);
    ylabel('X velocity (mm/s)','FontSize',14)
    title('Velocity of different particles in different images, recognized as the
same particle moved...');
    axislim = get(gca,'YLim');
    bands_y_location = [axislim(1) axislim(2)];
    plot(wavelength/4*ones(2,1),bands_y_location,'black');
    plot(zeros(2,1),bands_y_location,'red-.');
    plot(wavelength/2*ones(2,1),bands_y_location,'red-.');
    set(gcf, 'Position', get(0,'Screensize')); % Maximize figure.
end
% plotting the errorbars
if figure_avg_normalized_velocity_on
    % plotting all of the particles in one figure with dot symbol, the

```

```

% number of each particle can be written beside it as well.
fig_avg_normalized_velocity = figure;
hold on;
plot(normalized_location_velocity,avg_normalized_velocity,'-
blacks','MarkerSize',10);

errorbar(normalized_location_velocity,avg_normalized_velocity,std_normalized_veloc
ity);
axislim = get(gca,'YLim');
bands_y_location = [axislim(1) axislim(2)];
plot(wavelength/4*ones(2,1),bands_y_location,'black');
plot(zeros(2,1),bands_y_location,'red-.');
plot(wavelength/2*ones(2,1),bands_y_location,'red-.');
box on;
set(gca,'Linewidth',2,'FontSize',14);
xlabel('X position(mm)','FontSize',14);
ylabel('Average X velocity (mm/s)','FontSize',14)
plot(normalized_location_velocity,velocity_theoretical,'-
.black','linewidth',3);
set(gcf, 'Position', get(0,'Screensize')); % Maximize figure.
end

```

```

% making a movie of particles, tracked in field-of-view
if mov_particles_detected_on
    display('movie creation');
    image_particle_number=ones(500,30);
    for i=1:length(tracked_particle_number_filtered)
        for j=2:track_particle(tracked_particle_number_filtered(i),1)
            image_number =
final_matrix(track_particle(tracked_particle_number_filtered(i),j),3);

image_particle_number(image_number,image_particle_number(image_number,1)+1)=track_
particle(tracked_particle_number_filtered(i),j);

image_particle_number(image_number,1)=image_particle_number(image_number,1)+1;
        end
    end
    first_image_number = 1;
    last_image_number=length(find(image_particle_number(:,1)>1));
    fig = figure(200);
    count=1;
    for frm = first_image_number : last_image_number
        Frm = aviread(avi_name,frm+initial_image-1);
        Img = Frm(1).cdata;
        Img = imcrop(Img,rect);
        imshow(Img);
        hold on;
        for k = 2:image_particle_number(frm,1)
            H =
circle(final_matrix(image_particle_number(frm,k),4:5),sqrt(final_matrix(image_part
icle_number(frm,k),6)/pi),100,properties3{mod(final_matrix(image_particle_number(f
rm,k),8),5)+1});

```

```
text(final_matrix(image_particle_number(frm,k),4),final_matrix(image_particle_number(frm,k),5),num2str(f_filtered_particle_number(final_matrix(image_particle_number(frm,k),8))), 'color',properties4{mod(final_matrix(image_particle_number(frm,k),8),5)+1});
    end
    F(count) = getframe(fig);
    clf;
    count=count+1;
end
movie2avi(F, 'movie.avi');
end
toc;
```

```
% main_parameters_speculation.m
```

```
% This program is written by Alireza Setayeshgar. It sets the main parameters  
% for the PTV program for finding particle velocity in an acoustic field.  
% Date: July 2012, Mechanical Engineering, University of Alberta
```

```
% Finding the number of cores of the computer,  
% to use all for some for loops  
NumberOfCores = System.Environment.ProcessorCount;  
if (matlabpool('size')>0); matlabpool close; end
```

```
% name of mat file to be stored  
results_name = strcat(avi_name((length(avi_name)-3):end), '.mat');  
% 1 for Shadowgraphy technique and 2 for laser  
shadow_or_laser = 2;
```

```
figure_imgpreprocess_on = 0;  
figure_detection_on = 0;  
figure_number_of_particles_on_off = 0;  
figure_spectrum_on = 0;  
figure_intensity_on = 0;  
figure_band_location_time_on = 0;  
figure_band_time_on = 0;  
figure_tracked_particles_image_on = 0;  
figure_particle_trajectory_on = 0;  
figure_velocity_original_location_on = 0;  
figure_normalized_velocity_on = 0;  
figure_simulation_normalized_velocity_on = 0;  
figure_avg_normalized_velocity_on = 0;  
figure_avg_simulation_normalized_velocity_on = 0;  
figure_diameter_distribution_on = 0;  
mov_particles_detected_on = 0;  
properties = {'-blues', '-blackd', '-greens'};  
properties2 = {'-m*', '-co', '-red^', '-blues', '-greeno'};  
properties3 = {'-m', '-c', '-red', '-blue', '-green'};  
properties4 = {'magenta', 'cyan', 'red', 'blue', 'green'};
```

```
% The main criteria for detection of particles
```

```
% minimum area of the particle  
minimum_area_criteria = 1;  
% maximum area of the particle  
maximum_area_criteria = 15;  
% disk size for preprocessing  
StrelDiskSize = 4;  
% crop size of the image  
image_crop = [10 10 80 80]/100;  
% the last image number percent  
last_image_finding_factor = 0.7;  
% Banding image percent  
image_N_bands_percent = 0.9;
```

```

% The particle detection parameter for thresholding
particle_detection_param = 1;
% calculation of the primary acoustic force
std_calculation;

% Particle Tracking parameters

% delta_time is the time between two consecutive frames
delta_time = 1e-3;

% in plotting the bands over time, number of the images over which the
% bands are plotted are
image_N_band_timing = [130 700];

% The index number of the last image which the tracking should be performed
% up to.
final_image_number_tracking = 0;

% The interval for plotting the trajectory of the particles in one image
Interval_for_plotting = 2;

% pause time for plotting the first figure
pausetime = 0.01;

% number of times to do denoising using imopen command
numdenoising = 1;

% parameters to find the best choice for the consecutive particles in successive
diameter_weight = 1;
x_position_weight = 10;
y_position_weight = 10;
maximum_error_x = 1;
maximum_error_y = 1;

% finding the address of the mfile(code_address), adding the address to the path,
doing
% the same for the pivmat(pivaddress).
% This is done since while running the code, the local folder is changed to
% different folders containing data,
addpath(code_address);
addpath(results_address);
addpath(movie_pathname);

```

```

% particle_detection.m

% This program is written by Alireza Setayeshgar and is for
% detection of particles.
% Date: July 2012, Mechanical Engineering, University of Alberta

display('Starting particle_detection');
tic;

cd(movie_pathname);

% List of particles definition
particle_list = [];

% starting the figure
scrsz = get(0,'ScreenSize');
if figure_detection_on
    fig_detection = figure('Position',[1 scrsz(4)/2 scrsz(3)/2 scrsz(4)/2]);
end

% number of images to analysis
NumParFor = floor((last_image_number-initial_image)/interval)+1;
number_of_particle_found = zeros(NumParFor,1);
for ParCounter = 1 : NumParFor

    % frame number
    frm = initial_image + interval * (ParCounter-1);
    % reading the frame
    Frm = read(video,frm);
    Img = rgb2gray(Frm);
    % cropping the image
    Img = imcrop(Img,rect);
    % shoowing a sample o fthe images
    if figure_imgpreprocess_on figure;imshow(Img);set(gcf,'Position',[1 scrsz(4)/2
scrsz(3)/2 scrsz(4)/2]);title(num2str(frm));end
    if shadow_or_laser == 1; Img_Com = imcomplement(Img);else; Img_Com = Img; end
    background1 = imopen(Img_Com,strel('disk',StrelDiskSize));
    Img_noNoise = Img_Com-background1;
    % threshold
    threshold(ParCounter) = graythresh(Img_noNoise);
    avgin(ParCounter) = mean(mean(Img_noNoise));
    Img_bw = im2bw(Img_noNoise,threshold(ParCounter)*particle_detection_param);
    se = strel('disk',3);
    I = imerode(Img_bw,se);
    figure;
    imshow(I);
    I = Img_bw;
    if figure_imgpreprocess_on
figure;imshow(I);title('I');set(gcf,'Position',[scrsz(3)/2 scrsz(4)/2 scrsz(3)/2
scrsz(4)/2]);end

```

```

[B,L] = bwboundaries(I,'noholes');
STATS = regionprops(I,'Centroid','Area');
founds(ParCounter) = length(STATS);
% checking the conditions of the particles
idx = find(([STATS.Area] > minimum_area_criteria) & ([STATS.Area] <
maximum_area_criteria));
filtered_results = [reshape([STATS(idx).Centroid],2,length(idx))'
[STATS(idx).Area]'];
% showing the detected particles in image
if figure_detection_on
    figure;
    imshow(Img);
    set(gcf,'Position',[scrsz(3)/2 1 scrsz(3)/2 scrsz(4)/2]);
    hold on;
    pause(pausetime);
    for k = 1:size(filtered_results,1)
        H =
circle(filtered_results(k,1:2),sqrt(filtered_results(k,3)/pi),100,'r-');
    end
    title(strcat('frame number: ',num2str(frm),' particles found:
',num2str(size(filtered_results,1))));
    end
    number_of_particle_found(ParCounter) = size(filtered_results,1);
    filtered_results = [ones(size(filtered_results,1),1)*ParCounter
filtered_results];
    particle_list = [particle_list;filtered_results];
end
std_number_of_particle_found = std(number_of_particle_found);
mean_number_of_particle_found = mean(number_of_particle_found);
if figure_number_of_particles_on_off
    plot(number_of_particle_found);
    title(strcat('standard deviation: ',std_number_of_particle_found));
end
% setting the particles list
final_image_number = initial_image + interval * (NumParFor-1);
total_number_of_particles = size(particle_list,1);
particle_list=sortrows(particle_list,1);
% this is the main matrix, containing the particles list in all of the images
final_matrix = [ones(total_number_of_particles,1)...
(1:total_number_of_particles)' particle_list];
toc;

```

```
% primary_force.m
```

```
% This program is written by Alireza Setayeshgar and is  
% finding the velocity of particles and comparing that with primary acoustic force  
% theory
```

```
% Date: July 2012, Mechanical Engineering, University of Alberta
```

```
% clearing all variables
```

```
clear;
```

```
% closing all figures
```

```
close all;
```

```
% clearing the command area
```

```
clc;
```

```
code_address = fileparts(mfilename('fullpath'));
```

```
results_address = strcat(code_address, '\results');
```

```
sources_address = strcat(code_address, '\sources');
```

```
other_codes_address = strcat(code_address, '\other codes address');
```

```
addpath(code_address);
```

```
addpath(results_address);
```

```
addpath(sources_address);
```

```
addpath(other_codes_address);
```

```
movie_pathname = uigetfile();
```

```
counter_n = length(avi_list);
```

```
% The criteria which determines the relative direction
```

```
one_direction_criteria = 0.25;
```

```
% The interval between images to calculate the velocity
```

```
interval = 1; % Interval between the images for
```

```
%start
```

```
normalized_velocity_all = [];
```

```
max_velocity = zeros(1,counter_n);
```

```
particle_numbers = zeros(1,counter_n);
```

```
for counter = 1 : 1 : counter_n
```

```
    avi_name = strcat(num2str(avi_list(counter)), '.avi');
```

```
    save_file_name = strcat('p4_', movie_pathname((length(movie_pathname)- 1) :  
end), 'pdp = ', num2str(particle_detection_param), ', ', avi_name(1:length(avi_name)-  
3), 'mat');
```

```
    cd(sources_address);
```

```
    load(save_file_name);
```

```
    % condition on number of tracked series
```

```
    number_of_tracked_particles_criteria = 10;
```

```
    % delta_time_shift
```

```
    k_interval = 12;
```

```

figure_avg_normalized_velocity_on = 0;
cd(other_codes_address);
% filtering bubbles and short history particles
filtering;
% calculating velocity
velocity_calculation;
% mapping and normalizing velocity
gathering_velocities;
max_velocity(counter) = max(nanmean(normalized_velocity,1));
normalized_velocity = normalized_velocity/max_velocity(counter);
normalized_velocity_all = [normalized_velocity_all;normalized_velocity];
particle_numbers(counter) = number_of_tracked_series_filtered;
end
display('finished with different movies');

avg_normalized_velocity_all = nanmean(normalized_velocity_all,1);
std_normalized_velocity_all = nanstd(normalized_velocity_all,1);

maximum_velocity = max(avg_normalized_velocity_all);
avg_normalized_velocity_all = avg_normalized_velocity_all / maximum_velocity;
velocity_theoretical = sin(2*pi/(wavelength/2)*normalized_location_velocity);
velocity_std = velocity_theoretical * velocity_relative_variation;

% finding error wrt theoretical values
randomn_particles_number = size(normalized_velocity_all,1);
counter_n = length(randomn_particles_number);
avg_velocity_error_all_partial = zeros(1,counter_n);
for counter = 1 : counter_n
    avg_normalized_velocity_all_partial =
nanmean(normalized_velocity_all(1:randomn_particles_number(counter),:),1);
    avg_normalized_velocity_all_partial(1) = nan;
    avg_normalized_velocity_all_partial(end) = nan;
    avg_velocity_error_all_partial(counter) =
nanmean(abs((avg_normalized_velocity_all_partial -
velocity_theoretical)./velocity_theoretical)) * 100;
end
% acoustic energy density
wave_wavelength = fluid_speed_of_sound / wave_frequency;
normalized_location_velocity = normalized_location_velocity * wave_wavelength /
wavelength * 1000;
max_velocity = max_velocity * wave_wavelength / wavelength;
max_force = max_velocity * (3 * pi * viscosity * particle_diameter);
Eac = max_force / (3 * particle_volume * phi * k_wave);

set(0, 'DefaultAxesFontName', 'Times New Roman');
set(0, 'DefaultUIControlFontName', 'Times New Roman');
set(0, 'defaultUitableFontName', 'Times New Roman');
set(0, 'defaultTextFontName', 'Times New Roman');
set(0, 'defaultUipanelFontName', 'Times New Roman');

% finding the lower variation and higher one
min_variation = velocity_theoretical - velocity_std;

```

```

max_variation = velocity_theoretical + velocity_std;

font_size=12;
line_width_size = 1;
marker_size = 6;
figure1= figure('Color',[1 1 1]);
set(gcf,'PaperUnits','centimeters');
xSize = 15; ySize = 10;
xLeft = (21-xSize)/2; yTop = (30-ySize)/2;
set(gcf,'PaperPosition',[xLeft yTop xSize ySize])
set(gcf,'Position',[1 1 xSize*50 ySize*50])
box('on');
hold on;
exp_interval_plot = 5;
theo_interval_plot = 3;
plot(normalized_location_velocity(1:exp_interval_plot
:end),avg_normalized_velocity_all(1:exp_interval_plot:end),'-
blues','MarkerSize',marker_size,'linewidth',line_width_size);
plot(normalized_location_velocity,velocity_theoretical,'--
black','linewidth',line_width_size);
plot(normalized_location_velocity,min_variation,'-
black','linewidth',line_width_size);
legend('Exp.','Theo.','Theo. var. ');
errorbar(normalized_location_velocity(1:exp_interval_plot:end),avg_normalized_velo
city_all(1:exp_interval_plot:end),std_normalized_velocity_all(1:exp_interval_plot:
end),'linewidth',line_width_size);
plot(normalized_location_velocity,max_variation,'-
black','linewidth',line_width_size);
box on;
set(gca,'Linewidth',line_width_size,'FontSize',font_size);
xlabel('Horizontal location (mm)','FontSize',font_size);
ylabel('Normalized horizontal velocity','FontSize',font_size)
cd(results_address);
print -djpeg -r300 exp_theoretical_variation.jpg
print -dps exp_theoretical_variation.eps

```

```
% velocity_calculation.m
```

```
% This program is written by Alireza Setayeshgar and  
% is for calculating the velocity of particles  
% Date: July 2012, Mechanical Engineering, University of Alberta
```

```
velocity_calculated = x_dataset_filtered;  
location_velocity = x_dataset_filtered;  
for i = 1:number_of_tracked_series_filtered  
    diam(i) = mean(d_dataset_filtered(i,2:d_dataset_filtered(i,1)));  
    stddiam(i) = std(d_dataset_filtered(i,2:d_dataset_filtered(i,1)));  
    velocity_calculated(i,2:(x_dataset_filtered(i,1)-k_interval)) =  
(x_dataset_filtered(i,(2+k_interval)):x_dataset_filtered(i,1))-  
x_dataset_filtered(i,2:(x_dataset_filtered(i,1)-  
k_interval)))/(k_interval*delta_time);  
    location_velocity(i,2:(x_dataset_filtered(i,1)-k_interval)) =  
(x_dataset_filtered(i,(2+k_interval)):x_dataset_filtered(i,1))+x_dataset_filtered(i,  
2:(x_dataset_filtered(i,1)-k_interval)))/2;  
    velocity_calculated(i,1) = (x_dataset_filtered(i,1)-k_interval);  
    location_velocity(i,1) = (x_dataset_filtered(i,1)-k_interval);  
end
```

```
if figure_velocity_original_location_on  
    fig_velocity_original_location = figure;  
    hold on;  
    set(0,'CurrentFigure',fig_velocity_original_location);  
    for i = 1:number_of_tracked_series_filtered  
  
        plot(location_velocity(i,2:location_velocity(i,1)),velocity_calculated(i,2:velocity_calculated(i,1)),properties2{mod(i,5)+1});  
  
        text(location_velocity(i,2),velocity_calculated(i,2),num2str(i),'FontSize',16);  
        end  
        box on;  
        set(gca,'Linewidth',2,'FontSize',14);  
        xlabel('X position(mm)','FontSize',14);  
        ylabel('X velocity (mm/s)','FontSize',14)  
        title('Velocity of different particles in different images, recognized as the same particle');  
        axislim = get(gca,'YLim');  
        bands_y_location = [ones(1,length(bands_x_location))*axislim(1)  
ones(1,length(bands_x_location))*axislim(2)];  
        for i = 1:length(bands)  
            plot(bands_x_location(i,:),bands_y_location(i,:),'black');  
        end  
        line_antinodes = [antinodes antinodes];  
        antinodes_y_location = [ones(1,length(antinodes))*axislim(1)  
ones(1,length(antinodes))*axislim(2)];  
        for i = 1:length(antinodes)  
            plot(line_antinodes(i,:),antinodes_y_location(i,:),'red-.');  
        end  
    end
```

end

```
% Eacfit.m
```

```
% This program is written by Alireza Setayeshgar and is for determining  
% acoustic energy density by fitting a PDF of final location of particles to  
% intensity envelope of acoustophoresis densification.
```

```
% Date: September 2013, Mechanical Engineering, University of Alberta
```

```
% location_id is the location in the intensity envelope  
% intensity_test_normalized is the intensity in intensity envelope  
% Eac is the fitted acoustic energy density  
% shift is the allowed shift of centre of graphs for fitting  
% R is the residual for all of the locations  
% Ifit is the output of the fitting function compared with the intensity  
% plot
```

```
function [Eac, shift, R, Ifit] =  
Eacfit(location_id,intensity_test_normalized,const,test_times);
```

```
x0 = [1 1e-4];  
myfun2 = @(x,t) uniform_function(x,location_id,const,test_times);  
location = location_id(:,1);  
id = location_id(:,2);
```

```
options = statset(...  
    'tolx',1e-8,...  
    'tolfun',1e-8,...  
    'funvalcheck','on',...  
    'display','off');
```

```
main fitting  
[x,R,J,CovB,MSE] =  
nlinfit(location_id,intensity_test_normalized,myfun2,x0,options);
```

```
% fitted parameters
```

```
Eac = x(1);  
shift = x(2);
```

```
% Calculate fitted intensity
```

```
Ifit = uniform_function([Eac;shift],location_id,const,test_times);
```

```
% main PDF function
```

```
function Intensity = uniform_function(x,location_id,const,test_times)  
location = location_id(:,1);  
id = location_id(:,2);  
Eac = x(1);  
shift = x(2);  
A = 3 * const.eta / (4*const.Phi * (pi*const.a/const.w)^2);  
relative = exp((test_times)/(A / Eac));  
Intensity = (((exp(-(test_times(id))/(A / Eac)))) ./ ((exp(-(test_times(id))./(A  
./ Eac))).^2 .* (sin(pi ./ const.w .* (location - shift))) .^ 2 + (cos(pi ./  
const.w * (location - shift))).^2))) / relative;
```